Broadly Tunable External Cavity Quantum Cascade Laser

zur Erlangung des akademischen Grades
doctor rerum naturalium
(Dr. rer. nat.)
im Fach Physik
eingereicht an der

Mathematisch-Naturwissenschaftlichen Fakultät
der Humboldt Universität zu Berlin

von

M.Sc. Yohei Matsuoka

Präsidentin der Humboldt-Universität zu Berlin
Prof. Dr.-Ing. Dr. Sabine Kunst

Dekan der Mathematisch-Naturwissenschaftlichen Fakultät
Prof. Dr. Elmar Kulke

Gutachter/innen:

1. Professor W. Ted Masselink

2. Professor Henning Riechert

3. Professor Nick Stone

Tag der mündlichen Prüfung: 04. 11. 2019

Abstract

Mid-infrared (mid-IR) technology is a very powerful tool for molecular spectroscopy since vibration modes of many molecules lie in this wavelength range. The External-Cavity Quantum Cascade Laser (EC-QCL) is a mid-IR tunable laser, and can cover any part of this spectral range. For this reason, the EC-QCL has great potential for application as a standard light source at an industrial scale. In order to push this commercialization phase and to drive the contribution from the mid-IR applications forward, bottom-up understanding and optimization of the laser performance is strongly required.

Most mid-IR applications require a high-brightness light source that is tunable over a broad spectrum, and this work has been devoted mainly to maximizing such performances. The main goal of this study is to improve EC-QCL performance in terms of wavelength tunability and laser power. In order to address these objectives, the process is detailed in several steps. Firstly, fundamental physics of QCLs and EC-QCLs have been investigated in order to find the optimal conditions and the requirements for the elements of the EC-QCL for good performance. The theoretical study about QCL and EC systems has confirmed that the QCL plays the core role of EC-QCL systems; the power efficiency of an EC system is determined by the combination of the power efficiency of QCL and AR-coating of the laser facet. The width of the tuning range is determined by the gain spectrum of QCL. The waveguide loss of the amplifier is mostly dominated by the doping level of QCL. During this work, this core component was fabricated in our group while the optimization of these factors were carried out with various approaches, from QCL growth to facet coatings. The fabrication procedures and their performances are detailed in the related chapters.

One of the major challenges in making EC systems is to reduce the intra-facet reflectivity of the laser chip. To address this issue we first proposed a new anti-reflection (AR) coating concept, especially useful for the mid-IR range, and demonstrated its performance for the first time to the community. To realize this new coating concept, the optical properties of various dielectric

materials have been studied in order to find the materials that best fit the coating model in the mid-IR range. These findings were applied to designing a new AR-coating design, a "quasi-Lockhart" layout. The demonstrator achieved good reduction of reflection of the AR-coated substrate over a broad wavelength range of 7–12 μm, keeping below $R < 1\%$ reflection over the entire spectral range. The coating model was applied on broad-gain QCL facets, and the reflection was reduced to 0.75% over the entire emission wavelength range. This study is useful not only for EC-QCL physics but also for general uses of optical coating in the mid-IR range.

Furthermore, this work focused on the development and engineering of laser systems. During this work, two compact Littrow-type lasers and an EC system with a new optical configuration have been developed. Both conventional-type lasers achieved good performances as broadband mid-IR light sources, tunable from 920 cm^{-1} to 1190 cm^{-1} and 0.45 W pulse power. The new type of laser, an Intra-cavity out-coupling EC laser, was proposed to enhance the power output and achieved over 1 W pulse power, while keeping the same tuning range as the Littrow-type. Alongside of these works, some absorption measurements have been done using our lasers: IR-imaging of oesophagus cells were carried out with our project partner (The University of Exeter, UK) as a proof of concept and an absorption spectrum of ammonia was measured in our group.

Zusammenfassung

Mitt-Infrarot-Technologie (mid-IR) ist ein äußerst leistungsfähiges Werkzeug für die Anwendung in der Molekülspektroskopie, da die Schwingungsmoden vieler Moleküle in diesem Wellenlängenbereich liegen. Der Quantenkaskadenlaser mit externem Resonator (EC-QCL) ist ein abstimmbarer Mid-IR-Laser, der alle Bereiche dieses Spektrums abdecken kann. Aus diesem Grund besitzt der EC-QCL ein großes Potenzial um als Standardlichtquelle im industriellen Maßtab Verwendung zu finden. Um die Kommerzialisierungsphase voranzutreiben und den Anteil von Mid-IR-Anwendungen voranzutreiben, ist Bottom-Up-Verständnis und Entwicklung der Technologie dringend erforderlich.

Die meisten Mid-IR-Anwendungen benötigen eine Lichtquelle mit breitem Spektrum. Das Hauptanliegen dieser Forschungsarbeit ist die Verbesserung der Leistung des EC-QCL im Hinblick auf die Breite des Wellenlängen-Abstimmungsbereichs und die Laserleistung. Um dies zu erreichen, haben wir den Prozess in verschiedene Schritte aufgegliedert. Zuerst wurden die theoretischen Grundlagen der physikalischen Mechanismen der Quantenkaskadenlaser (QCL) und der externen Resonatoren (EC-QCL) untersucht, um die optimalen Bedingungen und Anforderungen der Elemente eines leistungsfähigen EC-QCL zu bestimmen. Die theoretische Untersuchung bestätigte, dass der QCL die Schlüsselrolle bei EC-Systemen einnimmt. Die Effizienz des EC wird bestimmt durch die Effizienz des QCL und der Güte der AR-Schicht der Laserfacette. Die Breite des Durchstimmbereichs wird bestimmt durch das Gain-Spektrum des QCL. Der Wellenleiter-Verlust ist hauptsächlich bestimmt durch die Dotierung des QCL. Während dieser Arbeiten wurden die Kernkomponenten in unserer Gruppe hergestellt – angefangen beim QCL-Wachstum hin zur Facettenbeschichtung. Die Herstellungsprozesse und ihre Leistung werden in den entsprechenden Kapiteln beschrieben.

Eine der größten Herausforderungen in der Herstellung des EC-Systems ist die Reduktion des Reflexionsvermögens innerhalb der Facetten des Laserchips. Dafür haben wir ein neues Konzept zur Antireflex-Beschichtung (AR)

entwickelt, das besonders für das mid-IR-Spektrum anwendbar ist. Zur Umsetzung des neuartigen Beschichtungskonzeptes haben wir die optischen Eigenschaften verschiedener dielektrischer Materialien untersucht, um die passendsten Materialien für die Beschichtung im mittleren IR-Spektrum ausfindig zu machen. Die Ergebnisse dieser Untersuchungen wurden für die Entwicklung eines neuartigen Beschichtungs-Designs im "Quasi-Lockhart"-Layout verwendet. Es konnte eine hervorragende Reflexionsreduktion auf dem beschichteten Substrat demonstriert werden, welche ein sehr breites Wellenlängen-Spektrum von 7–12 μm abdeckt und gleichzeitig unter 1% Reflexion über die gesamte Region bleibt. Diese Forschung ist nicht nur für EC-QCL-Physik nützlich, sondern auch für generelle Anwendungen optischer Beschichtungen im mid-IR-Spektrum.

Ein weiterer Schwerpunkt dieser Arbeit war die Entwicklung und Konstruktion von EC-Lasersystemen, die von unseren Projektpartnern im Projekt "Mid-TECH-ITN, Horizon 2020 Research and Innovation Programme" verwendet werden. Der Entwicklungsprozess sowie die Leistungsdemonstrationen dazu werden in dieser Arbeit detailliert beschrieben. Es wurden zwei Laser vom Littrow-Typ entwickelt. Außerdem wird eine neue optische Konfiguration des EC-Systems vorgeschlagen, der Intra-cavity Out-coupling Laser, der im Vergleich zu herkömmlichen Lasertypen eine höhere Ausgangsleistung erzielt. Neben diesen Arbeiten wurden einige Messungen mit unseren Lasern durchgeführt: IR-Bildgebung der Speiseröhrenzelle wurde mit unserem Projektpartner (The University of Exeter, UK) als Proof of Concept durchgeführt und das Absorptionsspektrum von Ammoniak wurde in unserer Gruppe gemessen.

概要

中赤外分光の技術は非常に有用である。これはとりわけ多くの分子振動モードがこの波長帯域に存在しているためである。可変長レーザーである外部共振器量子カスケードレーザー(External cavity quantum cascade laser, EC-QCL)は、これらスペクトル領域を網羅することが可能で、したがって、EC-QCLは産業スケールを含めた、標準的な光源として非常に潜在的である。商品化のフェーズをさらに推し進めるため、このレーザー性能におけるボトムアップの技術が求められてる。

多くの中赤外光のアプリケーションには広帯域の光源が求められている。この研究はおもにそうした性能を最大化することを背景としている。具体的な目的としては、波長の変調性および光源の強度の向上である。これらの目的に取り組むため、我々はいくつかの段階にステージ化して研究を進めてきた。まず初めに、QCLおよびEC-QCLの基本的な特性の追求から始めた。QCLおよびEC-QCLの物理機構の理論的な考察を行い、これらからEC-QCL形態における要素の最適条件もしくは要請を求めた。QCL素子が、その主要な部位であり、EC系におけるほとんどの性能特性である量子効率、変調領域幅、増幅器の光学損失を決定する。さまざまなアプローチによりこれら緒特性の最適化が行われた。この研究のなかで、我々グループ内でシステムの心臓となるQCL素子の全製造プロセス(結晶成長から素子コーティングに至るまで)をおこなった。これら製造手順および性能特性の詳細もまた本論文に記す。

ECレーザーにおける要請特性の中で特に困難な課題として、レーザー素子の内部断面(intra-facet)の反射率の低減があげられる。これに応じるものとして、我々は新たな反射防止膜のコンセプトで、特に中赤外光領域に有益なものを提案した。この実現のために、様々な誘電体物質の光学特性を調べ、中赤外光の応用に最適なものを選択し、実際のコーティングに応用した。ここで提案されたモデル“quasi-Lockhart” (疑ロックハート)のコーティングは、実験によりその高い性能が実証された。波長7–12 μmの領域をカバーし、かつその全領域内で反射率を1%以下に抑えることができた。またこのコーティングは広帯域ゲインのチップにも施され、その反射率を全体域をカバーしながら、0.75%まで低減させ

た。この成果はEC-QCLだけでなく、一般の中赤外光の光学コーティングにおいても大いに有用であろう。

さらに、我々は本研究の中でレーザーシステムの構築にも取り組んだ。この研究のなかで、二台のLittrow型レーザーと、新たな光学系をもつECレーザーを構築し、その高性能性を実証した。Littrow型では920 cm^{-1}–1190 cm^{-1}の帯域とパルス強0.45 Wを達成。新たなレーザーシステムであるIntra-cavity out-coupling系は従来の系にくらべ高出力することを目的とされ、その帯域を維持しながら、パルス強1 Wの出力を達成した。またこれら新たなシステムを用いて、またプロジェクトパートナーとの食道癌の細胞イメージングも試験、およびグループにおいてアンモニアの吸光度測定を実施した。

Contents

1 Introduction **11**
- 1.1 The infrared . . . 11
  - 1.1.1 The mid-IR range . . . 12
  - 1.1.2 Technologies of the mid-IR . . . 13
- 1.2 Quantum cascade lasers . . . 16
  - 1.2.1 High-power QCL . . . 17
  - 1.2.2 Broad-gain QCL . . . 19
- 1.3 External cavity quantum cascade laser . . . 23
  - 1.3.1 Brief historical overview of EC systems . . . 23
  - 1.3.2 Toward EC-QCLs . . . 25
  - 1.3.3 For better EC-QCLs . . . 26
- 1.4 Research flow and structure of the thesis . . . 27
- 1.5 Summery . . . 28

2 Fundamentals for QCL/EC-QCL **31**
- 2.1 Quantum cascade laser . . . 31
  - 2.1.1 The structure parameters . . . 34
  - 2.1.2 Eigenstates and wavefunctions . . . 34
  - 2.1.3 Self-consistent band diagram: doping effect . . . 36
    - 2.1.3.1 Example: a single QW structure . . . 37
    - 2.1.3.2 Example: QCL band diagram . . . 37
  - 2.1.4 Free carrier absorption . . . 40
- 2.2 External cavity quantum cascade laser . . . 42
  - 2.2.1 Basics for lasing . . . 42
  - 2.2.2 Optical loss of FP- / EC-mode . . . 43
  - 2.2.3 Lasing and parasitic oscillation . . . 45
  - 2.2.4 Tunability of EC-QCL . . . 46
    - 2.2.4.1 Grating in Littrow condition . . . 46
    - 2.2.4.2 Effective reflection in EC system . . . 47
    - 2.2.4.3 Lasing condition of Littrow-type EC laser . . . 48
    - 2.2.4.4 Coating effect to power restriction . . . 48

2.2.4.5 Coating effect to tunability 50
2.3 Summary 53

3 Dielectric coatings for mid-infrared 55
3.1 Introduction of the mid-IR optical coating 55
3.1.1 Theory of light propagation 57
3.1.1.1 Optical constants 57
3.1.1.2 General property of light propagation 58
3.1.1.3 The transfer matrix 59
3.1.2 Transmission property of media 61
3.1.2.1 Airy formalization 61
3.1.2.2 Spectral averaging 63
3.1.3 Fabrication process 66
3.1.4 Dielectric materials for the mid-IR 67
3.1.4.1 Coating materials 67
3.1.4.2 Adhesion promoter 69
3.1.4.3 Substrate 71
3.2 Anti-reflection coating 72
3.2.1 Optimization strategy for broadband AR coating . . . 73
3.2.2 Two layered coating 76
3.2.2.1 Design concept 76
3.2.2.2 Performance 76
3.2.3 Four layered coating 78
3.2.3.1 Design approach 78
3.2.3.2 Selection of materials 79
3.2.3.3 Coating designs 80
3.2.3.4 Fabrication details 82
3.2.3.5 Measurement and analysis 83
3.2.3.6 Coating performance 84
3.2.3.7 Performance of 7–12 μm 84
3.2.3.8 Performance of 10–12 μm 85
3.3 Summary 86

4 Device fabrication for EC system 87
4.1 Introduction 87
4.2 QCL growth 92
4.2.1 QCL structure 93
4.2.2 XRD characteristics 93
4.2.3 Doping effects 95
4.2.3.1 Optical loss 96
4.2.3.2 Emission shift 98

4.3 QCL Processing . . . 101
4.3.1 Processing Details . . . 101
4.3.2 Sub-mounting of QCL . . . 104
4.4 Anti-reflection coating of QCL facet . . . 105
4.4.1 QCL sample; a broad-gain QCL . . . 106
4.4.2 Coating details . . . 107
4.4.3 Coating performance . . . 110
4.4.4 Summary of AR-coating on QCL facets . . . 113
4.5 Angled facet QCL . . . 114
4.5.1 QCL sample . . . 115
4.5.2 Device performance . . . 115
4.5.2.1 Modal reflectance of angled facet . . . 115
4.5.2.2 Beam profile . . . 116
4.5.2.3 Laser performance . . . 117
4.5.2.4 Emission spectrum . . . 119
4.5.3 AR coating and packaging for EC use . . . 120
4.5.4 Summary and outlook . . . 122

5 Littrow-type EC-QCL 123
5.1 Introduction to Littrow-type EC-QCL . . . 123
5.2 The 1st generation: Prototype . . . 126
5.2.1 Gain medium: QCL Chip . . . 126
5.2.1.1 QCL feathures . . . 126
5.2.1.2 Laser performance . . . 127
5.2.1.3 Facet coatings . . . 129
5.2.2 Development of EC system . . . 132
5.2.2.1 QCL chip mount . . . 132
5.2.2.2 Optical system and its alignment . . . 133
5.2.2.3 System integration . . . 135
5.2.3 Characterization . . . 137
5.2.3.1 Laser performance . . . 137
5.2.3.2 Tuning performance . . . 138
5.2.4 Imaging test of bio-tissue . . . 140
5.2.4.1 Resolution target . . . 142
5.2.4.2 Bio-sample imaging . . . 143
5.2.5 Summary: Prototype . . . 143
5.3 The 2nd generation: New-model . . . 145
5.3.1 System details . . . 145
5.3.2 Performance: the straight bar . . . 148
5.3.2.1 QCL chip and coating performance . . . 148
5.3.2.2 Tuning performance in EC system . . . 148

5.3.3 EC system with angled facet QCL . . . 149
5.3.3.1 System details of angled facet QCL . . . 150
5.3.3.2 Basic performances . . . 151
5.3.3.3 Lasing mode development . . . 152
5.3.3.4 Tuning performance . . . 152
5.3.4 Summary: New-model . . . 152

6 Intra-cavity out-coupling EC-QCL 155
6.1 Introduction . . . 155
6.2 Issue of Littrow-type laser . . . 157
6.3 Principle . . . 157
6.4 System setup . . . 159
6.4.1 QCL sample . . . 159
6.4.2 Optical components and assembly . . . 159
6.5 Laser performance . . . 161
6.5.1 *P-I* characteristics . . . 161
6.5.2 Tuning performance . . . 161
6.6 Absorption demonstration . . . 164
6.7 Summary . . . 165

7 Conclusions and perspectives 167

A Process details 169
A.1 Plasma etching of SiO_2 . . . 169
A.2 Liftoff process and softening effect . . . 171
A.2.1 Liftoff process . . . 171
A.2.2 Softening effects of photoresist . . . 171

B Coating process on laser facets 173
B.1 Preparation of sample . . . 173
B.2 AR-coating process . . . 173
B.3 HR-coating process . . . 175

C Codes for coating optimization program 177
C.1 Optimization of AR coatings . . . 177
C.1.1 Two layer system . . . 177
C.1.2 Four layer system . . . 182
C.1.2.1 Constrain for 7–12 μm . . . 182
C.1.2.2 Constrain for 3.8–5.2 μm . . . 182
Bibliography . . . 183

Chapter 1

Introduction

1.1 The infrared

Light has a form of electromagnetic wave, which has a periodic form in time and space. One periodic length of such a wave form is called wavelength [1], and this "wavelength" is the starting point of modern optical science. Since the wavelength has a continuous scale change, the classification by wavelength range helps defining the optical regions. The infrared (IR) range covers relatively large area of wavelength range and is defined as a part from longer visible light to microwave area, i. e., 0.7 μm to 1.0×10^3 μm. This optical range was first discovered by William Herschel in 1800 when he measured a temperature increase at the outside of visible range of prism spectrum from sunlight, and this invisible range supports today's human life in many places.

According to ISO-20473 scheme, the infrared region itself is divided into three parts; near-infrared (NIR, near-IR, 0.7 μm to 3.0 μm), mid-infrared (MIR, mid-IR, 3.0 μm to 50.0 μm), and far-infrared (FIR, far-IR, or THz-range, $\lambda > 50$ μm). This classification is quite useful for different use purposes and different optical properties. Some parts of the wavelength (optical frequency) bands are now standardized for their different uses in modern optics applications. For example, some portions of near-IR are utilized as standard frequencies in optical communication, known as "commbands". The bands are listed as *S*- (1.46–1.53 μm) / *C*- (1.53–1.56 μm) / *L*- (1.56–1.62 μm) bands and so on. These bands are based on the availability of light source/detector materials. *C*-band is, for example, generated by a erbium doped fiber

amplifier (EDFA) and widely used in today's fiber communication. The far-IR is also quite in use for many fields of science and security. In astronomy, molecular cloud and protostars in space are investigated with their emissions, which lies in the far-IR range of few micrometer to submilimeter. In security domain, such longer ranges are now being used for human body detections, since thermal radiation from the body is also in the range of far-IR. The recent security and military concerns, referred to surveillance and passive heat seeking in missile detection, strongly motivate the study of the infrared domain.

Another major application of the far-IR spectral range is the molecular vibrational spectroscopy, where technology improvements have been studied for many decades. On the quantum scale, a molecule is vibrating at temperatures above absolute zero. The formal description of such vibrations can be complicated and even a single molecule has many inherent vibration modes. These vibration modes originates from the mass of constituent atoms, strength of molecular bonds, configuration of molecules, and molecular transform in space. Furthermore, these modes are quantized and well-defined in energy scales, thus each molecules has quite unique spectral features. This means that one can identify or deduce a molecule from a complex system, such as a bio-cell. or tissue, or from various environments. The frequency range of such molecular vibrations correspond to the wave frequency of infrared light, 10^1–10^2 THz. Therefore, the infrared light can interact resonantly with most of the molecules, resulting in the absorption of the light. The absorption spectrum are well-defined due to the features of molecular vibrations. Another aspect of infrared is its deep penetration depth into skin compared to other range of light. By mid-IR, it would be possible to monitor a health condition and it allows for in situ detection of disease by non-invasive way. For such reasons, the infrared technology is quite advantageous not only for its currently used applications but also for various applications in future.

1.1.1 The mid-IR range

As mentioned above, the mid-infrared is generally defined as a light with the optical range from 3.0 to 25.0 μm in wavelength. The mid-IR range is especially rich in absorption lines of various molecules from of atmospheric gases to biological molecules with large Dalton numbers[1]. In addition, the mid-IR range can generate well-defined and relatively strong resonance with molecules compared to other optical ranges. Since we can obtain strong and unique absorption features in the mid-IR range, we can easily identify the

[1]Unit for large molecule, mainly in biology use such as protein, lipid, DNA, etc.

present molecules. Due to this fact, this optical range is called "fingerprint" region in the community of molecular spectroscopy. Thus the mid-IR range is especially useful or practical applications of molecular spectroscopy.

A major obstacle in the mid-IR spectroscopy is a water absorption. Water has a large number of absorption lines in the mid-IR range, Figure 1.1 shows the absorption spectrum calculated using HITRAN database. In actual applications, the signal-to-noise ratio of the absorption measurement are low since the absorption features of the target molecules are usually hidden by the dominant water absorption. There are however two spots where the water absorptions are almost absent. These spots are known as "optical windows," which are represented by green areas in Fig. 1.1. "The first windows" exists from 3.0 to 5.0 μm, and "the second window" is in the range of 8.0 to 12.0 μm. Thus by using these spots, the mid-IR is still a powerful optical range for practical spectroscopy applications such as gas-trace sensing and medical imaging.

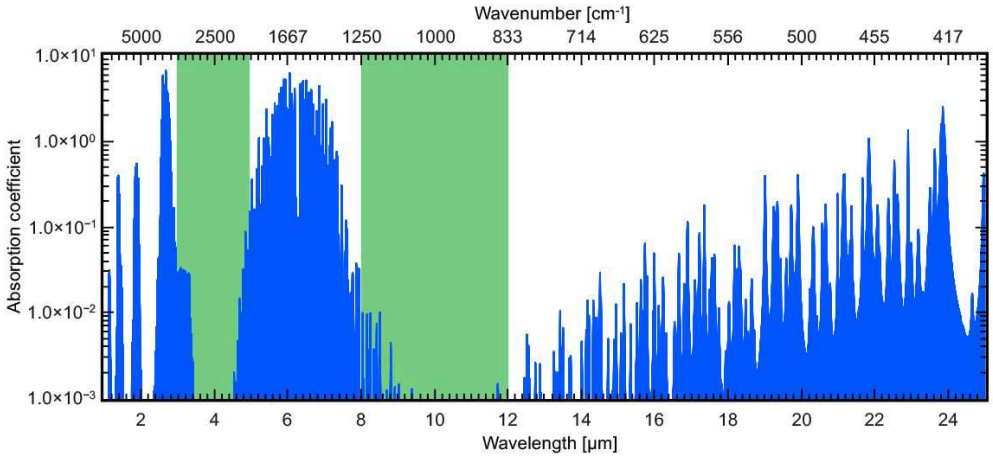

Figure 1.1: Water vapor absorption at mid-infrared range taken from HITRAN database (Voigt model, 1 atm at 296K), and green bands represent optical infrared windows; the first windows is at 3–5 μm, and the second window is at 8–12 μm.

1.1.2 Technologies of the mid-IR

For the mid-IR applications, many instruments are commercially available. The most well-established instrument is the Fourier transform infrared spectroscopy (FTIR), which is now widely used in many places. Figure 1.2-(a)

shows a schematic image of a most standard FTIR optics. FTIR uses a black-body radiation from a Globar as the light source. The data is generated in the form of interferogram by scanning the interference of the light, which is then Fourier-transformed to the wavelength domain. For such a measurement procedure, the system requires a large number of optics with high precision of optical alignment, thus it becomes inevitably bulky and sensitive to the environmental disturbance. Although it is possible to generate some parts of infrared region with interband semiconductor lasers, the spectrum coverage of such technologies is still limited.

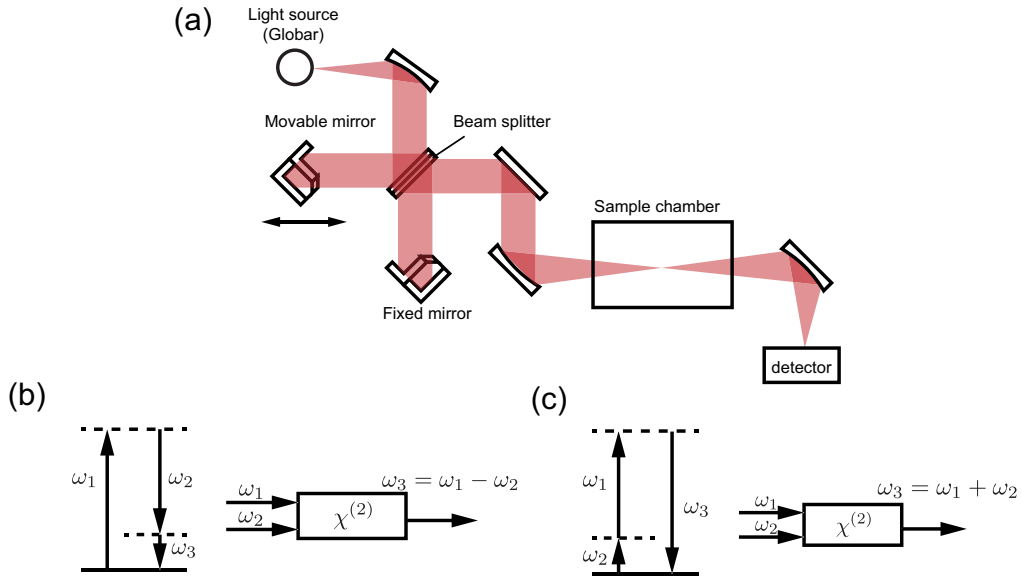

Figure 1.2: Schematic images of various mid-IR technologies: (a) schematic image of a standard FTIR system. The optical interferogram is generated by moving the movalble mirror. (b) a conceptual image of difference frequency generation (DFG). The technique is used in OPO to generate mid-IR light. (c) a conceptual image of sum-frequency generation, which is used to visualize mid-IR light in visible range camera. i. e., upconversion imaging.

One possibility to generate infrared light with a broad coverage of spectrum is to use a nonlinear optical phenomenon. which originates from the nonlinear polarizability of material $\chi^{(2)}$. The schematic diagram of the phenomenon is depicted in Fig. 1.2-(b), as the conceptual images of nonlinear process. The optical parametric oscillator (OPO) is a typical example of using difference frequency generation (DFG) and it can generate the mid-IR light with the frequency at ω_3 by combining the near-IR light, ω_2 with visible light ω_1. The major advantage of OPO systems is their good accessibility to

various pulse forms. By using ultra-short pulse laser in femtosecond scale, it is possible to generate an extremely strong peak power, of up to several mega watt in pulse mode. Such features are quite advantageous for nonlinear microscopy applications. The drawback of OPO systems is however their less robustness due to its complex optics, which is the same as FTIR, and the tuning range is still limited because of the wavelength accessibility of nonlinear crystals. In addition, the OPO needs a pump laser system for the optical pumping to generate the non-linear optical process. Thus, in general, the final form of the whole system is inevitably large and not suitable as a portable system but rather for lab-based experiments.

For mid-IR detection, narrow band gap materials such as mercury cadmium telluride (HgCdTe) detectors is commonly used. This type of device, however, needs to be operated at cryogenic temperature for suppressing the thermal noise. Consequently, the noise levels are still severe for clear signal detection, and not suitable as a portable system. Inter-subband devices such as quantum wells detectors are another option, while the selection rule of electron transition must be hold with actual device structure [2]. Recent demonstration of visualizing mid-IR light using sum frequency generation (SFG) shows a great potential not only for a good signal-to-noise ratio, but also as a compact imaging system [3, 4]. A conceptual image of SFG is shown in Fig. 1.2-(c). One requires a light source at a visible frequency range ω_1 and a signal of mid-IR light represented as ω_2. The SFG signal can be enhanced by phase-matching process and strong coherent signal can be obtained in the visible range, $\omega_3 = \omega_1 + \omega_2$. With this simple detection scheme, one can principally use a silicon-base detector, which does not require any cooling during the operation and is cheaply and easily available in the markets compared to a detector mentioned above. Today's CMOS imaging sensors are, needless to say, well sophisticated and perform high S/N imaging with high dynamics range. Therefore, this "upconversion" imaging technique is also strongly motivated as an integration of the existing technology with the newly emerging mid-IR technology.

1.2 Quantum cascade lasers

The idea of a cascaded amplification in inter-subbands was first proposed by R. Kazarinov and R. Suris in the early 1970s [5, 6]. This concept was however hardly achievable experimentally [7], since the proposed structure with single quantum wells and a barrier does not give a stable electric bias. Thus it is hard to have a population inversion in the energy states as was concluded at that time. Almost thirty years later, a successful demonstration, which is now known as quantum cascade laser (QCL), was fist demonstrated by J. Faist, *et al.* [8] at Bell Laboratory in 1994. The invention triggered great motivations toward the mid-IR technology and further extension for the longer optical range, i. e., THz region [9]. Ever since this invention, the QCLs have become one of the mainstreams of mid-IR light sources. The advantage of QCL is outstanding among the other mid-IR technologies not only in terms of its device compactness compared to FTIRs and OPOs, but also because of its strong versatility of the design concept.

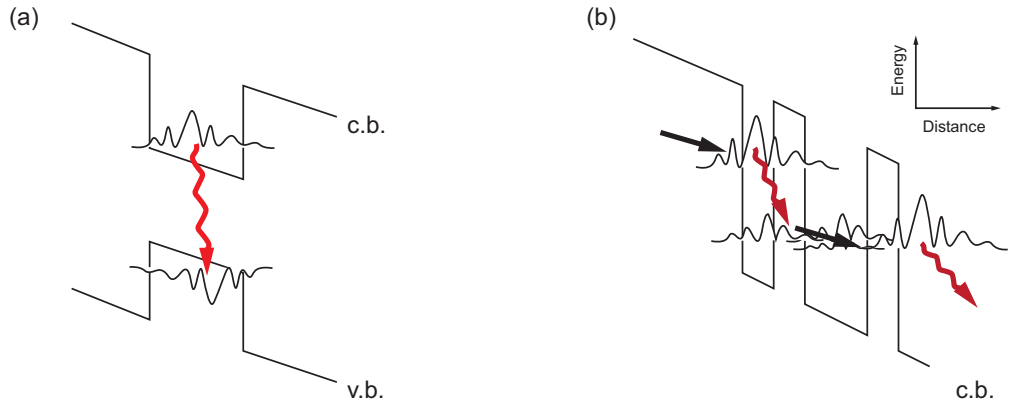

Figure 1.3: Schematic images of inter-band / inter-subband transition lasers; The wavelength of interband transition lasers (a) is mainly determined by the material of quantum well, while QCL (b) is a inter-subband laser thus, has a large versatility in designing emission wavelength in mid-IR.

For the inter-subband optical amplification, the active region must fulfill the three major requirements for laser operation [7]. Requirement (1); the structure enables a stable operation under a given electrical field. Requirement (2); In order to realize the population inversion, one needs to manipulate a scattering process at the lower levels. The electron–phonon scattering helps extracting the electrons rapidly from the lower levels and bringing to the next upper state, The process is schematically shown with

the black arrow in Fig. 1.3-(b). Requirement (3); the overall gain by the optical amplification must overcome the waveguide loss. Modern QCL structures fulfill all these requirements simultaneously. Adding to this, the more cascades the structure has, the stronger amplification is possible.

Another merits of QCLs is its large freedom in the structure designing. An optical transition of inter-bands semiconductor laser mainly takes place between the states at the conduction bands and the valance bands, which is illustrated in Fig. 1.3-(a) Consequently, the emission wavelength is largely determined by the material bandgaps of the active region, meaning the freedom of tailoring emission wavelength is limited. Although a electrical structure of QCL is of complex in the wavefunction alignment as well as in the manipulation of electron scattering [7], it is possible to tailor the emission wavelength by carefully designing the quantum wells / barriers thicknesses. The optical transition is then determined by position of the upper states and the lower states distributions. In other words, one can engineer the emission property by manipulating the quantum wells and barriers.

Until now, a number of QCLs with different emission ranges have been demonstrated [10], covering from the shorter mid-IR to THz regime with skipping over the reststrahlen band. Alongside such investigations, two major requirements motivated the QCL community at the same time; high-power and broad-gain QCLs. These performance improvements obviously contribute to many applications, including EC-QCL use.

1.2.1 High-power QCL

Enhancing output power has been always greatly motivated among any fields of optoelectric devices. The QCL is, of course, not exceptional in this sense. Great number of efforts have been undertaken since the QCL invention. To increase QCL output power, there are mainly two approaches. Figure 1.4 presents a series of high performance demonstrations carried out over a decade. One method is to engineer QCL structures for achieving more efficient lasing process; low-threshold and high-efficiency by means of smoother electron transport and better condition for population inversion [7]. A "**strain-compensated**" structure was one of the breakthroughs, especially for QCLs of wavelength shorter than $\lambda < 9.0$ μm. For such QCLs, the upper-laser-states are necessarily closed to the continuum states above the conduction bands. Then thermally activated electrons at upper states can easily escape to these continuum states. degrading the efficiency of optical transitions. This issue is specially critical for room temperature operation. This approach enables to increase the band discontinuity of conduction bands, thus can prevent electrons escaping to other states. For the case

of InP substrate system it can be increased by 200-250 meV, while a standard compound ratio gives 520 meV offset. Until now, a number of similar demonstrations have been done with various material systems [11, 12].

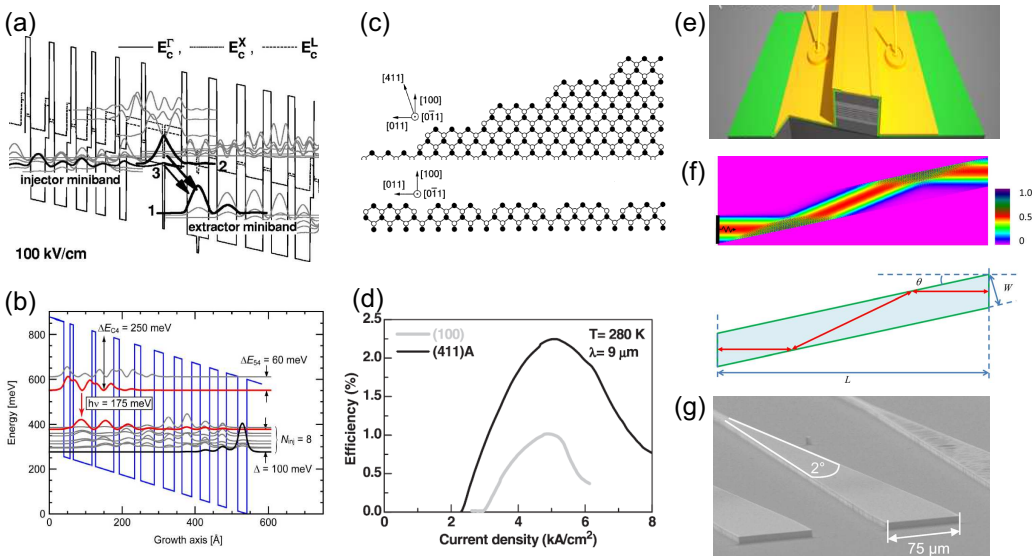

Figure 1.4: Overview slides for high power QCL demonstrations; images were taken from the corresponding references. Band diagrams of strain-compensated QCLs emitting (a) $\lambda \sim 3.05$ μm [12] and (b) of $\lambda \sim 7.1$ μm [11]. Interface roughness scattering reduction; schematic images of crystalline structure at (100) and (411)A are shown in (c) [13], and the laser performance of both crystalline structures are shown in (d) [14]. The various waveguide structures shown; (e) FIB cutting [15], (f) tilted broad waveguide [16], and (g) tapered wavegudie QCL [17]. (Figures are reprinted from [12] [14] [16] [17] with the permission of AIP publishing. The other figures are reprinted with permission from [11] and [15] Copyright The Optical Society, and [13] Copyright (1993) The Physical Society of Japan and The Japan Society of Applied Physics)

Another new approach might be to grow a QCL on an off-cut superlattice structure for reducing interface roughness (IF) scattering between quantum wells and barriers [14]. IF scattering is specially crucial for electron transport in quantum wells and barriers structure and causing low mobility of electrons especially during the quantum tunneling. The scattering effect can be reduced by not using (100) oriented substrate but rather using different crystalline direction oriented substrate [13], e. g. (411)A oriented InP substrate [18, 19]. This demonstration revealed a drastic increase in the power

performance [14]. This strategy does not require strain-balancing. Thus it is applicable for any wavelength range QCLs, especially for the wavelength range of 5–19 μm.

Meanwhile, many analogous trials from the inter-bands semiconductor laser field have been carried out by several groups. A "**buried heterostructure**" is commonly used for an efficient heat extraction and a stable laser operation. A high temperature generation at active region results in lower efficiency in laser operation due to several reasons such as thermal activation of electrons to non-contributing energy states for lasing, as well as crystal dislocation due to different thermal expansion properties of quantum wells, barriers and bulk materials. Such temperature enhancement generates positive feedback processes, which consequently burn the laser chips. For continuous-wave (CW) operation, this process is severe because of its high-power input into the QCL systems. Another approach is to apply various waveguide structures. For examples, a tapered waveguide enhances the output power drastically compared to a rigid wide waveguide structure [17] as well as a narrower beam divergence for its less confined divergence inside the waveguide, giving a 13 times larger output. Another possible method is to apply a tilted front facet. A reduced residual reflectivity of the front facet contributes to the asymmetric photon density in the waveguide, thus giving more power at the tilted facet side. This has been demonstrated in a series of experiments by S. Ahn, *et al.* using FIB-cutting technique [20, 15, 21]. A tilted broad waveguide is also attractive for high brightness [16], while the tilt-angle dependency for power performance is still unclear. The demonstration recorded a 203 W pulse power at 283 K. Such demonstrations have shown great benefits of waveguide structure optimization for certain uses.

1.2.2 Broad-gain QCL

Development of QCLs with broadband emissions has been always motivated by maximizing the tuning range of EC systems and distributed feedback laser arrays. In spectroscopy applications, a wide tunability of laser systems is preferable to cover every possible chemical compound as widely as possible. As shown in Fig. 1.5, various design schema of broad-gain QCL structure have been demonstrated over the last two decades and are now utilized in many places including industrial products [22].

Two remarkable approaches have been first carried out almost at the same time. One was the "**bound-to-continuum**" design of QCL active region, which was first demonstrated by J. Faist, *et al.* in 2001 [23]. The QCL structure is schematically shown in Fig. 1.5-(a). The design was initially aimed for good injection / relaxation efficiency due to the scattering resonance at

the lower levels of a active region. For its efficient electron extraction and its resulting good broadness, the design approach have been applied in many broad-gain lasers of various frequency ranges [24, 25].

Meanwhile, the "**multiple-stack approach**" of active region was first reported by C. Gmachl, *et al.* in 2001 [10]. This first demonstration was comprised of two active regions and achieved an emission width of 6.0 μm to 8.0 μm. This approach have been taken over in many places mainly in the EC-QCL community. A remarkable demonstration was done by J. Faist group, reporting an EC-QCL with a five-stack active region and achieving a tuning range of $\Delta \sim 430$ cm^{-1}, from 7.6 to 11.4 μm [26]. The schematic image of this active region is shown with Fig. 1.5-(c). Although this multi-stack design raises the drawback of inhomogeneous spectral behavior due to the special heterogeneity of the active region [27], this approach is practically useful for wide emission QCLs and used not only in EC systems [28, 29] but also in monolithic mid-IR tunable lasers [30, 31, 32].

In general, a broad-gain width necessarily leads to low peak gain, thus resulting in degrading the power and efficiency performance [35]. In order to overcome this issue, the third breakthrough has been done by series of demonstrations. In 2010, the "continuum-to-bound" design was proposed by Y. Yao, *et al.* at Princeton University [33]. This design was aimed to get a broadband QCL while keeping a larger optical gain by enhancing a strong coupling between the two lower injector states and the upper laser states of the next period at the operating electric fields. In the reported design, the upper levels consist from three states and total optical transitions contributed to the broad gain spectrum, giving a bandwidth of 7–9 μm range ($\Delta \sim 250$ cm^{-1} full width at half maximum). Soon later, the "**continuum-to-continuum**" design was demonstrated by the same group [35]. This work was done as the continuous work from the former demonstration and basically tried to extend the bandwidth of emission range. In this design, the upper laser levels were increased to four upper states and a single lower states were located close to the next upper states keeping the energy splitting within 3–6 meV, as can be seen in the diagram of Fig. 1.5-(b). The achieved wavelength emission range was in the range of 4–5 μm, and the gain spectral width was of $\Delta \sim 430$ cm^{-1}. Regarding the power performance, a large slope efficiency was obtained ($\eta \sim 5$ W/A) at room temperature as well as the low threshold current density ($J_{\text{th}} \sim$1.6 kA/cm^2).

The problem pointed out that the multiple-stack and bound-to-continuum approaches was a bias dependence of the gain shape. By increasing applied electric field, the spacing between the continuum bands (the lower states) increases, then the band-diagram eventually performs as a "bound-to-bound" case at around the maximum operating electric field [36]. This gain narrow-

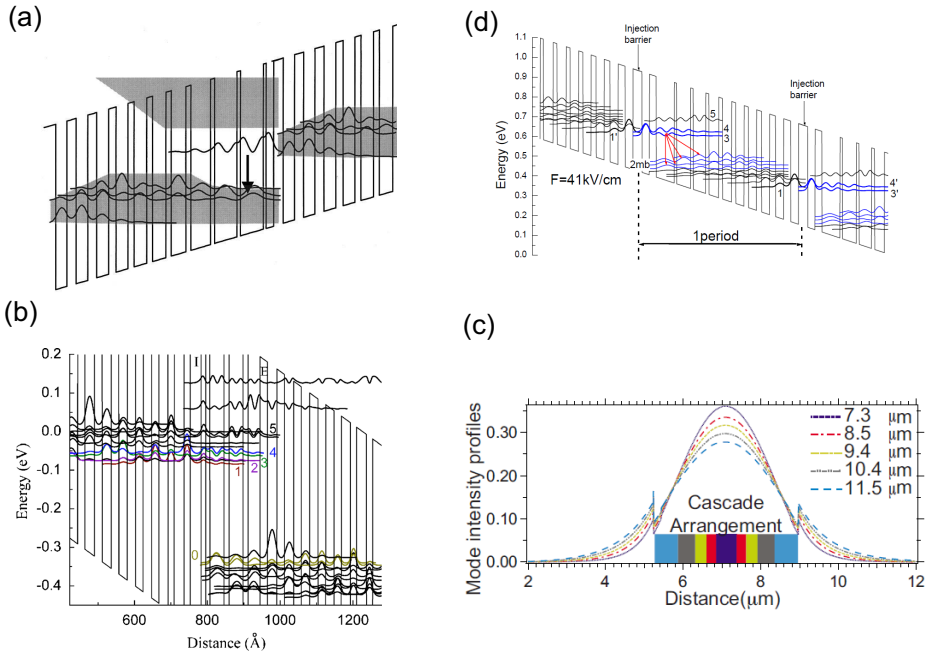

Figure 1.5: Band diagrams of broad-gain QCLs; (a) the "bound-to-continuum", the image was taken from Ref. 23, (b) the "continuum-to-continuum" design from Ref. 33, (c) the "multiple-stack" approach from Ref. 26; active regions are piled up to have good overlaps of wavelength. (d) the "dual-upper-states" from Ref. 34. (Figures are reprinted from [23] [33] [26] with the permission of AIP publishing and The other figure is reprinted with permission from [34] Copyright The Optical Society)

ing effect is obviously not suitable for EC tuning use. To address this issue, the "**dual-upper-states**" design was demonstrated by K. Fujita, *et al.* in 2010 [36]. The QCL structure was carefully designed to have a small energy gap between the two separate upper states. This feature gives a good overlap of wavefunction of both subbands. Thus the resulting gain spectrum forms a spectrally homogeneous gain profile [34]. By using this approch, two remarkable demonstrators are reported; $\Delta \sim 600$ cm^{-1} centered at 6.8 μm [27], and $\Delta \sim$500 cm^{-1} centered at 8.7 μm. Both lasers achieved good symmetric EL spectra and weak voltage-dependence of the ELs. Especially, the demonstrator of Ref. 34 recorded a high T_0-value, ($T_0 \sim 501$ K)..

1.3 External cavity quantum cascade laser

In general, semiconductor lasers without any optics are compact and easy to use, however, the performances are quite limited, since the emission wavelength is not in a single longitudinal mode, but often has a several lasing modes in the spectrum. In addition, the linewidth of each modes is not sufficiently narrow. Thus a form of Fabry-Pérot (FP) laser chip is not suitable for spectroscopy applications. The external cavity laser is a wavelength tunable laser, which comprises and optical gain media, optics for coupling the output of the gain-medium waveguide to the free space mode of external cavity, and a wavelength selective components such as interference filter or diffraction grating [37]. Other additional optics such as a polarizer, a beamsplitter, and a prism can be also integrated. Not only benefiting to the tunability, but the linewidth of the lasing modes can be greatly improved in EC system compared to FP laser. Here we briefly describe a historical overview of external cavity diode lasers (ECDLs) followed by external cavity quantum cascade lasers (EC-QCLs), and finally the requirements as state-of-arts laser system.

1.3.1 Brief historical overview of EC systems

In the early 1970s, several papers reported on external cavity lasers, which using a diode laser as the optical amplifier and a blaze grating for wavelength selective components. The great works have been done mainly in a telecommunication domain, such as at British Telecom Research Laboratories, AT&T Bell Laboratories, and Hewlett-Packard Laboratories in the 1980–1990s. The main targeted application was coherent optical communication, and now such laser systems have become standard tunable lasers and commercially available. Meanwhile, such telecommunication companies have realized the distributed feedback lasers (DFBs) for their use.

There are several types of EC-QCL configurations for their particular performance aims. Those have been mainly developed in ECDL studies, then analogously can be utilized as EC-QCL systems. Until now, many demonstrations also have been done with EC-QCLs as well. Figure 1.6 shows schematic images of EC laser configurations. Figure 1.6-(a) is called a backside extraction Littrow laser, which is widely used among the commercial products. Figure 1.6-(b) and -(c) are also Littrow-type lasers of front-side extraction design. These configuration have lower EC loss due to the HR-coating on the backside, thus allowing at least 4% wider tunabiltiy compared to the backside extraction type [38]. In both Littrow-type lasers, a blaze grating functions as a wavelength selective mirror depending on the angles. The reflected light goes back to the gain medium, either a diode laser or a QCL.

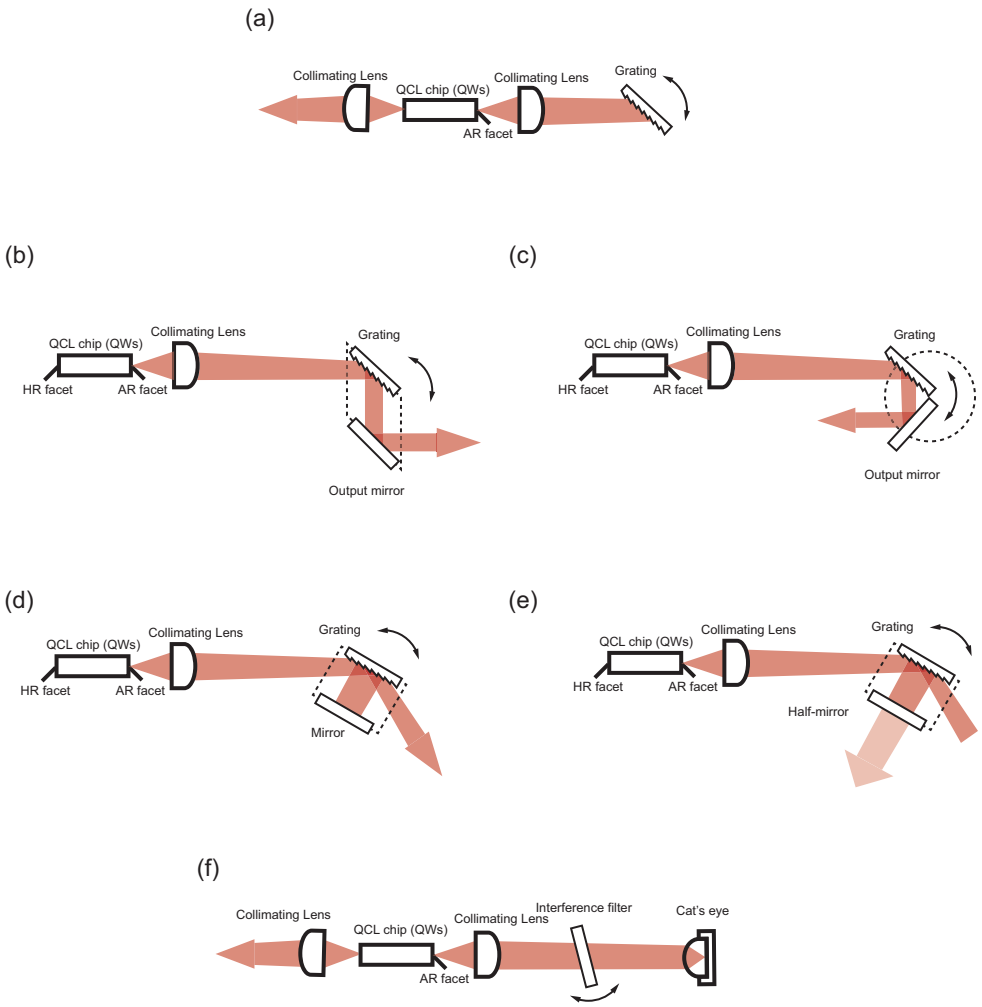

Figure 1.6: Schematics images of external cavity laser configurations:(a)backside extraction Littrow-type, (b) and (c)front-side extraction Littrow-type. Configuration (b) allows a beam walk-off while Configuration (c) does not. (d) Littman-Metcalf configuration and (e) transposed Littman-Metcalf configuration, (d) gives a narrower linewidth and (e) enables to suppress amplified spontaneous emission effect. (f) filter-tunable laser type.

The output is extracted from the other side of facet in the case of backside extraction type, or as the zeroth order diffracted light in front-side extraction. Littman-Metcalf configuration is depicted in Fig. 1.6-(d). The name of the configuration is taken from the first demonstrators [39]. The tuning is controlled by the angle of the mirror set next to the grating. This configuration enables the grating to filter the wavelength twice, thus possible to reduce the linewidth further compared to the Littrow-type lasers. Figure 1.6-(f) is a filter-tunable EC systems, i. e. interference-filter-stabilized EC laser, which were first demonstrated in 1988 with diode laser [40], and in 2014 with a QCL amplifier [41].

1.3.2 Toward EC-QCLs

The external cavity laser of mid-IR range was first demonstrated by H. Q. Le, *et al.* at Lincoln Laboratory of Massachusetts Institute of Technology in 1996 [42]. For this demonstration, GaSb-based heterostructure semiconductor laser was used, achieving a tuning from 3.3 to 4.0 μm. Few yeas later, the first demonstration of external cavity quantum cascade laser was carried out by G. Luo, *et al.*, at University of Houston in 2001 [43]. In this experiment, the tuning performance at from 80 K to 230 K was studied, and the wavelength tuning from 4.5 to 5.1 μm was achieved at 80 K. Although the tuning range of early days' EC-QCL was still limited as well as the operating temperature, the performances have drastically improved together with the QCL improvement. In addition, since the most of the technology developed in ECDL study have been useful for EC-QCL development, a number of analogous demonstrations have been carried out at the same time.

In EC-QCL community, several remarkable demonstrations have been carried out in the different groups. R. Maulini, *et al.* demonstrated a EC-QCL with a two-stage heterogeneous QCL at ETH Zürich in 2006 [44]. The resulting tuning range of this demonstration was from 8.2 μm to 10.4 μm ($\Delta \sim 265$ cm^{-1}) in pulse mode. Then A. Wittmann, *et al.* extended the pulse mode tuning range to $\Delta \sim 292$ cm^{-1} and $\Delta \sim 201$ cm^{-1} in CW mode at room temperature. A continuous work have been done in the same group and great demonstration have been done by A. Hugi, *et al.* in 2009 [28]. They fabricated a QCL chip of five-stage heterogeneous active region, and achieved a broadband tuning from 7.6 μm to 11.4 μm ($\Delta \sim 432$ cm^{-1}). All these QCL chips applied a bound-to-continuum design for the active regions [23, 45]. Later, a homogeneous QCL with dual-upper-state design active region [34] proposed from Hamamatsu Photonics [46] was integrated into EC system, achieving a good tuning range ($\Delta \sim 321$ cm^{-1}) in pulse mode [47]. Another broad tuning method is by switching several QCL chips

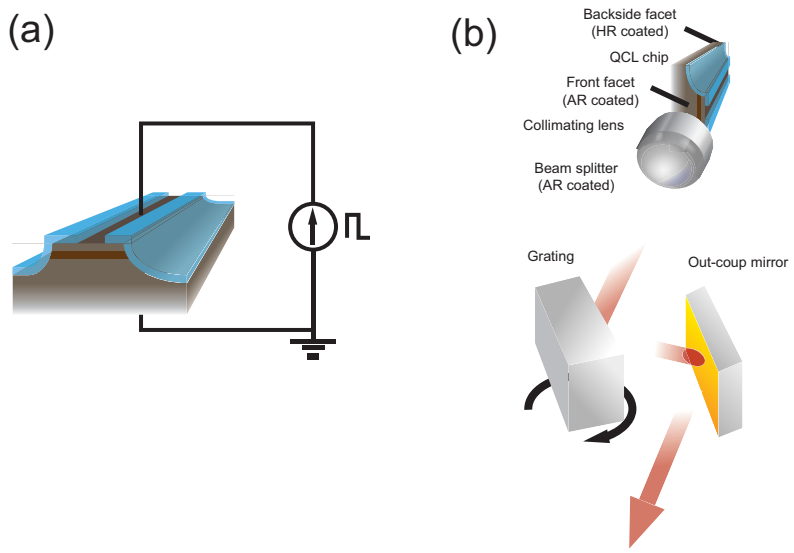

Figure 1.7: Schematic image of QCL and EC-QCL: In Littrow-type EC-QCL (b) the beam with large divergence is collimated with lens, then hits a blaze grating for selecting wavelength. The output is extracted either from the reflection or from uncoated facet on the backside.

with different gain regions, and such a system is now commercially available from Daylight Solution Inc. [22]

1.3.3 For better EC-QCLs

One of the critical requirements for EC laser systems is to reduce the facet reflectivity of optical gain medium. The residual reflectivity of laser facet restricts the laser performance when it is integrated into a EC system. Anti-reflection (AR) coating is the most common method for reducing an inherent facet reflectivity. Until now, a number of studies of AR-coating on laser facets have been done in EDL community as well as the good demonstrations [48, 49, 50]. Unlike the optical configuration, applying AR coating design of near-IR range to the mid-IR range is difficult. In the meantime of EC-QCL demonstrations, AR-coatings for QCL facets have been also studied [28, 51, 29], but the performances are still not satisfactory for its practical use.

1.4 Research flow and structure of the thesis

This work has been devoted for broadly tunable EC-QCLs. Figure 1.8 shows a flow chart of this work, which is divided to several steps. Each elements correspond to the chapter's topic. The main goal of the study is to **improve EC-QCL performance in terms of tunability and output power.** In order to address this aim, we have started from piece by pieces studies of EC-QCL elements, and finally integrated together for demonstration of lasers. Meanwhile, we have also focused on developing the laser system for its use by our project partners, "Mid-TECH project, Horizon2020 Research and Innovation Programme." Thus, the engineering and development of EC-QCLs is also a great portion of this work. We will detail the theoretical and experimental outputs for EC-QCL development, as well as its performance. The chapters are structured as follows.

In Chapter 2, we explain **the theoretical details of quantum cascade laser (QCL) and external cavity system (EC-QCL)**. For EC-QCL, QCL is a core part of the system, since it determines most of the specification, such as quantum efficiency, broadness of the tuning range, and optical loss of the amplifier. We studied the device performance in order to find a best fit QCL chip for EC system use. Besides, the tuning mechanism of EC-QCL was also studied with a numerical method.

Chapter 3 is mainly about **dielectric materials and dielectric coating for the mid-IR, mainly about anti-reflection coatings**, since, for EC-QCL, AR coating is a very crucial part for the EC performance. During this work, we explored the optical properties of several dielectric materials in order to search a best fit materials for the coating application in the mid-IR range. In the study of anti-reflection coatings, we have demonstrated "quasi-Lockhart" coating layout for a laser facet coating. We achieved quite high performance for reducing the reflection from a coated substrate. This Chapter explains the details for the new coating concepts together with the demonstrations of conventional layout films. This chapter would useful not only for EC-QCL physics but also for general uses of optical coating in the mid-IR range.

As mentioned, **the optical amplifier, i. e., QCL chip**, is the core part of the laser system. The performance of QCL determines the system performance, such as output power, tuning range, and linewidth, etc. During this work, this core component was fabricated in our group, from active region growths to facet coatings. **We describe in detail the fabrication procedures and their basic performances** in Chapter 4.

Chapter 5 and Chapter 6 is mainly about EC systems which were built during this work. We built two laser systems in total, while we changed

the QCL chips and conducted the performance evaluation with the different optical configuration. Chapter 5 is about **Littrow-type EC-QCL**. This type of laser is a conventional configuration in the community. We have also proposed **a new concept of optical configuration, named "infra-cavity out-coupling EC-QCL",** and demonstrated a tuning performance as well as a absorption measurement. This contents are described in Chapter 6.

1.5 Summery

In this chapter, we have briefly overviewed the merits of the mid-infrared spectroscopy, and technological requirement in the community. For the versatile measurement setup, a robust and compact mid-IR light source is required. There are several technologies which can address these demands. We explained that, ever since the invention of QCL, the EC-QCLs have demonstrated the outstanding performance and shown the great potential as the best suit laser system for the mid-IR spectroscopic applications, We have also described the research flow carried out during this work. The research elements will be integrated into the development of EC-QCL systems, which are presented in the last two chapters.

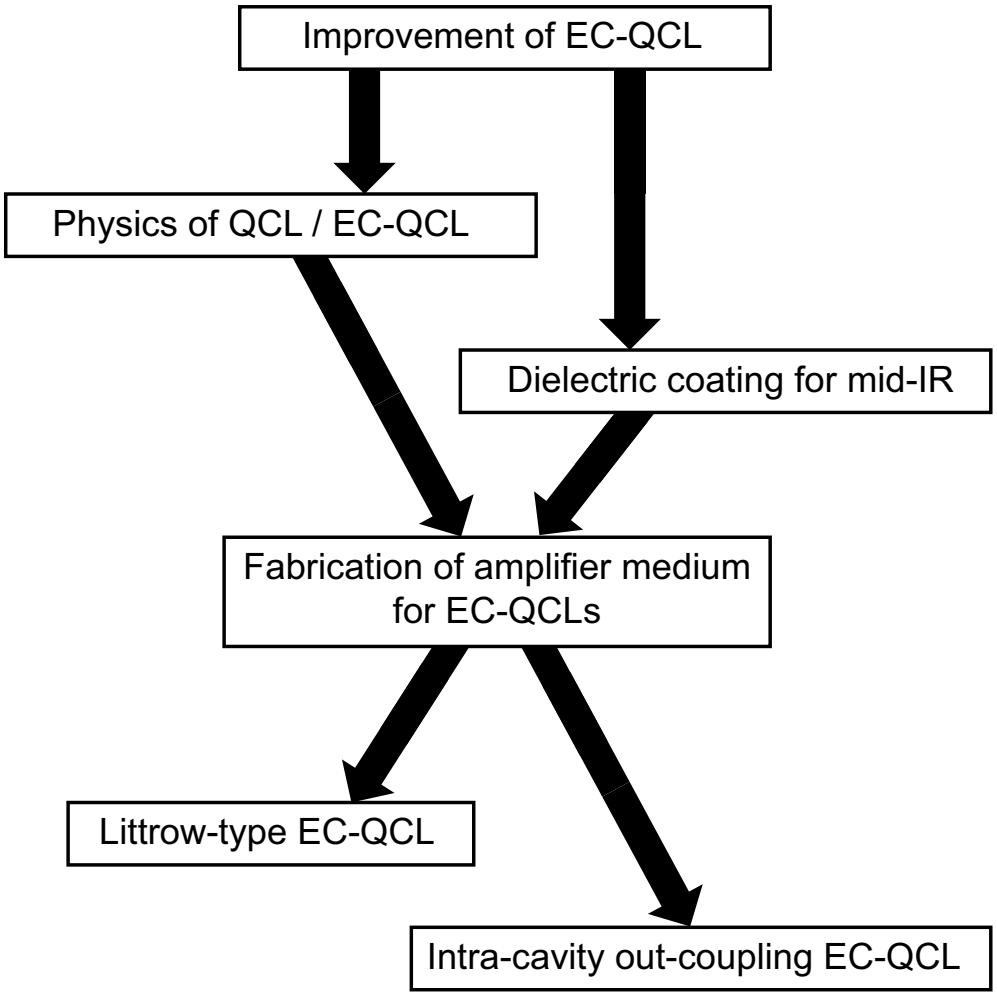

Figure 1.8: Research flow of this PhD work; The main goal was to improve of EC-QCL performance. To address this aim, we divided our work flow into several small elements. The two individual part of device theory and dielectric coating are integrated at the amplifier fabrication, and utilized in two laser systems; Littrow-type EC-QCL and Intra-cavity out-coupling EC-QCL.

Chapter 2

Fundamentals for QCL/EC-QCL

This chapter focuses on the fundamentals of QCLs and EC-QCLs. The principals of QCL simulation are explained in detail. The main aim of the chapter is to provide deep insights to QCL and EC-QCL physics useful for device fabrications. This chapter is partially reprinted from [52] with permission from Elsevier.

2.1 Quantum cascade laser

The quantum cascade laser (QCL) is a unipolar semiconductor device, which utilizes electron transitions between the subbands confined in the heterostructured conduction band for light emission. The electron distribution of QCL needs to be designed to have a population inversion by adjusting the thicknesses of quantum wells and barriers. Injected electron flows from the upper levels to lower levels by following the sequential wavefunctions which represents the electron probability. During this process, the electrons optically transit at the "active region." By piling the active region of the same design in sequence, light emission can be amplified. As a consequence, the light emitted from one active region stimulates the following radiation of photons, then achieving laser oscillation. During this process, the electrons flow through from one active region to the next active region, while generating the stimulated emission of photons and electrons. This is why the laser device is called

quantum "cascade" laser. The more cascades are built, the more electrons can contribute to the stream for light emission. This optical amplification mechanism gives higher quantum efficiency in the laser operation.

As reviewed in Chapter 1, historically, it took a while to realize an intersubband transition laser after the first concept proposal by Kasarinov and Suris in the early 1970s [5]. The idea was to use a cascaded quantum wells and barriers structure. In this idea, unlike the modern QCLs, the electron transition and tunneling take place within a single quantum well. By sequencing the quantum wells, the resonant tunneling between the two wells takes place under the negative differential bias. The electrons at the lower level are again transferred to the upper level of the successive well, then repeating the same transition process. This idea was difficult to realize since, for such simple superlattice structure, it is hard to obtain such a stable negative differential oscillation under the strong applied bias because of the current limitation under such a circumstance. Being inspired by this idea, J. Faist and co-workers first demonstrated a successful intersubband transition laser in 1994 [8]. Ever since their invention, the modern QCL structure is standardized based on their design.

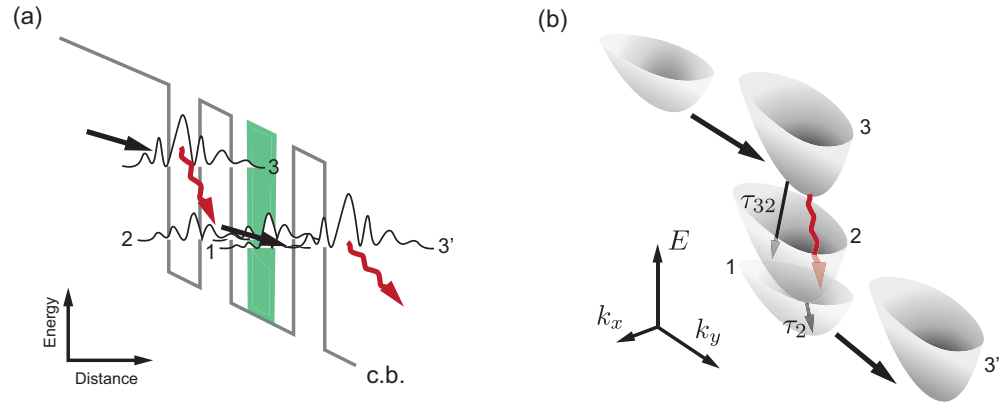

Figure 2.1: Schematic images of electron transport mechanism of QCL: (a) QCL diagram represented with energy versus growth direction and (b) a diagram in phase space. The parabolic envelopes represents energy distribution of the stationary energy states. Green area of (a) is a typical doping area of QCL. Solid black arrows indicate electron transport due to either scattering and resonant tunneling. Wavy red arrows represent optical transition for photon emission.

For a successful design of an intersubbands laser [7], one must fulfill the following requirements simultaneously; population inversion at active region,

a stable electrical structure, and an enough large gain to overcome waveguide and active region losses. Figure 2.1 shows an unit cell of QCL, which can be divided into two parts; active region and injection / relaxation region. the active region is usually referred as a part consisting with level 3 and level 2 energy states. the injection / relaxation region are the following area from level 2 till level 3'. Here Fig.2.1 (a) is represented in real space in growth direction versus energy levels of stationary states. Wavefunctions at conduction band schematically depicted represent the electron probability. As mentioned above, electrons are injected from state 3, and optically transit from level 3 to level 2, then the remaining electron are again recycled for the next periods. As is shown with the green area of Fig. 2.1-(a), the injection region are partially doped in order to provide more electrons for the operation. This helps to avoid space-charge formation, then provide a stable electric structure.

For laser operation, achieving population inversion is mandatory and the lifetimes of electron at each levels must satisfy,

$$\tau_{32} > \tau_2. \tag{2.1}$$

This relation means the total lifetime at the lower level 2 must be shorter than the electron scattering time from level 3 to level 2. Another important aspect is to extract the electrons from the lower states, i. e., level 2 to level 1, as soon as possible. This smooth extraction can be done by engineering the scattering mechanism. Fig.2.1 (b) shows a conceptual image of QCL structure in phase space. The energy states at the vicinity of Γ-point are represented by parabolic distribution. As shown in Fig. 2.1-(b), in the meanwhile of the optical transition, electrons are scattered between the different levels. These are mainly due to phonon scattering. In modern QCLs, the lower energy levels are specially designed for high resonance of electron and phonon scattering process. Due to this resonance, the electron can be quickly scattered from the level 2 to level 1, then can smoothly tunnel through the barriers to reach the upper level of the next period.

The great advantage of QCL is its design flexibility. The emission wavelength is determined by the states gap of the upper level and the lower levele, which come from the arrangement of the wavefunction distribution at the subbands. Therefore, it is possible to tailor the emission with good accessibility to any parts and also wide range of optical wavelength from the mid-IR to far-IR. For this reason, QCL is one of the dominant light sources for the infrared optics. Another advantage of QCL is its compactness and robustness. Unlike the other infrared light source, such as Fourier transform infrared (FTIR), optical parametric oscillators (OPO), QCL chip can be real-

ized in extremely compact form. Thus, QCL has a great potential to become as a standard infrared optical source of many practical applications.

2.1.1 The structure parameters

Everything of QCL simulation starts from defining a QCL structure. Ever since the first demonstration of QCL in 1994 [8], a number of QCL designs have been reported. The emission range is by now covered for the most of the mid-infrared range. Although there is still a room for the performance improvement in terms of quantum efficiency and broadness of gain spectrum, we can find quite good design for high performance lasers for external cavity use in many literature and reports. As examples, broad gain-QCL designs can be found in Ref. 53, 26.

To model QCL performance, selection of material parameters is important for accurate simulation. By now, many QCLs are demonstrated with various material systems, e. g., GaAs / $Al_{0.33}Ga_{0.67}As$, $In_{0.7}Ga_{0.27}As$ / AlAs(Sb), etc. During this work, we have used a hetero system lattice-matched to InP, consisting $In_{0.53}Ga_{0.47}As$ / $In_{0.52}Al_{0.48}As$ heterostructure. The important parameters of these III-V compounds are listed in Table 2.1. Due to the electron property, these parameters are mainly calculated for the vicinity of Γ–point in energy-space.

Table 2.1: Structure parameters at Γ-point of $In_{0.53}Ga_{0.47}As$ and $In_{0.52}Al_{0.48}As$ lattice matched to InP at $T = 300°C$; Parameter with $*$ is calculated from Vegard's law [54], while the others are taken from reference [55]

		Material	
Parameter	Symbol [unit]	$In_{0.53}Ga_{0.47}As$	$In_{0.52}Al_{0.48}As$
Effective mass	m^* $[m_0]$	0.041	0.069
Electron affinity	χ [eV]	4.72	4.20
Band gap	E_g [eV]	0.74	1.47
Relative permittivity	ϵ_r [-]	13.89	12.47
LO phonon energy	$\hbar\omega_{\mathrm{LO}}$ [meV]	34	47

2.1.2 Eigenstates and wavefunctions

As many literature show [56, 57], the very simple problem of quantum phenomena is a quantum well. The stationary energy states of electron inside

the well can be found by solving the Schrödinger's equation of a given system. The solution may find the discrete levels of electrons. Their energy intervals and the wavefunctions are determined by the materials of the system as well as its structure.

In production of semiconductor device [58], optimization of doping profile and its concentration of the device is one of the crucial factors for device performance. For QCL [59], it strongly affects to the laser performance, thus requires to have the optimal doping profile in the QWs.

In order to find the stationary states and the wavefunctions of a QCL structure, one must solve the Schödinger's equation of the given system. As well known, the original formula is given by,

$$H\psi = i\hbar\frac{\partial\psi}{\partial t} \tag{2.2}$$

where, H is Hamiltonian, defined as $H = -\hbar^2/2m^*\nabla^2 + V$, where V is the potential of the given system and m^* is the effective mass of electron in material. ψ represents the wavefunction of the given eigenstate. Since we discuss a steady state of the system, the equation is rewritten as,

$$\left(-\frac{\hbar^2}{2m^*\left(E,\mathbf{r}\right)}\nabla^2 + V\left(\mathbf{r}\right)\right)\psi\left(\mathbf{r}\right) = E\psi\left(\mathbf{r}\right) \tag{2.3}$$

with the eigenstate, E. The process of solving the Schrödinger equation is equivalent to find the solution of E of the given system, then one can derive the wavefunctions, $\psi\left(\mathbf{r}\right)$ for each states.

In general, the growth direction of quantum well structure is designated with z–direction, and in the xy–plane of the real space, the wavefunctions spread as the Block envelope functions. This means that the wavefuntions are symmetrically distributed in the quantum wells, hence the optical transition within such a plane is forbidden according to Fermi golden rules [56]. Therefore, for QCL analysis, it is enough to argue along the z–axis. As a result, the formula can be translated to,

$$\left(-\frac{\hbar^2}{2}\frac{d}{dz}\frac{1}{m^*\left(E,z\right)}\frac{d}{dz} + V\left(z\right)\right)\psi\left(z\right) = E\psi\left(z\right). \tag{2.4}$$

For the computation of eigenstate, it is simpler to apply the first approximation on the partial derivative to discrete portions rather than expanding directly. Thus the formula is translated as,

$$\frac{1}{m^*\left(E,z+\delta z\right)}\left[\frac{\psi\left(z+\delta z\right)-\psi\left(z\right)}{2\delta z}\right] - \frac{1}{m^*\left(E,z+\delta z\right)}\left[\frac{\psi\left(z\right)-\psi\left(z-2\delta z\right)}{2\delta z}\right] \tag{2.5}$$

$$= 2\frac{2\delta z}{\hbar^2}\left(E_c\left(z\right) - E\right) \tag{2.6}$$

This equation is, so called, a shooting equation, and make it possible to calculate $\psi(z+\delta z)$. By computing the equation by iteratively setting E and a convergence condition, we can solve the eigenstates, i. e.,Newton-Raphson method. Derived $\psi_j(z)$ $(j = 0,1,2,...)$ is not normalized, then normalized wavefunction can be calculated by,

$$\Psi_j(z) = \sqrt{|\psi_j(z)|^2} \Big/ \sqrt{\int |\psi_j(z)|^2 dz} \tag{2.7}$$

$$= \sqrt{|\psi_j(z_i)|^2} \Big/ \sqrt{\sum_i |\psi_j(z_i)|^2}. \tag{2.8}$$

Thus, we finally obtain a set of normalized wavefunction of j-th eigenstates, and the function satisfy,

$$\langle \Psi_j(z) | \Psi_j(z) \rangle = \sum_i |\Psi_j(z_i)|^2 = 1 \tag{2.9}$$

within the given system. Deriving the wavefunctions is a mandatory steps for QCL structure designing.

2.1.3 Self-consistent band diagram: doping effect

Like any other semiconductor devices [60, 61], QCL structure is a unipolar device, thus needs to have a reservoir of electron at injection/relaxation region, meaning n-type doping. The reason of the doping is, as mentioned above, for stable electronic structure. The doped region act as a reservoir of supplying extra carriers for the transport. Due to the space charge effect due to the dopant, the band diagram is no more flat even without any applied voltage. The band structure goes under the electrical equilibrium condition in order to neutralize the charge distribution of the system, i. e. "*band bending*." The moderation effect V_ρ contributes to the final potential V as,

$$V(z) \rightarrow V_{\mathrm{CB}}(z) + V_\rho(z). \tag{2.10}$$

Here, V_{CB} is the conduction band edge profile at Γ–point without any charge distribution effect of the structure. To calculate equilibrium band diagram of planar multilayer semiconductor structures, we need to solve "Poisson-Boltzmann equation" with finite difference method (FDM) and to derive the potential profile of band diagram [62]. Here, the band structure becomes equilibrium condition when the Fermi-level becomes flat due to the carrier redistribution inside the material under no applied potential, i. e., $V_{\mathrm{applied}} = 0$

and $I = 0$. By using this assumption, it is possible to realize in a relatively simple calculation process. [1] By implementing the doping profile and the electron density calculated from given conditions [60, 61] into ρ and ϵ in,

$$\nabla^2 V(\mathbf{r}) = -\frac{\rho(\mathbf{r})}{\epsilon}, \tag{2.11}$$

we can integrate the band bending effect into the simulation model.

Simulating device performance with accurate band structures is quite important especially for modeling intersubband devices since the discrete eigenstates can be affected by the potential profile. Here we will see the two examples of doping effect to the band diagram and, as a result, to the the energy states.

2.1.3.1 Example: a single QW structure

As a simple example, a highly doped quantum well was examined by a numerical method. The hetero system of lattice-matched to InP was simulated with our program. Figure 2.2 shows a comparison of two band diagrams with (a) and without (b) doping effect together with the eigenstates of electron. For this doped model, quantum barriers, i. e., InAlAs parts, are highly doped with 1.0×10^{18} cm^{-3}, as shown with reddish regions in Fig.2.2-(b). The eigenstates are determined by the band structure, then result the different distributions in the band diagram. Due to the doping effect, the conduction band edge bends upward, resulting the energy levels are also all shifted higher, while the intervals smaller. The energy gaps between the neighbouring levels are represented with ΔE, which are listed Table. 2.2. Clearly, the energy intervals duo to the doping result in smaller values, compared to the non-doping profile. For the longer mid-infrared range, this effect impacts on QCL performance since even a slight shift in eigenstates causes a shift in the emission wavelength, as well as higher optical loss of waveguide.

This effect is well utilized in modern semiconductor engineering in order to modify the band profiles depending on the applications. For conventional semiconductor devices, such as field effect transistor (FET) or photodiode detectors (PD), the doping is mainly optimized for better electron transport.

2.1.3.2 Example: QCL band diagram

Same as in a single QW structure, the energy states of QCL can be also affected by band-bending. Thus for more precise modeling, calculating the

[1] For more industrial oriented simulation, Technology Computer Aided Design (TCAD) is mostly used in this domain.[63, 64]

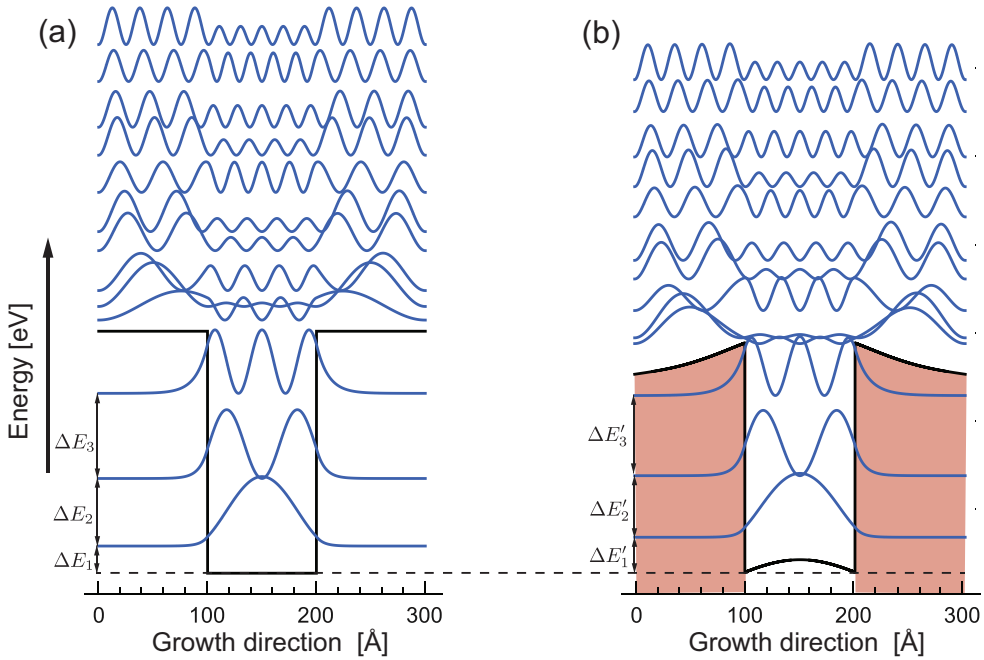

Figure 2.2: Schematic images of stationary wave function in quantum wells consisting InAlAs(100 Å)/InGaAs(100 Å)/InAlAs(100 Å): (a) without doping, and (b) with n+ doping (Si-dopant: 1.0×10^{18} cm^{-3}) at InAlAs regions (reddish area).

Table 2.2: Energy gap of quantum well depicted in Fig. 2.2: energy gaps, ΔE, of undoped/doped quantum well are listed. The stationary states energies are "compressed" due to band bending.

Undoped: (a)		Si-doped: (b)	
	ΔE [meV]		$\Delta E'$ meV
ΔE_1	79	$\Delta E'_1$	**59**
ΔE_2	150	$\Delta E'_2$	**138**
ΔE_3	182	$\Delta E'_3$	**177**

self-consistent diagram is quite important. Here, Figure 2.3 shows the band diagram of "dual-upper laser states design", reported in Ref. 53. The material system of the design is of InAlAs / InGaAs heterostructure lattice-matched to InP. The bending effect is clearly seen from the diagram. Since injector regions are negatively doped, the active regions are pushed upward. This bending effect obviously affects to the wavefunctions in the QWs structure.

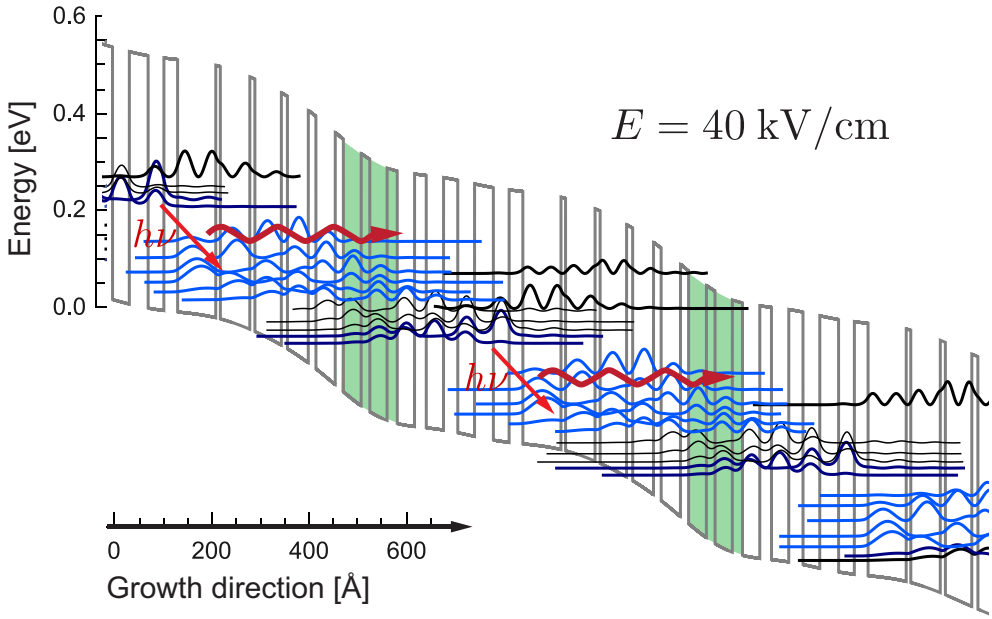

Figure 2.3: QCL band diagram including self-consistent effect due to doping: the green areas are negative-doped regions with 5.0×10^{16} cm^{-3}. The band diagram was calculated from InAlAs / InGaAs material system, which lattice-matches to InP substrate, and the bending effect was calculated by using Poisson-solver. The band bending is clearly seen, and such an energy structure affect to the wavefunctions.

Investigating doping level is the key part for QCL modelling. Figure 2.4 shows a comparison of two band diagrams zoomed in around the active region of QCL and the resulting wavefunctions; Fig. 2.4-(a) is without doping effect, while Fig. 2.4-(b) is with doping effect. The gaps between the upper level and the third energy states are shown. The gap of doping effect shifts a smaller value, $\Delta E' = 124$ meV. Such an effect is crucial especially for long range QCLs, since the emission wavelength is inversely proportional to the gaps of eigenstates of wavefunctions, as $\lambda \propto 1/\Delta E$. The more bending gives

more levels up of the wavefunctions of the lower states. Thus the emission wavelength range would be squeezed to the longer range.

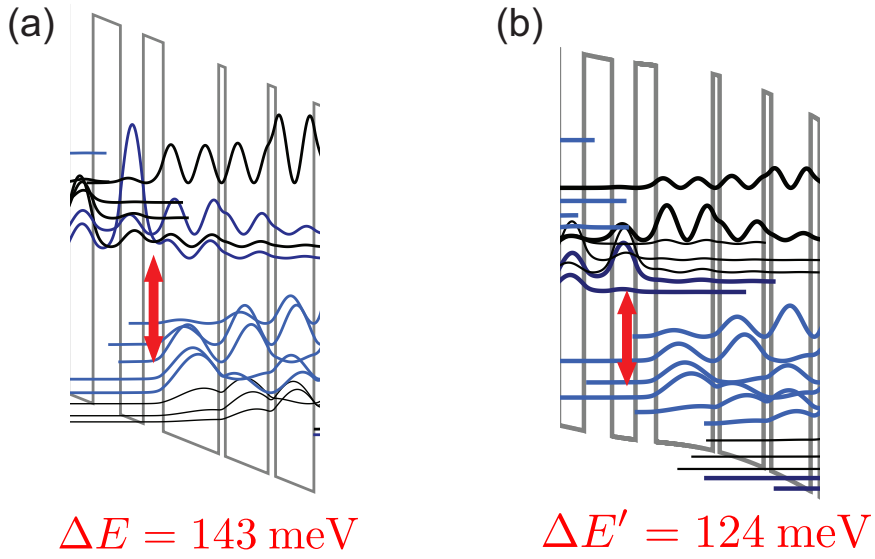

Figure 2.4: Zoom-in images of QCL band diagram around the active region: the energy gaps between the lowest upper state and third lower state ΔE are shown. (a) shows without doping effect and (b) with doping effect. Due to the band bending by doping, the lower states are lifted upward, thus resulting the narrower energy gaps. The different amplitude of wavefunctions are due to the different scaling factors

2.1.4 Free carrier absorption

Another effect due to carrier doping is free carrier absorption, which results in a waveguide loss of QCL. Dispersion of dielectric constant of semiconductor due to free carrier concentration can be formulated by Drude model expressed as [7, 57],

$$\epsilon(\omega) = \epsilon_\infty \left(1 - \frac{\omega_p^2}{\omega^2 + i\omega\gamma}\right). \tag{2.12}$$

where, $\omega_p = \sqrt{N_d e^2/\epsilon_0 \epsilon_\infty m^*}$, which is defined as the plasma frequency. $\omega = 2\pi c/\lambda$ is the frequency of the light, ϵ_∞ is the dielectric constant at high frequency, and γ is the damping coefficient, typically 100–200 fs for semiconductor materials. We can transform this formula to optical constants written

as,

$$n(\omega) = \sqrt{\frac{|\epsilon(\omega)| + \mathrm{Re}[\epsilon(\omega)]}{2}}, \tag{2.13}$$

$$\kappa(\omega) = \sqrt{\frac{|\epsilon(\omega)| - \mathrm{Re}[\epsilon(\omega)]}{2}}. \tag{2.14}$$

Figure 2.5 shows the dispersion characteristic of optical constants of InGaAs due to the different doping levels, with the range of 1.0×10^{16} to 1.0×10^{19} cm^{-3}. A drop of the refractive index is dominated by the plasma frequency, and can be also seen in Fig. 2.5-(a). The absorption increase with higher doping level, as seen Fig. 2.5-(b).

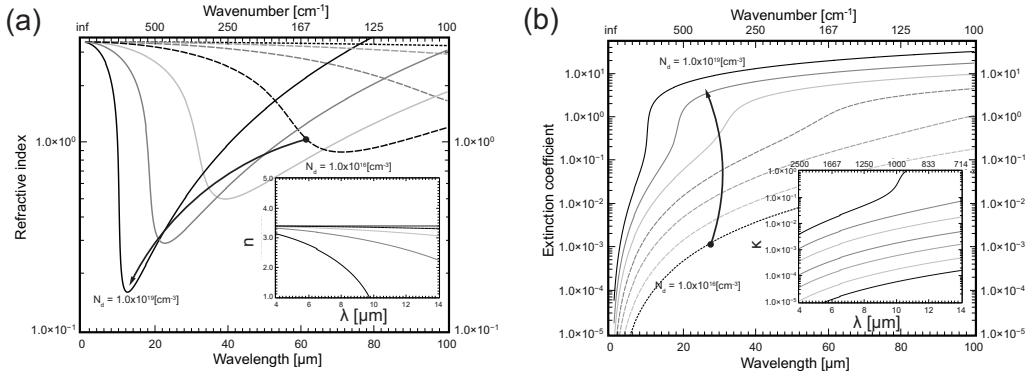

Figure 2.5: Dispersion relation of optical constant due to doping concentration in InGaAs; (a) refractive index and (b) extinction coefficient. Inserted graphs are of the range of the mid-infrared, 4–14 μm.

The doping is necessary for supplying carriers in QCL, meanwhile, causing the free carrier absorption of QCL waveguide. The optical loss is proportional to the concentration of free carriers, $\alpha_{\mathrm{fc}} \propto N_{\mathrm{carrier}}$, thus in QCL engineering, the doping level should be optimized in terms of the proper emission range and low-loss waveguide. Too low doping level results in lowe carrier concentration. Then only a few electrons contribute to the population inversion, thus the dynamic range of laser would be limited. On the other hand, high doping might increase the dynamic range of lasers, while the emission range would be not as designed and the higher waveguide loss results in the lower efficiency performance. These effects were experimentally observed and will be presented later.

2.2 External cavity quantum cascade laser

This section describes the fundamentals of external cavity quantum cascade laser (EC-QCL). The main goal of this section is to access to the relation between the tunability and the reflectivity of QCL facets. As we briefly explained in Chapter 1, the optical coupling efficiency between the external cavity and the gain medium is the critical factor for EC system performance [37, 65, 66, 38], and this can be improved by reducing the intra-cavity facet reflectivity of QCLs. In addition, the lower reflection on the facet contributes to the higher output with keeping a single mode operation, otherwise the parasitic modes start to oscillate. Thus to understand the tuning mechanism and the effect of facet reflection for power performance is quite important.

2.2.1 Basics for lasing

Light is a electromagnetic wave [1], and we can formulate the wave from with the amplitude of electric filed and the phase effect. In laser cavity, the spontaneous emission experiences gain and distributed loss while resonating within the optical cavity and the amplifier medium. In the formulation, we follow the assumptions from Ref. [67, 65]. In one dimensional propagation model, the electric field $E(z,t)$ is simply expressed as,

$$E(z,t) = E_0(z,t)\, e^{(\gamma-\alpha_{\text{loss}})z/2} e^{i\{\beta(\nu)z-\omega t\}}. \tag{2.15}$$

Here, E_0 is the slowly varying (complex) envelope function, thus the optical intensity is proportional to E^2. γ is the gain coeffiecint, α_w is the internal distributed loss, l is the length of optical amplifier. β is the wavevector of light, having a form as, $\beta(\nu) = 2\pi n_{\text{eff}}(\nu_0)\,\nu$. n_{eff} is the effective refractive index of gain medium of the mode with central wavenumber ν_0. ω as the optical frequency. In steady states, the wave must has the same form over the round trip in the optical cavity. By taking the mirror effects with complex reflectivity as r_1 and r_2, the wave must satisfy the following condition, i. e., lasing conditon,

$$r_1 r_2 e^{(\gamma-\alpha_{\text{loss}})l} e^{2i\beta(\nu)l} = 1. \tag{2.16}$$

This complex formula can be divided into two formulas by taking the real and imaginary parts into account and leads,

$$\gamma = \alpha_{\text{loss}} + \frac{1}{l}\ln\frac{1}{|r_1 r_2|}, \tag{2.17}$$

$$2\beta(\nu)\, l + \arg(r_1) + \arg(r_2) = 2m\pi. \tag{2.18}$$

Here, m is an integer. From Eq. 2.17, one can define a mirror loss, which is formulated as $1/l \ln|1/r_{\mathrm{i}}|$. By introducing the reflectance $R_{\mathrm{i}} = r_{\mathrm{i}}^2$ of the mirror, the mirror loss α_{m} is expressed as,

$$\alpha_{\mathrm{m}} = \frac{1}{2L} \ln \left| \frac{1}{R_i} \right|. \tag{2.19}$$

According to Eq. (2.17), the right hand side represents the summation of the waveguide loss and the optical cavity loss of the two mirrors. In steady states, the modal gain γ must be equal to the total loss. In the lasing condition, the gain stays at the value at which the oscillation started. This condition is so called "threshold", and the modal gain γ stays equal to the threshold gain γ_{th} during the single mode operation. Due to this "gain clamping", one can rewrite the relation, as

$$\gamma = \gamma_{\mathrm{th}}. \tag{2.20}$$

Meanwhile, the possible oscillation modes are determined by Eq. (2.18). Supposing that the mirror reflectivity does not give any changes in the optical phase, i. e., Fresnel reflection, $\arg(r_i) = 0$, the allowed (possible) oscillation modes ν_{m} can be obtained by solving,

$$\beta(\nu_{\mathrm{m}}) = \frac{m\pi}{l}. \tag{2.21}$$

Since the modal gain $\gamma = \gamma(\nu)$ has a wavenumber (wavelength) dependence as well as the total loss, $\alpha(\nu)$, the cavity oscillates at a lowest allowed mode which satisfy all these condition. This would become clear in the following.

2.2.2 Optical loss of FP- / EC-mode

In semiconductor laser, i. e., Fabry-Pérot (FP) type laser, the total loss is a sum of waveguide loss, α_{wg}, and mirror losses of the front side and backside facet, $1/L \ln|1/R_0|$, thus can be expressed as,

$$\alpha_{\mathrm{FP}} = \alpha_{\mathrm{wg}} + \frac{1}{L} \ln \left| \frac{1}{R_0} \right|. \tag{2.22}$$

Here, L is the chip length and R_0 is the mirror reflectance of the facets. For a QCL facet, the value is typically $R_0 \sim 0.28$–0.30. The total round trip gain, γ, is expressed as the product of applied current, J, and the confinement factor, Γ, and the gain coefficient, g, as,

$$\gamma = g\Gamma J. \tag{2.23}$$

For laser operation, the round trip gain must be equal to the total loss of the system. Figure 2.6 is a schematic images of gain development with the optical loss. The optical loss in FP mode is represented as a flat line. and the modal gain is shown with a series of reddish curves, as shown in Fig. 2.6-(a). Lasing condition can be achieved by increasing the applied current. When the gain curve touches to the total optical loss, α_{FP}, the system starts to lase. For the formulation of the threshold, one can connect the total gain and the loss as,

$$g\Gamma J_{\mathrm{th}} = \alpha_{\mathrm{wg}} + \frac{1}{L}\ln\left|\frac{1}{R_0}\right|. \tag{2.24}$$

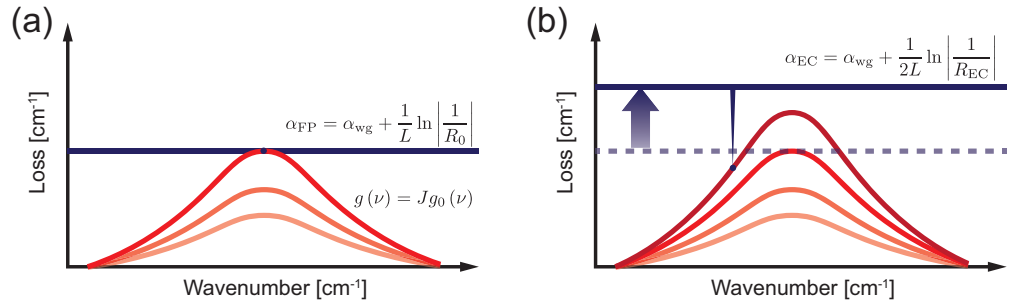

Figure 2.6: Schematic images of lasing mechanism: (a) gain development and the total optical loss of Fabry-Perot chip.

In EC system, the mirror loss of one side is replaced by the effective mirror loss of the EC system, R_{EC}, and the other mirror loss can be replaced depending on facet condition; HR-coating gives the zero loss since $R_{\mathrm{HR}} \sim 1$. In case of Littrow-type laser with front-side extraction, the total loss of EC system is rewritten as,

$$\alpha_{\mathrm{EC}} = \alpha_{\mathrm{wg}} + \frac{1}{2L}\ln\left|\frac{1}{R_{\mathrm{EC}}}\right|. \tag{2.25}$$

Schematic image of EC loss is shown in Fig. 2.6-(b). In the most cases, the base level of the optical loss shifts upward due to the AR coating on the intra-cavity facet of QCL, as indicated by the arrow in the figure. A wevelength selective element, e. g. a blaze grating, has a strong feedback at a certain wavelength. This effect is shown with the notch-like part of EC loss in Fig. 2.6-(b). The lower reflection on the intra-cavity facet gives the larger shift in the base level of optical loss and the larger depth of the notch. The details of the vicinity around the bottom of notch will be explained later.

2.2.3 Lasing and parasitic oscillation

For a single longitudinal mode operation, the modal gain should be kept under the base level of EC loss. Figure 2.7 shows a schematic diagram of gain development and lasing modes spectra of given applied current conditions. Fig. 2.7-(a) shows the operation under a certain applied current, $J < J_{\mathrm{para}}$. The modal gain develops with applied current so that the contact to the loss is only at the notch part. In this condition, the laser oscillates with the single longitudinal mode at the selected wavenumber. Further increase in the applied current, $J \geq J_{\mathrm{para}}$, gives a second touch to the base level of EC loss, while the contact at the notch part keeping the gain clamping. This situation is the threshold for the secondary oscillation in the spectrum, and this second optical mode is not tunable. This unwanted optical oscillation is called a "parasitic oscillation" of the laser system. This usually happens at the top area of the modal gain, since it can easily reach to the base loss. In this sense, the output power would be limited due to such a parasitic lasing. In this sense, flatness of the modal gain form is also quite important for EC-QCL use, while sharp gain can easily grow to reach such a condition.

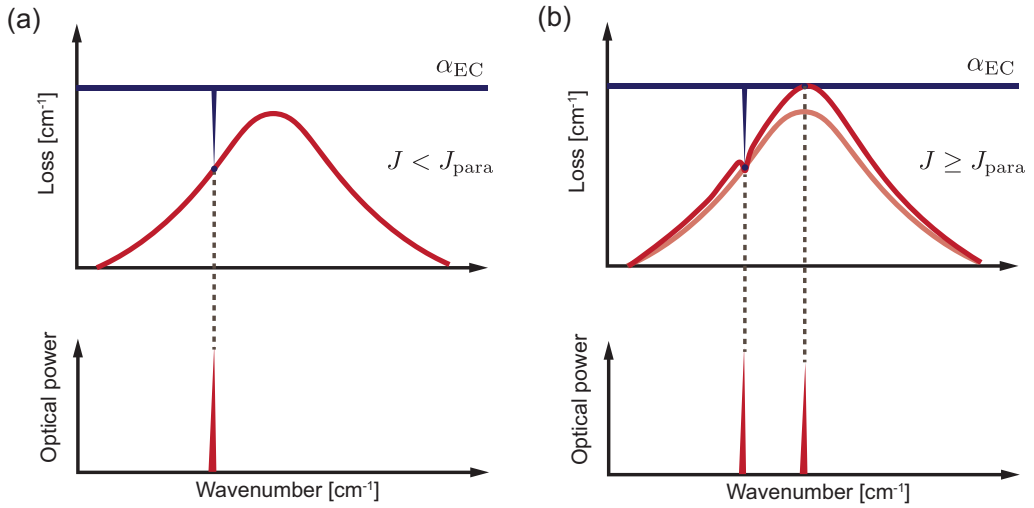

Figure 2.7: Schematic images of lasing and parasitic oscillation: (a) laser oscillation under a single longitudinal mode in the spectrum. The modal gain with corresponding applied current is under the EC loss. (b) threshold condition for parasitic oscillation. The modal gain growth becomes equal or over the EC loss, thus several modes starts to oscillate.

The lower residual reflection contributes to the level-up of this baseline. This means that, for example, the high performance AR coating results in

the higher loss in EC mode. Such a high baseline allows for the system to apply a higher current, resulting the higher output power with keeping the single mode oscillation. For this reason, lowering the the modal reflection of the intra-cavity facet is strongly required in order to operate at higher applied current.

2.2.4 Tunability of EC-QCL

In this part, tuning behavior of EC-QCL is explained. During this work, we mainly focus on Littrow-type EC-QCL. Diffraction grating is a wavelength selective component in optics, and now utilized in many places. Commercial gratings have their selectivity (efficiency) almost over 90%, thus we can say the performance is "perfect." In Littrow-type EC-QCL, a reflection type blaze grating is used for its wavelength (wavenumber) tuning. Thus we first start with the basics of grating performance, then tuning performance with given AR coating condition will be detailed.

2.2.4.1 Grating in Littrow condition

Blaze gratings are designed to have a maximum efficiency toward in Littrow direction, which corresponds to the first order diffraction direction. Thus, for optical resonator use, it is to be set with Littrow angle with respect to the optical amplifier. Supposing that the grating has a pitch d [1/mm] and set with an angle θ_G, the grating parameter q over the range of wavelength λ can be defined as,

$$q = \frac{2d \sin \theta_G}{\lambda}. \tag{2.26}$$

With this parameter q, the reflectivity of diffraction grating in Littrow condition can be expressed as [67],

$$r_G = \sqrt{\eta_G} e^{-\pi q} \frac{\sin\left(\pi\left(N+1\right)q\right)}{\left(N+1\right)\sin\left(\pi q\right)} \tag{2.27}$$

Here, N is the number of illuminated blazes of diffraction grating and η_G is the effective reflectivity of the grating. The detailed derivation of the formula is described in Ref. [65, 67]. The reflectance spectrum, i. e., grating intensity reflectivity, to the Littrow direction is given by $R_G = |r_G|^2$. The reflectance spectrum has a sinc function form, and, as well known, the width of the peak depends on the number of blazes illuminated by the light spot. For EC use as well, it is better to have large spot size on grating for better spectral confinement. As in principle of diffraction, the resonant wavelength inside the optical cavity can be tuned by changing the grating angle.

2.2.4.2 Effective reflection in EC system

To model the tuning performance of Littrow-type EC systems, the effective reflection from the intra-cavity needs to be considered. By taking into account the actual reflection from grating and facet reflectivity of the optical amplifier, the effective optical feedback can be calculated. We model a Littrow-type lasers of front side extraction tyep. Since the backside facet is highly reflective (HR-) coated, the reflectance is $r_{\text{backside}} \sim 1.0$. As derived in Ref. 66, by taking the series of reflection and transmission, the effective reflectivity of external cavity $\hat{r} = \hat{r}\,(\theta_G, \lambda)$ is formulated as,

$$\hat{r} = r_{\text{ic}}^{(-)} - r_G \frac{\eta^2 e^{2iL\beta(\nu)} t_{\text{ic}}^{(+)} t_{\text{ic}}^{(-)}}{\eta^2 e^{2iL\beta(\nu)} r_{\text{ic}}^{(+)} r_G - 1} \tag{2.28}$$

As shown in Fig. 2.8, $r_{\text{ic}}^{(+)}$, $r_{\text{ic}}^{(-)}$ are the reflectivity of the intra-cavity facet of the forward direction and the backward direction, respectively. In the same manner, $t_{\text{ic}}^{(+)}$, $t_{\text{ic}}^{(-)}$. are the transmittivity of the intra-cavity facet of forward and backward direction, respectively. We should note that $t_{\text{ic}}^{(+)} t_{\text{ic}}^{(-)} = T_{\text{ic}}$ is the intensity of transmission. Here we introduced the coupling efficiency η. This is to parametrize the beam overlaps of in- and out-coming light in the external cavity.

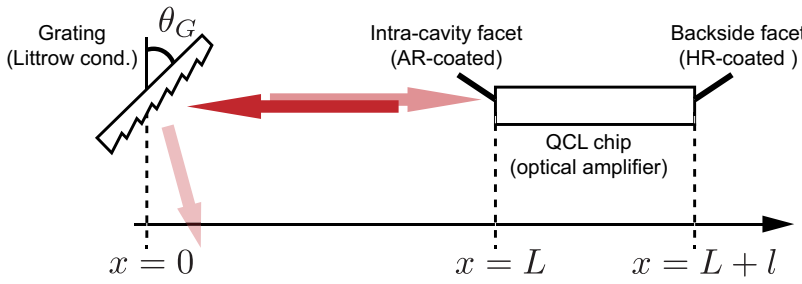

Figure 2.8: Schematic presentation of effective reflection from EC: Grating in Littrow condition and HR-coated backside facet function as the optical resonator. The effective reflection from the external cavity can be calculated by taking the series of reflection and transmission at intra-cavity facet and grating reflections.

In EC system, anti-reflection (AR) coating on the intra-cavity facet is applied reduce the reflectivity of intra-cavity facet, r_{ic}. In the case of successful AR-coating, $r_{\text{ic}} \ll 1$, Eq. 2.28 can be simplified as,

$$\hat{r}\,(\theta_G, \lambda) \simeq r_{\text{ic}} + \eta T_{\text{ic}} r_G\,(\theta_G, \lambda)\, e^{2i\beta(\lambda)L}. \tag{2.29}$$

Furthermore, we can redefine the net coupling efficiency of EC system as,

$$\eta_{\mathrm{EC}} = \eta T_{\mathrm{ic}}. \tag{2.30}$$

In general, EC system has a collimating lens, having a transmission T_{L}. Then, for the complete modeling, this term needs to be multiplied to the second term of Eq. 2.29. The net coupling efficiency is rewritten as,

$$\eta'_{\mathrm{EC}} = \eta T_{\mathrm{ic}} T_{\mathrm{L}}. \tag{2.31}$$

To increase the coupling efficiency of EC system is equivalent to say to increase this parameter. The overlap efficiency η can be improved by a better alignment of optics. T_L is strongly depends on the numerical aperture (NA) as well as the AR coating performance. The main restriction for this coupling factor is due to the facet reflectance of QCL chip, which is expressed with T_{ic} and this transmittance factor varis by the AR coating quality on the QCL's intra-cavity facet.

2.2.4.3 Lasing condition of Littrow-type EC laser

By using the effective reflectivity, which was derived above, we can again formulate the lasing condition for Littrow-type laser. By inserting $r_1 = \hat{r}$ of Eq. 2.28 and, $r_2 = r_{\mathrm{HR}} \sim 1.0$ into Eq. 2.17, we get the optical loss function of EC system, which is expressed as,

$$\alpha_{\mathrm{EC}} = \alpha_{\mathrm{wg}} + \frac{1}{l} \ln \frac{1}{|\hat{r}\left(\theta_G, \lambda\right)|} \tag{2.32}$$

In the same manner, the equation for allowed modes can be modified as,

$$2\beta\left(\nu\right) l + \arg\left(\hat{r}\left(\theta_G, \lambda\right)\right) = 2m\pi. \tag{2.33}$$

By solving this simultaneous equation of Eq. 2.32 and Eq. 2.33, one can investigate the lasing modes of EC system associted with the gain behavior. In the following, we explain the effect of intra-cavity reflectance to EC laser performance.

2.2.4.4 Coating effect to power restriction

By using the formula Eq. 2.32, baseline behavior of EC system was investigated. Since the baseline determines the saturation level, i. e., the threshold for parasitic oscillation, the higher bias is preferred for EC system, while the lowest level selected by Littrow-condition needs to be as low as possible.

The lowest level of EC loss around the grating wavelength, λ_G is determined by the net coupling efficiency η'_{EC}. On the other hand, the baseline level is mainly related to the facet reflectivity, $r_{\mathrm{ic}} = \sqrt{R_{\mathrm{ic}}}$. Therefore, we will see that AR coating performance of intra-cavity facet is a crucial factor for both parameters.

Figure 2.9 shows external cavity losses of different reflectance of intra-cavity facet. The parameters were set as follows; The overlap coupling efficiency η =0.80%, beam spot size 2.0 mm and the blaze number of grating 135 mm^{-1} with η_G = 95%. EC length L = 40 mm and chip length l = 6.0 mm. Waveguide loss is 5.0 cm^{-1}. The values of facet reflectance were set as R = 0.10, 0.02, 0.005, as shown in the graph. The lower reflectance contribute the level up of the baseline, while keeping the minimum point of the modal optical loss, i. e., the lasing levels.

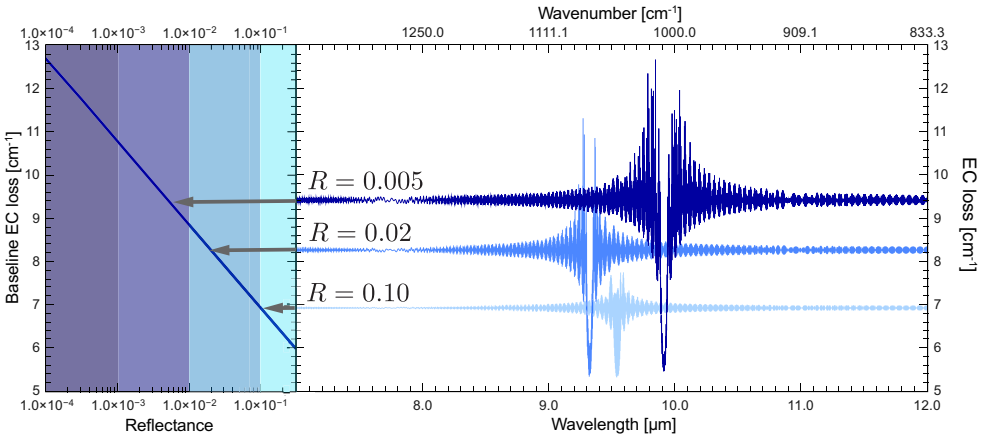

Figure 2.9: EC losses and their baselines with different facet reflectance: EC loss with different facet reflectances, R = 0.10, 0.02, 0.005, are depicted, together with the baseline level with respect to the reflectance.

As can seen the left graph of Fig. 2.9, the baseline level mainly depends on the facet reflectance in logarithmic scale. To increase the saturation level, extreme reduction by facet coating is required. This means that only the logarithmic scale change in AR coating performance would be apparent in EC laser use. In the community, R <1% is a required target value. Further reduction can be possible by angled facet lasers, by which achievements of $R < 1.0\times10^{-4}$ were demonstrated [15, 20, 68]. More importantly, a very partial wavelength reduction in reflection is not effective for broad tuning; The broadness is mandatory.

2.2.4.5 Coating effect to tunability

Tunability can be referred as the broadness of tuning range and the tuning resolution i. e., the linewidth of lasing modes. In pulse mode operation, the temperature of gain medium fluctuates due to the inconstant heat generation. This temperature drift in optical gain medium causes the maximum gain shift, resulting mode hopping of the lasing modes. The hopping interval is usually in the linewidth extent, thus the narrower possible hopping extent more suits for spectroscopic applications. Therefore to investigate mode hopping mechanism is quite important. Here we investigated tuning performance.

Table 2.3: Parameters used in tuning simulation: the listed parameters are mostly based on our actual setup.

Parameter	symbol	unit	value
Groove number	d	grooves/mm	135
Grating efficiency	η_G	-	95%
Beam spot size	-	mm	2.0
Coupling coefficient	η	-	60%
Chip length	l	cm	0.2
Cavity length	L	cm	5.0
Waveguide loss	α_{wg}	cm^{-1}	5.0

The possible tuning mode can be analyzed using the lasing conditions of Eq. 2.33 and Eq. 2.32. Here the optical loss and the allowed modes in the case of $R = 0.05$ and $R = 0.002$ are depicted in Fig. 2.10. The laser profiles are listed in Table 2.3. The zoom-out profile of EC loss is inserted in FIg. 2.10-(a). As can be clearly seen from the two figures, the lower facet reflectance contribute to the level up of the baseline of optical loss and less fluctuation in the optical loss. The allowed lasing modes are calculated by using Eq. 2.33. Two types of mode exist in the possible lasing modes; EC modes and FP modes. EC modes are calculated by approximating the argument functions as, $\arg(\hat{r}) \sim 2\,(nl + L)$, while or FP modes can be derived by $\arg(\hat{r}) \sim 2nl$ The orange dots are the allowed lasing mode derived by EC mode condition and the blue green dots are by FP mode condition. Both modes are distributed along the EC loss with different mode fluctuations depending on the facet reflectance. With lower reflectance, the EC modes are more localized closed to the bottom of the EC loss. This feature is advantageous for quasi-continuous tuning in EC operation, since the mode

spacing of EC modes are much narrower than the FP mode spacing, thus the possible mode hopping interval would improve due to the smaller possible jumping to the neighboring modes.

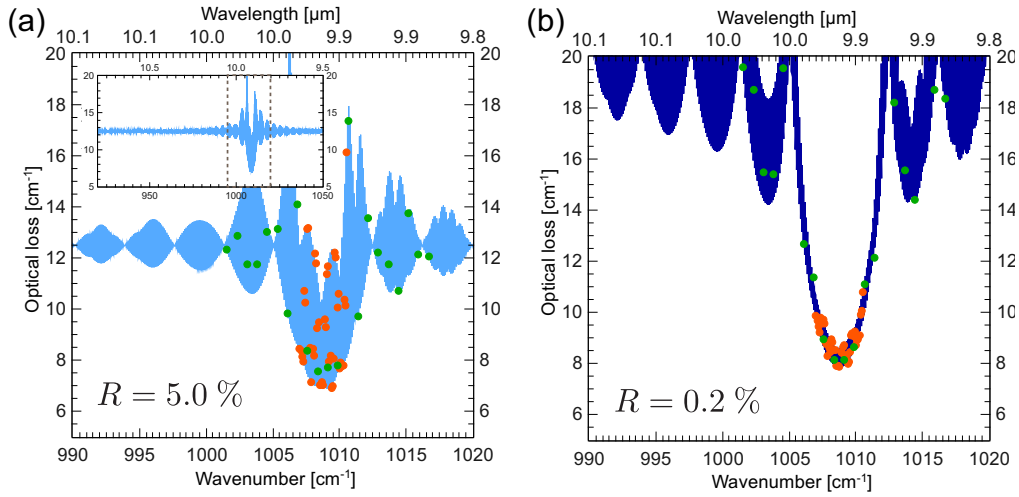

Figure 2.10: EC loss and allowed EC modes (orange dots) and FP mode (green dots): The allowed EP modes and EC modes are calculated by Eq. 2.33 in different facet reflectance condition. $R = 5.0$ % and 0.2 %.

EC laser starts to oscillate at the lowest allowed mode since it can reach to the gain of optical amplifier. Thus, by choosing the lowest allowed mode of the given tuning condition, we can see the tuning performance with grating angles, i. e., different oscillation condition. Figure 2.11 shows the tuning behavior of EC laser with different facet reflectance. When $R = 5.0\%$, the intervals of lasing mode are very discrete and obviously very bad performance in terms of continuous tuning, as can clearly seen in Fig. 2.11-(a). Although the lasing modes are still selected only from EC modes, in such a system, the smooth switch to the neighboring modes are quite difficult due to the large fluctuation of allowed mode distribution. Some range follow EC intervals but those are unpredictable.

With R =0.2 % facet reflectance, the tuning performance can be improved, as shown in Fig. 2.11-(b), Although the lasing modes are still dominated by FP mode intervals, overall tuning performance is following the EC oscillation. The mode interval can be calculated by $\Delta \sim 1/2(nl + L)$, so that having longer cavity in the external optics contributes to the narrower linewidth. Not only for power ramping issue coming from the lasing restriction by parasitic oscillation, but also for such a fine tuning, achieving

$R < 1.0$ % reflection is also mandatory for such quasi-continuous tuning, and further reduction would be very advantageous for such a performance.

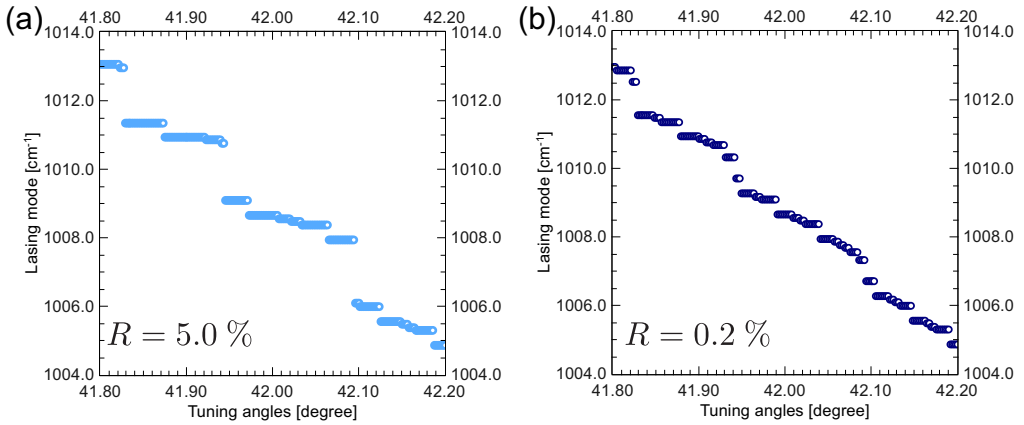

Figure 2.11: Tuning behavior of EC system with different facet reflectance: The tuning performance of $R = 5.0$ % and $R = 0.2$ % are shown. For this simulation, cavity length was set at 5.0 cm, which is a similar length of our setup. Smooth tuning behavior is clearly seen in (b), while the mode hopping is crucial in (a).

Here we have demonstrated the tuning performances of EC laser using different facet conditions, and have shown the effects of good reduction of modal reflectance of laser facets for the power performance as well as for the tuning. In reality, achieving $R < 1.0$ % of reflectance is quite difficult even with angled facet lasers. This means that, in most of the cases, the mode intervals during fine tuning are mostly dominated by FP mode spacing because of their insufficient facet coating performance. For this reason, using a longer chip rather than a shorter chip is a better choice for narrower FP mode intervals, which ultimately contributes to finer tuning resolution of the system from the practical point of view. In fact, reproducing high performance AR coating applied on laser facets is quite difficult due to a number of error factors during the fabrication process, such as system calibration of e-beam evaporator, sample's facet condition and so on. In order to increase the yield rate out of the production of optical amplifiers, this approach can still liquidate such issues. Using angled facet laser would, of course, provide another chance for better performance.

2.3 Summary

In QCL section, the basic theories for band diagram calculation as well as the derivation method of wavefunctions and eigenstates are first explained. Secondly, the effect of doping were shown by using self-consistent numerical method. We conclude that the optimal doping levels is necessary for good QCL operations as well as for achieving a designed range of emission.

In EC-QCL part, the canonical lasing theory was explained, followed by the basics of EC laser system. In order to access the fact that a low residual reflection on the amplifier facet, i. e., QCL, is strongly required for EC systems, we have simulated the power performance and tuning performance with different modal reflections. As a conclusion, achieving $R < 1.0\%$ of modal reflectance of laser facets would give a good performance in EC-QCL.

Since these theories are based on the results and know-how gained during the PhD work, the recommendation described here might be also helpful for actual device fabrications.

Chapter 3

Dielectric coatings for mid-infrared

In this chapter, we describe dielectric coatings for mid-infrared. As a part of the EC-QCLs study, anti-reflective coatings was intensively investigated during this work. The fabrication details of coatings and their performances are also presented.

3.1 Introduction of the mid-IR optical coating

Ever since Newton studied fundamentals of optical phenomena, manipulation of light propagation is of great interests for mankind and now plays a crucial role in many systems of modern optical applications [1, 69, 70, 71, 72, 73]. Along with such a historical passage, anti-reflection (AR) coatings and interference (IF) coatings have been developed and widely used , by starting with glass coating [74, 75] and now being integrated in micro-optoelectronic devices [58, 76, 77, 78, 79]. Together with such coating applications, the improvement of coating technologies have, nevertheless to say, also contributed for today's device technologies as well.

There are several approaches to achieve a reduction of reflection from surface. Owing to the today's nano-scale processing technologies, it is possible to fabricate two-/three-dimensional nano-/micro-structures of sub-wavelength range scale. Tailoring such structures, so called "meta-surface", enables to

manipulate optical ray in terms not only of the propagation direction but also the intensity as well as the polarization of ray. AR coatings using this technique are also demonstrated [80]. This method is however still not suitable for mass-production level. As a simpler method, a needle-shaped surface structure, so called "black silicon," has been demonstrated [81, 82]. The ensemble of needle-shaped materials enables a gradual refractive index changes, resulting a smooth transmission of light between two different media. This method is now widely spreading for many optoelectronic device applications, such as solar cells [83] and IR-cameras [82]. Among these new technologies, multilayer dielectric coatings are commonly used for reducing the reflection. The study has been done over a century, which was mainly boosted up during the World War II [84]. Thus, AR coating technique is well-established and the various coating models with their theoretical strategies can be found in many literature [1, 69, 70]. Dielectric multilayer coating is a major part of coating application due to its simplicity in processing and can be found in many commercial productions [85, 86]. Thus dielectric coatings are quite useful from an application point of view.

Recent interests in molecular vibrational spectroscopy and microscopy have triggered further improvements of optics in the mid-infrared (mid-IR). Optical coatings for the mid-IR range are also greatly in demand. This new frontier of applications however gives another challenge for optical coatings, because coatings of multilayer film of mid-IR range is quite difficult compared to visible and near-IR range. In general, for multilayer dielectric coatings, the film thickness is designed with the order of the target wavelength. For the mid-IR range, the coating thickness often reaches at several micrometers, which results in many issues. One is a stress issue of coating. Thick layered coating often results in flaking and delamination of the film, due to the internal stress of dielectric materials. Another issue is a lack of dielectric materials with appropriate optical constants for optimal layouts. For shorter wavelength range, there are a plenty of materials thus the freedom of selection is generally large. Compared to visible and near-IR range, most of dielectric materials possess phonon absorption in the mid-IR range, thus optical transparency is quite low. This fact gives another restriction for selecting materials in layout designing. Due to these issues, high performance coatings in mid-IR attracts great interests in the coating community. A number of papers have reported demonstrations of the mid-IR range with various approaches, such as a newly developed optimization method [87, 88, 89, 90] and a gradual refractive index profile.

During this work, we have addressed anti-reflection coatings and interference coatings for the mid-IR use. This study is motivated to improve AR coating performance and to apply on a laser facet. In external cavity quan-

tum cascade laser, the inherent facet reflectivity restricts the light coupling between the external cavity resonator and the QCL amplifier. This effect results in a limited output power and a narrow tuning range. In order to improve this, high performance AR coatings are necessary on the intra-cavity facet of QCL. Another motivation is to use for filter tunable external cavity lasers [91, 92]. Due to its compactness as well as system stability, filter tunable lasers are also attractive as a coherent light source. A narrow-band IF-filter for the mid-IR range is however also quite challenging due to the same reasons mentioned above. In this section, we describe basic theories of multilayer dielectric coatings, and optical properties of dielectric materials we used during this work.

3.1.1 Theory of light propagation

This section explains a fundamental theory of light propagation and the transfer matrix method for modeling multilayer coatings. This formalization is now a standard procedure for designing anti-reflection coating as well as interference coatings. By manipulating the formula, the method is quite useful to optimize the coating layouts.

3.1.1.1 Optical constants

The propagation property is characterized by optical constants. Speed of light inside an homogeneous material, v is written as [1, 69],

$$v = \frac{c}{n}. \tag{3.1}$$

Here, c is speed of light in vacuum and n is refractive index. In case of dielectric materials, the value of n is typically around 1.3–4.0, which also has a dependency on the wavelength. By considering the absorption of the material, refractive index can be formed as a complex number $\tilde{n}$, the refractive index n as a real part and the absorption coefficient, in other word, extinction coefficient, as a imaginary part κ. Thus the constants is expressed as,

$$\tilde{n} = n + i\kappa. \tag{3.2}$$

As the most simple case, the Fresnel reflection of the two materials, n_1 and n_2, is determined by,

$$R = \left(\frac{n_2 - n_1}{n_2 + n_1}\right)^2. \tag{3.3}$$

By manipulating these parameters, it is possible to engineer dielectric layers for particular use at the target wavelength range.

3.1.1.2 General property of light propagation

This section reviews the basic formulation of light propagation inside dielectric medium. We introduce Maxwell's formulas [1, 69, 73]

$$\nabla \times \mathbf{E} = -\frac{\partial \mathbf{B}}{\partial t}, \tag{3.4}$$

$$\nabla \times \mathbf{H} = \mathbf{i} + \frac{\partial \mathbf{D}}{\partial t} \tag{3.5}$$

$$\nabla \cdot \mathbf{D} = \rho, \tag{3.6}$$

$$\nabla \cdot \mathbf{B} = 0. \tag{3.7}$$

Here, $\mathbf{E}$ and $\mathbf{H}$ represent the electric field and the magnetic field, respectively. $\mathbf{D}$ and $\mathbf{B}$ are electric flux density and magnetic flux density inside the media, which are expressed as,

$$\mathbf{D} = \epsilon\mathbf{E} = \epsilon_0\mathbf{E} + \mathbf{P} \tag{3.8}$$

$$\mathbf{B} = \mu\mathbf{H} = \mu_0\mathbf{H} + \mathbf{M}, \tag{3.9}$$

where $\mathbf{P} = \epsilon\chi\mathbf{E}$ and $\mathbf{M} = \mu\mathbf{H}$ are electric and magnetic polarization inside the media. By assuming that $\rho = 0$ and $\mathbf{i} = 0$ inside the media, the electric field satisfies,

$$\nabla^2\mathbf{E} - \epsilon\mu\frac{\partial^2}{\partial t^2}\mathbf{E} = 0. \tag{3.10}$$

By solving this equation, the electric field can be expressed as,

$$\mathbf{E}(\mathbf{r}, t) = \mathbf{E_0} \exp\left\{i\left(\mathbf{k}\cdot\mathbf{r} - \omega t\right)\right\}. \tag{3.11}$$

Here, $\mathbf{k}$ is the wavevector and ω is the frequency of light. $\mathbf{E_0}$ is the amplitude of the electric field of light. By using $n = \sqrt{\epsilon\mu}$ as the refractive index of the media and λ as the wavelength of the light, the wavevector becomes,

$$\mathbf{k} = \frac{2n\pi}{\lambda}\hat{k}. \tag{3.12}$$

$\hat{k}$ is a unit vector of the direction of light propagation. As shown in FIg. 3.1, the relation of electric field and magnetic field is as [1, 73],

$$\mathbf{H} = \frac{i}{\mu\omega}\nabla \times \mathbf{E} \tag{3.13}$$

$$= \frac{1}{\eta_0}\hat{k} \times \mathbf{E}. \tag{3.14}$$

μ is relative permeability of vacuum, which equal to 1, and optical impedance of vacuum $\eta_0 = \sqrt{\mu_0/\epsilon_0}$, which is approximately equal to 120π. When the light goes through different media, the electromagnetic waves satisfy its boundary conditions. Supposing that $\mathbf{n}$ is a normal vector of boundary and there is no charge at the boundary, e.g., $\rho = 0$, the conditions can be expressed as,

$$(\mathbf{E_2} - \mathbf{E_1}) \times \mathbf{n} = 0, \qquad (\mathbf{D_2} - \mathbf{D_1}) \cdot \mathbf{n} = 0 \tag{3.15}$$

$$(\mathbf{H_2} - \mathbf{H_1}) \times \mathbf{n} = 0, \qquad (\mathbf{B_2} - \mathbf{B_1}) \cdot \mathbf{n} = 0 \tag{3.16}$$

The notations, **1** and **2**, represent different media. In the case of incident angle θ_1 and refraction angle θ_2, reflectivity coefficients and transmittivity coefficients are derived by using these equations and Snell's law, $n_1 \sin\theta_1 = n_2 \sin\theta_2$, as,

$$r_{12} = \frac{n_1 \cos\theta_1 - n_2 \cos\theta_2}{n_1 \cos\theta_1 + n_2 \cos\theta_2}, \qquad t_{12} = \frac{2n_1 \cos\theta_1}{n_1 \cos\theta_1 + n_2 \cos\theta_2}, \tag{3.17}$$

$$r_{21} = \frac{n_2 \cos\theta_2 - n_1 \cos\theta_1}{n_1 \cos\theta_1 + n_2 \cos\theta_2}, \qquad t_{21} = \frac{2n_2 \cos\theta_2}{n_1 \cos\theta_1 + n_2 \cos\theta_2}. \tag{3.18}$$

Because electromagnetic waves must satisfy the boundary conditions at every boundary of layers, it is possible to calculate optical coefficients by algebraic. The details of this method is explained in the following section.

3.1.1.3 The transfer matrix

As mentioned in the previous section, algebraic calculation is applicable for optical coefficients in layered media by setting the parameters of each layers with matrix forms with given thickness and given optical constants of the media. Here, by assuming the reflectivity $r_k = r_{k,k+1}$ and $t_k = t_{k,k+1}$ in the previous section, the reflectivity and the transmittivity become,

$$r_k^{\mathrm{p}} = \frac{n_k \cos\theta_{k-1} - n_k \cos\theta_{k-1}}{n_k \cos\theta_{k-1} + n_{k-1} \cos\theta_k}, \tag{3.19}$$

$$t_k^{\mathrm{p}} = \frac{2n_k \cos\theta_{k-1}}{n_k \cos\theta_{k-1} + n_k \cos\theta_{k-1}}, \tag{3.20}$$

where the notation p represents p-polarized light[1]. By defining a parameter δ_k with complex refractive index $\tilde{n}$ as,

$$\delta_k(\lambda) = \frac{2\pi \tilde{n}_k(\lambda)\, d_k \cos\theta}{\lambda}, \tag{3.21}$$

[1] we may need to consider s-polarized light. However in the case of normal incident light, these effect can be vanished.

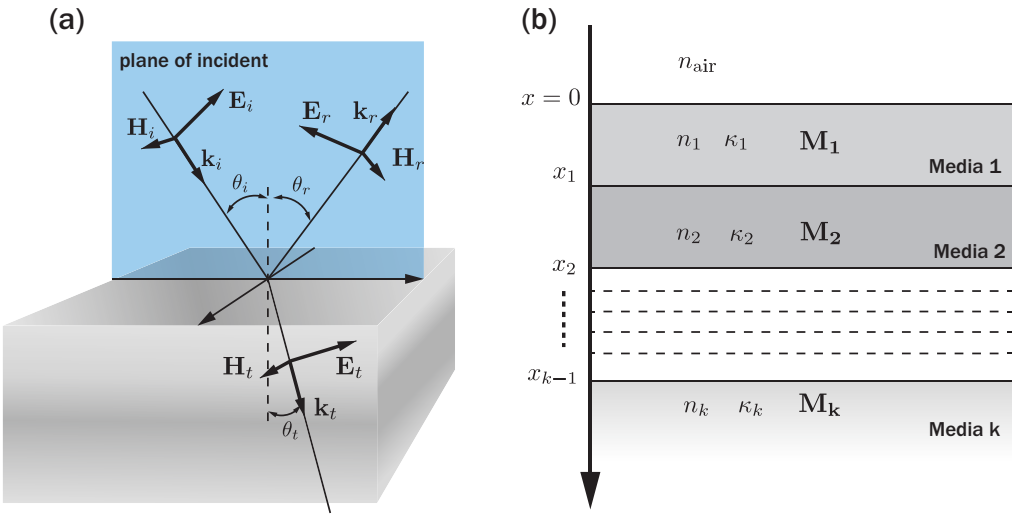

Figure 3.1: Schematic images of light propagation between different medium: Figure.(a) shows electromagnetic waves at medium boundary, and Figure.(b) of layered sequence of different medium with optical constants and transfer matrix of each layers.

Here we define the vector for the initial light from the vacuum as,

$$\mathbf{x_0}(\lambda) = \begin{pmatrix} 1 \\ r_1(\lambda) \end{pmatrix}, \qquad \mathbf{x_k}(\lambda) = \frac{1}{t_k^{\mathrm{p}}}\mathbf{x_0} \tag{3.22}$$

For the calculation, the matrix of media k is defined as,

$$\mathbf{M_k}(\lambda) = \begin{pmatrix} e^{-i\delta_k(\lambda)} & r_{k+1}(\lambda)\, e^{i\delta_k(\lambda)} \\ r_{k+1}(\lambda)\, e^{i\delta_k(\lambda)} & e^{i\delta_k(\lambda)} \end{pmatrix}. \tag{3.23}$$

By multipling this matrix as the layer's order, the reflectivity of multilayered structure becomes,

$$r_{\text{multi}}(\lambda) = \frac{\left|\mathbf{u}_+ \cdot \left(\prod_i \mathbf{M_k}(\lambda)\right)\mathbf{x_0}(\lambda)\right|}{\left|\mathbf{u}_- \cdot \left(\prod_i \mathbf{M_k}(\lambda)\right)\mathbf{x_0}(\lambda)\right|} \tag{3.24}$$

Here, the unit vectors are

$$\mathbf{u}_+ = \begin{pmatrix} 0 \\ 1 \end{pmatrix}, \qquad \mathbf{u}_- = \begin{pmatrix} 1 \\ 0 \end{pmatrix}. \tag{3.25}$$

Therefore, the reflectance becomes,

$$R_{\text{multi}}(\lambda) = \left| \frac{\mathbf{u}_+ \cdot \left(\prod_i \mathbf{M_k}(\lambda) \right) \mathbf{x_0}(\lambda)}{\mathbf{u}_- \cdot \left(\prod_i \mathbf{M_k}(\lambda) \right) \mathbf{x_0}(\lambda)} \right|^2 \tag{3.26}$$

By using these parameters in the same manner, the transmittance becomes,

$$T_{\text{multi}}(\lambda) = \frac{n_0}{n_k} \left| \frac{\prod_i t_i^{\text{p}}(\lambda)}{\mathbf{u}_- \cdot \left(\prod_i \mathbf{M_k}(\lambda) \right) \mathbf{x_0}(\lambda)} \right|^2 . \tag{3.27}$$

By setting the layer thickness d_k as variables, it is possible to derive the optimized thickness of anti-reflection for target wavelength, as well as interference applications

3.1.2 Transmission property of media

For the characterization of transmission measurement, we review the reflection and the transmission mechanism of a given system. The schematic image of media with different optical properties is depicted in Fig. 3.2-(a). Light propagation is also shown in Fig. 3.2-(b). This system is useful not only for simple transmission measurement, but also for reflection measurement of coated material. The following describes the formulation of light propagation, called "Airy formula", and analysis techniques for coating reflection measurement [73, 38].

3.1.2.1 Airy formalization

The expression for transmission and reflection can be derived by summing the amplitudes of successive reflections and refractions. By taking the phase shift at every reflection by a factor, $e^{-2i\phi}$, the total reflection becomes

$$\begin{aligned} r &= r_{12} + t_{12}t_{21}r_{23}e^{-2i\phi} + t_{12}t_{21}r_{23}r_{21}r_{23}e^{-4i\phi} + \cdots && (3.28)\\ &= r_{12} + \frac{t_{12}t_{21}r_{23}e^{-2i\phi}}{1 - r_{21}r_{23}e^{-2i\phi}} && (3.29)\\ &= \frac{r_{12} + r_{23}e^{-2i\phi}}{1 + r_{12}r_{23}e^{-2i\phi}}, && (3.30) \end{aligned}$$

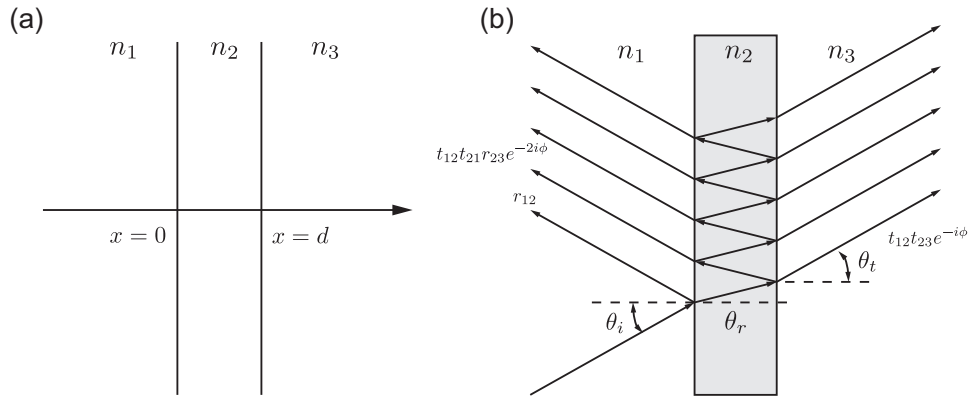

Figure 3.2: Schematic images of light propagation inside three different media and Airy formulas: (a) shows geometric representation of three different media. (b) shows multi-reflection inside a single substrate. In transmission measurement, n_1 and n_3 media can be assumed as vacuum, and n_2 medium as substrate.

where r_{ij} and t_{ij} represent the reflection coefficient and the transmission coefficient between medium i and medium j, respectively. Similarly, the total transmission coefficient t is also obtained as,

$$t = t_{12}t_{23}e^{-i\phi}\left[1 + r_{23}r_{21}e^{-2i\phi} + \left(r_{23}r_{21}e^{-2i\phi}\right)^2 + \cdots\right] \tag{3.31}$$

$$= \frac{t_{12}t_{23}e^{-i\phi}}{1 - r_{21}r_{23}e^{-2i\phi}}. \tag{3.32}$$

By using these formulas, the reflection and transmission of light can be characterized.

In the case of normal incident light, $\theta = 0$, medium 1 and medium 3 are vacuum, $n_1 = n_3 = 1$, and medium 2 is a substrate with $n_2 = n$, the reflectivity coefficients and the transmittivity coefficients are expressed as,

$$r_{12} = r_{23} = \frac{n-1}{n+1} \qquad r_{21} = r_{32} = \frac{1-n}{1+n} \tag{3.33}$$

$$t_{12} = t_{32} = \frac{2}{1+n} \qquad t_{21} = t_{23} = \frac{2n}{n+1}. \tag{3.34}$$

From these formulas, the following relation between r_{12}, r_{23}, t_{12}, and t_{23} can be derived,

$$t_{12}t_{23} - r_{12}r_{23} = 1. \tag{3.35}$$

3.1.2.2 Spectral averaging

If the plane wave light source is polychromatic and contains several components λ, ϕ is no longer well defined. Assuming $\Delta\lambda$ the spectral spread of the incident plane wave, the phase shift is expressed as,

$$\Delta\phi = -\frac{\Delta\lambda}{\lambda}\phi, \tag{3.36}$$

where λ is the central component of the wavelength. In the case of thin layer's transmission and reflection, the phase shift must be taken into account. However, for thick layer, the phase shift is no longer periodic because the spread of the phase shift is greater than π. That is,

$$|\Delta\phi| > \pi. \tag{3.37}$$

In order to satisfy this condition in transmission measurement fro normal incident light, the substrate thickness must be,

$$d > \frac{\lambda^2}{2n\Delta\lambda}. \tag{3.38}$$

Suppose that 10 μm is the central wavelength of the transmission measurement, and the measurement resolution is set as 8 cm^{-1}, which corresponds to 0.08 μm in this wavelength. In the case of InP substrate transmission measurement under this condition, the required thickness of substrate for spectral averaging analysis is about 0.215 mm. In our measurement, we used 0.3 mm thickness InP substrate, which satisfies this condition.

If the spectral distribution is uniform over $(\lambda_{k-1}, \lambda_k)$, the average transmittance of this interval is given by,

$$\langle T_k \rangle = \frac{1}{\lambda_k - \lambda_{k-1}} \int_{\lambda_{k-1}}^{\lambda_k} T(\lambda)\, d\lambda. \tag{3.39}$$

By applying Eq. (3.32), the transmittance is equivalent to,

$$\begin{aligned}
\langle T \rangle &= \frac{1}{\pi}\int_0^{\pi} T d\phi && (3.40)\\
&= \frac{1}{\pi}\int_0^{\pi} t * t d\phi && (3.41)\\
&= \frac{|t_{12}t_{23}|^2}{1 - |r_{12}r_{23}|^2} && (3.42)\\
&= \frac{T_{12}T_{23}}{1 - R_{12}R_{23}}. && (3.43)
\end{aligned}$$

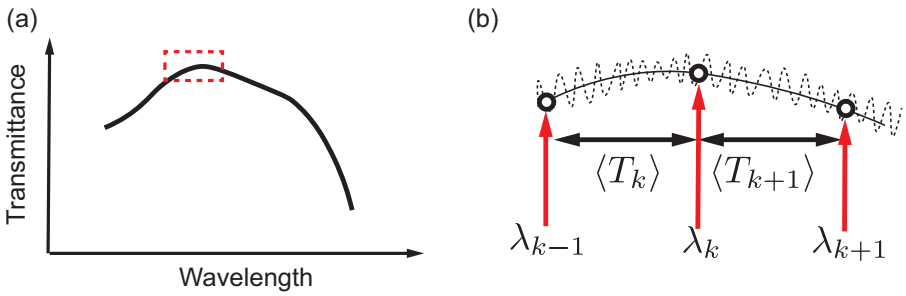

Figure 3.3: Schematic image of spectral averaging related to transmission measurement by FTIR: (a) shows transmittance curve, and (b) shows data points with low resolution wavelength. In this case, the transmission data has relatively uniform distribution regardless of the effect of fringe caused by the substrate.

By taking the absorption of the substrate into account, the transmission can be expressed as,

$$\langle T \rangle = \frac{T_{12}T_{23}e^{-\alpha d}}{1 - R_{12}R_{23}e^{-2\alpha d}}. \tag{3.44}$$

Here, α is the absorption coefficient of the substrate and the d is its thickness.

By inserting Eq. (3.35) to Eq. (3.42), the transmittance with spectral averaging condition becomes,

$$\langle T \rangle = \frac{|1 + r_{12}r_{23}|^2}{1 - (r_{12}r_{23})^2} \tag{3.45}$$

$$= \frac{1 + r_{12}r_{23}}{1 - r_{12}r_{23}}. \tag{3.46}$$

By replacing the relation $r_{12} = -r_{23}$ from Eq. (3.33) and Eq. (3.34), the reflectivity r_{23} can be expressed as,

$$r_{12} = -r_{23} = -\sqrt{\frac{1 - \langle T \rangle}{1 + \langle T \rangle}}. \tag{3.47}$$

Supposing that the reflectivity becomes r'_{12} after the transmission measurement of AR coated substrate, and then the reflectance becomes,

$$R_{12} = (r'_{12})^2 \tag{3.48}$$

$$= \left(\frac{\langle T' \rangle - 1}{\langle T' \rangle + 1}\right)^2 \left\{\sqrt{\frac{1 - \langle T \rangle}{1 + \langle T \rangle}}\right\}^{-2}, \tag{3.49}$$

where $\langle T' \rangle$ is also the transmittance of the AR coated substrate.

The final formula Eq. (3.49) enables to extract the reflectivity of AR coating. However the absorption of the substrate is not considered in this formula, neither the absorption of anti-reflection coating. Therefore, this analysis allows us to grab a rough property of the reflectivity without high accuracy.

3.1.3 Fabrication process

For dielectric material coating, physical vapor deposition (PVD) is commonly used to deposit thin film coatings. The instruments require high level of vacuum during the process so that the process gives a good reproducibility. Plasma ion assisted deposition and electron beam (e-beam) evaporation are used for dielectric coatings. These methods are well-used not only in industrial, also in research fields. During this work, we mainly used an e-beam evaporator (PVD75, Kurt J. Lesker. Inc. USA) for sample preparation as well as coatings on laser facets.

Figure 3.4-(a) is a picture of our e-beam system, a deposition chamber with a turbo molecular pump (HiPace 700, Pfeiffer Vacuum Technology AG, Germany) and a controlling unit. The substrate temperature can be controlled during the process. Deposition rate needs to be controlled with high accuracy. This can be done using PID (Proportional Integral Derivative) control of beam intensity, and tooling factors for each materials. The material thickness is monitored by quartz crystal oscillator (750-678-G1, Quartz Monitor Crystals, Inficon, Switzerland). Since some materials, such as zinc sulfide, sublimate with a sudden increase of e-beam intensity, the preparation and calibration of the system are quite important for reliable process. In addition, since the materials have different layer texture, appropriate deposition rate needs to be adjusted.

Figure 3.4-(b) is our tailor-made sample stage for material coating. The central part of the stage is for laser facet coating and 1.0×2.0 cm^2 holders are for reference samples. The stage is set at the top part of the chamber, which is about 40 cm above from the material boat. The more details of the system can be found elsewhere [93, 94].

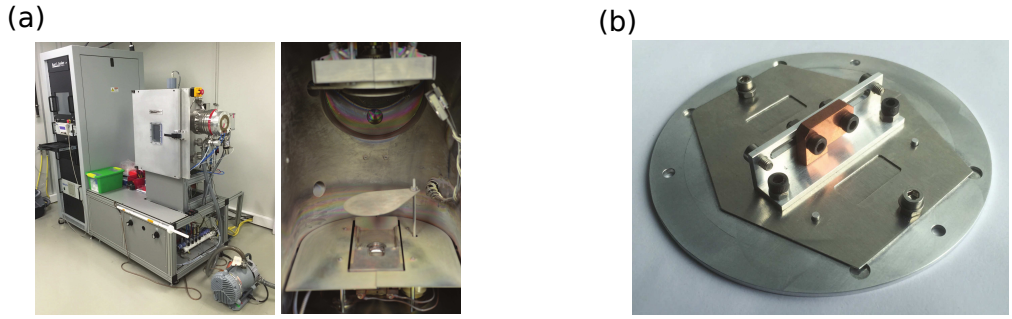

Figure 3.4: Sample stage (a) for the deposition of QCL facet and the outlook of electron beam deposition machine and its inside of the chamber (b)

3.1.4 Dielectric materials for the mid-IR

Dielectric materials possess electric polarizability, which gives a phase change in electromagnetic waves as well as in the traveling speed in the medium. Details of physical background can be found in literature [69, 73, 65]. In multilayer coating design, the performance is largely determined by the optical properties of materials, as introduced with Eq. 3.2. Refractive index, n, determines the reflection property, and extinction coefficient, κ, mainly causees optical loss. Thus for multilayer design, finding the appropriate refractive index with low-loss is the first task to be done. For mid-IR range, the number of such materials are quite limited. In this part, we present the materials we have investigated during this work.

3.1.4.1 Coating materials

We define materials with refractive index around $n \sim 1.0$–1.5 as a "low" refractive index. As a low refractive index material, we use yttrium fluoride (YF_3) and ytterbium fluoride (YbF_3). Figure 3.5 shows optical constants of YF_3 prepared with different substrate temperatures, at 100°C and 250°C. Regarding the refractive index, there are small difference between two samples at the longer range, but not dominant. On the other hand, a sample at 250°C shows remarkably larger absorption property. This may be due to the more crystalline-like structure of the coating rather than film-like structure of 100°C. Due to the large thermal expansion during the evaporation, the porous structure packs after the cooling, then become more dense compared to the lower temperature deposition. The adhesion of YF_3 is not always good, thus it needs a help of adhesion promoter for good coating. This will be presented later in this section.

Zinc sulfide (ZnS) has a refractive index around 2.2–2.3 in the mid-IR range. Zinc selenide (ZnSe) has around 2.4–2.5. These materials can be grouped as the middle refractive index materials. Due to the toxicity issue, we have used ZnS during this work. Here we have optical properties of ZnS prepared at 100°C and 250°C in Fig. 3.6. In the same manner of YF_3, a relatively stronger absorption was observed in a sample of 250°C, while a bare absorption can be seen in the lower temperature sample. Refractive index is relatively flat over the spectrum. This is quite advantageous for broadband coatings. We obtained good qualities of coating in both temperature conditions.

Germanium is known as a semiconductor material, but also processes a excellent dielectric property. Refractive index is around 4.0–4.1 over the entire mid-IR range, while having quite low absorption. Figure 3.7 shows the

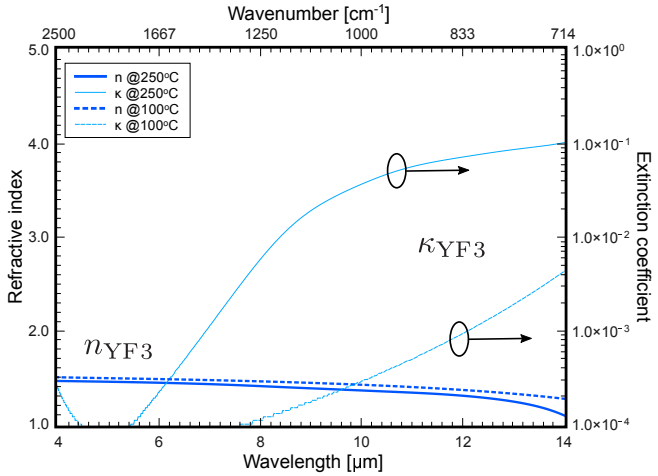

Figure 3.5: Optical constants of YF_3 deposited in two different temperatures, 100°C and 250°C. A dominant absorption was measured with higher temperature deposition.

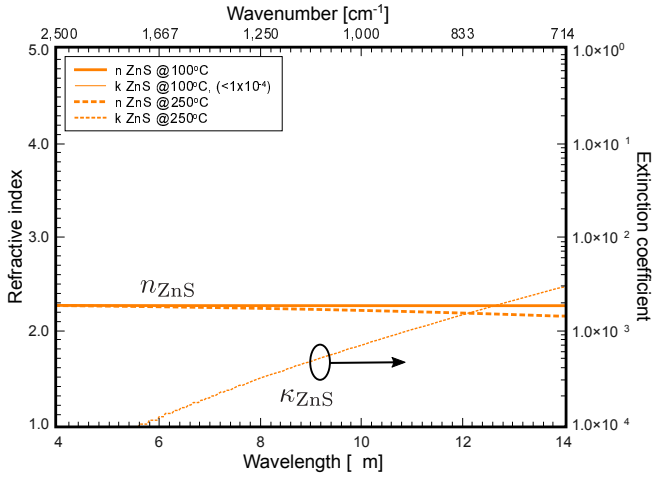

Figure 3.6: Optical constants of ZnS deposited in two different temperatures, 100°C and 250°C. A dominant absorption was measured with higher temperature deposition.

optical constants deposited in two different conditions at 100°C and 250°C, and both dispersions are identical. Ge has been used as a high refractive index material for coatings. During the process, it shows excellent adhesion, as well as good surface quality in both conditions.

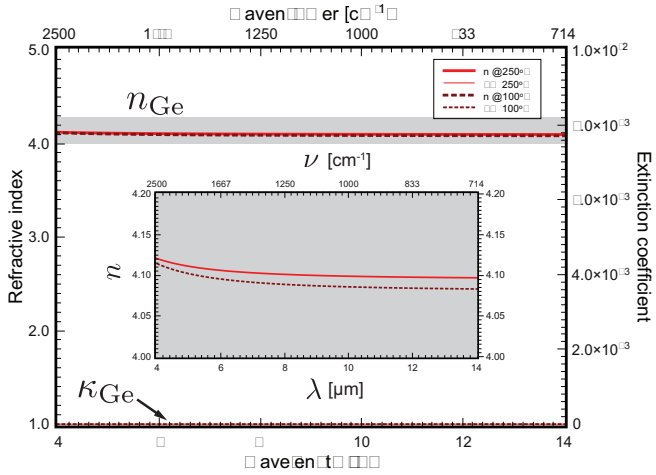

Figure 3.7: Optical constants of Ge deposited in two different temperatures, 100°C and 250°C. Inserted graph exhibits the zoom-in profile from 4.0-4.3 index region. Absorption were absent along the measured range, 4-14 μm.

3.1.4.2 Adhesion promoter

For dielectric coatings, adhesion promoter is commonly used since some materials does not possess adhesion and result in delamination. Some dielectric materials are useful to overcome such an issue by introducing as a quite thin layer between the main coating materials. We used silicon dioxide (SiO_2) and yttrium oxide (Y_2O_3) for this aim. Figure 3.8-(a) and (b) are optical constants of YF_3 and SiO_2, respectively. For longer wavelength range, Y_2O_3 is more appropriate since it does not have strong absorption in the entire wavelength range, while SiO_2 has a strong absorption from 8 to 10 μm. In addition, the adhesion promoter was mainly used for a help of YF_3 coating.

Here we present the effect of adhesion promoter applied on YF_3 coating. A set of micrograph of two demonstrators are shown in Fig. 3.9; (a) is YF_3 coating of 1.0 μm thick with 10 nm Y_2O_3, and (b) is of the same thick but without adhesion layer. Fig. 3.9-(a) exhibits a smooth surface, but (b) has flakings. As can be seen the clear difference, the coating quality can be greatly improved by an adhesion promoter.

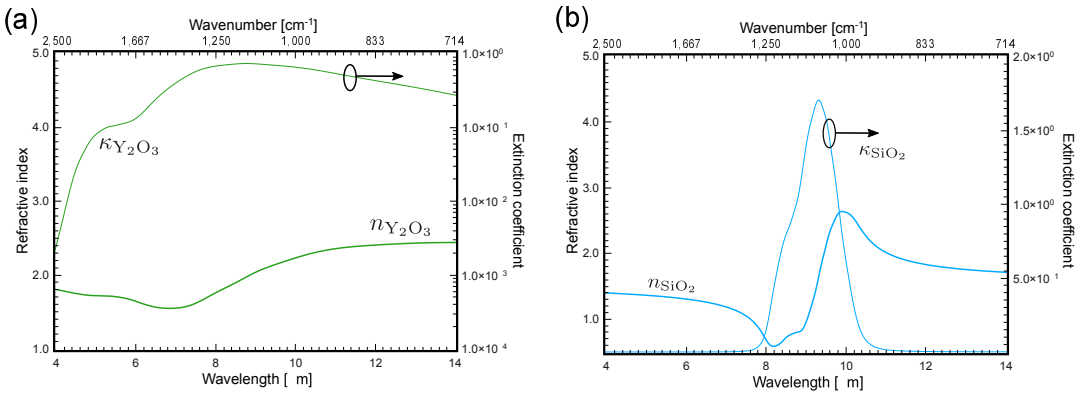

Figure 3.8: Optical constants of SiO_2 deposited at 250°C, measured by FTIR ellipsometry. The parameters from the measurement were fitted by the Brendel oscillator model.

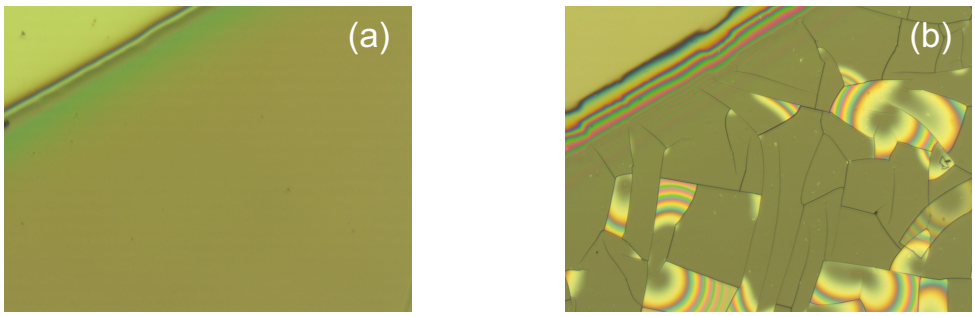

Figure 3.9: Effect of adhesion promoter, applied on YF_3 coating; (a) is YF_3 coating of 1.0 μm thick with 10 nm Y_2O_3, and (b) is of the same thick but without adhesion layer. Sample of (b) exhibits flaking.

3.1.4.3 Substrate

For coating optimization, the optical constant of coated material, i. e., a substrate, is also an important parameter. We mainly used silicon (Si) and indium phosphide substrate (InP) for coating demonstration. Figure 3.10 and Figure 3.11 shows optical constants measured by FTIR using Brendel oscillator model. As can be seen from Fig. 3.10 fabrication process also influences to the material property due to the impurity levels, resulting in free carrier absorption. The measured sample may have two types of carrier contribution by considering the Drude dispersion model. Ingot-made Si substrate, however, does not exhibit any absorption and optical constant is flat over the spectrum.

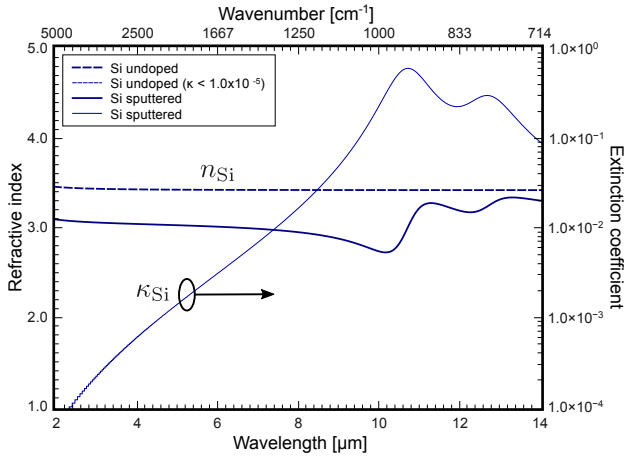

Figure 3.10: Optical constants of Si measured by FTIR ellipsometry. The parameters from the measurement were fitted by the Brendel oscillator model.

A similar example can be seen from Fig. 3.11. The three samples are also made with ingot process but with different doping levels. Here we remark that Fe-doping is to remove free carrier from the material by means of deep center, thus is non conductive substrate. The higher doped sample has stronger absorption. Because of Kramer-Kronig relation, the refractive indice are also slightly affected by the doping.

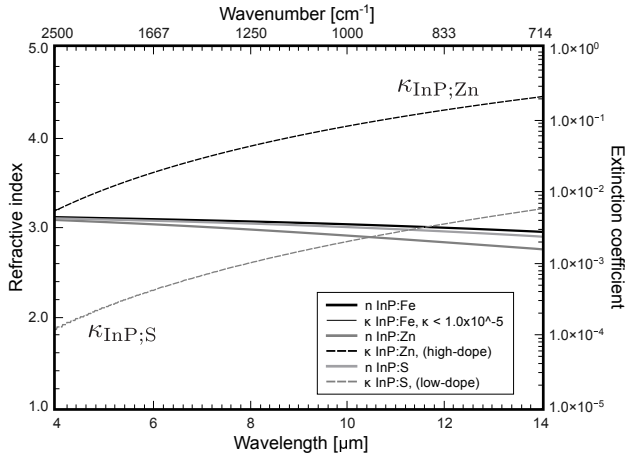

Figure 3.11: Optical constants of InP measured by FTIR ellipsometry. The parameters from the measurement were fitted by the Brendel oscillator model.

3.2 Anti-reflection coating

Anti-reflection (AR) coatings in the mid-infrared region are widely used for many applications, such as infrared semiconductor laser facets and detectors. The improvement of AR coating performance greatly contributes to these applications. The external cavity quantum cascade laser is one of the applications that requires a high-performance AR coating on the laser facet. Coated laser facets with low reflectance over a broad band are important for broad tunability of the laser [7, 24, 28, 91]. Therefore, high performance AR coatings in mid-infrared range still attracts great interest. Over the decades, dielectric coating technologies have been well developed. Many coating models and practical demonstrations can be found in the literature [1, 69, 70] as well as in commercial products[71]. However, it is still challenging to achieve high performance coatings in mid- and long-infrared optical regions, particularly for 7–15 μm, due to the quite limited number of materials having low loss in these wavelength ranges [95, 96]. Consequently, we are quite limited in the number of usable materials with appropriate refractive indexes for coating designs in mid- and long-infrared range.

Regarding multilayer coating models, high performance AR coating design can be obtained by simple computation methods [87]. The optimization allows the design of quite high-performance optical coatings, regardless of the limited number of materials available. However, as in the conventional theory of optical coating, the thickness of each layer is of the order of the target wavelength in the material. The total thickness of the coating is typ-

ically greater than the target vacuum wavelength by such computation as well as the conventional design approaches, resulting in films that easily exceed 10 μm in thickness. This is also one of the issues from the feasibility point of view. Practically, some materials possess internal stress. Thus, thick coating structures potentially have flaking and delaminating problems during the process [92]. With thicker layers, the integrated stress energy becomes too high, implying a need for few and thin layers. In addition, applying a larger number of layers introduces more opportunity for error in layer thickness. Therefore, the layout design with fewer layers and high reduction in reflection at the same time is strongly demanded for practical applications of optical coating. What is more important, such layout features ultimately contribute to the high tolerance in the reflection performance.

Recent investigations in optical coating demonstrate that coatings based on layers with thickness much smaller than the wavelength allow more freedom in the design [97, 98]. Such thin structures modulate effective refractive indexes of optical media and allow gradual refractive index changes [97, 99, 100]. By using this design concept, we can apply the conventional design approach even with the limited number of materials in this wavelength range. This approach have been demonstrated in AR coatings for mid-infrared, but still the total thickness of the coating is of several micrometers, and the spectral range is also limited [89].

In this paper, we demonstrate broadband anti-reflection coatings covering the 7 to 12 μm and 10 to 12 μm wavelength range. We design our AR coating by modifying the conventional design approach based on effective refractive index change, but, importantly, with relatively thin total thickness. We use yttrium fluoride (YF_3), zinc sulfide (ZnS), and germanium (Ge) for the coating layer materials. The simulation shows relatively large versatility for any mid-infrared spectral range as well as high tolerance against thickness errors. Furthermore, the coating approach is applicable for any coating materials, regardless of its refractive index. In the next section, we describe the concept of our AR coating design to realize high performance AR coatings, followed by the details of coating process. Our AR coating performance applied on indium phosphide (InP) substrate is demonstrated, which have n_{InP} $\sim$2.9–3.0 as material refractive indexes around 7 to 14 μm wavelength range.

3.2.1 Optimization strategy for broadband AR coating

Optimization method is widely used in the coating community. Various type of simulators are commercially available. In this study, we have also built a optimization program and designed AR coating layouts. In coating design, we define the sequence of the coating materials and optimized the thicknesses

of each layers. By setting the target wavelength and the performance of coatings, we design a tailor-made AR coating layouts. The source code is found on appendix part.

In order to optimize coating layouts. we captured the coating performance as shown in Fig. 3.12; (a) shows a performance profile of AR coating, and (b) represents a histogram data of data samples, of which the standard deviation is also useful for the optimization. The following lists all the parameters we define for calculation.

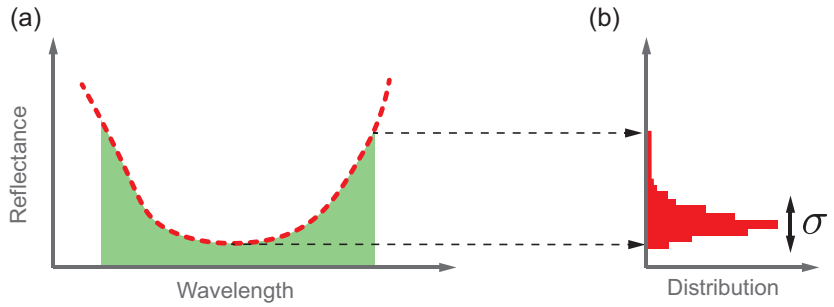

Figure 3.12: Parameters for AR coating optimization: green area in (a) relates to the parameter V_1, σ in (b) to V_2, the maximum and minimum value in blue area of (a) to V_3. V_4 and V_5 are for the maximum value and the minimum value in blue area of (a), respectively.

V_1: Integrated value of a target wavelength region,

V_2: Variance of data points, represented by σ

V_3: Difference of maximum and minimum in a targeted range,

V_4: Maximum in a targeted range,

V_5: Minimum in a targeted range.

V_1 is to minimize the reflectance over the target wavelength range. This parameter is to maximize the broadness of coating spectrum. V_2 is to make an equally reduced AR coating over the specrum. For laser facet coating, the residual reflectivity should be homogeneously suppressed for broad tuning. Therefore, minimizing the variance of data samples is quite important. In the same manner, we set the difference of the maximum and minimum reflectance within the target range with V_3. The rest two are also defined for a particular use. All the parameters are summed up linearly with weighting factors, a_i.

For the most of AR coatings during this work, we set the weighting factors as $(a_1, a_2, a_3, a_4, a_5) = (1, 1, 1, 0, 0)$. Then, the final formula for optimization becomes,

$$V_{\text{total}} = \sum_{i=5} a_i V_i \tag{3.50}$$

$$= V_1 + V_2 + V_3. \tag{3.51}$$

Here we should note that all the parameters are connected to the layer thickness of coatings, thus can be expressed as $V_{\text{total}} = V_{\text{total}}(d_i)$, where d_i represents the i-th layer's thickness. The summation value, V_{total} is minimized in the calculation and finally gives the optimal thickness with the given material sequence.

3.2.2 Two layered coating

We first demonstrated two layered AR coatings. To investigate coating performance using the same materials but different coating sequence, we optimized the coating layout using YF_3 and ZnS.

3.2.2.1 Design concept

Since two layer system is relatively simple, it can be formulated in a compact form as,

$$R = \frac{X}{1+X} \tag{3.52}$$

where X is represented with,

$$\begin{aligned} X &= \frac{n_s}{4n_a}\left[\left\{\left(\frac{n_a}{n_s}-1\right)\cos\hat{\phi}_1\cos\hat{\phi}_2+\left(\frac{n_1}{n_2}-\frac{n_a n_2}{n_s n_1}\right)\sin\hat{\phi}\sin\hat{\phi}\right\}^2\right. \\ &\quad \left.+\left\{\left(\frac{n_a}{n_1}-\frac{n_1}{n_2}\right)\sin\hat{\phi}\sin\hat{\phi}+\left(\frac{n_a}{n_2}-\frac{n_2}{n_s}\right)\cos\hat{\phi}\cos\hat{\phi}\right\}^2\right] \end{aligned} \tag{3.53}$$

and, $\hat{\phi}_i = 2\pi n_i d_i/\lambda$. n_i is the refractive index and d_i is the thickness of i-th layer. n_s and n_a is the refractive indexes of substrate and air, respectively. By solving Eq. 3.53, two different conditions for V-type / W-type coatings can be derived. For V-type coating, the refractive index has a relation of $n_2 > n_1$ and $n_2 > n_1$ for W-type. These conditions give an idea of coating profiles in terms of optical constant, finally resulting different reduction performances in reflection. The derivation together with their demonstrations are well-examined in various optical range [65, 69].

Inspired by these two-layer coating designs, we designed two different layer structures using the same materials but different sequences as, ZnS/YF_3 and YF_3/ZnS next to a InP substrate, These designs are quite standard designs also for facet coating, and demonstrated in EC use as well. The optimized structure using our program is listed in Table. 3.1. Both demonstrators were optimized from 10 to 12 μm wavelength range.

3.2.2.2 Performance

Simulations and measured reflectance are shown in Fig. 3.13. Both results shows relatively good agreements with the simulated performance. Small peaks observed around 12 μm are due to two phonon absorption of InP substrate. The ZnS/YF_3 shows broader anti-reflection compared to YF_3/ZnS. but have higher reflectance in all wavelength range. For external cavity use,

Table 3.1: AR coating of two layered systems comprising ZnS and YF_3; the models are optimized for InP plane substrate

	Design 1		Design 2	
	Matl.	Thk. [nm]	Matl.	Thk. [nm]
Substrate	InP	-	InP	-
1st layer	YF_3	694	ZnS	892
2nd layer	ZnS	568	YF_3	1529

the former performance is preferred, however not enough for a broadband optics use.

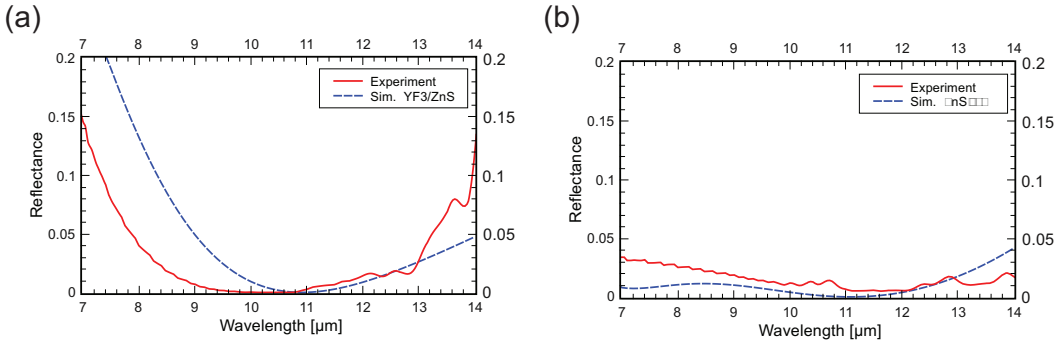

Figure 3.13: Reflectance of two layered AR coating deposited on InP:Fe (5.0×10^8 [cm^{-2}]) substrate: (a)YF_3/Zns, and (b)ZnS/YF_3.

We also captured SEM images of ZnS/YF_3 sample, which shows the porous structure in the YF_3 layer, as seen in on the top layer of Fig. 3.14. This structure results a high charge-up of the cleaved surface by the electron of SEM system.

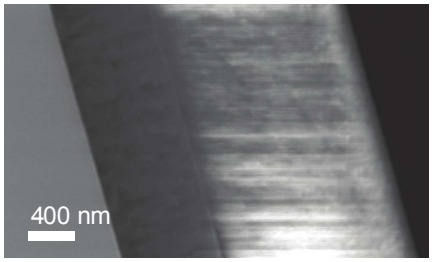

Figure 3.14: SEM images of two layered AR coating deposited on InP substrate: ZnS/YF_3.

3.2.3 Four layered coating

The content was reported in Ref. 101.

3.2.3.1 Design approach

Theoretical optimizations of AR coating with multi-layered dielectric materials have been studied over decades. A three-layer anti-reflection coating was proposed in 1947 by Lockhart and King [102]. This simple design is now one of the standard coating designs in today's optical coatings and used for many applications[50]. In this AR coating design, the refractive indexes of the various materials must satisfy the relation,

$$n_{\mathrm{b}}^2 = n_{\mathrm{s}} n_{\mathrm{t}}^2, \tag{3.54}$$

where n_{s} is the refractive index of the substrate, n_{b} is the refractive index of the bottom-most coating layer adjacent to the substrate, and n_{t} is the refractive index of the top-most coating layer adjacent to air. There is also a middle dielectric layer for which the index does not enter into the formula. The thicknesses of the bottom and top layers are each a quarter wavelength and the thickness of the middle is a half wavelength. Interestingly, the refractive index of the middle layer n_{m} is arbitrary, but by changing the middle layer material, equivalently the refractive index, it is possible to change the coating performance in terms of spectral breadth and reflectance in the target wavelength range. Specifically, a larger value of n_{m} results in a greater spectral range of efficient anti-reflectivity.

Because of the relatively small selection of dielectric materials transparent in the 7 to 14 μm wavelength range, we have modified the Lockhart approach to retain its key features, but allow for other refractive indexes. The core idea of our approach is to create a coating with a spatially averaged index profile

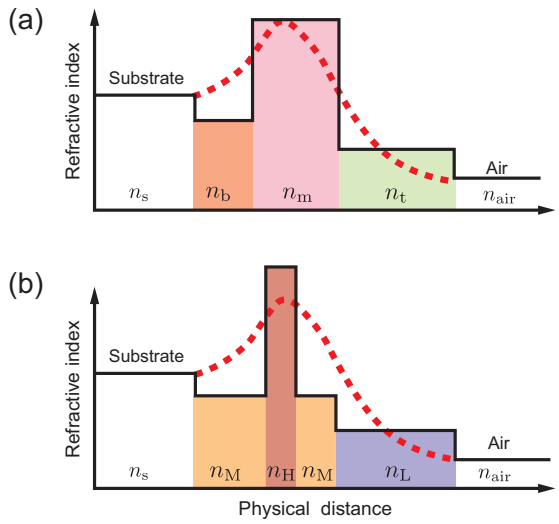

Figure 3.15: Conceptual images of Lockhart design (a) and the "quasi-Lockhart" design (b). Solid line and dash line represent the actual refractive indexes and and effective index, respectively. Both designs achieve step-up step-down profile by using different materials.

that corresponds to the Lockhart approach, but using different indexes than are foreseen in Eq. (3.54). Figure 3.15 compares the Lockhart design (a) to our "quasi-Lockhart" design (b). The dashed line is an effective index profile as experienced by the light field for both designs.

In order to realize this "quasi-Lockhart" approach, we utilized the effective, rather than the actual, refractive index change of the layer. When the layer thickness are of sub-wavelength thickness, the light overlaps each of the thin layers. As a result, light is not sensitive to each layer's individual refractive index, but, rather, sees the effective refractive index of the entire coating media. Ultimately, this effect enables us to engineer an optimal coating structure close to the original averaged refractive index profile. As a result, even without satisfying Eq. (3.54) with appropriate refractive index materials in the mid-infrared, we can design the coating by combining any high n_{H}, middle n_{M}, and low n_{L} refractive index materials.

3.2.3.2 Selection of materials

We used yttrium fluoride (YF_3), zinc sulfide (ZnS), and germanium (Ge) as low n_{L}, middle n_{M}, and high n_{H} refractive index materials, respectively. ZnS is preferred over ZnSe due to its non-toxicity. The thickness calibration of these materials were prepared on InP substrates. The optical constants were

measured by using Fourier transformation infrared spectroscopic (FTIR) ellipsometry: (SENDIRA, Sentech Instrument GmbH.). The Brendel oscillator model was used for fitting the ellipsometry data. As can be seen in Fig. 3.16, all these materials exhibit distinctively different refractive indexes and quite low absorption in the mid-infrared range. Remarkably, ZnS and Ge do not show measurable absorption in our measurement. The films that we used were deposited at 100°C and no appreciable extinction coefficient value was measured. We also characterized ZnS deposited at 250°C, for which there is a small, but measurable, value. That the 100°C films showed no extinction is indicative that it is very small, but a small, non-zero coefficient can also be obscured by the fitting process. We expect Ge to be truly transparent in this range. On the other hand, YF_3 shows a small, but measurable, increase of absorption in the longer wavelength range. For wavelengths beyond 14 μm, replacing the YF_3 with other fluorides such as ytterbium fluoride (YbF_3) will result in less absorption.

indexes

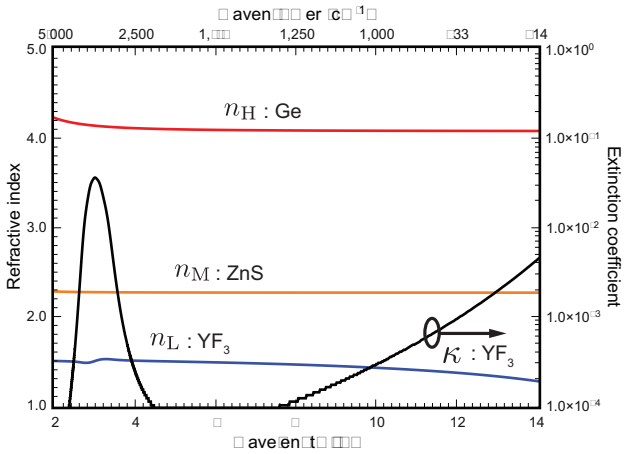

Figure 3.16: Optical constants of Ge, ZnS, and YF_3 measured by FTIR ellipsometry. The parameters from the measurement were fitted by the Brendel oscillator model.

3.2.3.3 Coating designs

By using these measured optical constants data, we optimized the layer structure for broadly reduced anti-reflection coatings. In our simulation, we use the transfer matrix method to optimize the layer thickness. We set the target wavelength range for the optimization and vary the constituent layers, maintaining the basic design sequence. The variations in layer thicknesses

are restricted to pre-determined ranges. The Ge thickness is restricted to the range of 10 nm to 100 nm, since it has the highest refractive index among the dielectric materials we used in this work. Then our program optimizes the layer thicknesses in terms of obtaining a broadly reduced reflection profile. We also simulated the thickness tolerance of our design by randomly changing the thickness with 5.0%, the typical precision of our evaporation system. Uniformly distributed random errors with an root means square (RMS) value of 5.0% of each layer were used in 300 calculations. The calculation also includes the imaginary part of optical constant, as $\widetilde{n} = n + i\kappa$, which ultimately determines the optical absorption of the coatings.

Figure. 3.17 shows the simulated reflectance profile including 5.0% thickness variations. Between 7 and 12 μm, the reflectance using the optimized design is less than 1.0%. Including the 5.0% thickness variations, the reflectance is less than 1.0% over the range 7.5–11.5 μm and between 7 and 12 μm remains less than about 1.5%. Thus, the calculation indicates that the optimized design results in low-reflectance over a broad wavelength range and is quite robust with respect to thickness fluctuations. Further, the coating has a total thickness of only 2.5 μm and is very transparent. The optical loss due to the YF_3 layer is ∼0.16% around 12 μm.

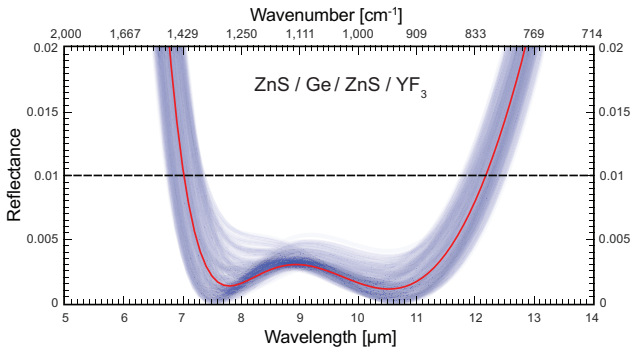

Figure 3.17: Calculated coating performance of an optized ZnS/Ge/ZnS/YF_3 coating with thicknesses 677/56/72/1680 nm (red line) deposited on a InP substrate and its tolerance against 5.0% independent thickness fluctuations of each layer (Blue envelope). The coating has a total thickness of only 2.5 μm.

For comparison, we also simulated double bilayer coatings for the same wavelength range, using ZnS and YF_3 as coating materials. As can be seen in Fig. 3.18, the results show that the optimized double bilayer coating does not have a tolerance of less than 1.0% reflection in the central wavelength range. Especially for laser facet coatings, uniform reduction of reflectance is

an important feature and quite important for laser tuning performance when used in external cavity system. Especially in this light, these double bilayer systems are not as suitable for mid-infrared device applications. In addition, other material combinations did not show better performance in our work.

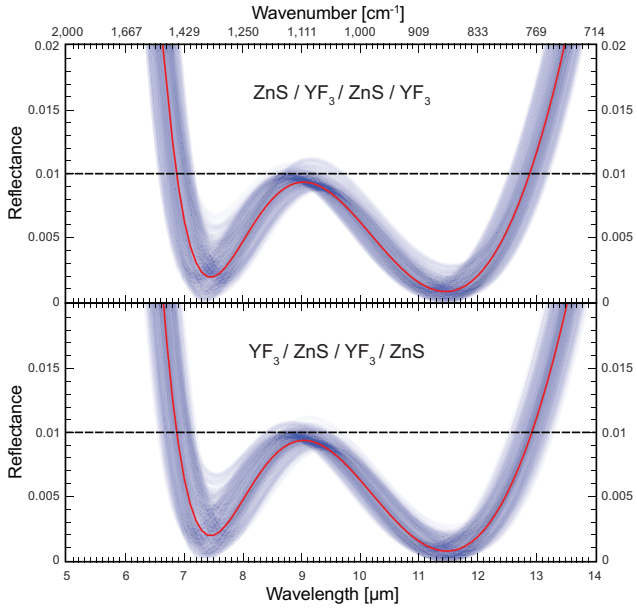

Figure 3.18: Calculated performance of optimized double bilayer systems, $ZnS/YF_3/ZnS/YF_3/Air$ (11/5.6/1018/1581 nm) and $YF_3/ZnS/YF_3/ZnS/Air$ (10/1022/1546/10 nm) (red lines) with 5.0% thickness errors of each layer (blue envelopes).

3.2.3.4 Fabrication details

We used an electron beam evaporator (PVD75, Kurt J. Lesker) for the deposition of coatings. Our system does not have cryocooler, then might have some water content during the deposition. We deposited the materials on double-side-polished InP substrates. The deposition rates of each material are listed in Table. 3.2. During the desorption of the substrate and the evaporation steps, the substrate temperature was kept at 100°C. After the deposition, the samples were cooled down at less than 0.1 °C/min. This slow rate is aimed for minimizing stress failure after the deposition. Especially for YF_3, the internal stress could be reduced by using a temperature above 160°C, this temperature is not suitable for ZnS. Further, since our motivation is to deposit these films onto laser facets that are already soldered to

a sub-mount, we see 100°C as the maximum temperature. The base pressure of the evaporation chamber was around 1.0×10^{-5} Torr, and kept below 1.0×10^{-4} Torr during the deposition process. After several calibrations of the deposition system by FTIR ellipsometry, the inaccuracies in thickness are seen to be less than 5%. We believe this level of fluctuation is due to the e-beam steering and not to the quartz crystal accuracy.

Table 3.2: Deposition rates and the roles

Material	Deposition rate [Å/s]	Comment
Ge	2.0	High refractive index
ZnS	6.5	Middle
YF_3	12.0	Low
Y_2O_3	2.0	Adhesion promoter

3.2.3.5 Measurement and analysis

We fabricated AR coatings on double-side polished InP substrates for both the 7–12 μm range and the 10–12 μm range for the versatility demonstration of this new design. The InP substrates we used for this experiment were Fe doped, the resistivity was over 1.0×10^7 Ωcm. The reflectance was extracted using ellipsometry and FTIR transmission measurement data, under $0\pm2^\circ$ incident angle of light.

The reflectance of the coatings were extracted by using Airy formula. The transmittance of thick dielectric slab (substrate and coating) $\langle T\rangle$ is expressed as,

$$\langle T\rangle = \frac{T_{12}T_{23}e^{-\alpha d}}{1 - R_{12}R_{23}e^{-2\alpha d}}, \tag{3.55}$$

where, $\alpha = (-4\pi\kappa/\lambda)\cos\theta_i$. κ is the extinction coefficient of the dielectric slab (dominated in our experiment by the InP substrate), λ is the wavelength of the incident light, and θ_i is the incident angle. In this study we measured with normal incident angle, $\theta_i = 0^\circ$. R_{12} and T_{12} are reflectance and transmittance from air to the coated side of the slab and R_{23} and T_{23} are reflectance and transmittance from the uncoated side of the slab to air. d is the thickness of the substrate.

Transmission data of the reference sample, $\langle T_0\rangle$ and the coated substrates, $\langle T\rangle$ were measured by using FTIR spectrometer. In order to remove fringing effects from the coating layer itself, spectral averaging was taken into account [73]. Therefore, the resolution in the transmission measurement were set at 8.0 cm^{-1}. By using these two data, the reflectance without coating R_{12} and with coating R'_{12} are extracted.

3.2.3.6 Coating performance

The two coatings investigated are separately described:

3.2.3.7 Performance of 7–12 μm

We coated the InP substrate with the design profile given in Table. 3.3. The design is optimized for 7 to 12 μm and the total thickness of the coating is less than 2.5 μm. The simulated reflectance is ¡1% over the range of 7–12 μm. To improve adhesion, we included 5 nm Y_2O_3 in every interface between adjacent layers and as the last covering layer. The coating exhibits a mirror-like surface after the deposition and we had no issue of delamination or flaking from the coating surface. The reflection spectrum is shown in Fig. 3.19. The coating reduces the reflectance to less than 1.0% between 8 to 12 μm and less than 1.5% over the target range. The central reflection is well below 1.0%. Small peaks around 10–11 μm are due to InP absorption, and at 6 μm to water vapor absorption in YF_3 layer[99].

Table 3.3: AR coating model optimized for 7–12 μm

	Coating material	Thickness [nm]
Substrate	InP	-
1st layer	ZnS	677
2nd layer	Ge	**56**
3rd layer	ZnS	72
4th layer	YF_3	1680

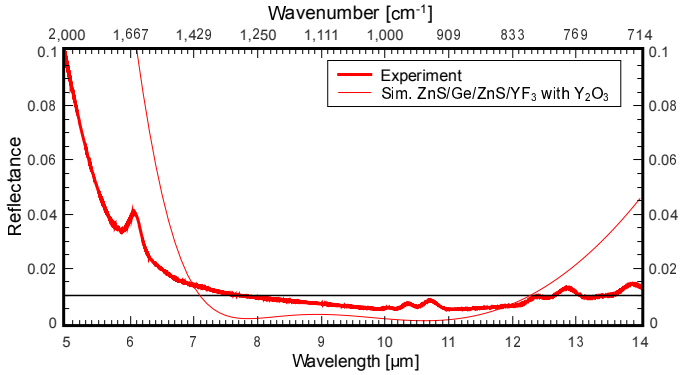

Figure 3.19: Simulated (thin line) and actual coating (thick line) performance optimized for 7–12 μm deposited on InP substrate. Reflectance over the target spectral range is kept below 1.0% over 8–12 μm.

3.2.3.8 Performance of 10–12 μm

Our coating design optimized for the 10–12 μm range is shown in Table. 3.4. The total thickness is below 3.2 μm. We should notice that the thickness of the Ge layer is quite thin compared to the other materials' thickness. The simulated reflectance is $< 0.1\%$ over the range of 10–12 μm. The measured reflectance using this design, however, is higher than the simulation due to absorption peaks in the InP substrate and is less than 1 % over the entire target wavelength range as can be seen in Fig. 3.21. Similar to the 7–12 μm coating, yttrium oxide (Y_2O_3) was included as an adhesion promoter, but in this coating is 10 nm thick because of the somewhat thicker structure compared to 7–12 μm.

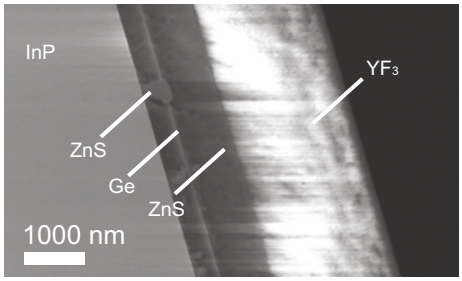

Figure 3.20: SEM images of four layered AR coating deposited on InP substrate: ZnS/Ge/ZnS/YF_3.

Table 3.4: AR coating model optimized for 10–12 μm

	Coating material	Thickness [nm]
Substrate	InP	-
1st layer	ZnS	434
2nd layer	Ge	**55**
3rd layer	ZnS	716
4th layer	YF_3	1991

The simulated data and the measured reflectance show a good agreement for the entire spectral range. In particular, the reflectance in the target wavelength range is less than 1.0%. Slight differences between the simulated and the measured data are due to the thickness error.

The sample is still mirror-like quality after half year from the fabrication. We also conducted re-heating the sample up to the deposition temperature, and confimed the stability of the coating.

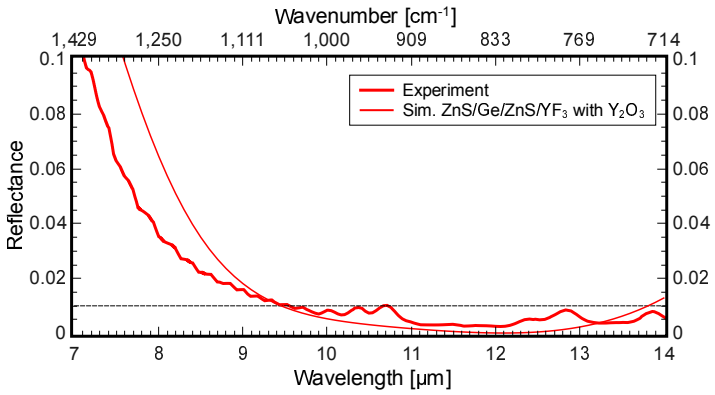

Figure 3.21: Simulated (thin line) and actual coating (thick line) performance optimized for 10–12 μm deposited on InP substrate. Reflectance over the target spectral range is kept below 1.0%.

3.3 Summary

In this chapter, we have described the fundamentals of dielectric coatings and demonstrated AR coatings for the mid-IR range.

For the fundamentals, we reviewed the basic properties of light propagation inside multilayer media and the transfer matrix method, which we have used to model AR coating designs to simulate its performance. The optical properties of various dielectric materials that we used during this work were also presented. For high performance AR coatings, we searched low-absorption materials with appropriate refractive index in the mid-IR range as well as due to the toxicity issues. In this work, YF_3, ZnS, and Ge were available as low- /middle- /high-refractive index materials, and we have used these materials in the coating demonstrators

we have demonstrated two AR coatings of two layer systems. Both coatings were designed for 10–12 μm range, and showed good reduction performances in reflection. The performances for the two coatings fit quite well to the numerical calculations. We have also described a versatile and broadband anti-reflection coating design concept and demonstrated its use in the 7–12 μm and 10–12 μm ranges of the mid-infrared spectrum. The coating design results in relatively thin total coating thickness when compared to conventional multilayer coating designs, a characteristic that is advantageous for applicability within any wavelength range in the mid-infrared. This coating design should find application in many mid-infrared technologies, including semiconductor laser facet coatings for broadly tunable external cavity quantum cascade lasers (EC-QCLs) with various optical configurations.

Chapter 4

Device fabrication for EC system

In this chapter, device fabrication and the performance are detailed. For EC-QCLs, QCLs are the core part of the laser system. During this PhD work, we have proceeded for all the productions of gain media of EC-QCLs with starting crystal growth till facet coatings. The performance of the gain chips are presented.

4.1 Introduction

For a practical use of EC-QCL, in general, the performance of laser system is referred by several factors; the linewidth of lasing mode, the broadness of tuning range, the optical power obtained out of the system, and the beam profile. Since EC laser have been mainly developed in the commband lasers in 1960s. basic flows of the engineering have been already established, while some parts are not applicable to EC-QCL domain. Although EC-QCL systems are quite of complex and there are several characteristics to be improved, these specifications can be tore down into two dominant factors; optical coupling efficiency and QCL performance. Figure 4.1 shows a element chart of EC-QCLs. As can be seen, these two factors are written in the middle of the chart and connected to all of the parts of EC-QCL performance. To engineer EC-QCLs is, equal to say, to maximize these two figure of merits.

For a clear insight, here we rewrite the lasing formula of EC-QCLs with EC reflection as [7, 66],

$$g\Gamma J = \alpha_{\mathrm{wg}} + \frac{1}{2L}\ln\left|\frac{1}{R_{\mathrm{ext}}}\right| \tag{4.1}$$

with,

$$R_{\mathrm{ext}} = \left\{r_{\mathrm{ic}} - \eta_{\mathrm{EC}}\sqrt{R_G}\right\}^2. \tag{4.2}$$

The lasing condition is from EC-QCL with front-side extraction Littrow-type. r_{ic} is the intra-cavity facet reflectivity. η_{EC} is the net coupling efficiency, which is defined as $\eta_{\mathrm{EC}} = \eta_{\mathrm{ol}}T_L(1 - r_{\mathrm{ic}}^2)$. where T_L is the transmittance of lens, and η_{ol} is the light overlap factor between EC part and an output beam from the facet. g is the gain coefficient of amplifier, Γ is the confinement factor of the waveguide and α_{wg} is the waveguide loss of gain chip. L is the chip length, and J is the driving current density.

The former parameter, "coupling efficiency," indicates the efficiency of light penetrating from the external cavity medium to the amplifier by crossing through the optical boundary of two different optical constants: gain chip and air. This terminology is common in use not only in EC laser but also in conventional solid state lasers [37, 103]. The more light couples with the gain medium, the stronger optical resonance can be achieved, then giving the stronger optical amplification. This effect results in stronger output power and fine tuning, as mainly explained in the external cavity section of Chapter 2. In order to enhance the coupling efficiency, there are several approaches in EC laser engineering One is to reduce the residual reflectivity of QCL facets. Since the laser waveguide inherently possess $\sim 29\%$ reflection, most of light does not couple from the external cavity to the QCL waveguide, and vice versa.

In order to address this issue, anti-reflection (AR) coating has been widely used to suppress such a reflection [37]. AR coating is the most well-established optical technology and one can reduce the reflection quite close to zero with AR-coating. By AR-coating on the wavegudie facet, one can also eliminate the residual reflection, eventually giving less optical boundary. This strategy is basically to increase η_{EC} by decreasing the facet reflectivity, r_{ic} in Eq. 4.2.

Angled facet laser is another promising method and well used for reducing facet reflection [37, 104, 105], and providing a extremely low modal reflection, $r'_{\mathrm{ic}} \ll 1\%$. A part from the reflection modification of intra-cavity facets, the accuracy of optical alignment is also crucial for optical coupling. This mainly

influences on the overlap factor η_{ol} of in-coming and out-coming light to the gain chip [66, 38]. Alignment stabilized EC systems tuned by interference filter [106, 92] is also well used as one of the EC laser applications. Such an EC system uses a retro-reflector for optical feedback and enables a better optical overlap compared to Littrow-type lasers, since Littrow grating sometimes suffers from the direction dispersion in reflected light [92, 65]. Thus the optics parts also plays a key role for coupling. Meanwhile, improving the optical confinement Γ gives another chance for a better coupling. Ideally, a single lobe beam shape can provide the maximum overlap of two laser beams coming from different directions. Thus a better confinement of optical beam would provide a better overlap, and this would be possible by having a optimal waveguide structure.

Improving a QCL performance is equally important in EC-QCL engineering. One of the great factors of QCL performance is a gain width of QCL chip. Tuning range of EC-QCL is determined by the intrinsic broadness of QCL emission spectrum, meaning $g = g(\Delta\nu)$ in Eq. 4.1. Until now, a number of demonstrations for broad gain emissions have been carried out by using various optical transition schema, e. g., continuum-to-continuum [33], bound-to-continuum [107], dual-upper-band-to-continuum [34, 27], and also stacking different active region designs in a single active region [108, 28, 29], alongside the power enhancement of QCLs. These are mainly explained in Introduction. The number of cascade also determines the amplitude of gain coefficient, then can be improved by growing a number of cascades. The secondary effect of such a thick active regions gives another chance for better optical overlap, η_{ol} in EC system. This strategy however take more time in QCL growth and more difficulty. The waveguide loss of QCL α_{wg} is also an important factor and needs to be optimized. This can be mainly adjusted by controlling the doping level of QCLs during the epitaxy growth process. One of the contributions for waveguide loss is carrier absorption due to the doped carriers and this parameter is quite hard to be optimized. Less waveguide loss provides less optical loss during the optical amplification. The optimal driving condition of laser chip also affect to QCL performance especially because of the thermal extraction, which results in higher quantum efficiency.

Although there are several factors to be improved for EC-QCL, during this work, we have focused on the following three factors,

- broad gain region
- anti-reflection coating on waveguide facets
- waveguide and its structure

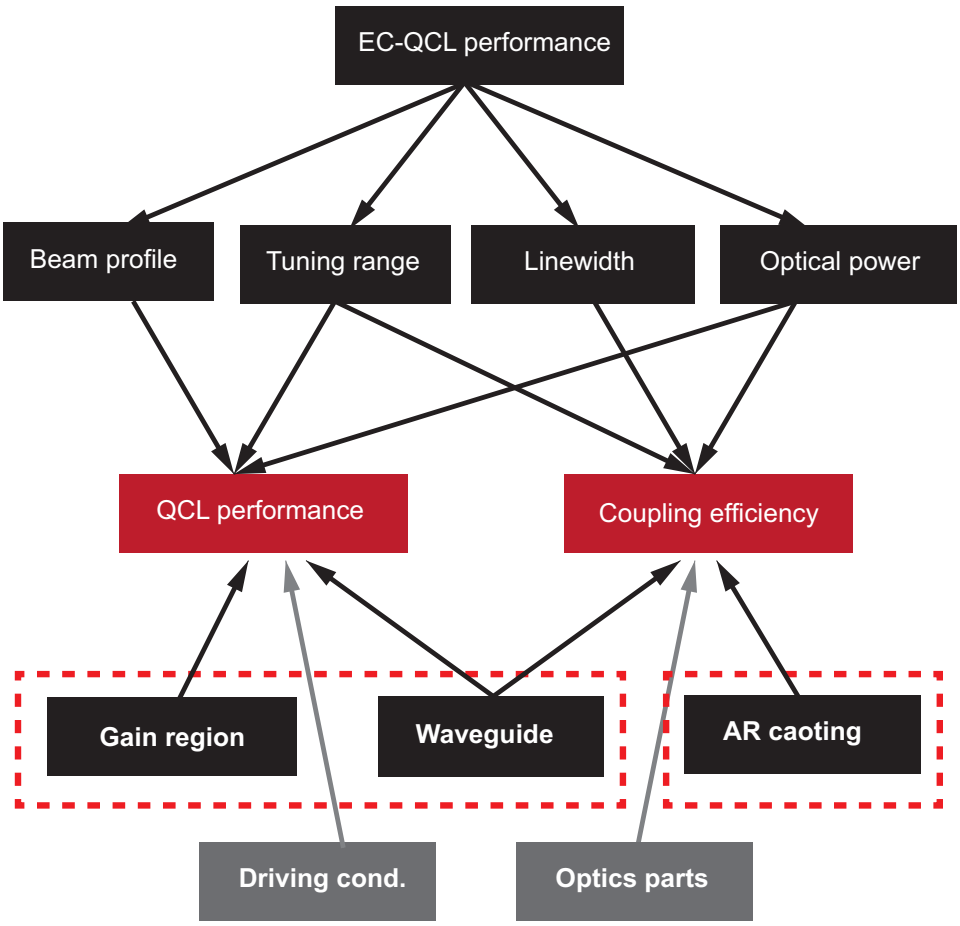

Figure 4.1: Element chart of EC-QCL performance: The QCL device including AR coatings determines most of the parts of EC-QCL performance. This chapter focuses on AR coating and QCL device fabrication process, which is countered with red-dash lines.

These factors are contoured with red dashed lines in Fig. 4.1. In order to address these performances, various approaches have been carried out during this work. For broad tuning, we grew broad gain QCLs in our group and processed to a waveguide structure. Details of the epitaxial growth and waveguide processing are explained in the next two section. For AR coatings, we have numerically designed layout models of coating and AR-coated QCL facets using electron beam evaporator. Optimization process and coating procedure will be also written. Meanwhile we designed and fabricated angled facet lasers and demonstrated its performance. This will be described at the end of this chapter.

4.2 QCL growth

Recent developments in crystal growth techniques have made more versatile semiconductor structures [57]. Molecular Beam Epitaxy (MBE) and Metal-Organic Chemical Vapor Deposition (MOCVD) allow to grow a crystal structure on a substrate with great precision. Also these techniques make it possible to synthesize artificial crystal structures, known as "supperlattice" and "quantum wells". The active region of QCL consists of thousands of quantum wells. The structure must be also grown with high precision of thickness controlled within angstrom scales. Therefore, these growth technologies needs to maximize their ability for structure growth of QCL. In other words, QCL is one of the most sophisticated quantum well devices in modern optoelectronic devices. During this work, all QCL structures are grown using Gas-Source Molecular Beam Epitaxy (GS-MBE, Riber 21T compact, Riber, France) in our group. Pictures of our system is shown in Fig. 4.2, together with a schematic image of MBE system [109].

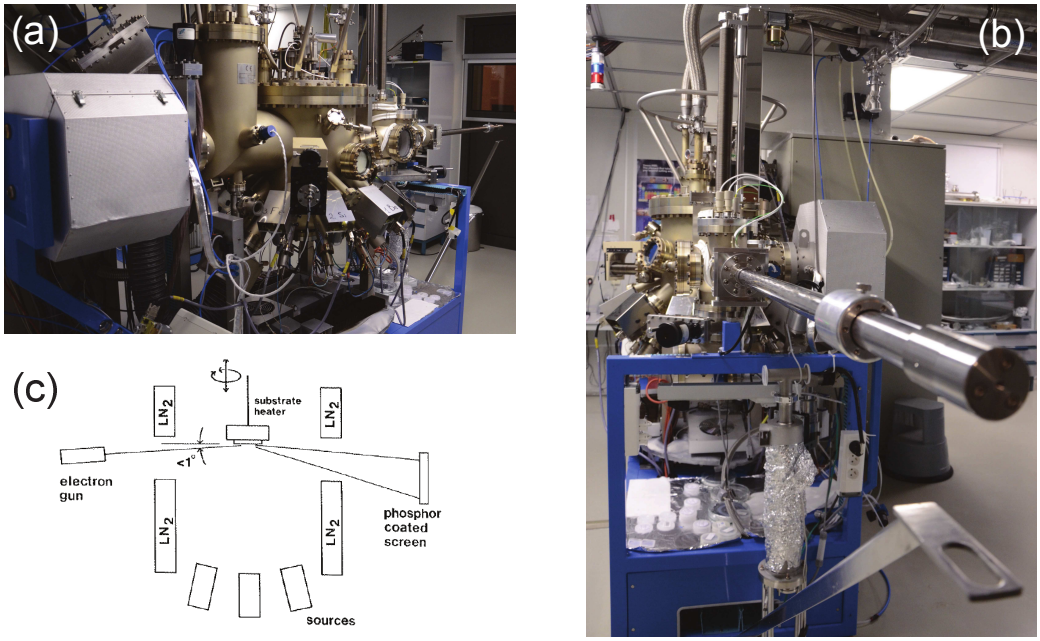

Figure 4.2: Pictures of Riber 21T compact and schematic image of MBE system: Side shot (a) and front shot (b), Schematic image of chamber and source cells of MBE system from Ref. 109. (Figure-(c) is reprinted from [109] with permission from Elsevier)

This section mainly details the procedure of QCL structure growth and

doping optimization, since these two factors are quite important in QCL fabrication. Today we can find many QCL designs of various wavelength range and also of various broadness range. Meanwhile, the reproducibility of these reported designs are quite important in a different growth system from EC-QCL production point of view,

4.2.1 QCL structure

In general, the QCL structure is made up from three parts, a bottom layer, active regions, and a cladding layer. The bottom layer and the cladding layer simply function as buffer layers, which are for electric contacts in the device operation. The core part of QCL is an active gain region which consisting from a number of periods of a pair of an active region and an injection region. Most of QCL performance is determined by this active region design since it determines the emission wavelength and gain broadness, as well as the quantum efficiency. Generally there is a trade-off in gain performance of QCL, either maximizing the amplitude of gain, or the broadness of gain. Nevertheless, for EC-QCL use, a broad-gain QCL is obviously required for broad tuning.

The sample structure that we have grown during the PhD work is depicted in Fig. 4.3. The sequence of the quantum wells **AlInAs**/GaInAs heterosystem is **37** / 31 / **27** / 75 / **9** / 58 / **10** / 52 / **12** /41 / **15** / 38 / **16** / 35 / **17** / 34 / **20** / 34 / **23** / 34 / **28** / 33, where doping areas are represented with underline. The QCL strucutre reported by Fujita et al. [27] is originally designed for broad-gain by dual-upper-state level to multiple-lower-state (DAU/MS) scheme. This transition scheme allows a stable operation in temperature characteristics, as well as its weak dependence on applied voltage. Thus, these features well suit for the EC use.

4.2.2 XRD characteristics

First, we grew a simple superlattice structure for the system calibration. The sample structure is depicted in Fig. 4.4-(a). The superlattice consists of InGaAs buffer layer on InP:Si substrate and 20 times InGaAs/InAlAs periodic quantum wells on the buffer layer. In order to characterize the grown sample, X-ray diffraction spectrometer is commonly used. The principle of XRD can be found elsewhere [57, 110]. Figure 4.4-(b) shows the experimental and simulated spectra. This superlattice structure appears as the peaks known as “the satellites” in the x-ray diffraction spectrum. The central peaks are from mainly InP substrate, and the others from the buffer. This well centered peak indicates a good lattice-matched to InP substrate. The

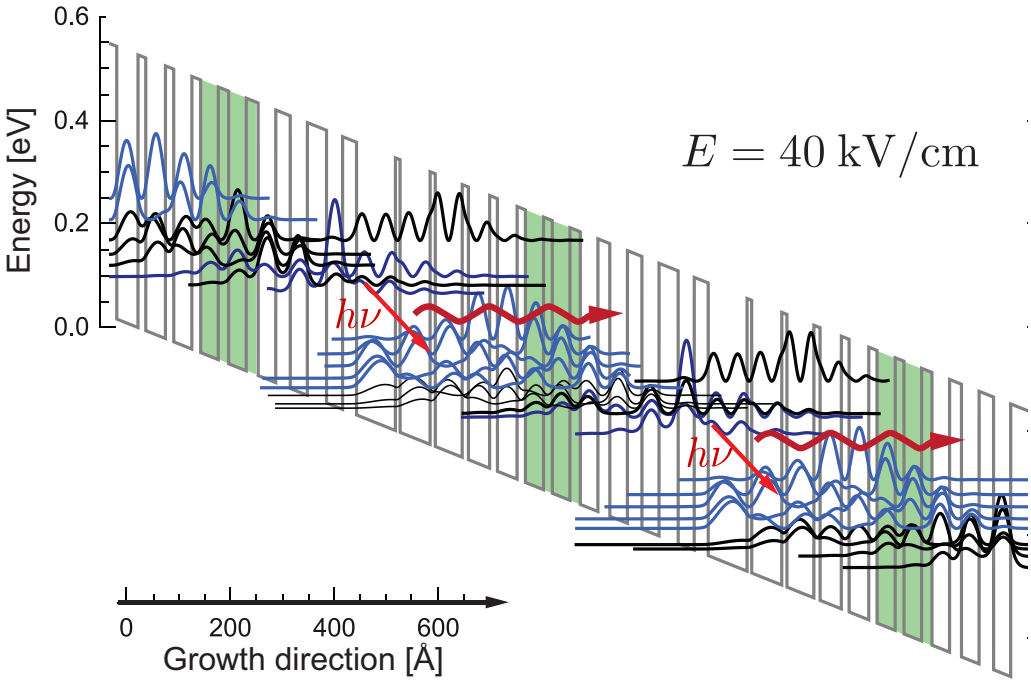

Figure 4.3: Schematic conduction band diagram and squared moduli wavefunctions of dual upper band scheme from Ref. 34: structure consists of **AlInAs**/GaInAs heterosystem, AlInAs barriers are in **bold** format and dopant area is indicated with underline, starting from the injection barrier (toward the right side) is as follows: **37** / 31 / **27** / 75 / **9** / 58 / **10** / 52 / **12** /41 / **15** / 38 / **16** / 35 / **17** / 34 / **20** / 34 / **23** / 34 / **28** / 33.

spectrum shows two distinctive first order satellites and two second order satellites away from the first order peaks, as can be seen in Fig. 4.4 (b). By simulating the ratio of the compound with simulator (software: RADmercury, Bruker. GmbH., Germany), we can analysis the actual layer's thickness. From the results, we can calibrate the system for more optimum temperature of Kundsen cell (K-cell) for growth conditions.

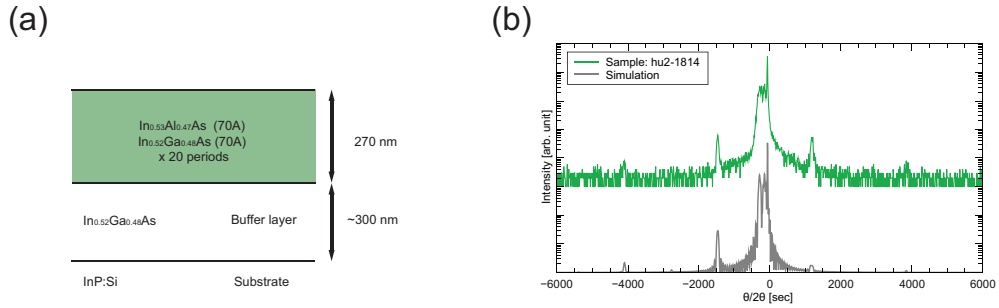

Figure 4.4: (a) schematic image of sample hu2-1814, superlattice structure grown on a InP substrate and (b) XRD data of sample hu2-1814; a green line indicates the experimental data and gray is the simulation result. Satellites of simulated and experimental correspond well. Thus result is feedbacked to system calibration.

We conducted x-ray diffraction measurement on a grown sample, hu2-1816, after MBE growth. the scanning range was from -6000 to 6000 sec, and the scanning resolution was at 0.1 sec. Figure 4.5 shows the measurement result and the simulation result based on the aimed sample structure. From the measured data, the single dominant peak reveals a perfect lattice match of grown layers on InP;Si substrate (Wafer Technology. Inc., UK). Quite small contamination is due to arsenic gas, and this effect can be seen by the broadening effect of the central peak. We also simulated the x-ray spectrum from the designed structure, and the peaks positions and their amplitudes well correspond to the experimental spectrum with quite good accuracy. This means that we have successfully achieved a structure growth of the QCL design as was designed.

4.2.3 Doping effects

As mentioned in Sec. 4.1, doping level affects to the QCL performance. For III-V compounds, Si is commonly used as a n-type dopant, and for p-type Be is used. In QCLs, dopant is usually injected around the injection region

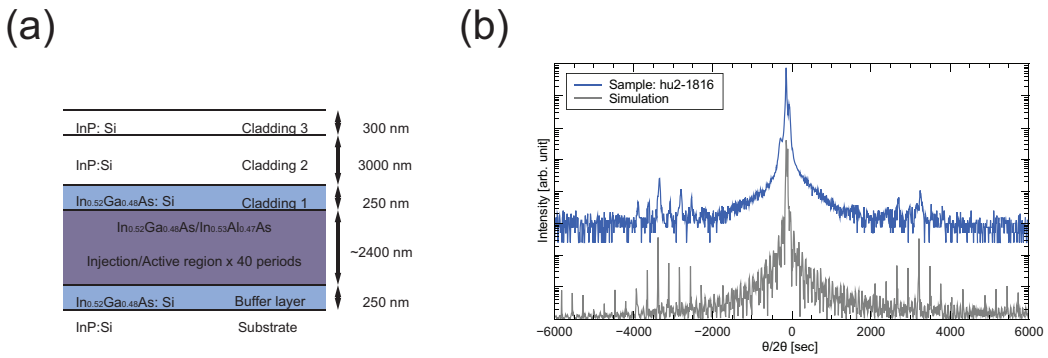

Figure 4.5: XRD data of sample hu2-1816 (black solid line) and the simulation result (blue line): The single central peak reveals lattice match structure of grown sample. The good matching shows the perfect growth of the designed structure.

of each periods, as shown with green area in Fig. 4.3. In other words, as far as possible away from the optical transition. so that we can minimize the free carrier absorption at optical transition area (active region), Another reason is for the smooth electron injection into the active area to induce population inversion for lasing. High doping concentration would contribute to optical gain, since more carrier would contribute to the transition in the active region. The drawback is to increase the waveguide loss and results in higher threshold current density for lasing operation. During this work, we grew a few samples with the sample QCL structure, but with different doping level by altering the evaporation temperature of Si-cell. The following discuss the doping effects on QCL performance in terms of the optical loss and the emission performance.

4.2.3.1 Optical loss

Doping concentration is controlled by cell temperature of growth system. Doping level is quite sensitive to the cell temperature, and gives exponential scale changes respect to the temperature, as $N_D \propto e^T$. Accurate calibration of doping is quite important in the procedure of a QCL growth. During this work, we grew three samples with different doping concentrations, and characterized their laser performances. Chemical etching was used for the waveguide processing and all the waveguide width is in the range of 32–35μm at the middle of the active regions. Figure 4.6 shows power-current (P-I) characteristics (a) and $1/L$ characteristics extrapolated from P-I curves

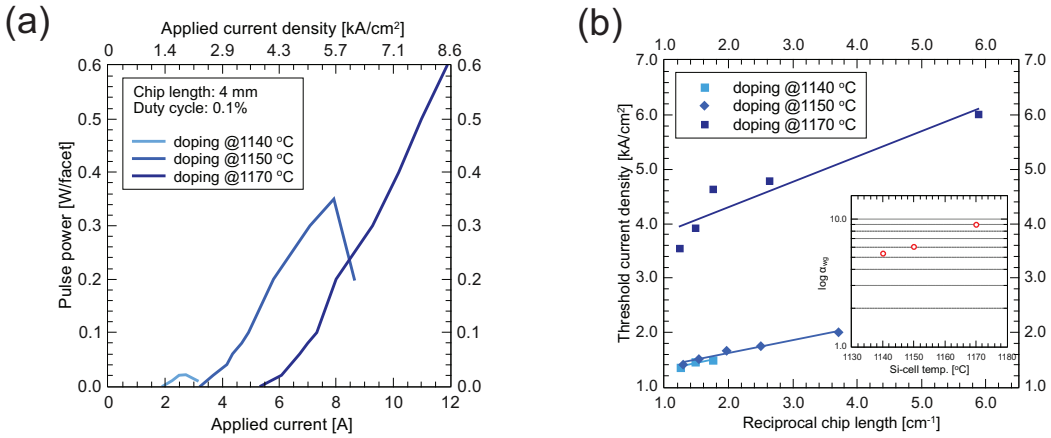

Figure 4.6: *P-I* curves of different doping levels and their waveguide loss: (a) *P-I* curves of different doping levels controlled by the Si-cell temperatures. (b) data plot of threshold current densities and reverse chip lengths. The waveguide losses and the modal gain coefficients were extracted. The inserted graph shows the waveguide loss plotted with the cell temperature.

of different chip length. As can be seen from Fig. 4.6-(a), higher doping concentration contributes to higher dynamic range, however shows higher threshold current for lasing. A sample with the lowest doping level has lower threshold current, while the power range is no more useful as of 1140°C. The sample grown at 1150°C shows the intermediate performance in terms of both factors.

We plotted the threshold current densities of different chip lengths with corresponding reversed chip lengths, By fitting these data with the lasing formula Eq. 4.1 and R_0 ∼0.29, we can extract the waveguide loss, $\alpha_{\rm wg}$, and the modal gain coefficient, $g\gamma$. The higher doped sample exhibits the higher waveguide loss. We also see the larger gap between 1150°C and 1170°C samples rather than the gap between 1140°C to 1150°C. Regarding to the modal gain coefficient, A sample with the higher doping shows a lower modal gain coefficient, as is listed in Table 4.1.

The increase of waveguide loss with doping concentration can be explained by free carrier absorption in the waveguide. From the Drude model [57], free carriers introduce optical absorption, $\alpha_{\rm wg}$, and this can be written as,

$$\alpha_{\rm fc} = \frac{e^2}{2\pi^2 c^3 \epsilon_0 n_{\rm eff}} \frac{N\lambda^2}{m^\star \tau} \tag{4.3}$$

$n_{\rm eff}$ is the effective refractive index of waveguide, and N is the doping concen-

Table 4.1: Si-cell temperature [°C] and waveguide loss α_{wg} [cm^{-1}] calculated from different chip length. From the lasing condition, $\ln 1/R \sim 1.24$ was used.

Si-cell temp. [°C]	$1/g\Gamma$ [kA/cm^{-1}]	α_{wg} [cm^{-1}]
1140	0.20	5.35
1150	0.19	6.03
1170	0.38	9.00

tration. τ is the inverse of the electron scattering time, typically 100–200 fs. As can be seen in Eq. 4.3, the absorption is proportional to its doping concentration. As shown in an insert in Fig. 4.6-(b), The plots of log-scaled waveguide loss shows a good linearity to the Si-cell temperature. Supposing doping concentration has a exponential characteristics of Si-cell temperature, this result agrees well with Eq. (4.3).

4.2.3.2 Emission shift

Another effect caused by doping can be found in the emission wavelength. Figure 4.7 shows the emission spectra measured with FTIR. The samples hu2-1819 and hu2-1816 were grown to have a different doping levels. The corresponding temperatures of the Si-cell during the growth were 1110°C and 1130°C, respectively. The higher doping sample, hu2-1816, shows the longer wavelength emission compared to hu2-1819. The observed emission of hu2-1819 is in the range of 950 to 1150 cm^{-1}, while hu2-1816 exhibits from 900–1050 cm^{-1}. The samples were grown in very sequential days, and the XRD spectra of both samples show quite good agreement with the aimed structures. Therefore, this difference can be considered due to the different doping levels.

In general, a doping in semiconductor gives a band-bending in the band diagram. This is due to the space charge effect [57, 111]. Since the wavefunctions of quantum wells structure are defined by the conduction band structure. the separation of energy levels also varies with the different doping levels. This effect ultimately gives the emission wavelength shift in QCL performance. In this case, hu2-1816 has a higher doping level compared to hu2-1819. Thus, the energy separation of hu2-1816 is narrower than the other.

This effect is more remarkable for longer wavelength QCLs since the emission wavelength become more sensitive with the separation of eigen-levels, as

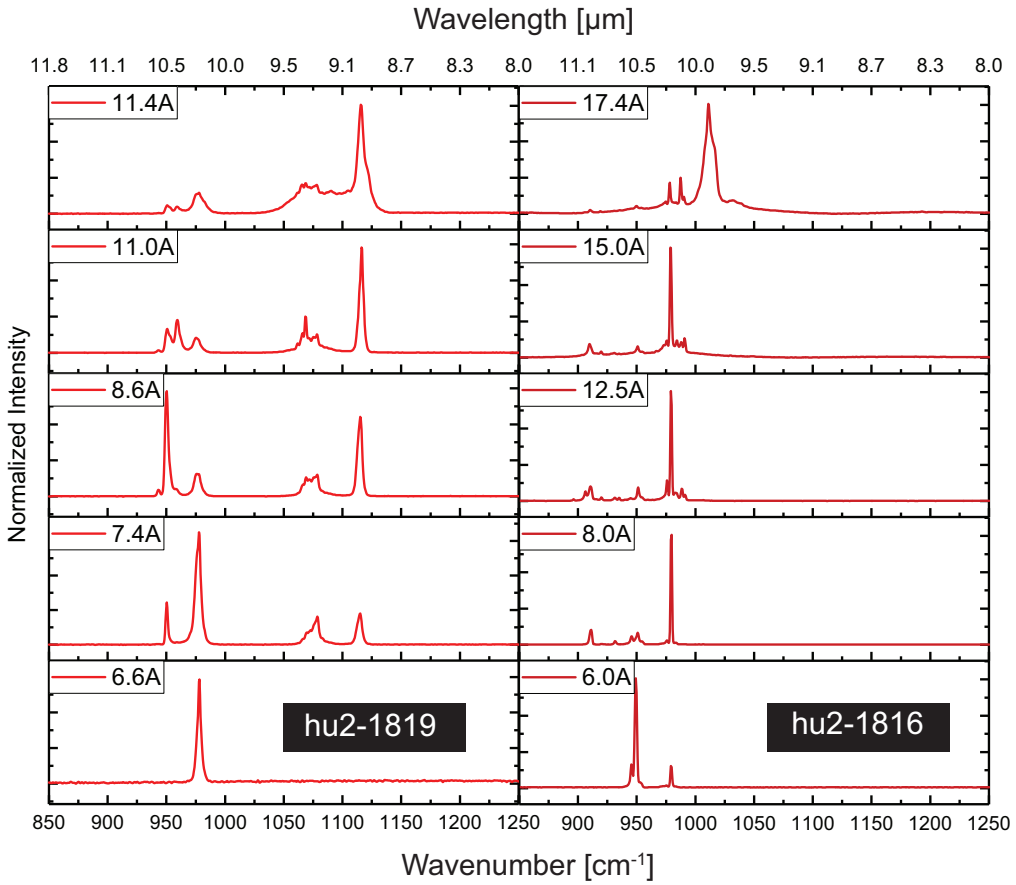

Figure 4.7: Emission spectra of hu2-1816 and hu2-1819 with different applied current density: The spectra were taken with FTIR spectroscopy. The emission spectrum of hu2-1819 develops broader with higher applied current density. The observed Fabry-Pérot limited gain is from 950 to 1100 cm^{-1}, while hu2-1816 shows the longer wavelength range, 900–1050 cm^{-1}.

seen in,

$$\lambda = \frac{hc}{\Delta E}, \tag{4.4}$$

where the energy gas is represented with ΔE. λ is the corresponding wavelength to the energy gap. This shifting effect may be useful also for quasi-stack active gain. By changing the doping concentrations during the growth of active regions, it is possible to fabricate the active regions of several different emission range as reported in Ref. 28.

4.3 QCL Processing

Details of waveguide processing is written in this section. We have processed all our sample from post-grown to various waveguide structures in our group. This section describe the processing techniques as well as the technical know-hows gained during this work.

The core part with n_{core} of dielectric waveguide is, in general, sandwiched by the lower refractive index materials n_{cladding}, n_{bottom}, then the structure must satisfy $n_{\text{core}} > (n_{\text{cladding}}, n_{\text{bottom}})$. For our QCL structure, InP is used for the cladding layer and the bottom layer, and the core part is a superlattice structure of InGaAs/InAlAs. The refractive index of InP and core parts are around $n_{\text{InP}} \sim 2.9$–3.0, and $n_{\text{QWs}} \sim 3.2$–3.4, respectively. For the optical confinement in lateral direction, we process to a trench structure, which also satisfies the condition above.

Buried heterostructure is also attractive for QCL, since it gives a better thermal conduction during the operation. thus operable in continuous wave mode. A number of demonstrations of high wall-plug efficiency using buried heterostructure have been reported [112, 11, 113]. This would help for anti-reflection coating process to avoid "edge effect"[65].

The beam profile is largely determined by the width of the active region, thus this needs to be well examined by FEM (Finite-Element Method) simulators[1] before the actual processing [7].

4.3.1 Processing Details

Figure. 4.8 depicts schematic images of waveguide processing, by starting with a post crystal growth. Here we describe the process details as well as the know-hows gained during this work.

(a) Quantum wells structure was grown on InP:S substrate (n-type) with GS-MBE (Riber compact 21T, Riber, Inc., France). Si-doped InP cladding layer was grown on top of the active region. Every time, a quarter wafer have been used for processing.

(b) A negative photoresist (AZ-15nRT, MicroChemicals, GmbH, Germany) was spin-coated under 3000 rpm for 1 min, after spin-coating, the sample was baked at 110°C for 3 mins. The stripe pattern was transferred under 2 mins UV light using photo-lithography system. The optical power was set at 2 W. The stripe pattern was set along [1-10] direction

[1]COMSOL, TCAD, for example.

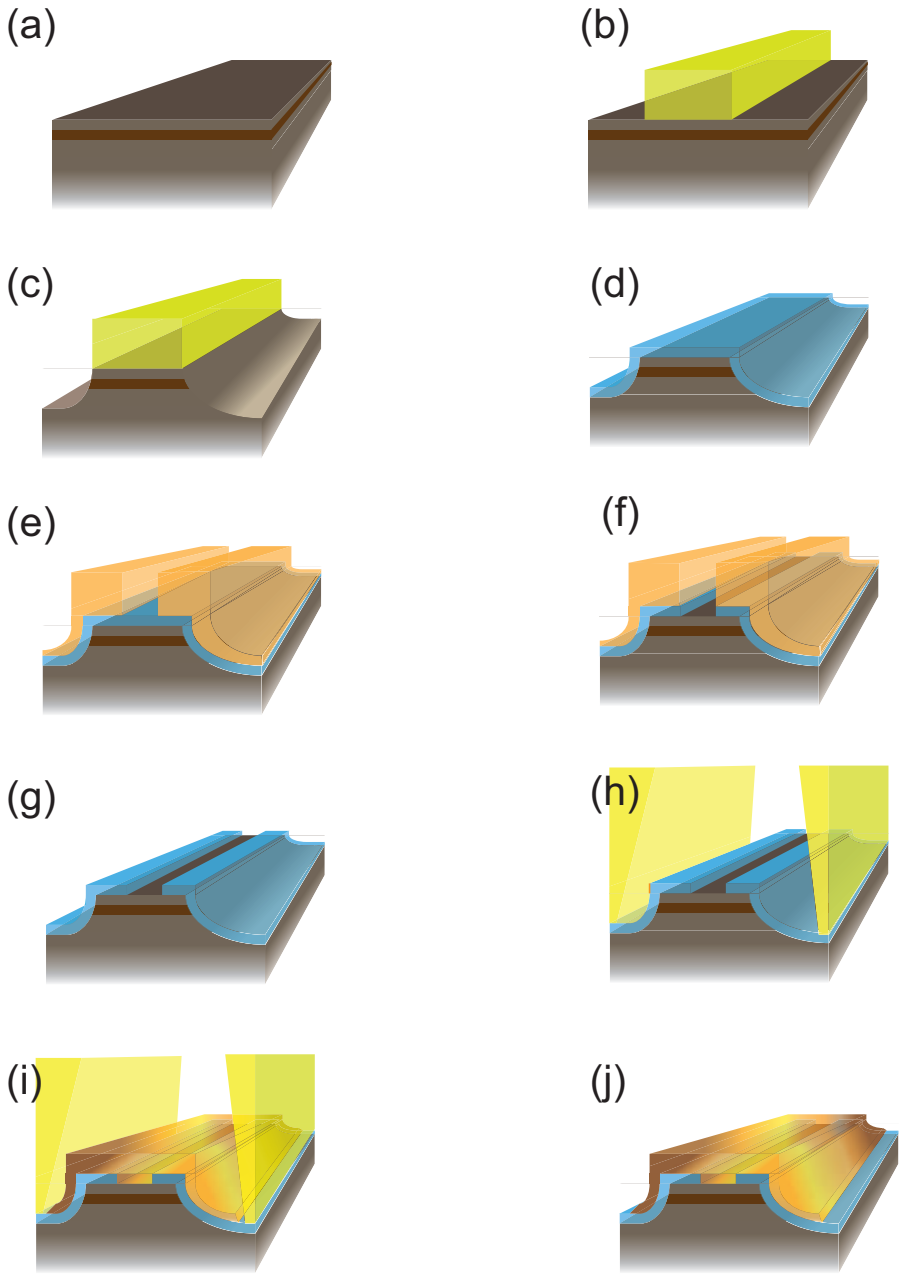

Figure 4.8: Illustrations of QCL processing: (a) a sample image of post crystal growth. (b)–(c) represent a process of making trench structures. (d)-(g) is about insulator deposition and its contact window opening process. (h)–(i) process is a contact metalization. All the yellowish parts are photoresists.

for good cleaving. The stripe patterns was gained after photoresist development with development solutions (AZ-300MIR, MicroChemicals, GmbH, Germany), followed by post-baking at 120°C for 1 min.

(c) The wafer was chemically etched with a solution mixture of HBr : H_2O_2 : H_2O. The volume ratio is 10 : 1.0: 50, respectively. The etching step is crucial part to gain the optimal waveguide width, thus we have checked the etching process with microscope every minutes.

(d) After removing the photoresist, SiO_2 layer was deposited by sputtering. The system detail can be found in Ref. 65. Silicon plate (99.999% purity, Kurt. J. Lesker, Inc., US) was used as the sputtering target and O_2 and Ar gas were supplied with 36 sccm and 5 sccm flow rate, respectively. We usually sputtered 1 μm SiO_2 for insulation.

(e) A negative photoresist (AZ15nXT, MicroChemicals, GmbH., Germany) was coated with 3000 rpm for 2 mins. A mask with 10 μm stripe widths was used. The photoresist was developed for 6 mins by mixed solution of AZ726MIF (MicroChemicals, GmbH., Germany) and H_2O with 1:1 ratio.

(f) Reactive ion etching (RIE) has been carried out for contact opening at the top of the stripes. Tetrafluoromethane (CF_4) gas and O_2 were used for SiO_2 etching.

(g) The residual photoresist was removed by a photoresist striper (NI555, MicroChemicals, GmbH, Germany). Samples were sometimes dipped in 12% hydrofluoric acid (HF) solution for 20 secs to remove the residual SiO_2 from the contact window,

(h) A positive photoresist (AR-P3520, AllResist, GmbH, Germany) was spun with the same condition above. When the trench depth is over 10 μm, we spin-coated at least two times with 3000 rpm for 1 mins for each. However, the pre-baking and post-baking have not extended, and carried out at 120°C and at 60°C for 1 min, respectively.

(i) Chromium (Cr) and Gold (Au) were deposited with thermal evaporation. The thicknesses are 20 nm for Cr, and 200 nm for Au, The sample stage was rotated during the evaporation. The deposition rates were 0.05-0.01 nm/sec for chromium and 0.1 nm/sec for gold deposition.

(j) After rinsing the photoresist with acetone, we obtained QCL stripes with contact metallization. Gold was electrochemically deposited on

top of the contacts, followed by tin (Sn) plating on both sides of the sample. For gold deposition, the bottom was covered by a commercial rack. A small current is preferred to avoid the internal stress of gold[2].

4.3.2 Sub-mounting of QCL

After the processing, the wafer was cleaved to a chip of the two stripes. For a proper mounting of our chips, aluminium nitride (AlN) plates with pre-gold-tin mixture plating were tailor-made by LEW technolog (UK). AlN has a high thermal conductivity (60–177 W/m·K) and has quite a similar thermal expansion coefficient (4.5×10^{-6}/°C) with InP ($\sim$ 4.6×10^{-6}/°C), and this property allows safe epi-down mounting. The prepared chips were set on the plate and heated up to 320 for the melting point of Au-Sn alloy formation ($\sim$ 280°C) on AlN plate epilayer-down.

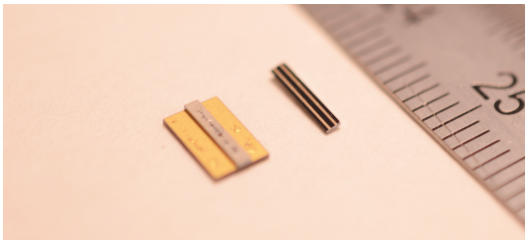

Figure 4.9: Picture of as-cleaved QCL chips and sub-mounted chips: right one is as cleaved chips, and the left chips is after sub-mounting on a AlN plate. Both chips are prepared with 6 mm.

Figure.4.10-(a) is a SEM (Gemini, Zwiss. Inc., [3] image of the QCL. The image shows the cross section of the QCL facet after galvanic gold deposition. The QCL sample captured consisting 200 cascades thus has a trench depth over 40 μm. The thickness of SiO_2 is nearly 2 μm, which are clearly seen from the image. The thickness of the active region is estimated 14.1 μm and the middle width is 29.4 μm. (b) shows the cross section after plating to AlN sub-mount.

[2]From a communication with NB technologies GmbH
[3]The system is owned in AG-SEM in HU-Berlin

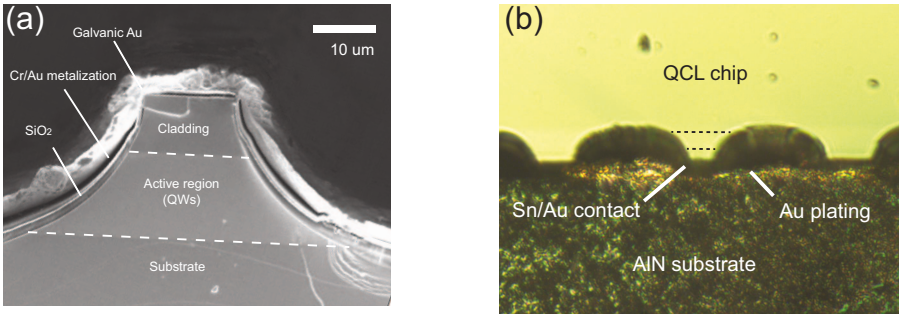

Figure 4.10: (a) SEM image of QCL facet and (b) optical image of epi-downed QCL facet.

4.4 Anti-reflection coating of QCL facet

There are two major approaches to reduce the reflectivity of laser facets. Angled-facet waveguide techniques are effective and attractive [68, 104]. The drawback of this approach, however, is the resulting system complexity of the optical configuration. Dielectric anti-reflection (AR) coatings represent the most straightforward approach and are used in most facet coatings. For the mid-infrared (MIR) spectral range, however, it is quite difficult to make high performance AR coatings on laser facets for several reasons. These reasons can be grouped into 4 issues that need to be adequately addressed for MIR application: (1) Flaking and delaminating of the coating due to the thick films (several micrometers) required for longer wavelengths; (2) the rather limited selection of materials with appropriate refractive indexes and high transparency results in difficulties to applying conventional design concepts of multilayer structures [1, 84]; (3) the target tunability ranges are quite wide for many applications and, since the QCL active regions can be engineered to cover these ranges, the AR coating must also cover a broad emission spectrum range; and (4) the refractive index of the multiple-quantum-well active region varies with QCL design, requiring the AR coating to be adjusted for various QCL designs. Several studies of coating optimization on planar substrates have approached the problem from a production point of view [114, 115, 116, 117], and are certainly useful for MIR device applications. In contrast to the situation of homogeneous media with constant optical properties, allowing ambiguous boundary conditions due varying device structures for a robust coating design presents a different challenge for such coating applications.

For MIR EC-QCLs, double layered AR coatings comprising zinc selenide (ZnSe) and yttrium fluoride (YF_3), for example, are widely used for intra-cavity facet coatings [28, 47, 51, 118, 119]. This design allows a relatively

thin coating and a large reduction in reflectance at the minimum point of spectrum. The resulting spectral band with $R < 1\%$, however, is narrow. Multilayer AR coatings may extend the bandwidth further, while increasing the number of layers, equivalently, the total thickness of the coating [29]. The error effect, however, becomes crucial in such coatings as well as coating quality. For this reason, achieving $R < 1\%$ residual reflectance with a broad spectrum breadth is quite challenging in the MIR range. For the near infrared (optical communication) part of the spectrum, three layered AR coatings, e.g., the Lockhart design, on diode laser facets show broad and large reflectance reduction [50].

Recently, we demonstrated multilayer AR coatings for the MIR, based on a new design concept and covering the 7–12 μm range [101]. The resulting reflectance was $R < 1\%$ over the entire target range, while the total thickness of the coatings are significantly thinner than for conventional design approaches. In this Letter, we describe a broadband multilayer anti-reflection coating optimized for a QCL facet with a broad gain region. To address the optimization for the facet coating, we describe the QCL sample and its laser performance, as well as the effective refractive index of the laser waveguide. The coating performance and its use in a Littrow-type configuration EC-QCL are also characterized.

This section has been reported in Ref. [120]

4.4.1 QCL sample; a broad-gain QCL

The QCL structure was grown lattice-matched to an InP substrate using gas-source molecular beam epitaxy (GSMBE). The structure based on the InGaAs/InAlAs heterosystem is designed for a broad gain spectrum, and is similar to that reported in Ref. 34. The sample was processed using wet chemical etching for the waveguide structure, followed by silicon dioxide (SiO_2) deposition for electrical insulation. Contact windows on the stripes were opened by dry etching with CHF_3. The width of active region is 35 μm at the active region, which was examined for a TM_{00} mode beam profile with IR camera. The waveguide loss is estimated at 5.4 cm^{-1} by measuring the threshold current density as a function of chip length. The chip was prepared with 6 mm length and mounted on an aluminum nitride plate epilayer-down.

The emission spectra of the QCL were measured under different bias conditions using an FTIR spectrometer. The spectra exhibit broad emission from 8.7 to 11.1 μm, as can be seen in Fig. 4.11. From these spectra, we set the range 8–12 μm as the target spectral range for AR coating optimization.

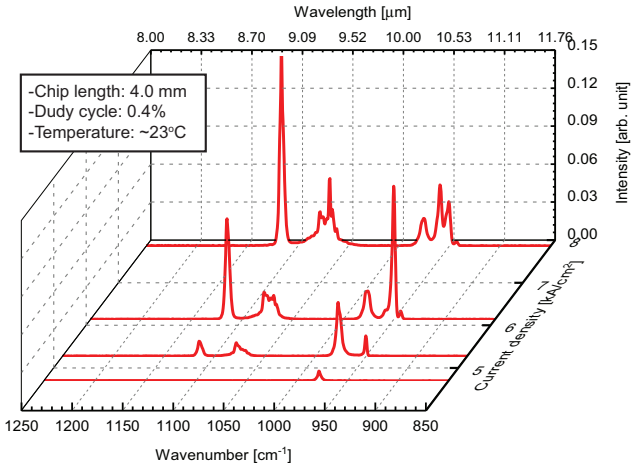

Figure 4.11: Emission spectra of our QCL sample prepared with 4 mm length and ascleaved facets, the light was collected with AR coated Ge lens. Spectra were measured with FTIR under different bias conditions.

4.4.2 Coating details

As noted as "issue (4)" above, determining the effective refractive index of the waveguide is a challenge. In general, a multilayer AR coating is designed by using the transfer matrix method (TTM) and the coating layout is optimized for a given refractive index of the coated material. Thus, the refractive index of the laser waveguide is a deterministic parameter for layout models. Unlike diode lasers, active region of the QCL is dominated by quantum wells, and the effective refractive index of the active region differs for every QCL design. Because the quantum wells and barriers are thin, the refractive index of waveguide can be treated as a virtual uniform core section, and since QCL mainly allows a TM mode to propagate in the waveguide, the effective phase index n_p of QCL can be calculated by [121],

$$\frac{1}{n_p^2} = \frac{\sum_j \frac{1}{n_j^2} l_j}{\sum_j l_j}. \tag{4.5}$$

n_j is the refractive index of jth material and l_j is that material's thickness. The observable refractive index from emission spectrum is the group refractive index n_g [122], given by $n_g = n_p - \lambda dn_p/d\lambda$.

Figure 4.12 shows the refractive indices of $In_{0.6}Ga_{0.4}As$ and $In_{0.44}Al_{0.56}As$ lattice-matched on a InP substrate, measured with FTIR ellipsometry (SENDIRA,

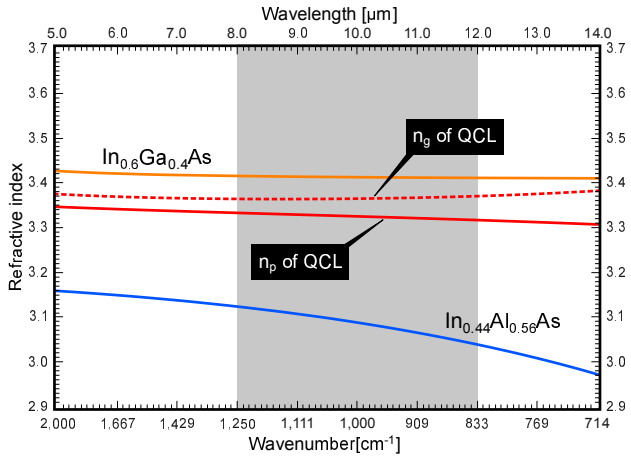

Figure 4.12: Calculated effective phase, n_p (solid red line) and group, n_g, (dash red line) refractive index dispersion based on the QCL design. The refractive index of $In_{0.6}Ga_{0.4}As/In_{0.44}Al_{0.56}As$ measured with FTIR ellipsometry were used for the calculation. Gray area is the target wavelength region for coating.

Sentech Instrument GmbH) and fitted by the Brendel oscillator model. The refractive index of quantum wells was calculated based on our QCL design, using Eq. (4.5). The value averaged over the entire target wavelength range, $n_{\text{avg.}} = 3.33$, was then used for coating optimization. In this work, the effect from the cladding and substrate layers was neglected for the waveguide coating [48, 49, 123] because the mode confinement is close to unity.

Table 4.2: The models of HR/AR coating: AR coating layout is optimized for $n_{\text{avg.}}$=3.33

Layer	HR coating		AR coating	
	Matl.	Thk. [nm]	Matl.	Thk. [nm]
Air				
1st layer	Au	200	YF_3	1796
2nd layer	Cr	20	ZnS	168
3rd layer	YF_3	800	Ge	89
4th layer	-	-	ZnS	586

By using $n_{\text{avg.}}$, we designed an AR coating for the QCL chip based on the "quasi-Lockhart" concept recently described in Ref. 101. The coating was

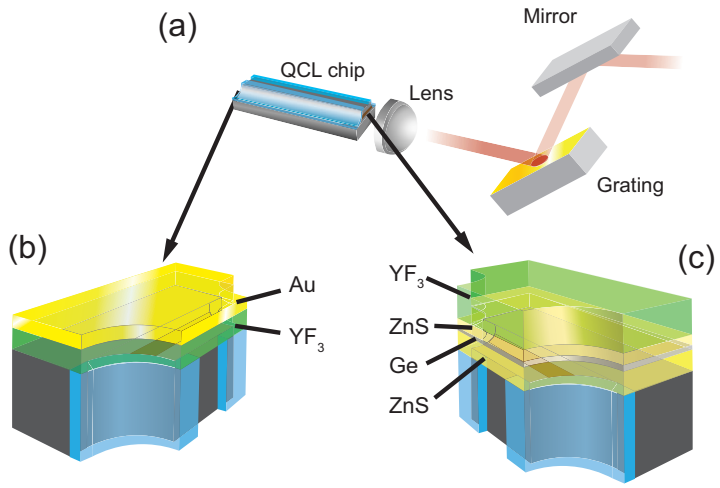

Figure 4.13: Schematic images of Littrow-type EC-QCL (a), and QCL facet coatings: (b) HR coating on backside facet, and (c) AR coating on intra-cavity facet, The details of the layout is listed in Table 5.1. The coating layout is optimized for the base reference, e. g. , QCL facet.

optimized for the range of 8–12μm. We considered only normal incident light for the optimization, since it has a dominant component in angle dispersion. The layout structure of the AR and high reflectance (HR) coating are listed in Table 5.1. For the HR coating, we used 20 nm chromium (Cr) and 200 nm gold (Au), with yttrium fluoride (YF_3) as the insulator between the metals and the active region in order to minimize the optical loss in this wavelength range. The AR coating is made up of four materials, YF_3, zinc sulfide (ZnS), germanium (Ge), and 5 nm yttrium oxide (Y_2O_3) as a adhesion promoter and a cap coating. Figure 4.14 shows the simulated reflectance performance of the AR coating. The envelope depicts the effect of a 10% errors in the reference refractive indices. The designed AR coating maintains a reflectance less than 1% over the entire target wavelength range, even including the error effect. This high error tolerance is quite advantageous for QCL facet coating, since this feature compensates well the ambiguity of reference index of QCL waveguide.

We deposited the AR coating on the laser facet using a electron beam evaporator (PVD75, Kurt J. Lesker, Inc.). The chip temperature was kept at 100°C during the process. This is due to the melting point of indium used as solder for chip mounting. The base pressure of the evaporation chamber was kept below 1.0×10^{-5} Torr during the deposition. The coated laser facet exhibits a mirror-like surface.

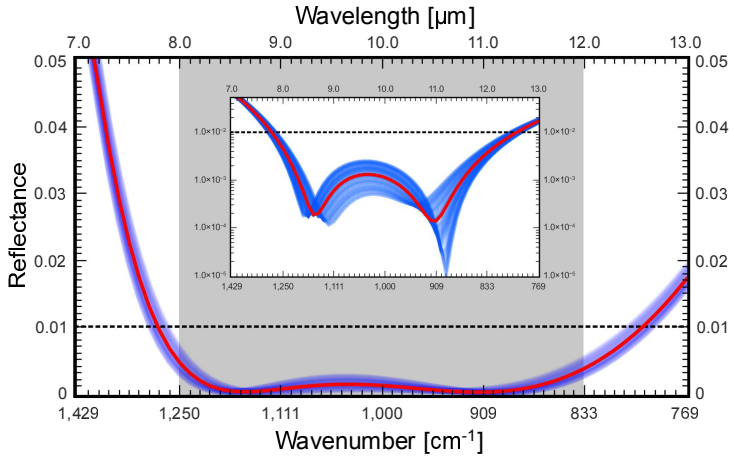

Figure 4.14: Simulated anti-reflection coating performance, optimized from 8.0 μm to 12 μm (red line) with 1% reference (dash line). Blue envelope exhibits the 10% error effect of coated material, QCL waveguide facet.

4.4.3 Coating performance

To characterize the coating performance, power-current (P-I) curves were measured under different facet conditions: as-cleaved, HR-coated-cleaved, and HR-AR coated facets. The results are shown in Fig. 4.15. In this measurement, the chip was driven at a 0.1% duty cycle (100 ns/10kHz) and the output power was collected by 30Hz chirped signals at room temperature. Table 4.3 lists the threshold current densities, J_{th} [kA/cm^2], and the slope efficiencies, η [W/A], which were measured from the linear parts of P-I curves. As can be seen from the results, the AR-HR coated QCL exhibits typical features as the highest threshold current and the highest slope efficiencies.

The residual reflectance of AR-coated facet and the waveguide loss were calculated using lasing condition formula, expressed as[7],

$$g\Gamma J_{\text{th}} = \alpha_{\text{wg}} + \frac{1}{2L} \ln \left| \frac{1}{R_i R_j} \right|. \tag{4.6}$$

$g\Gamma$ is the modal gain of QCL chip, α_{wg} is the waveguide loss, and L is the chip length. $R_{i,j}$ is the reflectance of QCL facets of different conditions. Here, we used $R_{\text{cleaved}} = (n_{\text{avg.}} - 1)/(n_{\text{avg.}} + 1)$ ~29% for as-cleaved facet reflectance. By taking the ratio of slope efficiencies from HR-coated and uncoated, we estimated $R_{\text{HR}} = \eta_{\text{HR}}/\eta_{\text{cleaved}} \sim 0.90$ for the reflectance of HR coating. The waveguide loss and the modal reflectivity of coated facet, R_{AR} were derived by taking the ratios of threshold current densities, as $\rho_{\text{HR}} = J_{\text{th}}^{\text{HR}}/J_{\text{th}}^{\text{Ascleaved}}$, and $\rho_{\text{AR}} = J_{\text{th}}^{\text{AR}}/J_{\text{th}}^{\text{HR}}$.

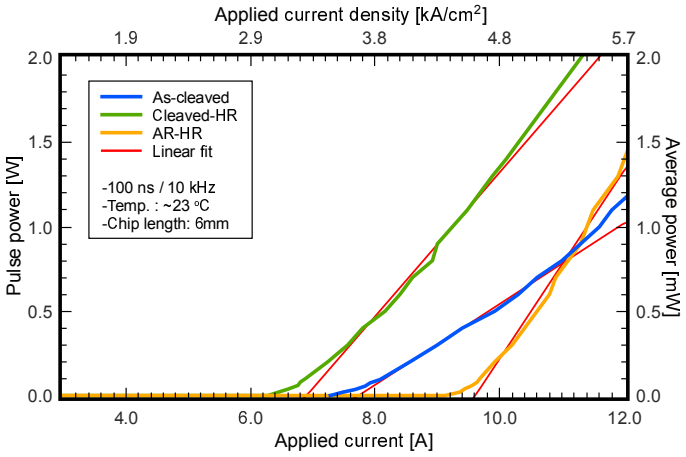

Figure 4.15: *P-I* curves measured in difference coating conditions: Red lines are fitting to extrapolate J_{th} and η.

Table 4.3: Extrapolated threshold current densities, J_{th}, and slope efficiencies, η, from different facet conditions

Facet condition	J_{th} [kA/cm^2]	η [W/A]
As-cleaved	3.68	0.24
Cleaved-HR	3.28	0.43
AR-HR	4.57	0.56

The calculated waveguide loss and the modal reflection of AR coated facet are 6.74 cm^{-1} and 0.75%, respectively. The waveguide loss estimated from the threshold current densities of different chip lengths is 5.4 cm^{-1}. These similar values supports our assumption on the reflectance of the HR coating. Importantly, from this characterization, we do not see the wavelength spectrum of the coating, meanwhile, the coating surely covers the entire emission range of our QCL.

Analysis procedure

For more details, we explain the calculation procedure for the modal reflectance of laser facets. This formulation can be found in many literature of related field[38, 65].

By taking the ratio of the threshold current densities from bare coating condition and HR-coated condition, we get,

$$\rho_{\mathrm{HR}} = \frac{\alpha_{\mathrm{wg}} - (1/2L)\log|R_{\mathrm{HR}}R_{\mathrm{cleaved}}|}{\alpha_{\mathrm{wg}} - (1/2L)\log|R_{\mathrm{cleaved}}|^2}. \tag{4.7}$$

By reforming this with the reflection of HR coating, the waveguide loss can be expressed as,

$$\alpha_{\mathrm{wg}} = \frac{1}{2L\left(1-\rho_{\mathrm{HR}}\right)}\log\left[\frac{R_{\mathrm{HR}}}{R_{\mathrm{cleaved}}^{(2\rho_{\mathrm{HR}}-1)}}\right]. \tag{4.8}$$

In the same manner, The formula for lasing condition with AR coating is still analogous to Eq. (4.6). The ratio between the threshold with HR and AR coatings is rewritten as,

$$\rho_{\mathrm{AR/HR}} = \frac{\alpha_{\mathrm{wg}} - (1/2L)\log|R_{\mathrm{AR}}R_{\mathrm{HR}}|}{\alpha_{\mathrm{wg}} - (1/2L)\log|R_{\mathrm{HR}}R_{\mathrm{cleaved}}|}. \tag{4.9}$$

By reforming Eq. (4.9), we finally get the reflectance of AR coating as,

$$\begin{aligned} R_{\mathrm{AR}} &= R_{\mathrm{HR}}^{\rho_{\mathrm{AR/HR}}-1} R_{\mathrm{cleaved}}^{\rho_{\mathrm{AR/HR}}} \exp\left[-2L\alpha_{\mathrm{wg}}\left(\rho_{\mathrm{AR/HR}}-1\right)\right] && (4.10)\\ &\approx R_{\mathrm{cleaved}}^{\rho_{\mathrm{AR/HR}}} \exp\left[-2L\alpha_{\mathrm{wg}}\left(\rho_{\mathrm{AR/HR}}-1\right)\right] && (4.11)\end{aligned}$$

We can estimate the modal reflectance of coated facets by using this final formula.

4.4.4 Summary of AR-coating on QCL facets

We addressed several inherent challenges to design and demonstrate a broadly and highly reduced anti-reflection coating integrated onto a QCL facet. The waveguide loss calculated in two different methods supports our measurement results and the coating performance. The modal reflectance was reduced to 0.75%, which is quite advantageous for the external cavity system and also enhancing laser power. The coating concept and its procedure will be of interest not only for the coating on quantum cascade laser facets, but also for any optical coatings on electro-optic devices in the mid-infrared range. Since QW-based optical devices often have uncertainties in their optical properties due to several reasons, such as optical confinement, waveguide structure, and plane wave propagations, the strong robustness of the coating against these factors, as shown Fig. 4.14, will help for successful production and achieving further improvement in the performance. Our coating design compensates these uncertainties, and, we believe, can become a standard coating model for Mid-IR optics.

4.5 Angled facet QCL

Tunable lasers with external cavity system have been studied over the decades, mainly for optical communication in the near infrared. For these systems anti-reflection coating have been used for reducing the facet reflctivity[50], and the technologies of coating on waveguide are well established. The mid-infrared, however, other technologies, because we are limited in the number of materials with low absorption and with appropriate refractive indices for designing AR coating. Another issue of mid-infrared AR coating is that, since the total thicknesses of AR coatings sometimes reach several micrometers due to longer wavelengths involved, the layered coatings often cause flaking and delaminating due to the internal stress during and after the coating process[124, 120]. Accurate thickness control during the coating is also difficult from the manufacturing point of view. Therefore, it is quite difficult to achieve high performance dielectric coatings on QCL facets for external cavity systems.

Angled-facet waveguides have been proposed as an alternative method for reducing the facet reflectivity[104, 105, 125], and the technique is very promising to achieve extremely low reflectance of diode laser facet; reflectances of 10^{-3}-10^{-4} are achievable without AR coatings. Quantum cascade lasers with tilted facet fabricated with focus ion beam (FIB) gun have also been demonstrated[20, 15, 21] and show the expected reflection reduction and the enhancement of the output power; thus, it is clear that the angled-facet waveguide approach will also be suitable for mid-infrared external cavity systems. Many QCL processes, however, are based on having facets parallel to the cleavage planes of the substrate. For this reason, the use of bent waveguides for the realization of an angled-facet waveguide will be advantageous for EC-QCL systems because of its simple processing procedure and simple cleaving of the laser facets.

In this section, we describe and characterize angled-facet waveguide quantum cascade laser, with the goal of producing a QCL active gain medium with one facet with very low reflectance for application in external-cavity systems. The angled facet is realized by processing a QCL structure with a bent waveguide, followed by simple waveguide processing cleaving the two facets. The straight facet is high-reflection coated. We investigate the laser performance and compare with the straight waveguide laser performance. This part has been reported mainly in Ref. [68].

4.5.1 QCL sample

The QCL structure was grown lattice-matched to an InP substrate using gas-source molecular beam epitaxy (GS-MBE). The structure is designed for a broad gain spectrum and is similar to that reported elsewhere[34]. In order to realize the angled-facet structure, we designed bent-stripe patterns with fixed curvature. The schematic image of the structure is depicted in Fig. 4.16. For this work, we processed a quarter of a 50-mm wafer. The waveguide was defined by optical lithography and chemical etching, followed by silicon dioxide (SiO_2) deposition as insulator. The contact was made with 20 nm chromium (Cr) and 200 nm gold (Au) by thermal evaporation. After Au and Sn galvanic plating, the chips were mounted on aluminum nitride (AlN) plates in epilayer-down. All the stripes are high-reflectance (HR)-coated on the non-angled facet side, as shown in Fig. 4.16. The sample details are listed in Table 4.4. Different chip lengths result in different facet angles. The angle 11.2° was the largest realizable after processing, but could be extended by processing a larger piece of wafer. We focussed on a 6 mm length chip that fits our standard sub-mount and results in a 9.8° output angle. We also prepared straight waveguide (Str. wg.) chips for the performance comparison.

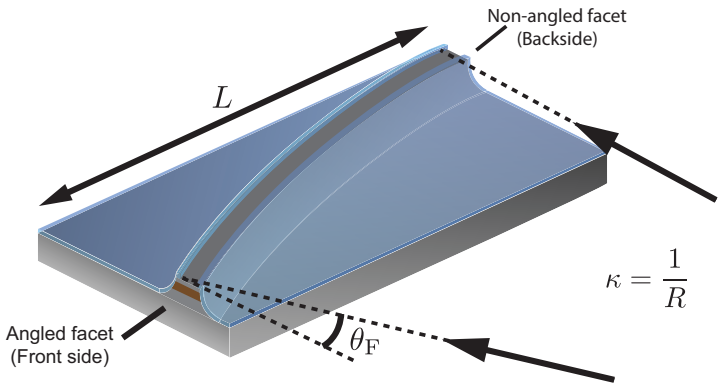

Figure 4.16: Schematic image of bent waveguide quantum cascade laser: The front is angled-facet and the backside is non-angled. The facet angle is determined by curvature and the length of the stripe as $\theta_F = \sin^{-1} \kappa L$.

4.5.2 Device performance

4.5.2.1 Modal reflectance of angled facet

To determine the modal reflectance of angled facet, Power-current (P–I) characteristics were measured from the angled-facet side and the non-angled

Table 4.4: Sample details of bent waveguide structure

Sample name	Curvature κ [1/mm]	length [mm]	Facet angle [°]
Bent wg.	1/35	6.0	9.8 (angled)–0.0 (non-angled)
Str. wg.	0	6.0	0.0 (-)–0.0 (-)

facet side without HR coating.

In general, the output slope efficiency is proportional to the facet loss of the emitting facet [65]. Thus, by taking the ratio of the slope efficiencies of the two facets, we get,

$$\rho = \frac{\eta}{\eta_0} \tag{4.12}$$

$$= \frac{1/(2L)\ln|1/R|}{1/(2L)\ln|1/R_0|}. \tag{4.13}$$

Here, η and η_0 are the slope efficiencies from P–I curves for the angled and non-angled facets and R and R_0 are the facet reflectances of the angled and non-angled facets, respectively. We used $R_0 \sim 0.29$, which is determined by the effective refractive index of the active region, $n = 3.33$ of our design. Finally, the facet reflectance can be expressed by,

$$R = (R_0)^{\rho}. \tag{4.14}$$

Thus, by taking the ratio of the slope efficiencies of the output from the angled and non-angled facets, we obtain the modal facet reflectance of the angled facet with a given angle. The different chip length L gives different front facet angle, as $\theta_F = \sin^{-1}(L/35)$. Therefore, we can easily fabricate the different facet angles by simple cleaving.

Figure 4.17 shows the modal reflectance of different facet angles. The slopes were taken from the linear parts of each curve. The reflectance decreases with higher facet angles, and this result agrees well with Ref. 20. The modal reflectance is independent of waveguide structure but only depends on the facet angles of the stripes.

4.5.2.2 Beam profile

Figure 4.18-(a) shows a beam profile from the 9.87° angled facet waveguide. The waveguide width is 35 μm. The beam appears to be primarily composed of the TM_{00} mode. The single lobed beam is important for use in an external-cavity system because it needs to be re-focused back into the gain region. Although the output beam angle respect to the angled facet is ambiguous,

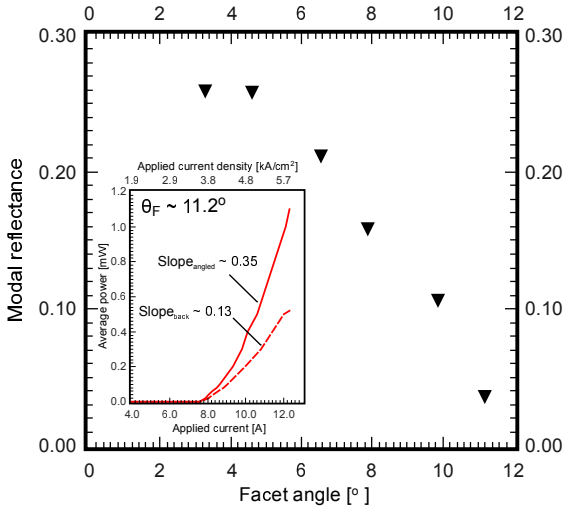

Figure 4.17: Modal reflectance of as-cleaved angled facet calculated from P-I curves of different chip length. The inserted graph is an example of the laser performance of two side facets at 11.2° as cleaved.

this can be collimated by adjusting a lens and the rotating the chip stage, which is shown later. A good Gaussian fitting was obtained as shown in Fig. 4.18-(b). The noise level can be more suppressed by averaging the data samples.

4.5.2.3 Laser performance

Power-current (P–I) characteristics of QCLs using both the bent waveguide and straight waveguide were measured. Figure 4.19 shows the results of two chips of as-cleaved (without HR coating) and HR-coated facets. In order to compare the angled facet effect, both P-I curves are shown in the same graph. The HR coating sequence are for both chips: 800 nm yttrium fluoride (YF_3) and 250 nm gold (Au). After HR coating, the threshold current shifts due to the elimination of loss at the HR coated facet. For both facet conditions, the threshold currents of bent waveguide QCLs are clearly larger than straight ones. This indicates that the modal reflection is reduced due to the angled facet.

The threshold current densities and slope efficiencies were extracted by linear-fitting from the P-I curves and listed on Table 4.5.

The waveguide loss of bent waveguide QCL can be calculated by considering the ratio of the threshold currents of stripes with and without the HR coating, as explained in Section 4.4. The waveguide loss will depend on the

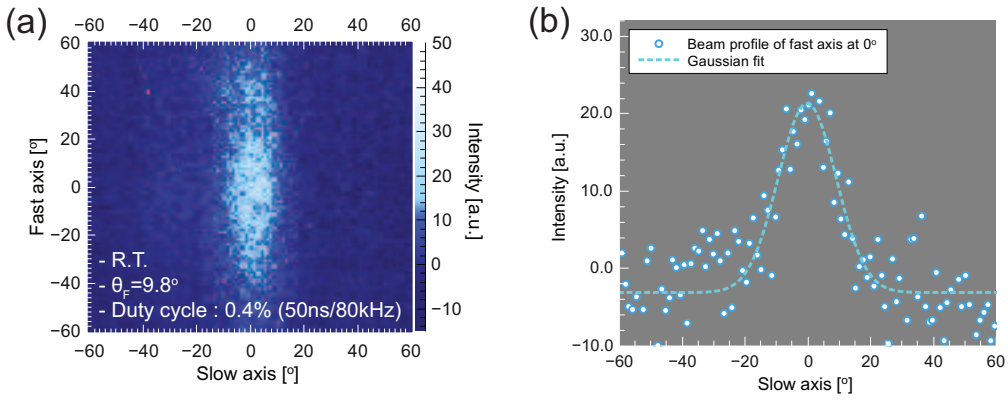

Figure 4.18: Beam profile of SAF-QCL captured by IR-camera:(a) beam profile from angled facet side, a clear TM_{00} mode was obtained. (b) cross section distribution of beam profile at 0° of fast axis of capture (a).

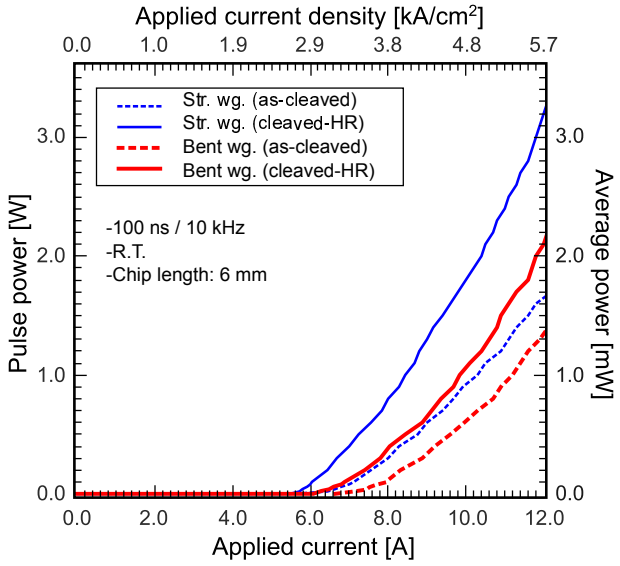

Figure 4.19: *P-I* characteristics of bent waveguide (red lines) / straight waveguide (blue lines) QCL measured in as-cleaved and HR-coated conditions. Both chips were prepared with 6 mm length, corresponding 9.87° reflectance of angled facet. For both waveguide, dash lines solid line exhibit as-cleaved facet and HR-coated facet, respectively.

Table 4.5: Thresholds [kA/cm^2] and slope efficiencies [W/A] of bent waveguide QCL, extracted from P-I curves

Sample	Bent wg. ($\theta_{\mathrm{F}} \sim 9.87°$)		Str. wg. ($\theta_{\mathrm{F}} = 0.0°$)	
	η_{bent}	$J_{\mathrm{th}}^{\mathrm{bent}}$	$\eta_{\mathrm{str.}}$	$J_{\mathrm{th}}^{\mathrm{str.}}$
As-cleaved	0.272	3.66	0.309	3.31
Cleaved-HR	0.383	3.43	0.466	2.95

angle of the angled facet. The ratio is expressed as,

$$\rho_{\mathrm{HR}} = \frac{J_{\mathrm{th}}^{\mathrm{HR}}}{J_{\mathrm{th}}^{0}} \tag{4.15}$$

$$= \frac{\alpha_{wg} - 1/2L \ln |RR_{\mathrm{HR}}|}{\alpha_{wg} - 1/2L \ln |RR_0|} \tag{4.16}$$

Here, $J_{\mathrm{th}}^{\mathrm{HR}}$ and J_{th}^{0} are the threshold current densities with and without the HR coating, α_{wg} is the waveguide loss of QCL stripe, R, R_0, and R_{HR} are the reflectance values of the angled facet, the non-angled facet, and the HR coated facet, respectively. Thus, in the same manner as Eq. 4.8, we measure ρ_{HR} to obtain the waveguide loss using,

$$\alpha_{\mathrm{wg}} = \frac{1}{2L\,(1-\rho_{\mathrm{HR}})} \ln \left| \frac{R^{1-\rho_{\mathrm{HR}}} R_{\mathrm{HR}}}{R_0^{\rho_{\mathrm{HR}}}} \right|. \tag{4.17}$$

In the case of the straight waveguide laser, we have $R = R_0$. In this work, we assumed $R_{\mathrm{HR}} \sim$0.98. For straight waveguide, calculated waveguide loss is $\alpha_{\mathrm{wg}} \sim 7.44$ cm^{-1}. By using $R \sim$0.098 that was found for $\theta_{\mathrm{F}} \sim 9.87°$, we get $\alpha_{\mathrm{wg}} \sim$13.3 cm^{-1}. This higher waveguide loss is due to the bent waveguide structure, and further work is now being done.

4.5.2.4 Emission spectrum

The emission spectra of bent waveguide QCL and straight waveguide QCL were measured using FTIR. Both lasers were driven at a 0.4% duty cycle (50 ns/80kHz). As can be seen from Fig. 4.20, the spectra from the bent-waveguide laser show broadening of the dominant peaks, which become larger with the larger applied current densities. In addition, the angled-facet emits fewer dominant oscillation modes, while the straight stripe emits a larger number of dominant oscillation modes. This smoothing effect may be due to the reduction of reflection of the front facet, meanwhile, the dominant Fabry-Pérot oscillation become less influential.

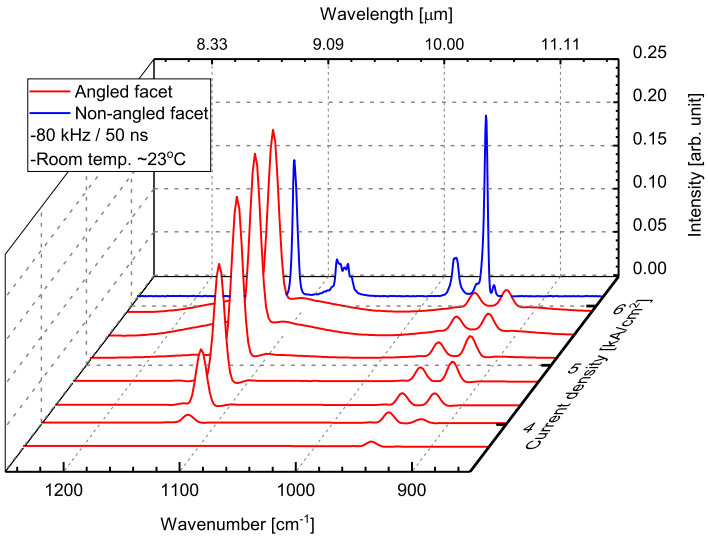

Figure 4.20: Emission spectra of angled facet and non-angled facet QCL: Red curves represent the emission from angled facets and blue curve is from non-angled facet; straight waveguide QCL. The smoothing along the dominant peaks are observed at the spectra of angled facet.

4.5.3 AR coating and packaging for EC use

For a EC use, we processed a chip of κ=1/35 mm^{-1}. The contacts were made with 20 nm chromium (Cr) and 200 nm gold (Au) using thermal evaporator and additional galvanic gold plating. The chip was prepared with 6 mm length by cleaving, which gives 9.8° facet angle, which gives a reflectance of $\sim$9.87$\times$10^{-2}, and mounted on an aluminum nitride plate epilayer-down. Non-angled side facet was HR-coated: 800 nm yttrium fluoride (YF_3) and 250 nm Au. For further reduction of reflection, the angled facet was AR-coated. Since the QCL has a broad gain spectrum, we coated with broadband (8–11 μm) multilayer AR coating using a design concept reported in Ref. 101, which surely covers the entire emission range of our QCL. Our coating design comprises germanium (Ge), zinc sulfide (ZnS) and yttrium fluroide (YF_3) as the main coating materials, and yttirum oxide (Y_2O_3) as adhesion promoter. All these materials exhibit quite high transparency in this wavelength range. The details of coating process is found in Ref. 120. Since the front facet is angled, we re-optimized the coating layout for 34.5° incident angle, calculated by Shell's law. The AR coating layout is listed in Table 4.6. The facet was coated using electron beam evaporator. During the coating process, the chip temperature was kept at 100°C. The thickness error of our system is

estimated below 5%. The coating quality was mirror-like surface.

Table 4.6: The models of HR/AR coating: AR coating layout for angled facet QCL. The layout is optimized for 34.5° incident angle calculated by Snell's law and using $n_{\text{avg.}}$=3.33

Layer	HR coating		AR coating	
	Matl.	Thk. [nm]	Matl.	Thk. [nm]
Air				
1st layer	Au	200	YF_3	1750
2nd layer	Cr	20	ZnS	219
3rd layer	YF_3	800	Ge	70
4th layer	-	-	ZnS	366

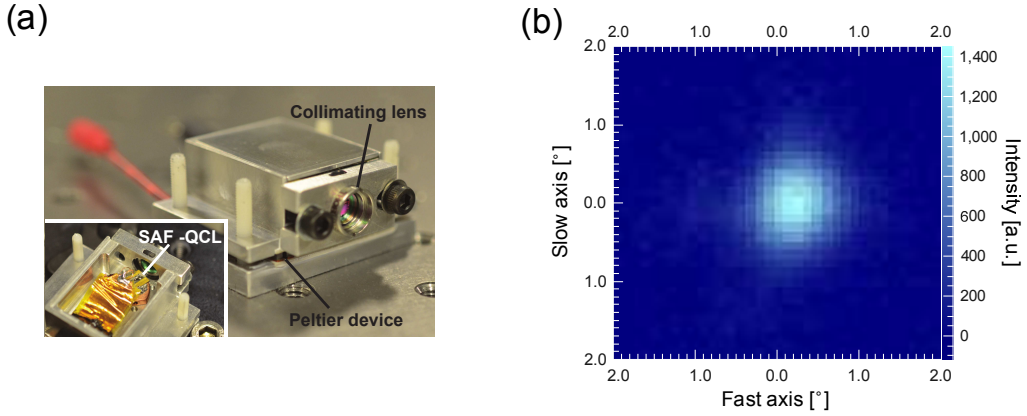

Figure 4.21: Picture of a laser package of SAF-QCL and the beam profile: Angled facet QCL was place with a certain angle inside the box as in the inserted picture.(a), Beam profile captured out of the package (b).

A major issue of using angle facet laser is its system complexity. In order to address this, we built a front-side extraction Littrow-type external cavity system. We made an angle-adjustable copper plate, and the chip was placed with the optimal angle for the good beam alignment, as shown by the inserted in Fig. 4.21-(a). The amplifier module is realized in compact with the size of 2.5×3.4×1.2 cm^3. The output beam from the AR-coated facet was collected with a broadband (8–12 μm) AR-coated aspheric lens and the numerical aperture (NA) was 0.56. The estimated modal reflectance of AR-coated facet is ∼0.54%. The details of laser performance are presented later. In addition, the beam profile captured with an IR-camera exhibits a good

TM_{00} mode as in Fig. 4.21-(b). This feature is quite advantageous of angled facet QCL for EC use, since the amplifier medium can be packaged in such a compact package with high reduction of the residual reflection.

4.5.4 Summary and outlook

In this section, we demonstrated an angled-facet quantum cascade laser with bent waveguide structure for reducing the facet reflectance. This waveguide structure is well suited for external cavity systems because of its simple fabrication process and simple cleaving. The single-beam profile after the packaging is also quite advantageous for field imaging. To address a complexity issue in the integration of angled facet, we designed and built a compact module for packaging the amplifier. The demonstration suggests its good use in front-side Littrow laser systems. The EC-QCL performance using this laser chip will be written in Chapter 5.

Chapter 5

Littrow-type EC-QCL

In this chapter, we describe Littrow-type external cavity quantum cascade lasers (EC-QCL). We have developed three laser systems during this work. The details of the development and the characterization of their performances are explained.

5.1 Introduction to Littrow-type EC-QCL

The Littrow-type external cavity laser is widely used as the standard external cavity configuration [28, 65]. The laser systems are now commercially available and used in many places including biological applications as well as gas-trace sensing applications [31, 126, 127]. The motivation of such researches is now being boosted up due to its potential of the greater markets. Supported by such a background, engineering Littrow-type laser is still quite motivated. Our motivation was to perform Littrow-type lasers and, meanwhile, feedback obtained results and insights into the next generation of the laser system and improve the performance further.

As repeated many times, Littrow-type laser is a tunable laser. The emission wavelength of the laser is tuned by a blaze grating set in, so called, "Littrow" condition [1]. The diffracted light from the grating feeds back to a gain medium and optically amplified. As a result, the optical cavity oscillates with the selected wavelength in the diffraction process. By changing the angle of the grating, it is possible to tune the output wavelength λ, which is given as,

$$\lambda = 2d \sin \theta_G. \tag{5.1}$$

Here, d is the width of grating pitch, and θ_G is the grating angle set in Littrow condition.

Unlike Fourier transform infrared (FTIR) and optical parametric oscillator (OPO), EC laser systems comprise only a few optics, mainly the QCL chip functioning as the optical amplifier, the collimating lens and the grating only. Therefore it is possible to realize in a compact and portable. This scaling down in the system size ultimately contributes for the higher robustness, while such FTIR and OPO normally consist of several optical components, then sensitive for environmental situation of its use. In addition, because the tuning process of EC-QCL is relatively simple and quick, the coarse-tuning contributes shorter measurement time. This is another advantage of Littrow-type lasers. Therefore, EC-QCLs have a great potential as a standard mid-IR light source of many molecular vibrational spectroscopy applications with industrial scales [22, 59, 128].

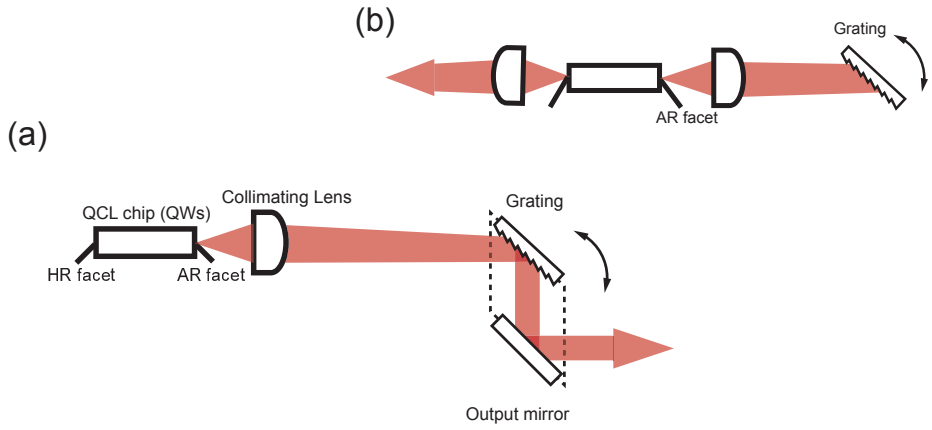

Figure 5.1: Schematic images of standard Littrow-type EC-QCLs; (a) front-side extraction and (b) backside extraction configs. The resonant wavelength is tuned by rotating the grating set in Littrow condition. The output beam is extracted as the zeroth order diffraction light in front-side, and through the QCL output in backside type.

There are two major types of Littrow configurations, as shown Fig. 5.1; front-side extraction type (Fig. 5.1-(a)) and backside extraction (Fig. 5.1-(b)). Today, commercial reflection-type blaze gratings are technologically well-developed and their performances are maximized in the first order diffraction, meaning most of the optical power reflected back to the Littrow direction [129, 130, 131]. For the front-side EC-QCL, the output power is out-coupled from the zero-th order diffraction. This means the output power is limited due to the grating specification; thus giving typically $< 10\%$ order of

the resonant optical power in the cavity. On the other hand, backside extraction type can produce the higher power compared to the front-side extraction type since the out-coupled light is not restricted by the grating. The latter configuration is thus widely used in the commercial product for this reason [22, 59, 128]. Meanwhile, the tuning range of EC system is determined by the ratio of external cavity loss,α_{EC}, and Fabry-Péot mode loss, α_{FP}.

For the coarse tuning of Littrow EC systems, the gain of EC-mode and FP-mode must satisfy the following condition [38],

$$\frac{g_{\mathrm{EC}}}{g_{\mathrm{FP}}} \geq \frac{\alpha_{\mathrm{EC}}}{\alpha_{\mathrm{FP}}}. \tag{5.2}$$

Here α_{EC} and α_{FP} are EC loss and FP loss, respectively, and these are expressed as,

$$\alpha_{\mathrm{EC}} = \alpha_{\mathrm{wg}} + \frac{1}{2L} \ln \left| \frac{1}{R_{\mathrm{EC}} R_2} \right| \tag{5.3}$$

$$\alpha_{\mathrm{FP}} = \alpha_{\mathrm{wg}} + \frac{1}{2L} \ln \left| \frac{1}{R_1 R_2} \right| \tag{5.4}$$

where $R_{1,2}$ is the mirror losses of the cavity system. α_{wg} is the waveguide loss of chip, and L is the length of chip. As written in Chapter 2, the reflectance of external cavity is approximate as, $R_{\mathrm{EC}} = \left| r_{\mathrm{ic}} + T_{ic} T_L \sqrt{R_g(\lambda)} \sqrt{\eta(\lambda)} \right|^2$. Here, r_{ic} is the reflectivity of intra-cavity facet and T_{ic} and T_L is the transmittance of intra-cavity facet calculated by $1 - r_{\mathrm{ic}}^2$ and the transmittance of collimating lens, respectively.

Tuning range can be analysed by looking at Eq. 5.2. To increase the tuning range, one straight way is to increase g_{EC}, which means increasing the intrinsic gain curve of QCL chip. On the other hand, the external system can also contribute for broadening the tuning range. By HR-coating on the backside of laser facet and AR-coating on the intra-cavity side, it is possible to increase the relative loss of α_{FP} compared to the increase of α_{EC} within the same system. Moreover, for broad tuning, $\alpha_{\mathrm{EC}}/\alpha_{\mathrm{FP}}$ should be minimized. By comparing the ratio analysis, it is said that front side extraction allows at least 4.0% broader tuning compared to the backside extraction, while the output power would be lower [38].

5.2 The 1st generation: Prototype

In this section we describe a long-wavelength ($\lambda \sim 11$ μm) EC-QCL. Our primary goal was to produce a laser system for mid-IR hyperspectral imaging, which is advantageous for cancer diagnosis at their early stage. To investigate developing processes of cancer, bio-markers have been widely studied since it is quite useful for efficient biopsy tests. The aim of our project partners was to investigate breast cancer process of human. The wavelength of our interest was at around 11 μm. where we can distinguish invasive / non-invasive micro-calcification in the tumour by the different type of carbonate bonds [132, 133]. Oesophagus is of another interest in cancer diagnosis which might be detectable by hyperspectral imaging in mid-IR range [134].

For hyperspectral imaging, a mid-infrared light source with broad tunability and high optical output is mandatory to order to cover a wide range of spectrum as well as for better optical noise ratio. Compared to FTIR, high optical coherency might help clear determination in classifying the tumors. Adding to the fact, the system required to be compact for its easy delivery to our partner's institute. To reach these requirements, we designed and fabricated a compact EC-QCL system with front-side extraction scheme. Primarily, the laser did not necessarily have to have a narrow linewidth for such applications, since the spectrum of such tissue samples are generally broadened. $\Delta\nu \sim$4 cm^{-1} is the minimum requirement for such applications [134]. while a good beam quality is preferred for its good illumination on samples.

In this section, we describe details of a prototype EC-QCL system and the results of characterization. This work has mainly been done as a part of the project deliverables; "Medical QCL 5-12 μm" of the PhD project[1]. At the end we present some results of experiment collaborated with our project partner[2].

5.2.1 Gain medium: QCL Chip

5.2.1.1 QCL feathures

An active region, sample hu2-0446, was grown lattice-matched on an (100) InP wafer by gas-source molecular beam epitaxy (GS-MBE). The quantum wells structure is similar to the one reported in Ref. 135. The laser per-

[1]WP2 of Mid-TECH project: The European Union's Horizon 2020 research and innovation programme under Grant Agreement No. 642661.

[2]Mr. Michael Hermes and Prof. Nicolas Stone of Bio-imaging team at Exeter University in UK.

formance was also reported in Ref. 136. It should be noted that the active region consists of 200 cascaded units, allowing higher quantum efficiency, and larger facet area of active region. These features contribute for higher coupling efficiency, since the larger area the active region can give a larger overlap between the in- and out-put light [66], thus contributing to the coupling efficiency.

Figure 5.2 shows the band diagram of quantum wells of sample hu2-0446 at 60 kV/cm applied electric field. The details of the simulator are described in Ref. 137. The chip was originally designed for 10.8 μm, which corresponds 114 meV optical transition, as seen the diagram. Since the actual thickness of the active region is 14.1 μm. the total voltage applied across the QCL chip is 95.2 V in laser operation.

The quarter wafer was processed by chemical etching for trench waveguide structures. The active region width was aimed for a single beam mode, $\sim$ 19 μm at the middle of the active region, Silicon dioxide was deposited for insulation, followed by the contact opening, and metallization for electric contact. A chip was prepared with 6 mm for characterization use and 4 mm for EC use.

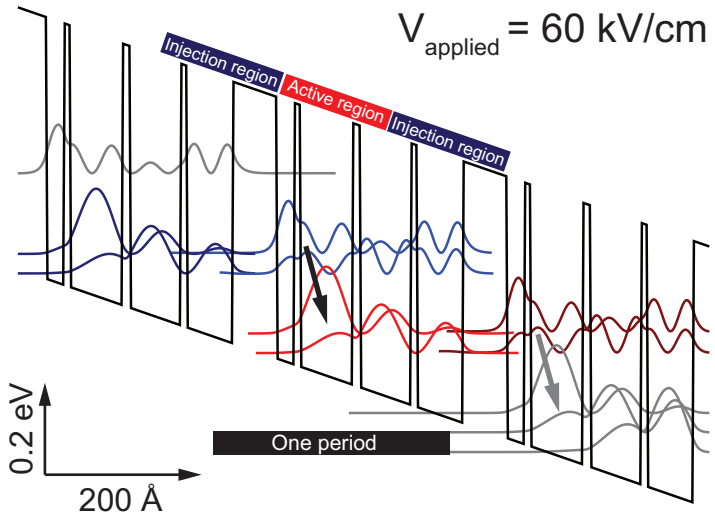

Figure 5.2: Energy band diagram of sample hu2-0446 calculated using *Zigler*.

5.2.1.2 Laser performance

Power-current (P-I) and power-frequency (P-ν) with fixed driving current were measured with as-cleaved chip. The threshold current is the extrapo-

lated value for the zero output power from the linear region of power-current (P-I) characteristics. For P-I curve, the chip was driven at 0.1% duty cycle, e. g., 100 ns pulse duration and 10 kHz repetition rate. As can seen in Fig. 5.3-(a), three emission modes were clearly seen as spontaneous emission, and lasing region, and saturated region. The threshold current is in general extrapolated from lasing region [60]. The measured threshold current density for lasing was 3.67 kA/cm^2 and the slope efficiency was 1.12 W/A. The frequency dependence shows that the laser maximizes the pulse power at around 0.5-5.0 % duty cycles, while the average power increases with increasing the driving frequency. All the data were measured at room temperature.

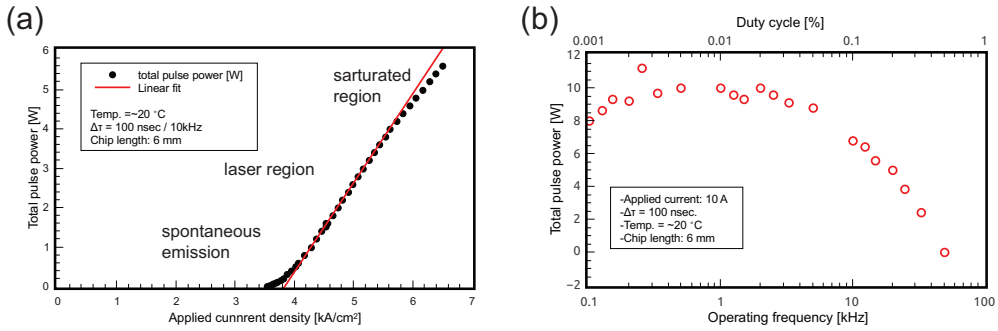

Figure 5.3: P-I curve and the operation frequency dependence of HU2-0446: figure (a) shows power to applied current density characteristics. Figure (b) shows driving frequency dependence of applied current. The pulse duration is set at 100 nsec and the operating frequencies lead the duty cycle.

We also carried out a durability test of the chip. The chip was connected to a pulse generator (LaserPulser, Quantiox GmbH, Germany) via a pulse amplifier (LDP-V 50-100 V3.3, PicoLAS GmbH, Germany), and driven with a duty cycle of 0.4 %, which was obtained from the P-ν measurement (Fig. 5.3-(b)). The stage was water-cooled, and giving a good heat extraction and a stable temperature at ∼15°C on average. The average power stayed at around 11.1 mW over 40 hours at current of 8.33 kA/cm^2. The stability of output power was also good, the overall fluctuation stayed at 1.78 % room mean square (RMS).

We captured the collimated beam profile. The beam was collimated with a black diamond aspheric lens (C037TME-F, Thorlabs, Inc., US), while the laser chip was water-cooled. The laser was operated at the same condition in the durability measurement. Figure 5.4 shows the beam profile captured with IR camera (Ophir. Inc., USA). The axis values were calculated from the setup and camera spec (1/2×1/2 inches image sensor set at 41 mm away from

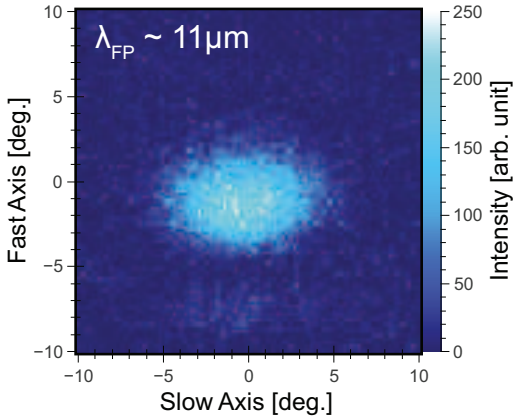

Figure 5.4: Beam profile of hu2-0446C; The beam was collimated with AR-coated aspheric lens. The image was captured with IR-camera. The divergence was calculated from the measurement condition.

the front facet and the sensor). As can be clearly seen, a single lobe as well as a small divergence were successfully obtained after the optical alignment in manual. This feature would be advantageous for homogeneous illumination on sample in microscopy application use.

FP-mode spectra were measured with FTIR[3]. Figure. 5.5 shows the spectrum development under the different driving conditions. The duty cycle was fixed at 0.4% (80 ns / 50kHz). We observed two dominant peaks at around 830 and 870 cm^{-1} which appears over 6.6 kA/cm^2. The observed emission range was from 10.8–12.1 μm at 8.0 kA/cm^2. The small fringes over the spectra is due to the FP mode oscillation of the chip length. As can clearly see, broadening effect in the emission spectrum was observed with higher applied current. From this measurement, This data is important for AR-coating optimization.

5.2.1.3 Facet coatings

The QCL chip was HR- and AR-coated. The coating layouts are listed in Table. 5.1. The AR coating was optimized for 11–12 μm range with two-layered model, consisted from yttrium fluoride (YF_3) and zinc sulfide (ZnS). Both materials have good transparency up to 14 μm, when deposited at 100°C with e-beam evaporator. For adhesion promoter, yttrium oxide has been inserted between every interface of materials as well as the laser

[3]Collaboration with Dr. Martin Hempel, and Dr. Xiang Lu at Paul-Drude Institut

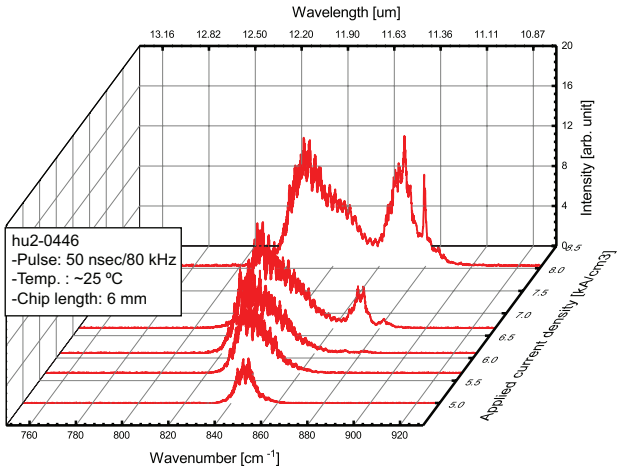

Figure 5.5: Emission spectra of hu2-0446: The laser chip was driven at 0.4% pulse mode at room temperature. The chip setup is the same as durability test.

facet. The layer structure of AR coating is optimized for 10.5 μm to 12 μm wavelength range with our numerical program. For HR coating, we used YF_3 as insulation layer then coated by 20 nm chromium and 200 nm gold. Using YF_3 would contribute for less absorption rather than SiO_2 at this wavelength range, as explained in Chapter 3.

Table 5.1: The models of HR/AR coating: AR coating layout for the range of 12 μm optimized with n_s=3.2; For HR- / AR-coatings, Y_2O_3 layers were introduced as adhesion promoter

Layer	HR coating		AR coating	
	Matl.	Thk. [nm]	Matl.	Thk. [nm]
Air				
1st layer	Au	200	YF_3	710
2nd layer	Cr	20	Y_2O_3	**10**
3rd layer	YF_3	800	ZnS	520
4th layer	Y_2O_3	10	Y_2O_3	**10**

P-I curves of different coating conditions were measured with the same driving conditions (100 ns/10kHz, 0.1% duty cycle). In order to calculate the residual reflectance of the front facet, the threshold current, I_{th}, and the slope efficiency, η, were extrapolated from linear regions (lasing regions), which are

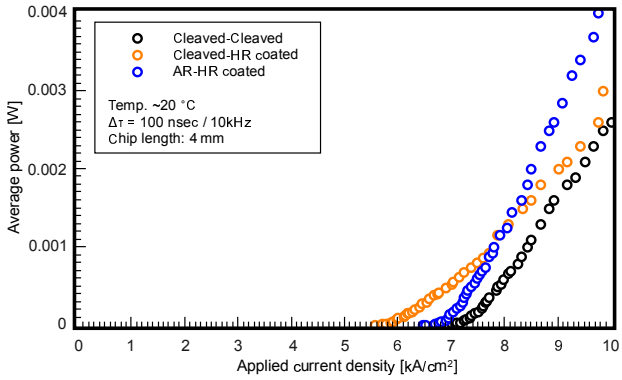

Figure 5.6: P-I curve with different coating profiles: Cleaved facet, HR coated and AR-HR coated facet.The laser was operated with 100 nsec/10 kHz pulse operation under room temperature condition.

listed in Table. 5.3. The calculated reflectance and the waveguide losses were calculated were $\sim$ 10% and 5.77 cm^{-1}, respectively. The performance of AR-coating is still not good enough for our target reflectance of $R < 1$.

Table 5.2: Threshold current and slope efficiencies with different coatings.

Facet cond.	I_{th} [A]	η [W/A]
As-cleaved	8.81	0.78
HR-coating / As-cleaved	7.23	0.41
HR- / AR coating	8.42	1.10

Several reasons for this poor coating performance can be considered. One reason can be due to a non-correct refractive index for coating optimization, as we used $n_s \sim 3.2$ for designing the coating, since the QCL is designed for the longer wavelength, meaning contains larger component amount of InGaAs (n_{InGaAs} ~3.4) rather than InAlAs (n_{InAlAs} ~3.0–3.1). This results in higher effective refraction index of the facet, thus the layout model also change by the optimization. The calibration error of e-beam system crucially affects to the coating thicknesses of the layers. In addition, the broadness of two-layered coating is limited, compared to the actual emission of the laser as seen in Fig. 5.5. Therefore, the two-layered design might be not optimal for this chip's performance, and using a four-layered coating can cover the whole emission range. These possible error factors need to be improved for better facet coatings from the engineering point of view.

5.2.2 Development of EC system

By completing facet coatings, we proceeded to the next step; integrating the QCL chip into the EC system. As is mentioned, we applied the front side extraction type as our prototype laser, since this configuration allows broad tunablity compared to the backside type. To compensate the drawback, we used less efficient braze gratings at Littrow direction, which would contribute for the higher power. Figure 5.7 shows the optical scheme of our laser configuration. QCL chip is HR- and AR-coated and the beam is first collimated by a lens. Resonant wavelength is selected by the blaze grating, which is mounted on a rotation stage. The zero-th order diffraction light reflects by a extraction mirror, and leads to the outside by a out-coupling mirror. By suing this double mirror out-coupling configuration, a beam walk-off can be avoided.

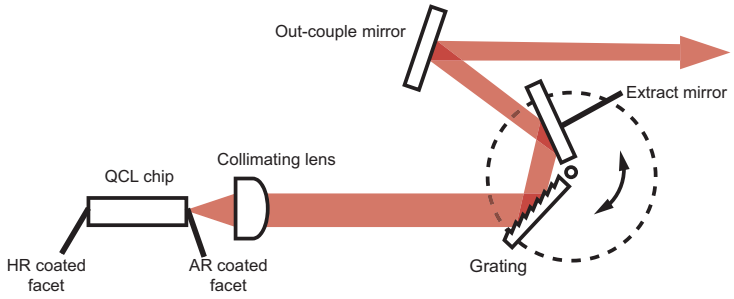

Figure 5.7: Schematic image of our prototype EC-QCL; HR- / AR-coated QCL chip is set and the beam is collimated by a lens. The grating selects the wavelength and the resonance between the grating and the HR-coating takes place. The output beam is extracted by a out-coupling mirror via extraction mirror set next to the grating.

We designed and fabricated all the components necessary for the system setup, including the laser chip package and the module cover for laser system using the computer aided design (CAD) tool. We also made a controlling box to drive the electronic units and programmed the user interface in Labview program. In the following, we describe the development procedure and details of the system.

5.2.2.1 QCL chip mount

We used a QCL chip prepared with 4 mm length. The laser chip was soldered on a AlN plate and then soldered on a copper plate as can be seen in Fig. 5.8-(a) The mounted chip was inserted in a tailor-made chip house, as shown

in Fig. 5.8-(b). An AR coated aspheric lens (C037TME-F, Thorlabs, Inc., USA) was used for the beam collimation from the front facet of the chip. The collimation was manually done. A Peltier device is inserted between the chip holder and the stage, as is indicated in Fig. 5.8-(b) and several holes of thermosensors are made for temperature monitoring. The beam is horizontally polarized to the ground. This is to illuminate the grating with p-polarized light.

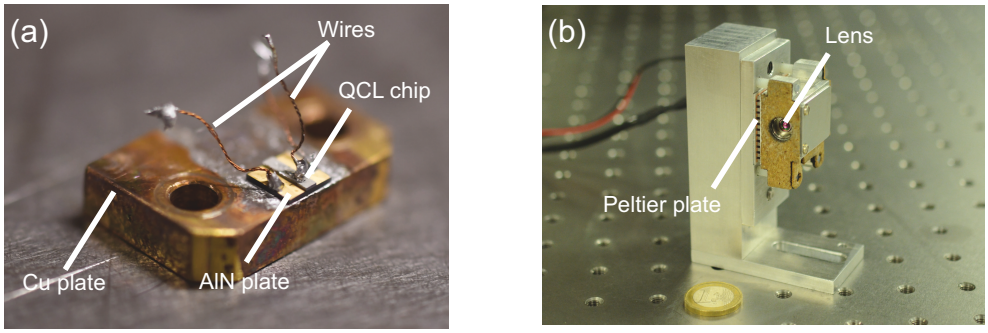

Figure 5.8: QCL chip on a copper plate and the chip holder; the QCL chip was mounted on a AlN ceramic plate, and then soldered on a copper plate. The laser chip holder was tailor-made for our prototype EC-QCL system. The output beam is horizontally polarized to the ground for grating.

5.2.2.2 Optical system and its alignment

Figure 5.9 is a zoom-in picture of the optical setup of our EC-QCL. In Fig. 5.9-(a), We can see the laser holder depicted in Fig. 5.8-(b) at the front of the picture. We used a commercial blaze grating (ML401, Optmetrics. Inc., US) and a high reflectance mirror (PFSQ10-03-M01, Thorlabs, Inc., US) for a extraction mirror. The blaze grating was set in Littrow condition. The angle between the grating and the mirror was set at 104.6°. This is an optimal angle for the beam spot on the grating and the mirror in different angles. The reflected light by the extraction mirror is led to the output window by a gold plated mirror (PF07-03-M01, Thorlabs, Inc., US) set next to the rotation stage, which can be seen at the front of Fig. 5.9-(b). The grating angle is directly controlled by a motorized rotation stage (CR1-Z7, Thorlabs, Inc., US). The grating stage rotates together with the extraction mirror, while the out-coupling always keep the output beam at the same point, and go out through the output window. The rotation stage was mounted on a pitch and yaw platform (PY003/M, Thorlab. Inc., US) for the sake of optical align-

ment. The external cavity length defined from the HR-coating of the chip and the grating is ∼40 mm.

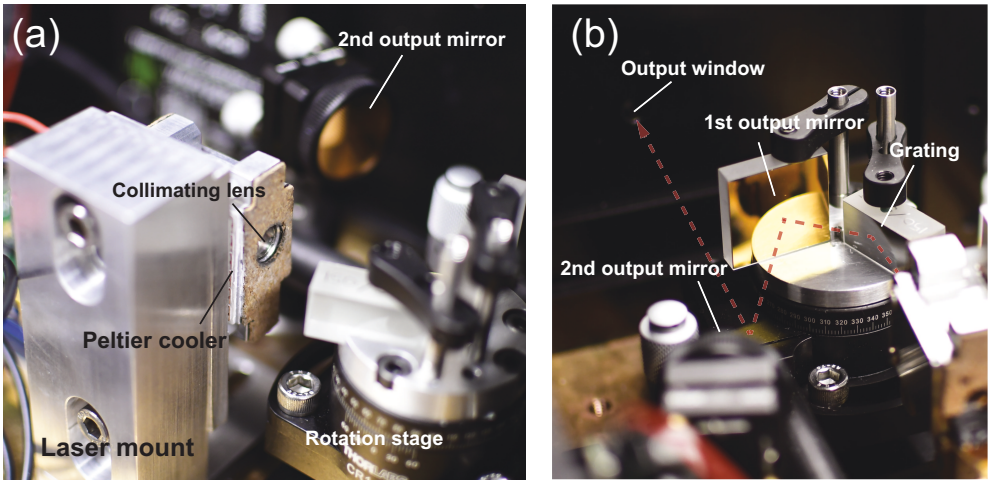

Figure 5.9: Pictures of optics system of our prototype EC-QCL: (a) the laser holder with a Peltier cooler and stage can be seen at the front and the grating was set in front of the lens mounted on the holder. (b) the grating was set at Littrow condition, and the output was extracted by a out-coupling mirror via the extraction mirror set next to the grating. For optical alignment, a InP substrate was placed between the holder and the grating.

For the optical alignment of the system, we set a double-side polished InP substrate set at 45° to the input beam between the laser holder and the grating. The substrate functions as a beam splitter inside the cavity. We have used the split beam for direct monitoring of optical power inside the cavity. which is limited around 30% of the total power inside the optical cavity. The reason of this procedure is because the usual output beam out of the out-coupling mirror did not give an enough power due to the high grating specification. To align in the optical resonance, the grating was set at the angle of wavelength at which the gain region should be covered. By changing the yaw degree of the stage while monitoring the intensity of output beam out of the beam splitter, we can test the power amplification by manual. By this procedure, we could finally align the system for the external cavity oscillation. By tuning the grating, we could see the similar power spectrum from the two output power, while the split beam has a intensity fluctuation due to FP oscillation of the InP substrate.

5.2.2.3 System integration

Figure 5.11 shows a schematic overview of our EC-QCL system. The system is mainly made up from the four parts, a laser system at center, a grating controlling unit, a QCL driving unit, and a thermal device controlling unit. The grating unit and thermal sensor unit are connected to a computer and monitored with the programs. QCL divining unit is isolated, however also is controllable as the other two controlling units.

The details of the optics system as well as the laser chip were written in the previous section. The laser driving unit are consists of a pulse generator and a pulse amplifier, which are embedded inside the laser head.

The resonant wavelength of EC is controlled by a rotation stage as mentioned in the previous section. To communicate with computer, ActiveX controller is used, which adapts its earlier Component Object Model (COM) and Object Linking and Embedding (OLE). For easy-handing of the user interface of our system, we modified the grating controller unit for out specific use; a wavelength controlling. The synchronization speed is still limited. Although this can be improved by replacing Qt-base program, this was however out of our scope in this PhD work.

The Peltier device (30×30 mm^2, QC-71-1.4-8.5M) is controlled with a commercial driving module, which contains the PID temperature controller (PTC10K-CH WavelengthElectronics, UK) and monitoring interface (USBKIT, WavelengthElectronics, UK). The target temperature was set at 18°C, which has a good match to the dew point of our experiment environment.

All the controlling units are divided into two groups and one was packaged in the laser head (Fig. 5.8-(a)) and the other was arranged in the controlling box, as can be seen in Fig. 5.8-(b).

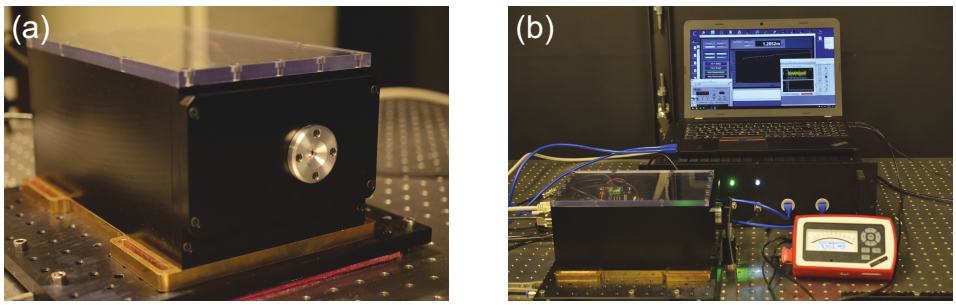

Figure 5.10: System outlook (a) laser head and (b) whole system: the laser head was made in a compact form. (b) shows a picture of whole system, together with a laptop and a minitor and its detector.

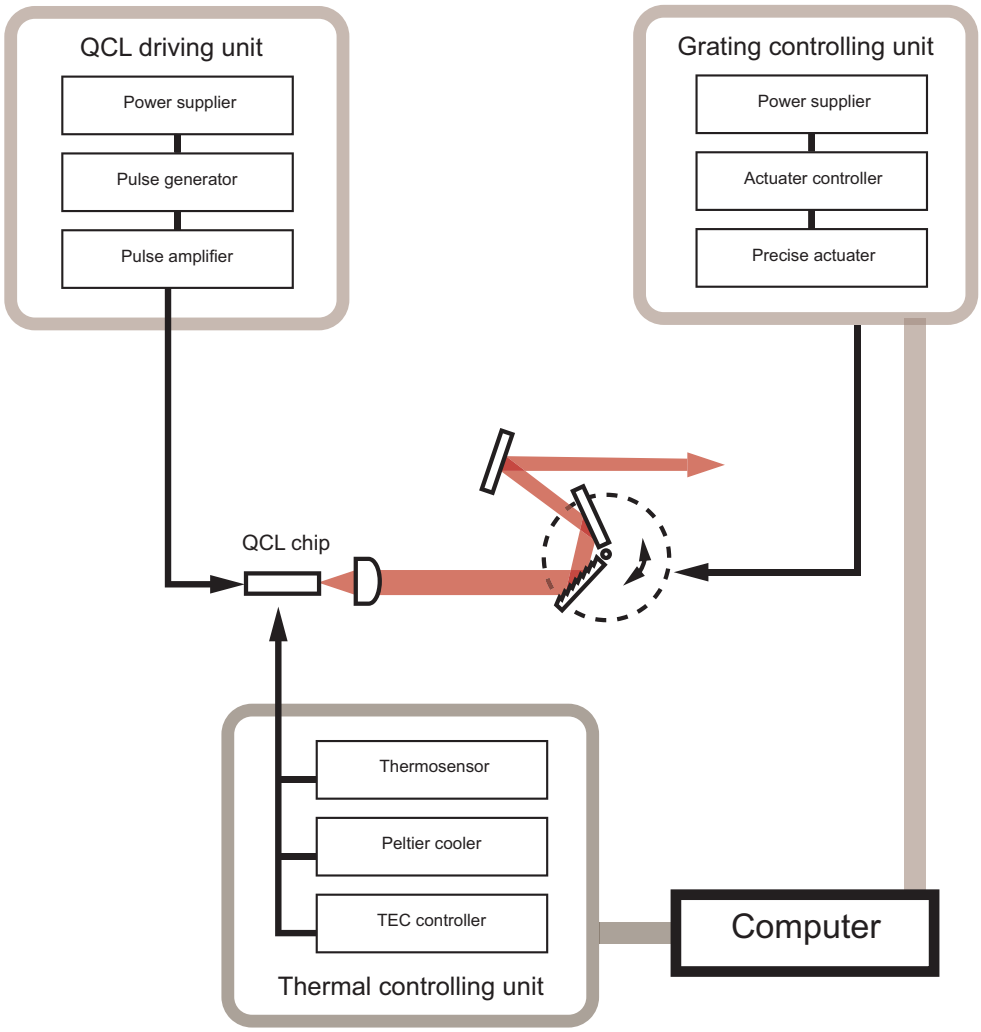

Figure 5.11: System overview of our prototype EC-QCL system: Optical setup is illustrated in the center, and other driving and control units are indicated. QCL chip and diffraction grating function as the optical resonator. Grating control unit and thermal sensor unit are connected to computer, although QCL driving unit is isolated.

5.2.3 Characterization

In this section, we detail the "prototype" laser performance.

5.2.3.1 Laser performance

We measured the optical outputs both in non-EC mode (Fabry-Pérot mode / FP mode) and external cavity mode (EC mode). The driving condition is the same as described in previous (0.4% duty cycle). Figure. 5.12 shows the results. For FP mode, the detector was set in front of the collimating lens, and in front of the first mirror for EC-mode. The grating angle was set at 58.0°, which gives 11.3 μm as the resonant wavelength.

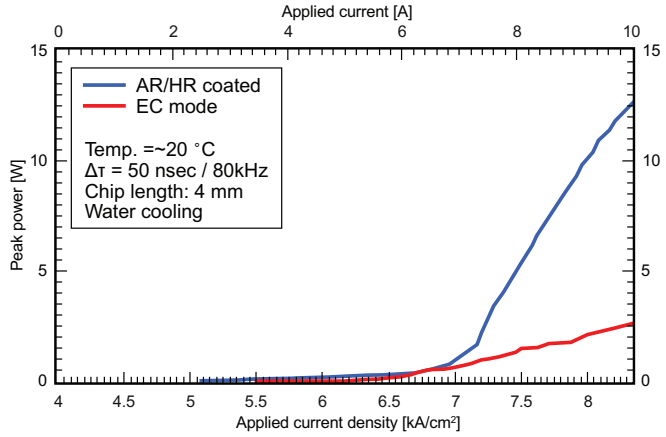

Figure 5.12: *P-I* curves of non-EC mode (FP mode) and EC mode: FP mode is represented with blue line and EC mode is with red line. In EC mode, grating was set at 11.3 μm. The EC-mode has lower threshold current and lower slope efficiency compared to FP mode.

Threshold currents, I_{th}, and slope efficiencies, η, were extrapolated from the linear regions of the curves. Slope efficiencies were calculated in average output power. The results are listed in Table. 5.3. Compared to non-EC mode (FP mode), EC mode has lower threshold current for lasing, while the slope efficiency is also lower than that of non-EC mode. This is either due to the lower coupling efficiency and also due to the high grating specification. The small shift of the threshold currents can be improved by a better AR coating and ultimately good coupling at the amplifier and the EC system.

Table 5.3: Threshold current and slope efficiencies of prototype EC-QCL: the results were extrapolated from the two laser mode performances represented in Fig. 5.12

Laser mode	I_{th} [A]	η [mW/A]
non-EC mode	8.29	3.86
EC mode	7.87	0.61

5.2.3.2 Tuning performance

Power spectra were measured by rotating the grating. Figure 5.13 shows the power spectrum of our prototype system. The left shows the whole spectrum range and the right shows the zoomed-in spectra from 880 to 890 cm^{-1}. All the spectra were centered at $\sim$ 11.3 μm. The spectrum broadening was clearly observed at the higher applied current. The resulting tuning range covers from 830 cm^{-1} to 920 cm^{-1} at 10.0A. Compared at 8.0 A, this range corresponds to 37% increase in terms of the spectrum width. This can be either due to the change of the band structure under the higher applied electric fields and larger carrier contribution for optical transition.

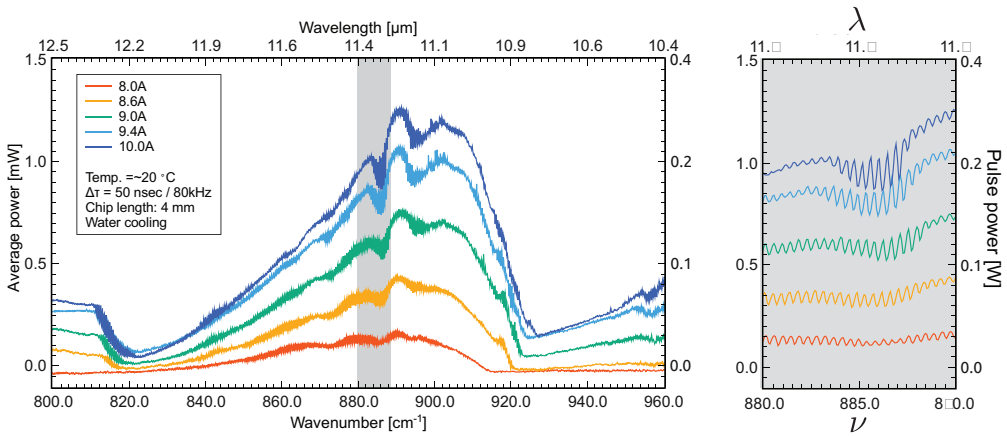

Figure 5.13: Power spectrum of the EC-QCL: the QCL chip was driven at different current from 8.0 A to 10.0 A. The wavenumber was tuned to cover the whole gain spectrum range. The right graph shows the zoom-in of 880–890 cm^{-1}. The unified oscillations were observed in all the driving conditions in keeping the same intervals

In high resolution measurement, we obtained the power fluctuation along

the spectrum in every applied current condition. The clear picture is shown with the zoomed-in spectra, as shown in the right graph of Fig. 5.13. All the fringe positions respect to the wavenumber and the separation intervals are the same except the oscillation amplitude. Since we operated the system in pulse mode, thus this can be due to the mode-hopping of lasing mode. In our case, the separation would be basically determined by the chip length, by taking into account our AR coating performance; 10% modal reflectance.

In order to optimize the applied current, we investigate the development process of lasing mode. We set the resonant wavenumber near an edge of the gain region, $\nu \sim 900$ cm^{-1}. Figure 5.14 shows the spectrum of our laser system set at 900 cm^{-1}. At small applied current, the laser oscillates with a single mode, while the mode split were observed as can be seen in the inserted of Fig. 5.14. By increasing the current, the amplitude of the oscillating mode develops. Up to 12.0A, a single dominant lasing mode was obtained. At 12.5A, the second dominant mode starts to oscillate at around 890 cm^{-1}. This is due to the gain saturation of QCL chip respect to EC loss. The maximum point of QCL gain curve equalized to EC loss regardless of the grating selected loss, thus start to lase at the wavenumber at which the gain is maximum. For a laser system, a single oscillation is mandatory. Thus we have operated our system at 12.0A.

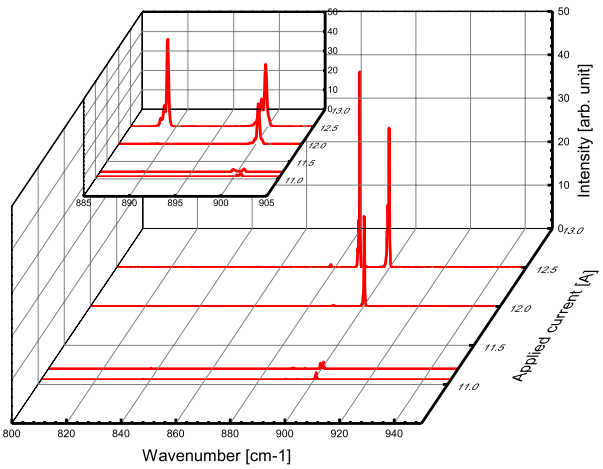

Figure 5.14: Lasing mode development by applied current on laser chip: the grating angle was set to target at the edge of the gain spectrum range, at 900 cm^{-1}. Until 12.0 A, the single dominant mode was achieved, while the second mode started to lasing at 12.5A.

We measured the tuning spectra with FTIR as well as the final power spectrum operated at 12.0A. Figure 6.6 shows the power spectrum and lasing

modes of different wavenumber. The resolution of FTIR is $\Delta \sim 0.15$ cm^{-1}. The amplitudes of each lasing modes are normalized. Good tuning performance was achieved from 820 to 915 cm^{-1}. Small parasitic modes are still observed at longer wavelength. The maximum average power is at $\sim$ 4.80 mW, which gives 120 mW in pulse power.

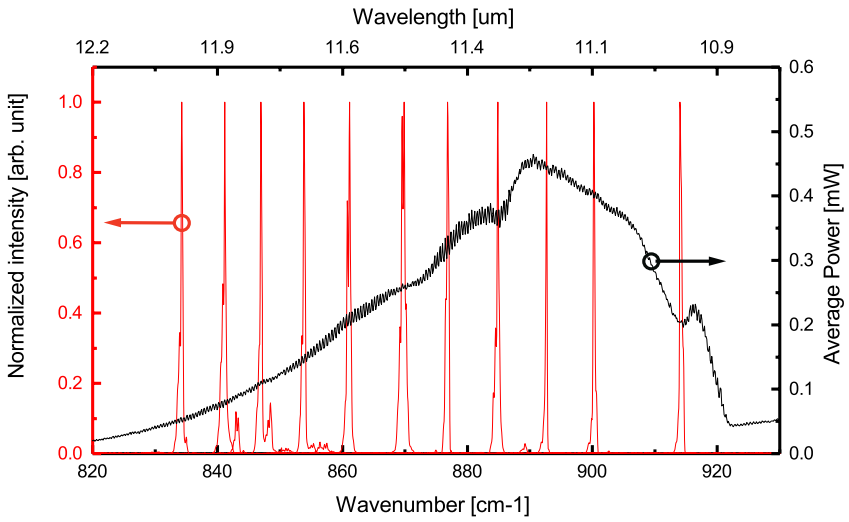

Figure 5.15: Tuning performance of Prototype EC-QCL with power spectrum: lasing modes were measured with FTIR. For the single lasing mode, the driving current of the QCL chip were set at 12.0A. The resulting tuning range was from 820 to 915 cm^{-1}, and the maximum power is $\sim$ 0.120 W at 890 cm^{-1} in pulse mode.

At several wavenumber, we obtained multi-peaked single modes in the FTIR measurement. Meanwhile the power spectrum also oscillate with small amplitude as seen in Fig. 6.6. Figure 5.16 shows the zoomed-in portion at $\sim$ 870 cm^{-1} from Fig. 6.6. The spike measured with FTIR shows the split two mode (red line). The power spectrum also shows the two peak, which almost correspond to the lasing mode measured with FTIR. This correspondence of the intervals as well as the wavenumber reveals that these power fringes are due to the mode-hopping of lasing mode.

5.2.4 Imaging test of bio-tissue

As mentioned at the beginning of this section, the recent studies demonstrates the great advantages of using mid-IR microscope for the early stage cancer diagnosis. The demonstration of the longer mid-IR is however still

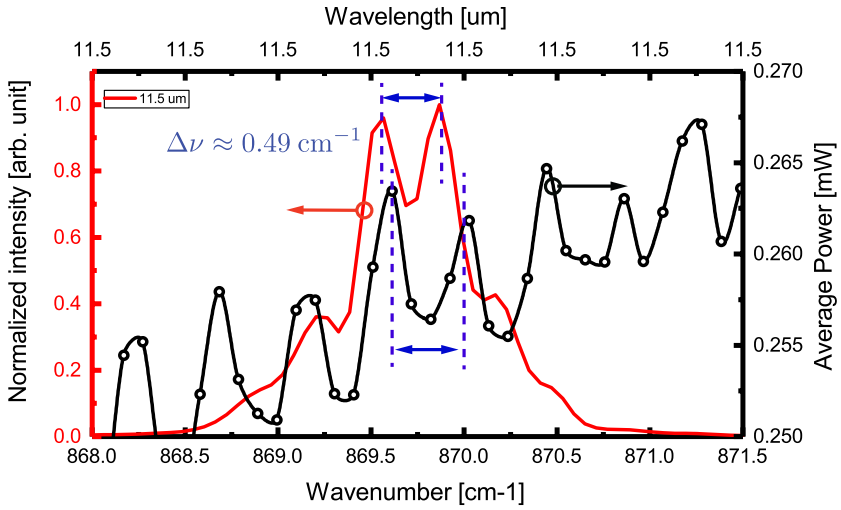

Figure 5.16: Zoom-in picture of Fig. 6.6 at 890 cm^{-1}: the mode spectrum represented with red line shows the mode separation with the interval of 0.49 cm^{-1}, and the power spectrum of black line shows the power fluctuations with constant intervals. The mode separation is almost the same which was measured with FTIR measurement.

lacking in the community, specially $\lambda \sim 10$–$12\ \mu$m. The advantages of using EC-QCL as a light source is for its coherency. EC-QCL is a coherent light source, then optical signal to noise ratio and brightness for the sample are much higher than FTIR system. The second advantage is for its higher scan speed. In general, FTIR requires a long time for scanning measurement, while that of EC-QCL is relatively faster. The third reason is for the system compactness. FTIR is bulky then requires a large space and the system robustness is also not so good. Due to these reasons, we were motivated to build a laser system which suits for this application.

As a part of the project, the laser system was delivered to our partners[4] for a collaboration experiment. Our primary goal was to demonstrate hyperspectral imaging of cancer tissue by combining our EC-QCL as a mid-IR light source and their microscope system. We measured a sample with oesophagus. We integrated our laser system with a partner's FTIR microscope system (Agilent Cary 620 series, Agilent Inc., USA). The light was illuminated on a sample in transmittance configuration. The images were captured with a focal plane array (FPA) of mercury cadmium telluride (HgCdTe) imaging sensor.

[4]Mr. Micheal Hermes, Ms. Pascaline Bousy, and Prof. Nick Stone in Bioimaging group

5.2.4.1 Resolution target

We first imaged a 1951 USAF resolution test chart with our EC-QCL as well as Globar. Figure 5.17 shows a part of resolution chart (a) and the captured images illuminated by the EC-QCL ((b), (d)) and by Globar ((c),(e)). We could resolute two targets; the lines of (group 5, element 3) which corresponds to 12.4 μm, and the number 4 at (group 6, element 4). As can be seen from the pictures, the images captured by EC-QCL is obviously brighter than the ones by Globar, while the resolution is not worse. The reason of better resolution in (c) and (e) is because of its broad spectrum from a black body radiation of Globar. The shorter wavelength contributes to such resolutions, while our EC-QCL emits a single wavelength of the 11 μm range.

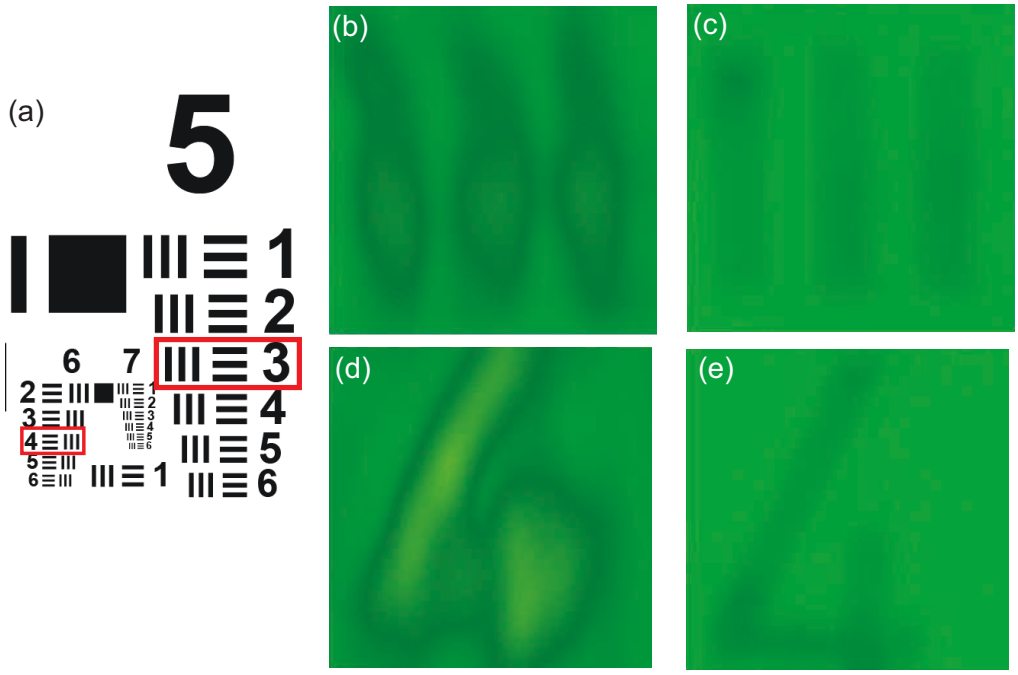

Figure 5.17: A image of a 1951 USAF resolution test chart and images captured by our EC-QCL and Globar: (a) is a part of the resolution target, and (b) and (c) are the lines of (group 5, element 3) taken by EC-QCL and Globar, respectively. (c) and (e) are the number 4 at (group 6, element 4) with the same methods.

5.2.4.2 Bio-sample imaging

We carried out imaging tests of biological sample. The sample was a slice of oesophagus cell. Figure 5.18-(a) is a normal photo captured in visible range. Figure 5.18-(b) shows the images illuminated by our EC-QCL set at 11 μm wavelength range. In order to capture the whole area of the sample, images were separately taken and all the pictures are combined afterwards. The image shows a little contrast of the sample's edge, however no distinctive difference was observed from the data. For the test imaging, this result revealed a good proof of concept regarding a imaging of the longer mid-IR range light source.

The issues of our EC-QCL system were considered. A better average power would help for higher contrast of the image. Figure 5.18-(b) did not have a good contrast to the background. The power of the laser system we used in this experiment was $\sim$ 1 W on average, and did not show a clear contrast during the measurement. Besides, for good illumination, the beam shape and wider diameter after passing though the several opticcal components become crucial for the clear imaging.

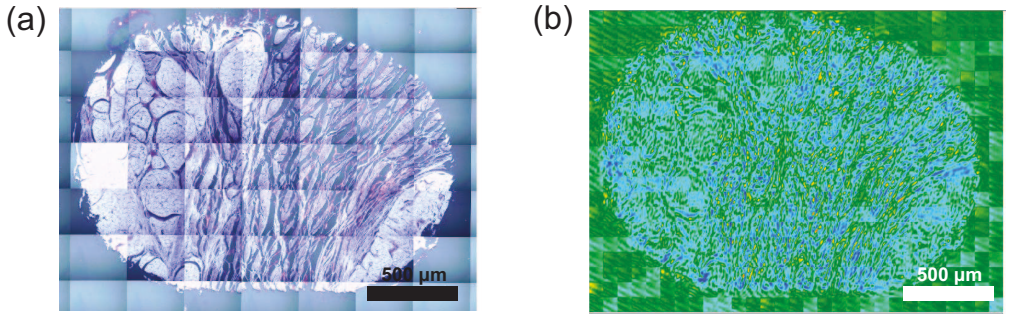

Figure 5.18: The sample images of oesophagus captured in visible region (a) and mid-IR region (b): (a) was captured with a while lamp and Si-based image sensor. (b) was illuminated with our EC-QCL set at $\lambda \sim 11$ μm and imaged by HgCdTe sensor camera.

5.2.5 Summary: Prototype

We successfully processed QCL chips and characterized the laser performance, we optimized the duty cycle of driving condition in pulse mode. We coated the chip facets with HR- and AR-coating, and characterized the coating performance. The resulting modal reflection was reduced to $\sim$ 10%.

The chip was integrated into an external cavity system. We successfully built a Littrow configuration EC-QCL. The laser system emits the full range of the 11 μm wavelength. The system was packaged as a compact and ragged setup. The achieved spectrum resolution was 0.49 cm^{-1}, which fulfils the requirement for medical hyperspectral imaging; typically Δ $\sim$4.0 cm^{-1}. The spectrum broadening effect was observed under the higher applied currents.

Finally we demonstrated the medical hyperspectral imaging with the EC-QCL system as a proof of concept. We conclude that our nice beam profile is advantageous and that higher average power will aid the further improvement in quality of mid-infrared imaging.

5.3 The 2nd generation: New-model

This section explains the second laser system, "New-model". We have gained many know-hows during the "Prototype" laser construction, and could also consider the crucial factors for a better performance in terms of tuning range as well as the output optical power. These considerations were fed back to this newer model, and the performance of the components were maximized with the series of engineering. Meanwhile we optimized the package system for the better compactness. Since our target application is a broad range hyperspcetral imaing, we again applied the front side extraction configuration for this new design. In the following we mainly describe,

1. new laser system,
2. the performance of New-model
3. the use of angled facet QCL amplifier

We would first describe the system designs and also about the other system units. The main interest of this step was the system miniaturization. Since the last model weights $\sim$ 12 kg only with the laser head, and was not suitable as a portable system, we have tried to make a more compact system. The system performance is presented in the next section. We first used a straight waveguide QCL with a broad gain region. The details of the QCL chip as well as the coating process can be found in chapter 4. We have also fabricated a angled facet QCL for further reduction of reflection of the front facet. This is also presented in Chapter 4.

5.3.1 System details

Here we describe the system details of "New-model". Figure 5.20 shows the outlook of CAD design with its schematic image of optical configuration. The laser system applies a Littrow-type with front-side extraction. The grating (ML-304, Dynasil Inc., US) was mounted on a sub-stage, which was hold by a cylinder type pivot (Pivot bearing 5010-800, Riverhawk, US) and a base stage. The angle was controlled by a precise actuator (Z825B, Thorlabs Inc., US). Out-coupling mirror shown in the inserted image of Fig. 5.20 are fixed on the sub-stage, then rotates together with the grating. The drawback of the system is a walk-off the beam path. Our system size is relatively compact at 20 cm $\times$ 10 cm $\times$ 8 cm, including some electronics and the motor: the optics part is 9 cm $\times$ 7 cm $\times$ 6 cm. The external cavity length is changeable in the range of 20 mm to 40 mm.

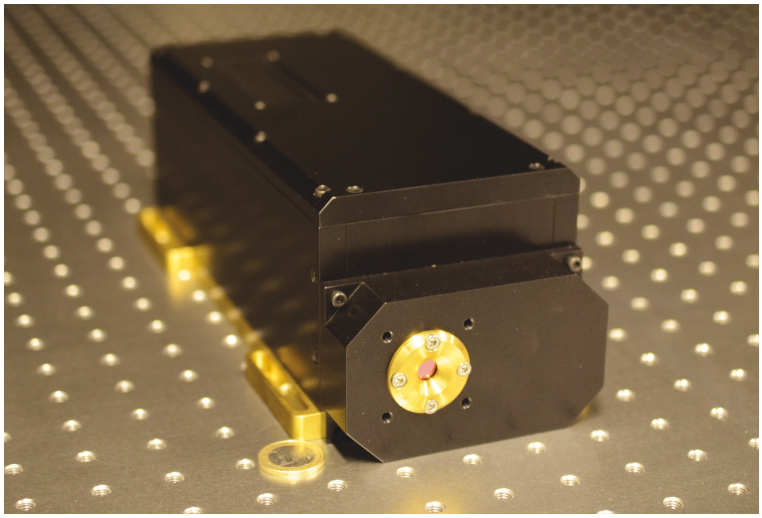

Figure 5.19: Outlook of 2nd generation laser; "New-model"

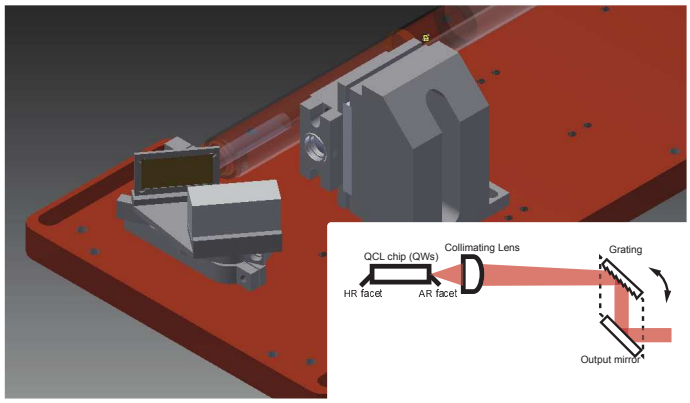

Figure 5.20: Outlook of New-model, CAD design and schematic of optical: the grating was mounted on a stage, and controlled by the precise actuator. The total optics size is at 9 cm $\times$ 7 cm $\times$ 6 cm.

Figure 5.21 shows a CAD design image of a new QCL holder for New-model; the optical amplifier unit. The system supposed to have two types of laser chips; a QCL with a straight waveguide and with a bent-waveguide structure aimed for angled facet. The former chip can be easily mounted on a plate as indicated in Fig. 5.21-(a). The angled facet laser, however, does have a angled output with an uncertain direction, thus requires some degree of freedom, thus a angle adjustable plate. In order to address this issue, we designed a copper plate with rounded corners, as can be seen in Fig. 5.21-(b). The laser beam can be aligned manually by adjusting the angles of the stage as well as the lens position. For easier alignment, we used a low numerical aperture lens (f = 4.0 mm, NA = 0.54, AR coating: 8 – 12 μm, C036TME-F, Thorlabs Inc., US) for the angled facet QCL, thus we can avoid the collision of the stage corner and the holder. The laser holder was placed on a Peltier device same as Prototype.

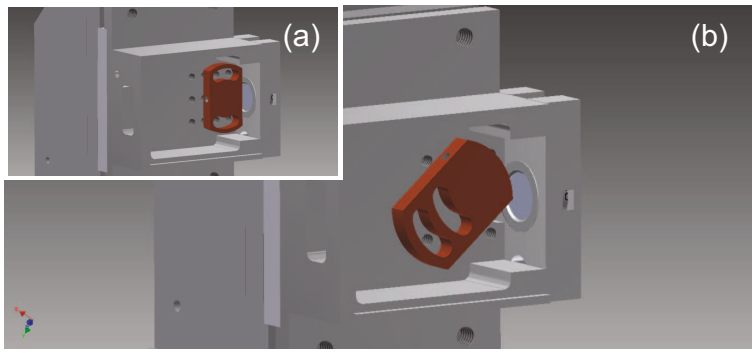

Figure 5.21: A CAD design image of the new QCL holder: a stage shown in (a) is for a straight waveguide structure, which allows a easy alignment. (b) represents a special stage for angled facet QCLs. The chip angle is widely adjustable for different output angles.

Figure 5.22 shows pictures of the accomplished holders. (a) is the laser holder shown in Fig. 5.21. The Peltier element is inserted underneath of the main holder. The holder was minimized in a relatively compact form, and the different units are exchangeable once each chips and lens are aligned. (b) is a another holder designed for a backside extraction configuration. This holder can be used only for a straight waveguide QCL. The stage size is the same with the holder (a), thus adaptable for New-model.

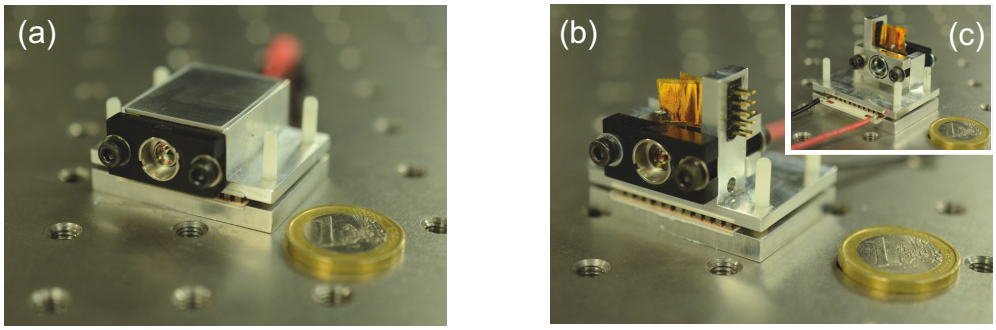

Figure 5.22: Chip holders for New-model; (a) is for front-side extraction Littrow-type and (b) for backside extraction Littrow-type. The both holders are adaptable for our new system. Peltier elements are inserted underneath of the main holders, and can be easily connected with the two cables.

5.3.2 Performance: the straight bar

5.3.2.1 QCL chip and coating performance

A broad-gain QCL were processed and HR- / AR-coated on the facets. The details are written in Chapter 3.

5.3.2.2 Tuning performance in EC system

We placed the coated QCL into an external cavity in a Littrow-type configuration. The output laser beam was collimated with a broadband (8–12μm) AR coated aspheric lens and a numerical aperture (NA) at 0.85. For wavelength tuning, a Au-plated blaze grating of 135 grooves/mm with over 90% efficiency in Littrow direction (Dynasil) was used. The optical output was extracted from the zeroth-order diffracted light from the grating and outcoupled by a Au plated mirror. Due to a walk-off of the output beam of Littrow-type laser, a Au plated parabolic mirror was used for power measurement. The chip was driven in pulsed mode (80 kHz/50 ns) with a current of 13 A. The tuning spectra were measured with an FTIR. The spectral resolution is limited at 1.0 cm^{-1}. Good tuning was achieved around from 920 cm^{-1} to 1190 cm^{-1} and 0.45 W at the maximum pulse power, which are shown in Fig. 5.23. Further increase in applied current causes distinctive parasitic oscillations within the tuning range. Backside extraction in optical setup may enhance the performance in terms of the output power, since in the current configuration the output is limited to less than 10%.

This part is reported in Ref. 120.

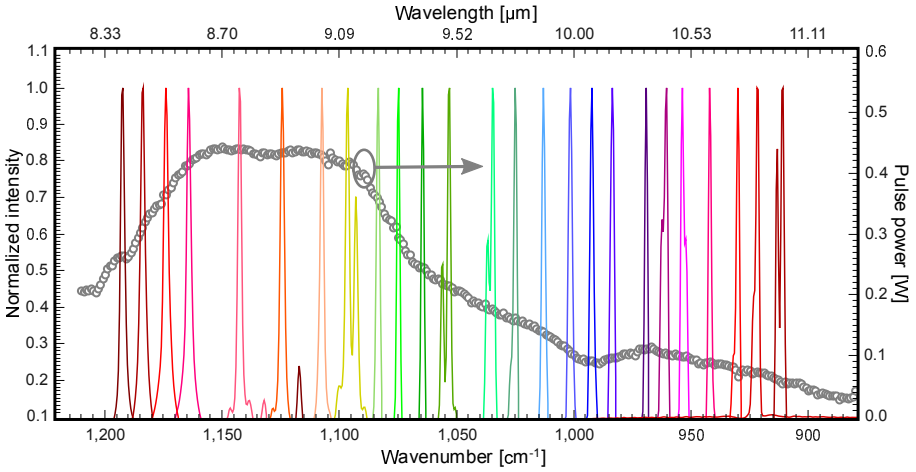

Figure 5.23: Tuning performance of EC-QCL system with a straight bar QCL: the QCL chip was operated at 13.0 A applied current. Achieved tuning range was from 920 cm^{-1} to 1190 cm^{-1} and 0.45 W pulse power was obtained.

5.3.3 EC system with angled facet QCL

One of the requirements for EC-QCL is to reduce the residual reflectivity of the optical gain media, i. e., QCL faect, typically $R < 1\%$ [47]. The lower reflectance of the facet contributes to the higher coupling efficiency between the optical resonator and the gain medium. As a results, broader tuning range and higher output power can be realized. Therefore, minimizing facet residual reflectance is strongly required for the higher performance of EC-QCL.

As explained in Chapter 4, angled facet waveguide is a promising and one of the standard methods for reducing modal reflectivity of laser facets, and have been demonstrated with diode lasers for optical commbands [104, 105]. Applying AR coating on angled facet enables further reduction of reflection, easily achieving 10^{-3}–10^{-4} order of magnitude in reflectance. The drawback of angled facet laser in EC use is its system complexity when it is used in backside extraction type, as shown in Fig. 5.24-(b). Most of the commercial EC laser products apply this configuration for its good power. Angled facet QCLs were also demonstrated by means of focus ion beam (FIB) cutting, and the resulting reflectivity can be around 10^{-3} order of magnitude and enhance the power slope [20, 15]. As written in Chapter 3, we demonstrated angled facet QCLs realized by bent waveguide structure and simple cleaving process [68]. This method allows easier production of laser bars and a good yield rate.

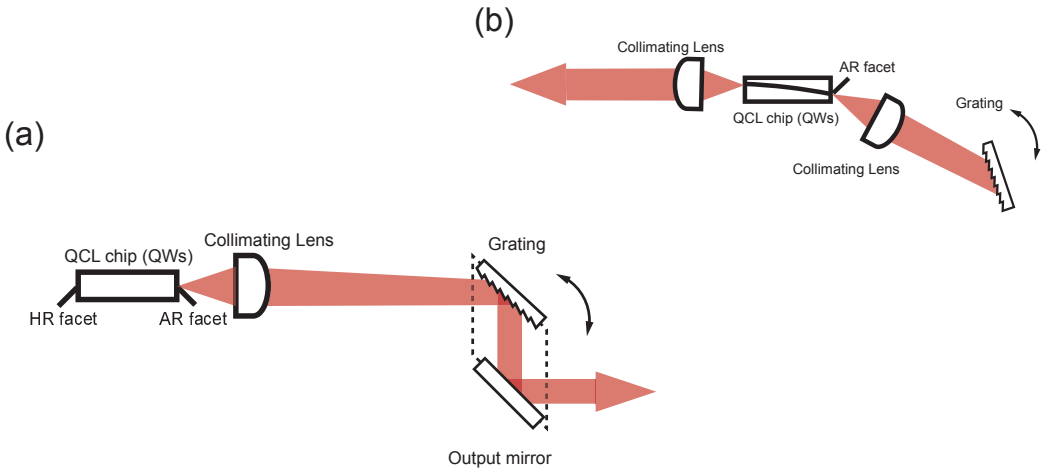

Figure 5.24: Conventional Littrow-type laser using a straight (a) and bent waveguide QCL (b); configuration (b) results in its complex system.

In this section, we present a mid-infrared tunable external cavity laser using an angled facet waveguide quantum cascade laser as the gain media. The angled facet is realized by transferring bent waveguide patterns onto the laser wafer. The angled facet was AR-coated for further reduction of reflection and the coating details are already described in Chapter 4. The tuning performance with Littrow-type external cavity system is mainly described. In this work, we applied a front-side extraction configuration to avoid the system complexity in the EC use, as shown in Fig. 5.24-(a).

5.3.3.1 System details of angled facet QCL

As written in section 5.3.1, a major issue of using angle facet laser is its system complexity. In order to address this, we built a front-side extraction Littrow-type external cavity system. We made an angle-adjustable copper plate, and the chip was placed with the optimal angle for the good beam alignment. The amplifier module is realized in compact with the size of 2.5×3.4×1.2 cm^3, and shown in Fig. 5.22-(b). The output beam from the AR-coated facet was collected with a broadband (8–12 μm) AR-coated aspheric lens and the numerical aperture (NA) was 0.56. The resonance wavelength is tuned by a Au-plated blaze grating of 135 grooves/mm (Dynasil), which has over 90% efficiency in Littrow direction over the 6–14 μm range. The output beam was extracted from the zero-th order diffraction light with a Au-plated mirror. The system was assembled in a relatively compact setup; 20×10×8 cm^3 laser box, including the optics part of 9×7×6 cm^3.

5.3.3.2 Basic performances

Figure 5.25-(a) shows power-current (P–I) characteristics of Fabry-Pérot (FP) mode with AR- and HR-coated condition and external cavity mode set at 1110 cm^{-1}. Emission spectrum of FP mode measured with Fourier transform spectroscopy infrared (FTIR) is also inserted. For P-I curve measurement, the chip was driven at 0.1% duty cycle (100 ns/10kHz) in both conditions. The laser performance was characterized by the lasing condition formula, $J_{\mathrm{th}} \propto \alpha_{\mathrm{wg}} - 1/2L \ln R_1 R_2$, where J_{th} is the threshold current density, and α_{wg} is the waveguide loss of QCL. R_1 and R_2 represent the reflectances of QCL facets. The thresholds were extrapolated from P-I curves by linear-fitting. From cleaved-HR curve, the waveguide loss was estimated at 13.3 cm^{-1}. With AR coating on the angled facet, the lower threshold and the higher slope efficiency are clearly observed compared to cleaved-HR chip. The estimated modal reflectance of AR-coated facet is ∼0.54%. The spectrum range of the coating surely covers the entire emission range of our QCL. More angled facet and further optimization of AR coating may improve further reduction of modal reflection.

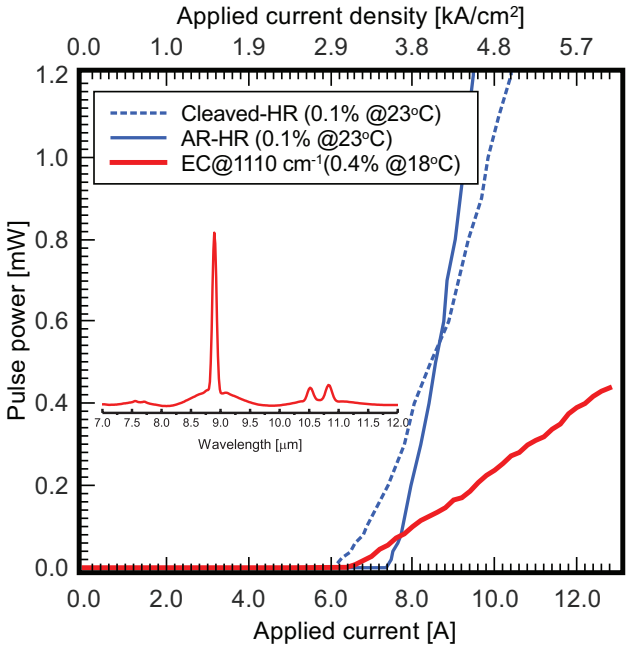

Figure 5.25: P–I characteristics of angled facet QCL with different coating conditions. Cleaved-HR and AR-HR coating were measured at the same driving condition; 0.4% (50 ns/80kHz) pulsed current at room temperature.

For the external cavity performance, lower threshold current for lasing was observed, while the slope efficiency is limited mainly due to the optical configuration. For Littrow-type EC system, the output is restricted by the grating performance, which allows the output less than 10% output power from the resonating power in the external cavity. Backside extraction or other configuration [138] will enhance the output power. In addition, a lens with higher NA will give more power due to the better collection of light from the angled facet. The beam profile captured with an IR-camera exhibits a good TM_{00} mode (Fig. 5.25-(b)).

5.3.3.3 Lasing mode development

Tuning performance was also investigated. The lasing mode was tuned by rotating the grating. In order to optimize the driving condition of the laser chip, we measured the development of lasing modes closed at the shortest and the longest points of the gain region. Figure 5.26 shows the mode development with different applied current at 985 cm^{-1} for the shortest and at 1180 cm^{-1} for the longest wavenumber. From this measurement, we concluded that 12.0 A is the optimal driving condition for single mode operation. As can be seen in Fig. 5.26, more current causes the parasitic oscillations at around the high gain area. This is due to the mode competition between EC loss and FP loss.

5.3.3.4 Tuning performance

Figure 5.27 shows the power spectrum measured with a power meter and lasing modes measured with FTIR. In this measurement, the QCL chip was driven at 0.4% duty cycle (50 ns/80kHz) with a current of 12.0 A, and kept at 18.0°C with Peltier device set underneath of the gain chip. The resolution of FTIR was at 1.0 cm^{-1}. Over the entire spectrum range, good longitudinal modes were observed without any parasitic modes. The resulting tuning range was from 950 cm^{-1} to 1180 cm^{-1}, and the achieved maximum power was 0.45 W. Higher numerical aperture will improve the power performance, since the collection of light is about 60% higher when a NA = 0.86 lens is used.

5.3.4 Summary: New-model

In this section we demonstrated the Littrow-type EC-QCL. During this work, we have addressed inherent issues for the good laser performance. We also demonstrated the external cavity quantum cascade laser with an angled facet

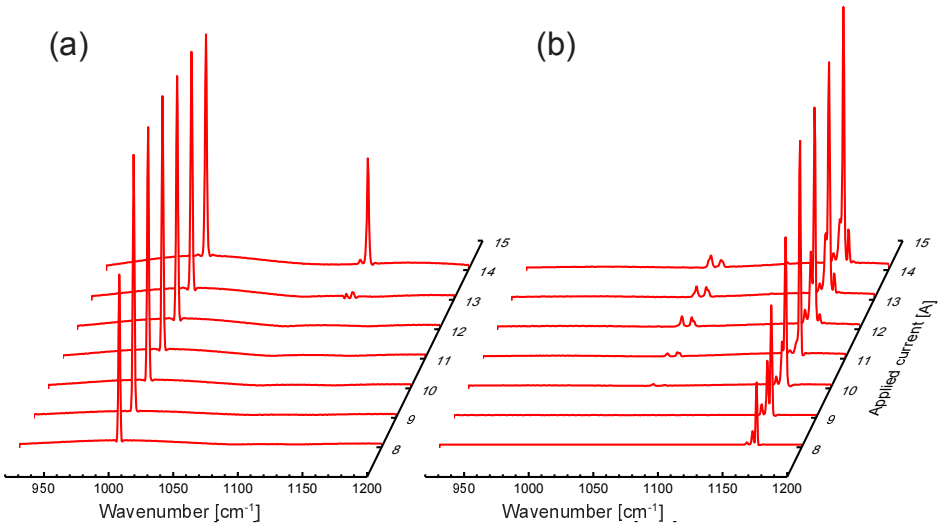

Figure 5.26: Lasing mode development due to the different applied currents on the QCL chip. Pulse mode current was applied at 0.4% duty cycle, and chip was kept at 18°C during the measurement. Dominant parasitic mode were observed around 14.0 A, corresponding to 5.7 kA/cm^2.

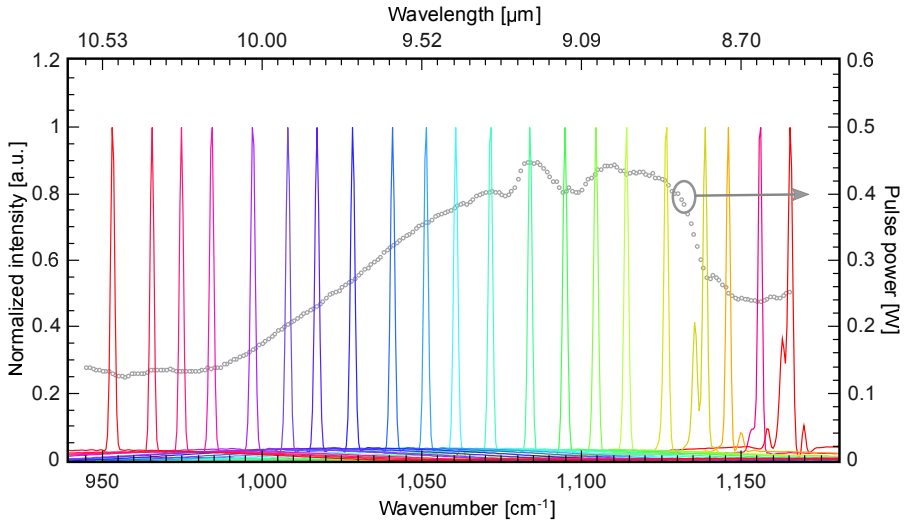

Figure 5.27: Lasing mode spectra corresponding tuning wavenumber and P–ν spectrum of our Littrow-type EC-QCL system

QCL realized by bent waveguide structure. We achieved further reduction of the residual reflection with an additional broadband multilayer AR coating on the angled facet. We achieved good tuning over 230 cm^{-1} range and 0.45 W as the pulse power in our EC performance. Overall, the output power is still limited due to the zero-th order diffraction in the Littrow configuration. Meanwhile, this broad tuning performance and relatively high pulse power may find many mid-IR applications, and especially suits for imaging application in the mid-IR.

Chapter 6

Intra-cavity out-coupling EC-QCL

In this chapter, we describe an external-cavity quantum cascade laser with an intra-cavity out-coupling optical system, tunable from 8.4 μm to 10.8 μm. The new optical configuration allows higher output power compared to a conventional Littrow-type external cavity approach, while keeping the broad tunability of wavelength. We achieved 1 W output power at the maximum in pulse-mode operation, which is more than twice the optical power using the Littrow design with the same gain chip. This section is reported in Ref. 138.

6.1 Introduction

One of the most important applications of infrared technology is vibrational mode molecular spectroscopy. The 8–14μm part of the mid-infrared wavelength range is especially interesting due to many molecular species having characteristic absorption lines that allow detailed analysis. For most such applications, the external cavity quantum cascade laser (EC-QCL) is quite advantageous as a light source in order to enhance the measurement sensitivity, and the measurement through-put because of the coherence of the light, the wide and fast tunability, and the compactness of the system compared to

conventional mid-infrared light sources [7, 28]. These features allow a higher optical signal-to-noise ratio, wider spectrum in the measurement, and easy handling for various type of system integration. Research and development of today on EC-QCLs are now being focused for further improvements of the laser performance from various aspects.

Because of the progress made in QCLs, today it is the quality of the anti-reflection (AR) coating on laser facet that determines EC laser performance. Lower residual reflectivity on the laser facet is essential for higher output power and broader tuning range of an EC system. For the longer wavelength part of the mid-infrared region, however, it is difficult to fabricate a high performance AR coating on a laser facet [47, 101, 118, 139], since we are limited in the number of materials with an appropriate index and low loss for designing coatings. In addition, coatings typically have thickness of several micrometers, resulting in flaking and delaminating during coating process.

In a typical EC-QCL system, the output power is limited due to the blaze grating used in the Littrow configuration, since most of the power is kept in the optical resonator. The output power is determined by non-Littrow condition reflection, i.e., the zeroth order diffraction light, thus normally about less than 10% of the amplified optical power. Littrow configuration with backside extraction is an alternative configuration to maximize the output power and is mostly used in the community and commercial products [139, 140, 141], however resulting in a narrower tuning range. Ring external cavity configuration can keep the light inside the cavity and can also maximize the optical power and the tuning range [142]. Drawback of this system is its system complexity, therefore difficult to build as a robust and compact module for practical applications. In addition, a various type of tunable QCL are demonstrated [31, 143, 144]. Such devices, however, requires high levels of processing instruments as well as high environmental stability.

In this chapter, we propose a new optical configuration for further improvement in the external cavity quantum cascade laser performance. By placing a beam splitter inside the optical cavity, we extract much more power directly from the resonating system; we refer to this configuration as an intra-cavity out-coupling external cavity (Intra-EC). We built an EC-QCL system that can be configured either as a conventional Littrow or an Intra-EC system. We demonstrate an Intra-EC system as well as Littrow-type EC-QCL, by comparing the two laser performances.

6.2 Issue of Littrow-type laser

As mentioned above, the output of Littrow-type EC-QCL is still limited due to the commercial grating performance, which are optimized for Littrow direction reflection, and not for the other order diffractions. Figure 6.1-(a) shows a typical commercial grating performance, and (b) shows a schematic image of grating performance. The reflection efficiency to the Littrow direction is over 90% within the designed wavelength. Backside extraction type can overcome issue in terms of power limitation, while the tunability becomes a new issue. These gaps are due to the mirror loss of the optical cavity. In the case of front-side extraction, the fixed mirror loss is about 0 cm^{-1} by the HR coating on the laser facet. In backside extraction follows $1/2L \ln 1/R_0$, where $R_0 \sim 0.29$.

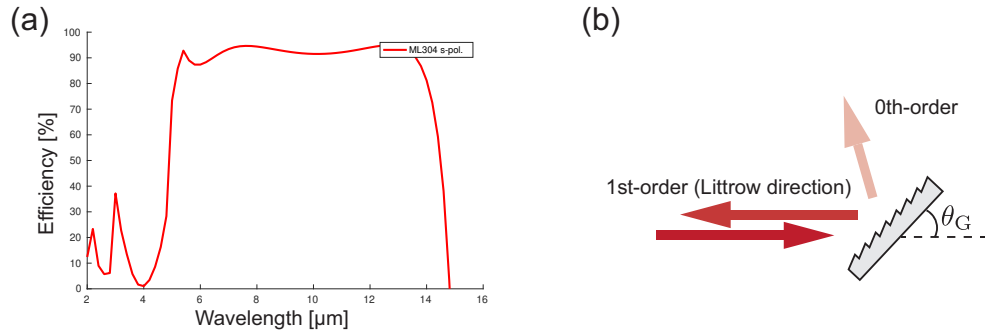

Figure 6.1: Commercial grating performance: grating is optimized for the Littrow direction reflection. The zoro-th order diffraction is less than 10%.

Therefore, a new optical configuration needs to be considered, which fits between the front-side extraction and backside extraction type in terms of the optical loss. Intra-cavity out-coupling EC-QCL is proposed during this work.

6.3 Principle

Due to Fresnel reflection law, a reflection relates to a incident angle of light and a refractive index of a substrate [1], written as,

$$R_p(\theta_i) = \left| \frac{n_s \cos\theta_{i'} - n_{air} \cos\theta_i}{n_s \cos\theta_{i'} + n_{air} \cos\theta_i} \right|^2, \qquad R_s(\theta_i) = \left| \frac{n_{air} \cos\theta_{i'} - n_s \cos\theta_i}{n_s \cos\theta_i + n_{air} \cos\theta_{i'}} \right|^2 \quad (6.1)$$

Here, n_{air} and n_s is the refractive index of air and a substrate, respectively. θ_i is the incident angle and $\theta_{i'}$ is the refraction angle in the substrate, which

are connected by Snell's law, $n_s \sin\theta_{i'} = n_{air} \sin\theta_i$. Thus, by changing the angle of the substrate, it is possible to tune the reflection, equivalently the output power, without any loss when a transparent substrate is used in the resonance cavity of a laser system. One of the merits of this new optical configuration is loss tuning by adjusting the angle of a beam splitter, equivalently tuning the mirror loss of external cavity. Normally modifying the loss can be accomplished through the use of a partial reflective (PR) coating on laser facets. Using the beam splitter allows the output power and its associated loss to be an adjustable parameter.

Compared to the backside extraction Littrow-type, Intra-EC enables to tune the optical loss more easily rather than applying a partial reflective (PR) coating on extraction side facet, since the optical loss is determined by the reflection of the external cavity part. To adjust the reflection, we can change by means of the angle of the beam splitter as well as the materials of the splitter inside the optical cavity. Moreover, the resulting optical loss determined by the splitter's angle is insensitive to the wavelength due to its low dispersion of optical constants, while the PR coating is, in general, wavelength sensitive. Figure 6.2 shows the reflection dispersion to the incident angle of light. Since germanium has a higher refractive constant ($n_{\mathrm{Ge}} \sim 4.0$), then should give more power than indium phosphide substrate ($n_{\mathrm{InP}} \sim 3.0$).

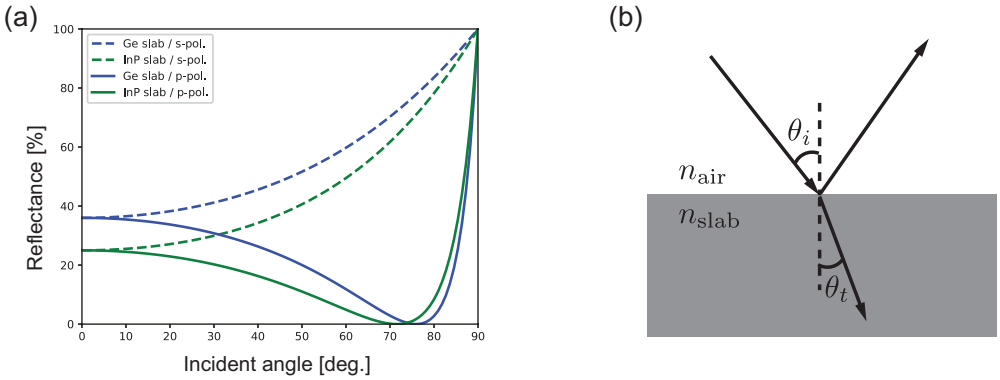

Figure 6.2: (a)Reflectance with different polarizations from InP substrate ($n_{\mathrm{InP}} = 3.0$) and Ge substrate ($n_{\mathrm{Ge}} = 4.0$), and schematic image of incident and reflection rays.

As mentioned above, both polarizations can be used in Intra-EC system. In our system, we designed the system for p-polarized light. The optical configuration of Intra-EC system is depicted in Fig. 6.3-(b), together with a Littrow configuration (Fig.6.3-(a)). Unlike that the Littrow-type system

has a beam walk-off during the grating tuning, Intra-EC system has a fixed beam output.

6.4 System setup

Here the details of our tailor-made Intra-EC system are described.

6.4.1 QCL sample

The QCL structure was grown lattice-matched to an InP substrate using gas-source molecular beam epitaxy (GS-MBE). The structure comprising InGaAs/InAlAs hetero-system is designed for a broad gain spectrum, and is similar to that reported in Ref.53. The sample was processed, and prepared with 6 mm length and mounted on an aluminum nitride plate in epilayer-down. The laser facet was coated with high-reflective (HR) and anti-reflective (AR) coating. The laser chips with 0.75% residual reflectance was set in an optical cavity together with a collimating lens and a blaze grating.

6.4.2 Optical components and assembly

The schematic images of the intra-EC and Littrow-EC configurations are depicted in Fig. 6.3. The intra-EC system includes two gold (Au) plated mirrors and a beam splitter with a multilayer anti-reflection (AR) coating coated on a double-side polished indium phosphide (InP) substrate with thickness of 0.5 mm, and as in Littrow-type laser, a laser chip, a collimated lens and a diffraction grating. The InP substrates we used for a beam splitter were Fe-doped, and the resistivity was over 1.0×10^7 Ωcm. The gain chip was prepared with 6.0 mm. The waveguide structure was made by wet-etching, and the central width of active region was 35 μm, which was optimized for a single lobe beam profile.

Laser system was manufactured by a workshop at Humboldt-Universität zu Berlin. Figure.6.4 shows pictures of 3D-CAD design and our system. The system was designed for both optical configurations,a conventional Littrow-type (Fig. 6.4-(a)) and Intra-EC (Fig. 6.4-(b)), and can be easily switched by setting the mirrors and the beam splitter. The core components, the grating and the QCL modules are fixed. In this work, the beam splitter was set at 30° to the beam path, which gives a 20% reflection from the cavity. Our system size is relatively compact at $20\times10\times8$ cm^3 including some electronics and the motor; the optics part is $9\times7\times6$ cm^3. All the other optics including the holders are fabricated in our group, except the optical grating (Fig. 6.4-(c)).

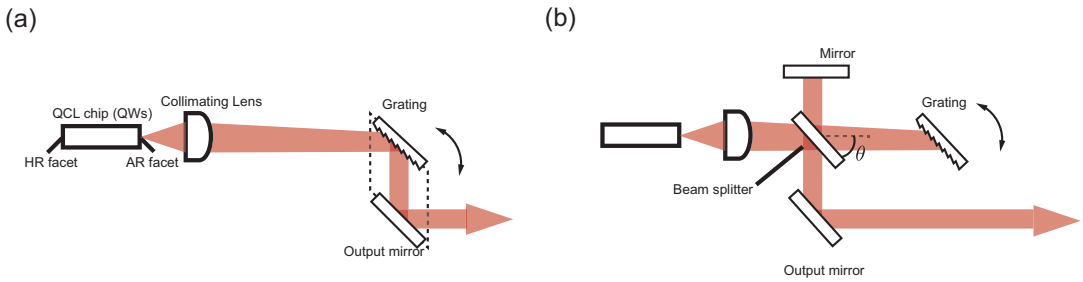

Figure 6.3: Optical configuration of EC-QCLs; (a) Intracavity outcoupling configuration and (b) Littrow configuration .

The beam splitter was AR-coated. The AR coating design was optimized to cover the entire laser's tuning range, 8.0–12 μm, and was fabricated using electron-beam evaporation with yttrium fluoride (YF_3), zinc sulfide (ZnS), and germanium (Ge). The front facet of the laser chip was also similarly AR-coated. The details of the AR coating layout and fabrication process are described in Ref. 101.

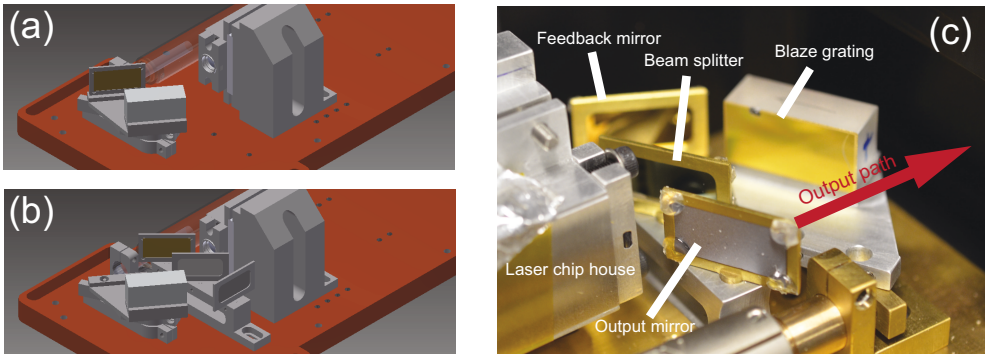

Figure 6.4: 3D-CAD images of our tailor-made system (a) and (b), and a picture of the Intra-EC optics parts (b): The system is designed for both optical configurations, and easily switchable. All the optics including the holders are tailor-made, and fabricated in our group, except the grating.

6.5 Laser performance

6.5.1 *P-I* characteristics

Power-current (*P-I*) measurements were carried out using the same QCL gain-chip with different optical configurations. The results are shown in Fig. 6.5. All the lasers were driven at the same condition; 0.4% duty cycled pulse mode at 18°C chip temperature. Facet-coated Fabry-Perót (FP) mode was also operated at the same current range as the EC configurations. The power of FP mode increases linearly and gives 2.75 W pulse power at 13.4 A, which is not depicted in the figure. For the intra-EC, the beam splitter was set at 30° and determined the output power. We clearly see the lower threshold current density for lasing in both external cavity (EC) modes than Fabry-Perót mode operation. The intra-EC mode exhibits a higher slope efficiency than the Littrow configuration, while maintaining a similar threshold current. The intra-EC and Littrow-EC exhibited almost the same threshold current for lasing. The threshold current density is given by

$$J_{\text{th}} = \frac{\left[2L\alpha_w + \ln\left(\frac{1}{RF}\right)\right]}{2Lg\Gamma}, \tag{6.2}$$

where $g\Gamma$ is the gain including optical confinement factor, α_w is the waveguide loss, L is the gain length, F is the feedback coupling factor, and R is the reflectance of the system due to the beam splitter. The feedback coupling factor is the overlap of the waveguide mode of the gain-chip and the reflected beam. The value of F depends on the mode structure, the focus, and the optical alignment. A lower value of R results in greater out-coupled light. If the only loss mechanisms were waveguide losses and the out-coupled light, we would expect the intra-EC laser to have a higher threshold current density. However, F is generally around 30% and can be higher or lower in a given configuration [41]. Thus, it difficult to predict the product RF. Further, J_{th} depends on both only logarithmically, so not very much variation is expected in J_{th}.

6.5.2 Tuning performance

Tuning spectra and the power spectrum along wavenumber of the intra-EC configuration were measured by rotating the grating. We applied a current of 13 A for this measurement, which is a optimum value for single mode operation in the tuning performance. The higher current causes parasitic oscillations. As can be seen in Fig. 6.6, we achieved the single mode tuning from to 880 cm^{-1} to 1200 cm^{-1}. The power spectra from both laser systems

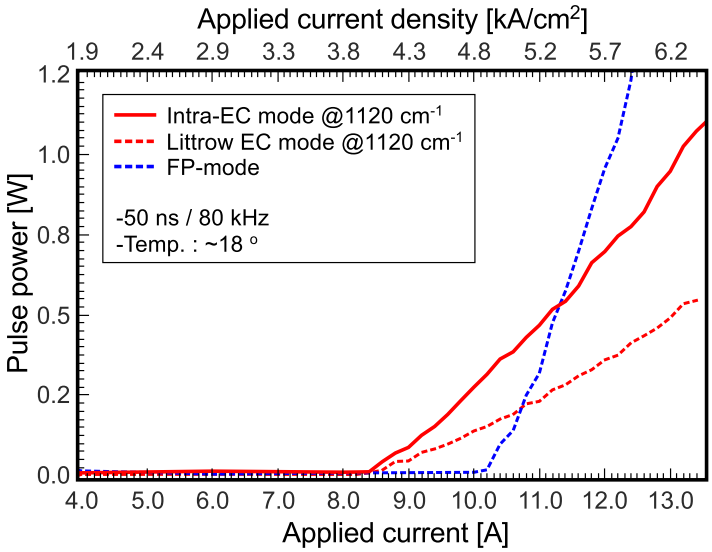

Figure 6.5: P-I curves at 1120 cm^{-1} of EC-QCL systems for the comparison of Littrow configuration, Red solid line represents intra-EC mode and red dash line is of the Littrow-type EC-mode. Blue line is of HR- and AR-coated FP-mode.

reveal that the output power increases more than twice in the range when the intra-EC is applied. Achieved maximum pulse power was 1 W at 1080 cm^{-1}, and the second peak was also observed at 960 cm^{-1}, which was absent in the Littrow-type EC performance. Since the intra-EC configuration forms an interferometer consisting of the feedback mirror and the beam splitter, the laser beam interferes at the out-coupling path. Since the intensity of out-coupled light can be expressed as $I_{\mathrm{out}}^{\mathrm{Intra}} = \alpha I_0 + \beta I_0 + 2\sqrt{\alpha\beta} I_0 \cos\phi$, the intensity modulation from Littrow-type laser is written as,

$$I_{\mathrm{out}}^{\mathrm{Intra}} / I_{out}^{\mathrm{Littrow}} = \frac{1}{1-\eta_g}\left(\alpha + \beta + 2\sqrt{\alpha\beta}\cos\phi\right), \tag{6.3}$$

where I_0 is the light intensity kept inside the optical cavity, and α is the reflectance of the beam splitter, β is the intensity of feedback light, ϕ is the phase shift due to the grating. η_g is the grating efficiency towards the Littrow direction. Here, α can be R_{InP} ~0.2 as a Fresnel reflection of InP substrate, $\beta = R_{\mathrm{mirror}} R_{\mathrm{InP}} (1 - R_{\mathrm{InP}})$ ~0.15. Considering the grating efficiency we used has $1 - \eta_g \sim 0.1$, the maximum modulated power can reach up to 7.5 times compared to Littrow-type. This can be seen at around 950 cm^{-1}. Small fringes in the power spectrum were observed at some parts of intra-EC tuning performance, on the other hand, Littrow-type tuning does not show such

power fluctuations. This is due to the interference by the beam splitter.

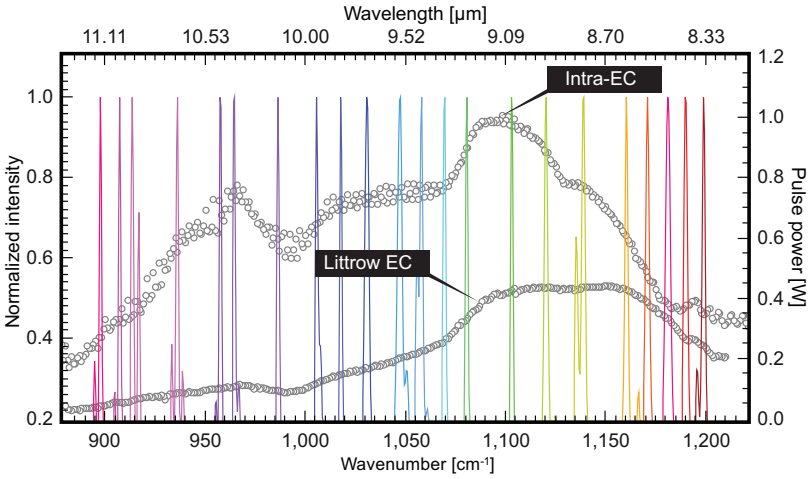

Figure 6.6: Tuning spectra of intra-EC type QCL, measured with FTIR and power spectrum of intra-EC and Littrow-type configuration under 13 A applied current on the QCL chip. Tuning range of both configuration: $\sim \Delta 320$ cm^{-1}.

We also investigate the mode separation mechanism in the intra-EC configuration. The power spectrum was Fourier-transformed from the range of 1110 cm^{-1} to 1180 cm^{-1}. Figure. 6.7 shows the frequency spectrum. Different contributions for the power fluctuation can be clearly seen. The mode frequency corresponds well with the mode separation calculated from each contributions. The Fabry-Perót (FP) mode is due to the mode hopping effect and determined by $1/\Delta_{\mathrm{FP}} = 2n_{\mathrm{QCL}}l_{\mathrm{QCL}} = 3.96$ cm. Beam splitter (BS) mode is due to the interference of InP substrate. The separation frequency is calculated by $1/\Delta_{\mathrm{BS}} = 2n_{\mathrm{InP}}L_{\mathrm{Slab}}/\cos\theta_{\mathrm{BS}} = 0.35$ cm. This mode affects only to the power fringes, but not to the lasing modes. Higher performance AR coating on the beam splitter can reduce this effect. The AR-coated collimating lens used in our system has a 3.0 mm thickness as the maximum, and contributes for a 2.0 cm peak. Since pure EC mode fluctuations may have a $1/\Delta_{EC} = 2(n_{\mathrm{QCL}}l_{\mathrm{QCL}} + L_{\mathrm{EC}})$ ~12 cm peak, the distribution around from 5 cm to 7 cm is considered as coexisted fluctuations of the FP and EC modes ($1/\Delta_{\mathrm{FP+EC}}$), in other words, intermediate hopping effects between FP modes and EC modes. This instability of mode hopping can be improved either by using a longer pulsed or continuous-wave operated chip, or with a better AR coating on the laser facet.

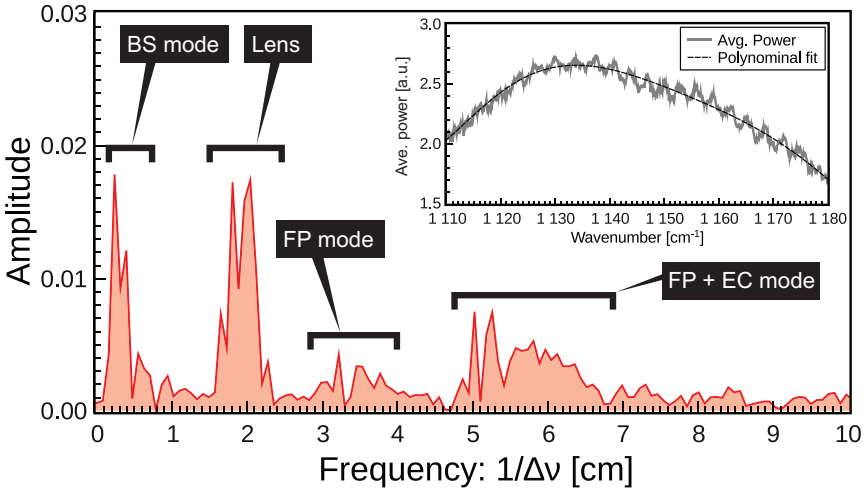

Figure 6.7: Frequency spectum of power fluctuation in intra-EC mode. Inserted graph is the power spectrum; $1/\Delta_{\mathrm{FP}} = 3.96$ cm is due to FP mode effect and $1/\Delta_{\mathrm{BS}} = 0.34$ cm is due to the interference of beam splitter. A contribution from the colllimating lens can be seen at 2.0 cm.

6.6 Absorption demonstration

We demonstrated the tuning performance by measuring ammonia (NH_3) absorption. Figure 6.8 shows the absorption spectrum together with HITRAN data convoluted by using Voigt model. Ammonia solution (∼25%) is set below the optical path between an AR-coated Ge window of our system and a power meter without any purge. The 5000 data were sampled and averaged for each set wavenumbers, For the spectrum measurement, the grating was coarsely tuned with 0.25 cm^{-1} steps. The absorption lines were well resolved with the coarse tuning, achieving around 2.0 cm^{-1} resolution. The inserted spectrum in Fig. 6.8 around 1122 cm^{-1} was measured with smaller motor steps, $\Delta\nu = 0.05$ cm^{-1}, aimed for higher resolution. This results tells the resolution is at least 0.85 cm^{-1} from FWHW of the corresponding peak compared with HITRAN profile. By taking into account the contributions of power fluctuations, the maximum resolution of our system is mainly limited by the simultaneous fluctuation between the neighboring three to six lasing FP modes or FP+EC modes for some parts, and not affected by the beam splitter, $\Delta_{\mathrm{BS}} = 2.94$ cm^{-1}. A CW operation would improve the resolution further since the heat generation of gain chip would be stabilized during the operation.

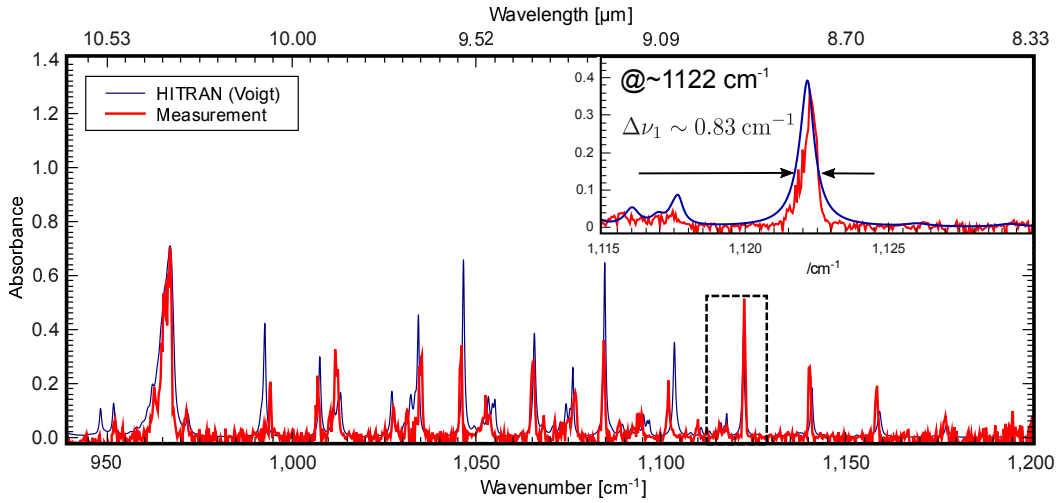

Figure 6.8: Ammonia absorption spectrum measured with Intra-EC system (red line), Hitran database (black dash line), and power spectrum of our laser system (solid gray line).

6.7 Summary

We demonstrated and characterized an EC-QCL based on intra-cavity out-coupling quantum cascade laser. This configuration almost doubled the output power compared to the conventional Littrow configuration with the same QCL gain medium, while maintaining the tunability and resolution. We achieved 1 W pulse power and demonstrated that the tuning performance is quite useful for molecular vibration spectroscopy.

Chapter 7

Conclusions and perspectives

This PhD work was devoted for the study and development of external cavity quantum cascade lasers and we presented the details in this thesis. The series of theoretical and experimental demonstrations are organized mainly for the manufacturing purposes as a part of laser engineering. Meanwhile, the knowledge gained from our experience were also integrated into every part. Overall, the presented outputs would be practically helpful for any parts of EC laser developments, especially in the mid-IR laser community.

We started with theoretical investigations on quantum cascade laser and external cavity laser, and these studies gave us a broad scope on the laser development from various aspects. The optical amplifier (QCLs) is the core part of EC laser system, and the optimization would lead the bottom-up of the laser performance in the external cavity form. To achieve this, we have carried out the series of experiments from QCL growth to facet coatings. Remarkable demonstrations in the part of QCL fabrication were (1) demonstration of high performance AR coating by dielectric coating approach, (2) low-loss broadband QCL growth, and (3) angled facet waveguide. From these achievements, we were constantly able to achieve $R < 1\%$ as the final reflection covering over the entire broad spectra of gain chips with ~ 5.0 cm^{-1} waveguide loss on average, and this demonstration can give a good scope on the chip manufacturing for the EC use.

Alongside these works, we have proposed the new concept of multilayer anti-reflection coating for the mid-IR range. To overcome its difficulty of fabricating due to the material limitation as well as its mechanical issues of layers in such a longer wavelength range, we utilized a classical design concept by combining the sub-wavelength effect. The coating demonstrated the high reduction of reflection and good robustness against thickness errors.

Although this coating model would be useful for many mid-IR applications, these properties best suit for QCL facet coatings.

One of our goals was to develop laser systems during this PhD work. The work was staged in two steps by accomplishing totally three systems; Prototype and New-model. Prototype is of Littrow-type and New model is transformable for two different configurations. Prototype was developed during the first year of my doctorate study, The achieved tuning range covers the 11 μm range and the setup was delivered as a work package of this PhD project (Mid-TECH). With this system, we demonstrated a mid-IR imaging of human tissue samples as a part of a collaboration experiment with our project partner. The captured images at 11 μm gave the conclusion that the quality of the experiments still needs to be improved by means of laser's specification. From this experience, we have gained practical knowledge regarding EC lasers and fed back to the next generation; New-model. The motivation for the device improvement also triggered further investigations regarding an AR-coating and a gain chip, which were described in Chapter 3 and Chapter 4. New model is capable to transform two configurations; the conventional type of Littrow laser and Intra-cavity out-coupling EC laser, which were presented in Chapter 5 and Chapter 6, respectively. With these systems, we have gain quite good improvements in every aspect compared to Prototype, achieving the tuning from 820-1170 cm^{-1}, and $\sim$ 1.0 W as the maximum pulse power.

For the future work, a heterostructure gain designing should be addressed. The broadness of laser system is determined by the spectral width of gain region, and this approach promisingly helps for a broader tuning. Filter-tuned laser would be also an interesting approach, which allows a better coupling in external cavity system compared to Littrow-type lasers. Adding to these, more compact and less cost for manufacturing would be possible with IF configuration. The EC-QCL is quite useful and has a great potential as a standard tunable light source of mid-IR range, our work would contribute for the industrial and research community, and ultimately for our society.

Appendix A

Process details

During this work, we have processed all the laser samples in our group. Photoresist development is the key part of semiconductor processing. Here we briefly describe the properties of photoresists used during this work.

A.1 Plasma etching of SiO_2

Plasma etching is a form of plasma processing, which is commonly used for nano and micro scale structure fabrication. Since reactive ion etching (RIE), i.e., selective ion etching, achieves high anisotropic and selective structure process, the technique is the standard processing technique in modern semiconductor industry.

During this work, silicon dioxide (SiO_2) etching has been carried out for contact window opening[1]. In this work, we used fluorocarbon (CH_4) gas for selective silicon dioxide etching. The series of the reactions are as follows,

$$CF_4 \rightarrow CF_3 + F + e^- \quad \text{(A.1)}$$

$$SiO_2 + 4F \rightarrow SiF_4 + O_2 \quad \text{(A.2)}$$

$$CH_4 + H + Si \rightarrow CH_xF_y \quad \text{(A.3)}$$

First, fluoric-radicals are formed by the impact ionization (Eq. (A.1)). Secondly volatile silicon compounds are formed from the silicon dioxide and produce the fluoric-radicals (Eq. (A.2)).

[1]As well known that SiO_2 etching is also chemically possible by using hydro-fluoride (HF) solution. This etching process obviously requires a great attention in manipulating the solution as well as in the actual etching the process.

During the actual process, as in Eq. (A.3), non-volatile fluorocarbon polymer (CH_xF_y) is also formed on the surface, as in Fig. A.1-(a). This polymer is usually aimed for the perpendicular sidewall coverage for anisotropic etching with high aspect ratio, known as "*Bosch Process*". Supplying additional oxygen during the process reduces this polymer formation, but also cause lower selectivity in etching materials. To keep high aspect ratio in etching, plasma oxidation helps to avoid unintentional polymerization on the surface or inhomogeneity in etching [145].

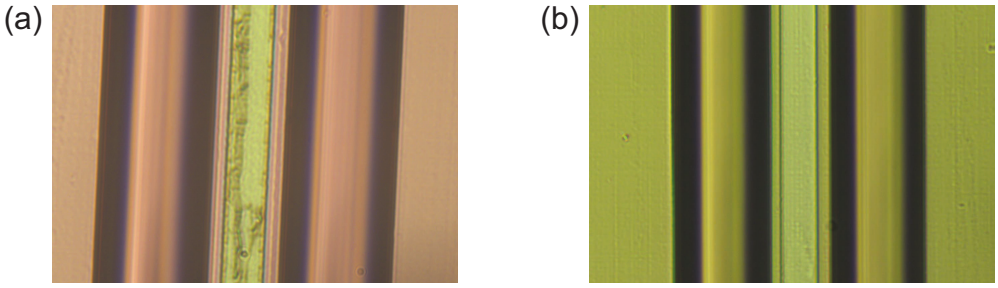

Figure A.1: QCL stripe before and after plasma oxidation: (a) shows a contact window for laser operation. The dendrite part on the window is considered fluorocarbon polymer formed during the dry etching. After plasma oxidation the dendrite part was removed (Fig. (b)).

This oxidation cleaning is a keen process for the next step; gold contact by thermal evaporation, since the residual polymer results in the high resistance, or non-electrical contact in the worst case.

A.2 Liftoff process and softening effect

During this work, we used liftoff process for metallization and also for insulating layer deposition. For successful processing, we exploited the photoresist properties with a number of test samples. The details of liftoff and photoresist properties are described in this section.

A.2.1 Liftoff process

Metallization is one of the semicondutor processing techniques, and used for electric interconnection of the circuit such as very large scale integrate (VLSI) and system on chip (SoC). Generally, electron beam (e-beam) and thermal evaporation are used for metal deposition, since these evaporation techniques enables high anisotropic deposition of the material on the surface. On the other hand, isotropic deposition can be achieved by sputtering deposition, but results in a bombardment of photoresist during the process and destroys the developed profile.

For liftoff process, negative offcut is required in the photoresist profile after the development. The angles of the offcuts strongly depends on the development time, as shown in Fig. B.1 (ma-N440, micro resist technology GmbH, Germany). We can clearly see the development time dependencies of the offcut angles.

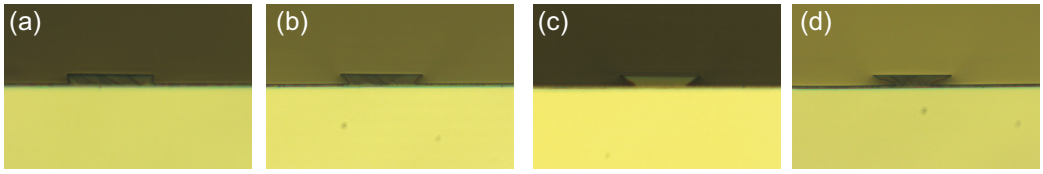

Figure A.2: Time dependence of photoresist development: the pictures show the different negative offcut angles of the photoresist (ma-N440) with different development times. (a) is for 3'40", (b) 5'40", (c) 7'40", and (d) 9'40".

A.2.2 Softening effects of photoresist

Generally, positive photoresist has high reflective index due to high density of polymer. Because of its low melting point, the photoresist exhibits softening (rounding) effect at certain baking temperature, which affects the offcut profiles. We also tested the melting effect due to the different baking temperature, in order to see the photoresist behavior during the processing.

Figure.A.3 shows examples of ma-N440 (Micro Resist Technology. GmbH, Germany). The photoresist were baked with different temperature to check the melting point. The melting point of ma-N440 is from 105°C to 110°C, which agreed with the company's suggestion.[2].

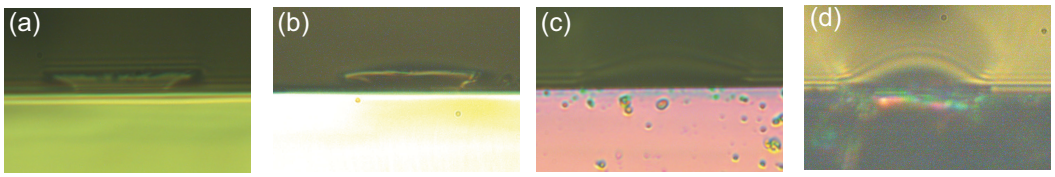

Figure A.3: Pictures of photoresists, ma-N440 after baking in different temperatures: profiles after baked at 70°, (b) at 100°C, (c) at 110°C, and (d) at 120°C. At 110°, the photoresist starts to exhibit melting effect.

[2]Communication with Dr. A. Voigt, Micro Resis Technology. Inc., Germany

Appendix B

Coating process on laser facets

Coating process of laser facets are explained. This section mainly describes the coating procedure. The ultimate goal of this section is to share the know-hows, which the author gained during this work.

B.1 Preparation of sample

The performance of HR- and AR-coatings are evaluated from P–I characteristics of QCL chips. In order to minimized the error factors during the measurements, P–I performances of QCL chip should be recorded in the same electric contact condition. For this aim, a QCL chip is to be mounted on a ceramic plate and wired by soldering. The small differences in the contact resistance might affect to the laser performance, and ultimately affect to the results of coating performance.

B.2 AR-coating process

The following is the details of coating process. The important parts are stylized in **bold** format.

1. Fix the sample to the sample stage, and cover with a Capton tape so that the deposition on the extra area can be avoided.

2. Run a plasma oxidation for 5 mins with **50 W from power supply**. **More power gives a heat to the stage, and melt the solder of the laser chip.**

3. Set the sample stage in the evaporator chamber, and start evacuation. **This process should be done very quickly to avoid water vapour adhesion on the laser facet**. The experimenter should avoid the exposure of the sample from the breath.

4. After reaching a certain vacuum condition, ($\sim 5.0\times10^{-5}$ Torr), start to heat the sample stage upto 100°C. This temperature is for good deposition, and also due to the melting point of indium solder. Wait at least for an hour for the desorption.

5. Meanwhile, pre-melt all the deposition materials to remove possible residual water from the materials. **Especially powder materials such as yttrium fluoride (YF_3) and ytterbium fluoride (YbF_3) requires this pre-condition.**

6. Deposit the materials. During the deposition, the stage must be rotated for homogeneous coating.

7. Pose for an hour after completing the deposition. This process is to reach the equilibrium state of the coating in the given environmental condition.

8. Cool down the sample stage with 0.3°C/min to 25°C. Slower speed might also effective.

9. **Start ventilation and wait at least for an hour till opening the chamber.** This process is to avoid a sudden pressure change, which might cause the delamination of the coating. For thicker coating system, this process is crucial and the experimenter had many failures at this step, otherwise can be skipped.

10. Take out the sample stage and remove the sample. A sudden temperature change of the sample stage should be avoided.

Figure B.1 shows QCL facets of as-cleaved (a) and AR-coated (b) facets. From Fig. B.1-(a), one can clearly see the active region of QCL facet. AR-coated facet shown in Fig. B.1-(b), however, does not have such a clear appearance of active region but the colored surface. The main picture is of ZnS / Ge / ZnS / YF_3 layout coating and the inserted is of ZnS / Ge / ZnS / YbF_3 layout coating. As can be seen from the two pictures, the coating with YbF_3 has small visible dots on the surface. From these results, use of YF_3 is obviously preferred for a homogeneous coating, while the absorption is slightly higher at around 10 μm and become crucial at the longer wavelength when YF_3 is used.

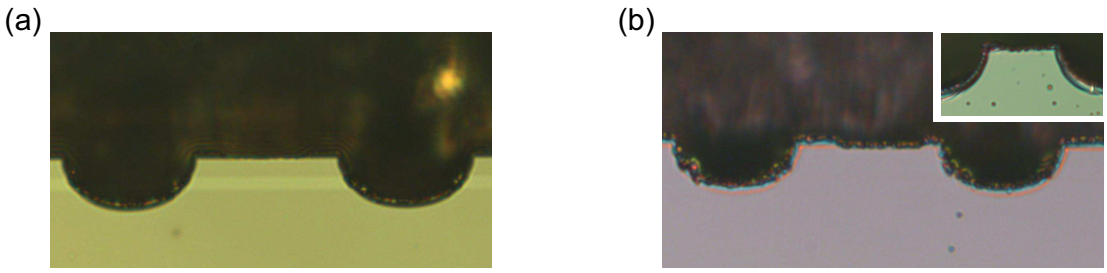

Figure B.1: Pictures of bare (a)/ AR-coated facets (b); The main picture is of ZnS / Ge / ZnS / YF_3 layout coating and the inserted is of ZnS / Ge / ZnS / YbF_3 layout coating.

B.3 HR-coating process

For some application, HR-coating is required for power enhancement. The process details are written.

1. Dielectric coating in the same procedure of AR-coating, but only a single layer, such as yttrium fluoride (YF_3) for the longer wavelength, and silicon dioxide (SiO_2) for the shorter range.

2. Cover the waveguide facet by aluminium scotch tape.

3. Set in the thermal evaporator. Evaporate 20 nm chromium (Cr) and over 200 nm gold (Au). This thick gold deposition is to avoid the evanescence effect of the light. Due to the penetration of the light with longer wavelength, some light possibly escape through the coating.

Appendix C

Codes for coating optimization program

The source codes for anti-reflection coating optimization were written in Mathematica.

C.1 Optimization of AR coatings

Source codes for AR coating is written in Mathematica. The optimization method is automatically selected from the program. For the calculation, nk-data are to be prepared in the separate directory. The program has been developed from the one in Ref. 65

C.1.1 Two layer system

```
1  (*clear data parameters*)
2  Clear[d1, d2, d3]
3  Clear[ x, x0, DataMatrix, delta, WaveLength, IncidentAngle, R, \
4  LayerThickness ]
5  (*clear optical constant database set*)
6  Clear[ nkdataYF3, nkdataZnSe, \
7  nkdataY2O3 , nkdataCdTe, nkdataGe, nkdataZnS, nkdataCu2O ]
8
9  IncidentAngle = 0; (*incident angle of ray*)
10
11 (*defining the refractive index of base-material*)
```

```
ns = 3.0;
nair = 1.0; (*air*)

(*setting for wavelength*)
StartWavelength = 8.0;
EndWavelength = 11.0;
deltaWavelength = 0.01 ;(*delta of data plot micrometer*)

WaveRange = ( EndWavelength - StartWavelength ) /deltaWavelength ;
WaveLength = Table[ StartWavelength + deltaWavelength*i, {i,0,WaveRange}];

(*setting for nk data loading*)
SetDirectory[NotebookDirectory[]];
nkdataZnS =
  Import["../../parameters/nk_ZnS.dat",
   "Table"];(*import nk data of ZnS *)

nkdataGe =
  Import["../../parameters/nk_Ge.dat",
   "Table"];(*import nk data of Ge *)

nkdataY2O3 =
  Import["../../parameters/nk_Y2O3.dat",
   "Table"];(*import nk data of Y2O3 *)

nkdataYF3 =
  Import["../../parameters/nk_YF3.dat",
   "Table"];(*import nk data of YF3 *)


(*structure definition*)
DataMatrix = Table[ {0 , 0, nair}, {s, 1, Length[WaveLength]}];

(*for intermediate value calculation*)
nrefCalc[w_, a_, b_, c_, d_] := (d - b)/(c - a)*w + (b*c - a*d)/(c - a);

Do[
  Do[
   If[
    WaveLength[[k]] >= nkdataYF3[[i, 1]] &&
     WaveLength[[k]] < nkdataYF3[[i + 1, 1]],
    DataMatrix[[k, 1]] =
     nrefCalc[WaveLength[[k]], nkdataYF3[[i, 1]], nkdataYF3[[i, 2]],
       nkdataYF3[[i + 1, 1]], nkdataYF3[[i + 1, 2]]]
```

```
     + I nrefCalc[WaveLength[[k]], nkdataYF3[[i, 1]],
       nkdataYF3[[i, 3]], nkdataYF3[[i + 1, 1]],
       nkdataYF3[[i + 1, 3]]]
    ]
   , {i, 1, Length[nkdataYF3] - 1}
   ]
  , {k, 1, Length[WaveLength]}
  ];

Do[
  Do[
   If[
    WaveLength[[k]] >= nkdataZnS[[i, 1]] &&
     WaveLength[[k]] < nkdataZnS[[i + 1, 1]],
    DataMatrix[[k, 2]] =
     nrefCalc[WaveLength[[k]], nkdataZnS[[i, 1]], nkdataZnS[[i, 2]],
      nkdataZnS[[i + 1, 1]], nkdataZnS[[i + 1, 2]]]
     + I nrefCalc[WaveLength[[k]], nkdataZnS[[i, 1]],
       nkdataZnS[[i, 3]], nkdataZnS[[i + 1, 1]],
       nkdataZnS[[i + 1, 3]]]
    ]
   , {i, 1, Length[nkdataZnS] - 1}
   ]
  , {k, 1, Length[WaveLength]}
  ];

LayerThickness = { d1, d2, d3 };

(*Phase shift*)
delta = Table[{
    2*Pi/WaveLength[[j]] Cos[2 Pi/360 IncidentAngle ] DataMatrix[[
      j]]  LayerThickness }, {j, 1, Length[WaveLength]}];

(*transmittance of each layer*)
tr[j_, i_] :=
  2 If[ i <= Length[Transpose[DataMatrix]], DataMatrix[[j, i]],
     nair ]/(If[ i <= Length[Transpose[DataMatrix]],
       DataMatrix[[j, i]], nair] +
      If[ i >= 2, DataMatrix[[j, i - 1]], ns]);

(*reflectance of each layer*)
re[j_, i_] :=
  (If[i <= Length[Transpose[DataMatrix]], DataMatrix[[j, i]], nair] -
     If[i >= 2 , DataMatrix[[j, i - 1]], ns])/(
```

```
100     If[i <= Length[Transpose[DataMatrix]], DataMatrix[[j, i]],
101       nair ] + If[i >= 2, DataMatrix[[j, i - 1]], ns]);
102
103 (*transfer matrix *)
104 M[i_] := Table[
105    1/tr[j, i] {{Exp[-I delta[[j, 1, i]]],
106       re[j, i + 1] Exp[I delta[[j, 1, i]]]}, {
107       re[j, i + 1] Exp[-I delta[[j, 1, i]]],
108       Exp[I delta[[j, 1, i]]] }}
109       ,{j, 1, Length[WaveLength]}
110       ];
111
112 x0 = Table[{1, re[j, 1]}, {j, Length[WaveLength]}];
113 x = Table[
114    1/tr[m, Length[Transpose[DataMatrix]] + 1] x0[[m]]
115    ,{m, 1, Length[WaveLength]}
116    ];
117
118 (*Matrix Value*)
119 Do[
120   Do[
121    x[[j]] = M[i][[j]].x[[j]]
122    , {i, 1, Length[Transpose[DataMatrix]]}
123    ]
124   , {j, 1, Length[WaveLength]}
125   ];
126
127 (*Reflection & Transmssion*)
128 R = Table[Abs[x[[j, 2]]/x[[j, 1]]]^2, {j, 1, Length[WaveLength]}];
129 T = Table[ns/nair Abs[1/x[[j, 1]]]^2, {j, 1, Length[WaveLength]}];
130
131 Print["---------OUTPUT␣SECTION--------------------"]
132 (*Weighting Factors*)
133 a1 = 1.0;
134 a2 = 1.0;
135 a3 = 1.0;
136 a4 = 0.0;
137 a5 = 0.0;
138
139 LayerThickness =
140   LayerThickness /. Last[
141     NMinimize[
142      Hold[
143       a1 Total[R] + a2 Variance[R] + a3 Abs[Max[R] - Min[R]] +
```

```
      a4 Min[R] + a5 Max[R]
     ]
    , {

       (*Restrain conditions for intended designs*)
     0.3 <= d1 && d1 <= 1
      && 0.3 <= d2 && d2 <= 1
      && 50 <= d3

     }, LayerThickness
    ]
   ];

(*LayerThickness data, d1, d2, d3*)
Print["Layer Thicknesses"]
LayerThickness // MatrixForm
d1 = LayerThickness[[1]];
d2 = LayerThickness[[2]];
d3 = LayerThickness[[3]];

(*Reflection data output*)
RefData = Table[{WaveLength[[i]], R[[i]]}, {i, 1, Length[WaveLength]}];
ListPlot[RefData, PlotRange -> {0.0, 0.01},
       AxesLabel -> {"lambda(microns)", "Reflectivity"}]
Export["Reflectivity.dat", RefData];

(*Transmittance data output*)
TransData = Table[{WaveLength[[i]], T[[i]]}, {i, 1, Length[WaveLength]}];
ListPlot[TransData, PlotRange -> {0.7, 1.0},
       AxesLabel -> {"lambda(microns)", "Transmittance"}]
Export["Transmittance.dat", TransData];

(*Parameters for evaluation*)
Print["Integrate Value[-]"]
Total[R]
Print["Variance of Distribution"]
Variance[R]
Print["Abs[maximum - minimum"]
Abs[Max[R] - Min[R]]
Print["maximum"]
Max[R]
Print["minimum"]
Min[R]
```

C.1.2 Four layer system

For four layer system, only the layer definition section and `LayerThickness` are to be modified. The constrain conditions for the optimization should be also adjusted for the target wavelength range. Here some conditions are listed to realized "*quasi Lockhart*" AR-coating designs for 7–12 μm range and 3.8–5.2 μm, however these are just examples.

```
1 LayerThickness = { d1, d2, d3, d4, d5 };
```

C.1.2.1 Constrain for 7–12 μm

```
1 0.1 <= d1 && d1 <= 0.8
2 && 0.01 <= d2 && d2 <= 0.1
3 && 0.1 <= d3 && d3 <= 1.0
4 && 0.1 <= d4 && d4 <= 2.0
5 &&  d5 >= 50
```

C.1.2.2 Constrain for 3.8–5.2 μm

```
1 0.1 <= d1 && d1 <= 0.6
2 && 0.01 <= d2 && d2 <= 0.08
3 && 0.1 <= d3 && d3 <= 0.5
4 && 0.3 <= d4 && d4 <= 1.0
5 &&  d5 >= 50
```

Bibliography

[1] Max Born, Emil Wolf, A. B. Bhatia, P. C. Clemmow, D. Gabor, A. R. Stokes, A. M. Taylor, P. A. Wayman, and W. L. Wilcock. *Principles of Optics: Electromagnetic Theory of Propagation, Interference and Diffraction of Light*. Cambridge University Press, 7 edition, 1999.

[2] Harald Schneider and Hui C. Liu. *Quantum Well Infrared Photodetectors*. Springers, 2010.

[3] Jeppe Seidelin Dam, Peter Tidemand-Lichtenberg, and Christian Pedersen. Room-temperature mid-infrared single-photon spectral imaging. *Nature Photonics*, 6(788), Sep 2012.

[4] P. Tidemand-Lichtenberg, J. S. Dam, H. V. Andersen, L. Høgstedt, and C. Pedersen. Mid-infrared upconversion spectroscopy. *J. Opt. Soc. Am. B*, 33(11):D28–D35, Nov 2016.

[5] R. Kazarinov and R. Suris. Possible amplification of electromagnetic waves in a semiconductor with a superlattice. *Soviet Physics Semiconductors*, 5(4):707–709, 1971.

[6] R. Kazarinov and R. Suris. Electric and electromagnetic properties of semiconductors with a superlattice. *Soviet Physics Semiconductors*, 6(1):120–131, 1972.

[7] Jérôme Faist. *Quantum cascade laser*. Oxford University Press, 2013.

[8] Jerome Faist, Federico Capasso, Deborah L. Sivco, Carlo Sirtori, Albert L. Hutchinson, and Alfred Y. Cho. Quantum cascade laser. *Science*, 264(5158):553–556, 1994.

[9] C. Sirtori, F. Capasso, J. Faist, L. N. Pfeiffer, and K. W. West. Far-infrared radiation ($\lambda = 60$ μm) by difference frequency generation in coupled quantum welis. In *International Quantum Electronics Conference*, page QMB6. Optical Society of America, 1994.

[10] Claire Gmachl, Federico Capasso, Deborah L Sivco, and Alfred Y Cho. Recent progress in quantum cascade lasers and applications. *Reports on Progress in Physics*, 64(11):1533, 2001.

[11] Richard Maulini, Arkadiy Lyakh, Alexei Tsekoun, and C. Kumar N. Patel. λ 7.1 μm quantum cascade lasers with 19% wall-plug efficiency at room temperature. *Opt. Express*, 19(18):17203–17211, Aug 2011.

[12] M. P. Semtsiv, M. Wienold, S. Dressler, and W. T. Masselink. Short-wavelength (λ=3.05 μm) inp-based strain-compensated quantum-cascade laser. *Applied Physics Letters*, 90(5):051111, 2007.

[13] Satoshi Shimomura, Akio Wakejima, Akira Adachi, Yasunori Okamoto, Naokatsu Sano, Kazuo Murase, and Satoshi Hiyamizu. Extremely flat interfaces in gaas/algaas quantum wells grown on gaas (411)a substrates by molecular beam epitaxy. *Japanese Journal of Applied Physics*, 32(12A):L1728, 1993.

[14] M. P. Semtsiv, S. S. Kurlov, D. Alcer, Y. Matsuoka, J.-F. Kischkat, O. Bierwagen, and W. T. Masselink. Reduced interface roughness scattering in ingaas/inalas quantum cascade lasers grown on (411)a inp substrates. *Applied Physics Letters*, 113(12):121110, 2018.

[15] Sangil Ahn, Daniela Ristanic, Roman Gansch, Peter Reininger, Clemens Schwarzer, Donald C. MacFarland, Hermann Detz, Werner Schrenk, and Gottfried Strasser. Quantum cascade lasers with a tilted facet utilizing the inherent polarization purity. *Opt. Express*, 22(21):26294–26301, Oct 2014.

[16] D. Heydari, Y. Bai, N. Bandyopadhyay, S. Slivken, and M. Razeghi. High brightness angled cavity quantum cascade lasers. *Applied Physics Letters*, 106(9):091105, 2015.

[17] Lars Nähle, Julia Semmel, Wolfgang Kaiser, Sven Höfling, and Alfred Forchel. Tapered quantum cascade lasers. *Applied Physics Letters*, 91(18):181122, 2007.

[18] T. Kitada, T. Aoki, I. Watanabe, S. Shimomura, and S. Hiyamizu. Extremely high electron mobility of pseudomorphic $in_{0.74}ga_{0.26}as$ / $in_{0.46}al_{0.54}as$ modulation-doped quantum wells grown on (411)a inp substrates by molecular-beam epitaxy. *Applied Physics Letters*, 85(18):4043–4045, 2004.

[19] D. Alcer, M.P. Semtsiv, and W.T. Masselink. Interface roughness scattering in ingaas/inalas double quantum wells grown on (100) and (411)a inp substrates at different growth temperatures. *Journal of Crystal Growth*, 477:110 – 113, 2017. Proceeding of the 19th International Conference on Molecular Beam Epitaxy.

[20] Sangil Ahn, Clemens Schwarzer, Tobias Zederbauer, Hermann Detz, Aaron M. Andrews, Werner Schrenk, and Gottfried Strasser. Enhanced

light output power of quantum cascade lasers from a tilted front facet. *Opt. Express*, 21(13):15869–15877, Jul 2013.

[21] Sangil Ahn, Clemens Schwarzer, Tobias Zederbauer, Donald C. MacFarland, Hermann Detz, Aaron M. Andrews, Werner Schrenk, and Gottfried Strasser. High-power, low-lateral divergence broad area quantum cascade lasers with a tilted front facet. *Applied Physics Letters*, 104(5):051101, 2014.

[22] www.daylightsolutions.com. `https://www.daylightsolutions.com/`, 2013.

[23] Jérôme Faist, Mattias Beck, Thierry Aellen, and Emilio Gini. Quantum-cascade lasers based on a bound-to-continuum transition. *Applied Physics Letters*, 78(2):147–149, 2001.

[24] A. Wittmann, T. Gresch, E. Gini, L. Hvozdara, N. Hoyler, M. Giovannini, and J. Faist. High-performance bound-to-continuum quantum-cascade lasers for broad-gain applications. *IEEE Journal of Quantum Electronics*, 44(1):36–40, Jan 2008.

[25] Joshua R. Freeman, Anthony Brewer, Julien Madéo, Pierrick Cavalié, Sukhdeep S. Dhillon, Jérôme Tignon, Harvey E. Beere, and David A. Ritchie. Broad gain in a bound-to-continuum quantum cascade laser with heterogeneous active region. *Applied Physics Letters*, 99(24):241108, 2011.

[26] Andreas Hugi, Romain Terazzi, Yargo Bonetti, Andreas Wittmann, Milan Fischer, Mattias Beck, Jérôme Faist, and Emilio Gini. External cavity quantum cascade laser tunable from 7.6 to 11.4 μm. *Applied Physics Letters*, 95(6):061103, 2009.

[27] Kazuue Fujita, Shinichi Furuta, Atsushi Sugiyama, Takahide Ochiai, Akio Ito, Tatsuo Dougakiuchi, Tadataka Edamura, and Masamichi Yamanishi. High-performance quantum cascade lasers with wide electroluminescence (600 cm^{-1}), operating in continuous-wave above 100°c. *Applied Physics Letters*, 98(23):231102, 2011.

[28] Andreas Hugi, Richard Maulini, and Jérôme Faist. External cavity quantum cascade laser. *Semiconductor Science and Technology*, 25(8):083001, 2010.

[29] Feng Xie, C. Caneau, H. Leblanc, M.-T. Ho, and C. Zah. Ultra-broad gain quantum cascade lasers tunable from 6.5 to 10.4 μm. *Opt. Lett.*, 40(17):4158–4161, Sep 2015.

[30] N. Bandyopadhyay, M. Chen, S. Sengupta, S. Slivken, and M. Razeghi. Ultra-broadband quantum cascade laser, tunable over 760 cm^{-1}, with balanced gain. *Opt. Express*, 23(16):21159–21164, Aug 2015.

[31] Andreas Hugi, Gustavo Villares, Stéphane Blaser, H. C. Liu, and Jŕôme Faist1. Mid-infrared frequency comb based on a quantum cascade laser. *Nature*, 492(229), 2012.

[32] Wenjia Zhou, Donghai Wu, Ryan McClintock, Steven Slivken, and Manijeh Razeghi. High performance monolithic, broadly tunable mid-infrared quantum cascade lasers. *Optica*, 4(10):1228–1231, Oct 2017.

[33] Yu Yao, William O. Charles, Tracy Tsai, Jianxin Chen, Gerard Wysocki, and Claire F. Gmachl. Broadband quantum cascade laser gain medium based on a "continuum-to-bound" active region design. *Applied Physics Letters*, 96(21):211106, 2010.

[34] Kazuue Fujita, Shinichi Furuta, Tatsuo Dougakiuchi, Atsushi Sugiyama, Tadataka Edamura, and Masamichi Yamanishi. Broad-gain ($\delta\lambda/\lambda$0 0.4), temperature-insensitive (t0 510k) quantum cascade lasers. *Opt. Express*, 19(3):2694–2701, Jan 2011.

[35] Yu Yao, Xiaojun Wang, Jen-Yu Fan, and Claire F. Gmachl. High performance "continuum-to-continuum" quantum cascade lasers with a broad gain bandwidth of over 400 cm^1. *Applied Physics Letters*, 97(8):081115, 2010.

[36] Kazuue Fujita, Tadataka Edamura, Shinichi Furuta, and Masamichi Yamanishi. High-performance, homogeneous broad-gain quantum cascade lasers based on dual-upper-state design. *Applied Physics Letters*, 96(24):241107, 2010.

[37] Paul Zorabedian. 8 - tunable external-cavity semiconductor lasers. In F.J. Duarte, editor, *Tunable Lasers Handbook*, Optics and Photonics, pages 349 – 442. Academic Press, San Diego, 1995.

[38] Andreas Hugi. *Single-mode and comb operation of broadband quantum cascade lasers*. PhD thesis, ETH Zürich, 2013.

[39] Michael G. Littman and Harold J. Metcalf. Spectrally narrow pulsed dye laser without beam expander. *Appl. Opt.*, 17(14):2224–2227, Jul 1978.

[40] P. Zorabedian and W. R. Trutna. Interference-filter-tuned, alignment-stabilized, semiconductor external-cavity laser. *Opt. Lett.*, 13(10):826–828, Oct 1988.

[41] Jan Kischkat, Mykhaylo P. Semtsiv, Mikaela Elagin, Grygorii Monastyrskyi, Yuri Flores, Sergii Kurlov, Sven Peters, and W. Ted Masselink. Alignment-stabilized interference filter-tuned external-cavity quantum cascade laser. *Opt. Lett.*, 39(23):6561–6564, Dec 2014.

[42] G. W.and Ochoa J. R.and Manfra M. J. and Cook C. C. Le, H. Q.and Turner and Y.H. Zhang. Broad wavelength tunability of gratingcoupled external cavity midinfrared semiconductor lasers. *Applied Physics Letters*, 69(19):2804–2806, 1996.

[43] G. P. Luo, C. Peng, H. Q. Le, S. S. Pei, W.-Y. Hwang, B. Ishaug, J. Um, James N. Baillargeon, and C.-H. Lin. Grating-tuned external-cavity quantum-cascade semiconductor lasers. *Applied Physics Letters*, 78(19):2834–2836, 2001.

[44] Richard Maulini, Arun Mohan, Marcella Giovannini, Jérôme Faist, and Emilio Gini. External cavity quantum-cascade laser tunable from 8.2to10.4μm using a gain element with a heterogeneous cascade. *Applied Physics Letters*, 88(20):201113, 2006.

[45] J. Faist, D. Hofstetter, M. Beck, T. Aellen, M. Rochat, and S. Blaser. Bound-to-continuum and two-phonon resonance, quantum-cascade lasers for high duty cycle, high-temperature operation. *IEEE Journal of Quantum Electronics*, 38(6):533–546, June 2002.

[46] hamamatsu.com. `https://www.hamamatsu.com/`, 1953.

[47] Tatsuo Dougakiuchi, Kazuue Fujita, Naota Akikusa, Atsushi Sugiyama, Tadataka Edamura, and Masamichi Yamanishi. Broadband tuning of external cavity dual-upper-state quantum-cascade lasers in continuous wave operation. *Applied Physics Express*, 4(10):102101, 2011.

[48] G. Eisenstein. Theoretical design of single-layer antireflection coatings on laser facets. *AT T Bell Laboratories Technical Journal*, 63(2):357–364, Feb 1984.

[49] G. Eisenstein, L. Stulz, and L. Van Uitert. Antireflection coatings on semiconductor laser facets using sputtered lead silicate glass. *Journal of Lightwave Technology*, 4(9):1373–1375, September 1986.

[50] David M. Braun and Roger L. Jungerman. Broadband multilayer antireflection coating for semiconductor laser facets. *Opt. Lett.*, 20(10):1154–1156, May 1995.

[51] Y. Bidaux, R. Terazzi, A. Bismuto, T. Gresch, S. Blaser, A. Muller, and J. Faist. Measurements and simulations of the optical gain and anti-reflection coating modal reflectivity in quantum cascade lasers with multiple active region stacks. *Journal of Applied Physics*, 118(9):093101, 2015.

[52] Yohei Matsuoka, Mykhaylo P. Semtsiv, and W. Ted Masselink. 4 - quantum cascade lasers. In Eric Tournié and Laurent Cerutti, editors, *Mid-infrared Optoelectronics*, Woodhead Publishing Series in Electronic and Optical Materials, pages 131 – 179. Woodhead Publishing, 2020.

[53] Kazuue Fujita, Shinichi Furuta, Tatsuo Dougakiuchi, Atsushi Sugiyama, Tadataka Edamura, and Masamichi Yamanishi. Broad-gain ($\delta\lambda/\lambda$0 0.4), temperature-insensitive (t0 510k) quantum cascade lasers. *Opt. Express*, 19(3):2694–2701, Jan 2011.

[54] I. Vurgaftman, J. R. Meyer, and L. R. Ram-Mohan. Band parameters for iii-v compound semiconductors and their alloys. *Journal of Applied Physics*, 89(11):5815–5875, 2001.

[55] Servin Rathi, Jyotika Jogi, Mridula Gupta, and R.S. Gupta. Modeling of hetero-interface potential and threshold voltage for tied and separate nanoscale inalas-ingaas symmetric double-gate hemt. *Microelectronics Reliability*, 49(12):1508 – 1514, 2009. Special Section on Electrostatic Discharge Reliability.

[56] Franz Schwabl. *Quantum mechanics*. Springer, 2007.

[57] Peter YU and Manuel Cardona. *Fundamentals of Semiconductors*. Springers, 2010.

[58] Chipworks inc. `https://www.chipworks.com/index.php`, 2013.

[59] www.alpeslasers.ch. `http://www.alpeslasers.ch`, 2013.

[60] Simon M. Sze and Kwok K. Ng. *Physics of Semiconductor Devices*. 2006.

[61] Ming-Kwei Lee and Simon M. Sze. *Semiconductor Devices: Physics and Technology, 3rd Edition*. 2012.

[62] Paul Harrison. *Quantum wells, wires and dots: theoretical and computational physics of semiconductor nanostructures, 3rd edition*. Wiley, 2011.

[63] Synopsys inc. `https://www.synopsys.com/`.

[64] Silvaco inc. `https://www.silvaco.com/`.

[65] Jan-Ferenc Kischkat. *External cavity quantum cascade lasers*. PhD thesis, Humboldt-Universität zu Berlin, 2014.

[66] Richard Maulini. *Broadly tunable mid-infrared quantum cascade lasers for spectroscopic applications*. PhD thesis, Université de Neuchâtel, 2006.

[67] Guipeng Luo, Chuan Peng, H. Q. Le, Shin-Shem Pei, Hao Lee, Wen-Yen Hwang, B. Ishaug, and Jun Zheng. Broadly wavelength-tunable external cavity, mid-infrared quantum cascade lasers. *IEEE Journal of Quantum Electronics*, 38(5):486–494, May 2002.

[68] Yohei Matsuoka, Sylvain Mathonnière, Mykhaylo P. Semtsiv, and W. Ted Masselink. Angled facet waveguide quantum cascade laser for external cavity system. *Proc. SPIE*, 10553:10553–10553–6, 2018.

[69] H. Angus MacLeod. *Thin-Film Optical Filterst*. CRC Press, 4 edition, 2010.

[70] Alfred Thelen. *Design of Optical Interference Coatings*. McGraw-Hill, 1988.

[71] Michael Bass, Casimer DeCusatis, Jay Enoch, Vasudevan Lakshminarayanan, Guifang Li, Carolyn Macdonald, Virendra Mahajan, and Eric Van Stryland. *Handbook of Optics, Third Edition Volume I: Geometrical and Physical Optics, Polarized Light, Components and Instruments(Set)*. McGraw-Hill, Inc., New York, NY, USA, 3 edition, 2010.

[72] Norberts Kaiser and Hans K. Pulker. *Optical Interference Coatings*. Springer, 2003.

[73] Pochi Yeh. *Optical Waves in Layered Media*. Wiley, 2005.

[74] Katharine B Blodgett. Reduction of surface reflection, 06 1938.

[75] Katharine B Blodgett. Low-reflectance glass, 04 1939.

[76] Howard E. Rhodes. Image sensor and pixel having an anti-reflective coating over the photodiode, 11 2004.

[77] Kazuhiro Yamada, Yasuhiro Sakai, Hiroyuki Nakayama, and Maki Yamada. Image sensor and pixel having an anti-reflective coating over the photodiode, 01 2005.

[78] A. Lambrechts, P. Gonzalez, B. Geelen, P. Soussan, K. Tack, and M. Jayapala. A cmos-compatible, integrated approach to hyper- and multispectral imaging. In *2014 IEEE International Electron Devices Meeting*, pages 10.5.1–10.5.4, Dec 2014.

[79] Andre G. Lareau, Bradford Speer, William R. Pfister, Stephen R. Beran, Barry Swartz, James P. Karins, Robert J. Lintell, and Christopher P. Warren. Multispectral or hyperspectral imaging system and method for tactical reconnaissance, 04 2002.

[80] Boyang Zhang, Joshua Hendrickson, Nima Nader, Hou-Tong Chen, and Junpeng Guo. Metasurface optical antireflection coating. *Applied Physics Letters*, 105(24):241113, 2014.

[81] III James Edward Carey and Eric Mazur. Silicon-based visible and near-infrared optoelectric devices, 05 2001.

[82] Sionyx inc. `https://www.sionyx.com/`, 2001.

[83] Svetoslav Koynov, Martin S. Brandt, and Martin Stutzmann. Black nonreflecting silicon surfaces for solar cells. *Applied Physics Letters*, 88(20):203107, 2006.

[84] Angus Macleod. The early days of optical coatings. *Journal of Optics A: Pure and Applied Optics*, 1(S):779, 1999.

[85] throlabs.com. `https://www.thorlabs.com/`, 1989.

[86] edmondoptics.com. `https://www.edmundoptics.com`/, 1942.

[87] A. V. Tikhonravov, M. K. Trubetskov, and G. W. DeBell. Optical coating design approaches based on the needle optimization technique. *Appl. Opt.*, 46(5):704–710, Feb 2007.

[88] Alexander V. Tikhonravov, Michael K. Trubetskov, and Gary W. DeBell. Application of the needle optimization technique to the design of optical coatings, Oct 1996.

[89] A. V. Tikhonravov, V. G. Zhupanov, V. N. Fedoseev, and M. K. Trubetskov. Design and production of antireflection coating for the 8–10 µm spectral region. *Opt. Express*, 22(26):32174–32179, Dec 2014.

[90] Optilayer. `https://www.optilayer.com/`.

[91] Jan Kischkat, Sven Peters, Mykhaylo P. Semtsiv, Tristan Wegner, Mikaela Elagin, Grygorii Monastyrskyi, Yuri Flores, Sergii Kurlov, and W. Ted Masselink. Ultra-narrow angle-tunable fabry–perot bandpass interference filter for use as tuning element in infrared lasers. *Infrared Physics & Technology*, 67:432 – 435, 2014.

[92] Jan Kischkat, Mykhaylo P. Semtsiv, Mikaela Elagin, Grygorii Monastyrskyi, Yuri Flores, Sergii Kurlov, Sven Peters, and W. Ted Masselink. Alignment-stabilized interference filter-tuned external-cavity quantum cascade laser. *Opt. Lett.*, 39(23):6561–6564, Dec 2014.

[93] Kurt j. lesker inc. `https://www.lesker.com/`.

[94] Tristan Wegner. Ultra-narrow mid-infrared band path interference filteres, 2014.

[95] Jennifer D. Traylor Kruschwitz and Walter T. Pawlewicz. Optical and durability properties of infrared transmitting thin films. *Appl. Opt.*, 36(10):2157–2159, Apr 1997.

[96] P.W. Black and J. Wales. Materials for use in the fabrication of infrared interference filters. *Infrared Physics*, 8(3):209 – 222, 1968.

[97] W. H. Southwell. Gradient-index antireflection coatings. *Opt. Lett.*, 8(11):584–586, Nov 1983.

[98] William H. Southwell. Coating design using very thin high- and low-index layers. *Appl. Opt.*, 24(4):457–460, Feb 1985.

[99] Frederic Lemarquis, Gerard Marchand, and Claude Amra. Design and manufacture of low-absorption zns–yf3 antireflection coatings in the 3.5–16-μm spectral range. *Appl. Opt.*, 37(19):4239–4244, Jul 1998.

[100] Haluk Sankur and W. H. Southwell. Broadband gradient-index antireflection coating for znse. *Appl. Opt.*, 23(16):2770–2773, Aug 1984.

[101] Yohei Matsuoka, Sylvain Mathonnèire, Sven Peters, and W. Ted Masselink. Broadband multilayer anti-reflection coating for mid-infrared range from 7 μm to 12 μm. *Appl. Opt.*, 57(7):1645–1649, Mar 2018.

[102] Luther B. Lockhart and Peter King. Three-layered reflection-reducing coatings. *J. Opt. Soc. Am.*, 37(9):689–694, Sep 1947.

[103] Anthony E. Siegman. *Lasers*. University Science Books. Oxford University Press.

[104] P. J. S. Heim, S. A. Merritt, Z. F. Fan, M. Dagenais, and R. Leavitt. Single-angled-facet laser diode for tunable external cavity lasers. *IEEE Princeton Section Sarnoff Symposium*, pages 0130–0132, April 1995.

[105] Z. Wang, B. Mikkelsen, K. E. Stubkjaer, and D. S. Olesen. Single-layer coating for angled facet amplifier. *Electronics Letters*, 25(17):1139–1141, Aug 1989.

[106] X. Baillard, A. Gauguet, S. Bize, P. Lemonde, Ph. Laurent, A. Clairon, and P. Rosenbusch. Interference-filter-stabilized external-cavity diode lasers. *Optics Communications*, 266(2):609 – 613, 2006.

[107] Richard Maulini, Mattias Beck, Jérôme Faist, and Emilio Gini. Broadband tuning of external cavity bound-to-continuum quantum-cascade lasers. *Applied Physics Letters*, 84(10):1659–1661, 2004.

[108] Claire Gmachl, Deborah L. Sivco, Federico Capasso, and Alfred Y. Cho. Ultra-broadband semiconductor laser. *Nature*, 415(883).

[109] Robin F.C. Farrow. *Molecular Beam Epitaxy Applications to Key Materials*. Noyes Publications, 1995.

[110] Charles Kittel. *Introduction to Solid States Physics, 8th Edition*. Wily.

[111] Romain Terazzi. *Transport in quantum cascade lasers*. PhD thesis, ETH Zürich, 2012.

[112] A. Evans, S. R. Darvish, S. Slivken, J. Nguyen, Y. Bai, and M. Razeghi. Buried heterostructure quantum cascade lasers with high continuous-wave wall plug efficiency. *Applied Physics Letters*, 91(7):071101, 2007.

[113] Y. Bai, N. Bandyopadhyay, S. Tsao, S. Slivken, and M. Razeghi. Room temperature quantum cascade lasers with 27% wall plug efficiency. *Applied Physics Letters*, 98(18):181102, 2011.

[114] Alexander V. Tikhonravov, Michael K. Trubetskov, Tatiana V. Amotchkina, and J. A. Dobrowolski. Estimation of the average residual reflectance of broadband antireflection coatings. *Appl. Opt.*, 47(13):C124–C130, May 2008.

[115] Steffen Wilbrandt, Olaf Stenzel, and Norbert Kaiser. All-oxide broadband antireflection coatings by plasma ion assisted deposition: design, simulation, manufacturing and re-optimization. *Opt. Express*, 18(19):19732–19742, Sep 2010.

[116] Tatiana V. Amotchkina, Michael K. Trubetskov, Vladimir Pervak, and Alexander V. Tikhonravov. Design, production, and reverse engineering of two-octave antireflection coatings. *Appl. Opt.*, 50(35):6468–6475, Dec 2011.

[117] A. V. Tikhonravov, V. G. Zhupanov, V. N. Fedoseev, and M. K. Trubetskov. Design and production of antireflection coating for the 8–10 µm spectral region. *Opt. Express*, 22(26):32174–32179, Dec 2014.

[118] A. Wittmann, A. Hugi, E. Gini, N. Hoyler, and J. Faist. Heterogeneous high-performance quantum-cascade laser sources for broad-band tuning. *IEEE Journal of Quantum Electronics*, 44(11):1083–1088, Nov 2008.

[119] Jeyran Amirloo, Simarjeet S. Saini, and Mario Dagenais. Comprehensive study of antireflection coatings for mid-infrared lasers. *Journal of Vacuum Science & Technology A*, 34(6):061505, 2016.

[120] Yohei Matsuoka, Mykhaylo P. Semtsiv, Sven Peters, and W. Ted Masselink. Broadband multilayer antireflection coating for quantum cascade laser facets. *Opt. Lett.*, 43(19):4723–4726, Oct 2018.

[121] S. Ohke, T. Umeda, and Y. Cho. Tm-mode propagation and form birefringence in a gaas-algaas multiple quantum well optical waveguide. *Optics Communications*, 70(2):92–96, 1989.

[122] Q. Yang, M. Kinzer, R. Aidam, R. Driad, W. Bronner, S. Hugger, R. Ostendorf, F. Fuchs, and J. Wagner. Dispersion of effective refractive indices of mid-infrared quantum cascade lasers. *Journal of Applied Physics*, 112(10):103109, 2012.

[123] D. R. Kaplan and P. P. Deimel. Exact calculation of the reflection coefficient for coated optical waveguide devices. *AT T Bell Laboratories Technical Journal*, 63(6):857–877, July 1984.

[124] Jan Kischkat, Sven Peters, Bernd Gruska, Mykhaylo Semtsiv, Mikaela Chashnikova, Matthias Klinkmüller, Oliana Fedosenko, Stephan Machulik, Anna Aleksandrova, Gregorii Monastyrskyi, Yuri Flores, and W. Ted Masselink. Mid-infrared optical properties of thin films of aluminum oxide, titanium dioxide, silicon dioxide, aluminum nitride, and silicon nitride. *Appl. Opt.*, 51(28):6789–6798, Oct 2012.

[125] Bozena Jaskorzynska, Johan Nilsson, and Lars Thylén. Modal reflectivity of uptapered, tilted-facet, and antireflection-coated diode-laser amplifiers. *J. Opt. Soc. Am. B*, 8(2):484–493, Feb 1991.

[126] A. Kosterev, G. Wysocki, Y. Bakhirkin, S. So, R. Lewicki, M. Fraser, F. Tittel, and R.F. Curl. Application of quantum cascade lasers to trace gas analysis. *Applied Physics B*, 90(2):165–176, Feb 2008.

[127] Steffen Lüdeke, Marcel Pfeifer, and Peer Fischer. Quantum-cascade laser-based vibrational circular dichroism. *Journal of the American Chemical Society*, 133(15):5704–5707, 2011. PMID: 21446655.

[128] www.blockeng.com. `http://www.blockeng.com/`, 2013.

[129] www.dynasil.com/. `https://www.dynasil.com/`, 2016.

[130] www.horiba.com/. `https://www.horiba.com/`, 2016.

[131] www.shimazu.com/. `https://www.shimazu.com/`, 2016.

[132] Nicholas Stone Pavel Matousek. Prospects for the diagnosis of breast cancer by noninvasive probing of calcifications using transmission raman spectroscopy. *Journal of Biomedical Optics*, 12:12 – 12 – 8, 2007.

[133] Yu-Pei Tseng, Pascaline Bouzy, Christian Pedersen, Nick Stone, and Peter Tidemand-Lichtenberg. Upconversion raster scanning microscope for long-wavelength infrared imaging of breast cancer microcalcifications. *Biomed. Opt. Express*, 9(10):4979–4987, Oct 2018.

[134] O. J. Old, G. R. Lloyd, J. Nallala, M. Isabelle, L. M. Almond, N. A. Shepherd, C. A. Kendall, A. C. Shore, H. Barr, and N. Stone. Rapid infrared mapping for highly accurate automated histology in barrett's oesophagus. *Analyst*, 142:1227–1234, 2017.

[135] R. P. Green, L. R. Wilson, E. A. Zibik, D. G. Revin, J. W. Cockburn, C. Pflügl, W. Schrenk, G. Strasser, A. B. Krysa, J. S. Roberts, C. M. Tey, and A. G. Cullis. High-performance distributed feedback quantum

cascade lasers grown by metalorganic vapor phase epitaxy. *Applied Physics Letters*, 85(23):5529–5531, 2004.

[136] O. Fedosenko, M. Chashnikova, S. Machulik, J. Kischkat, M. Klinkmüller, A. Aleksandrova, G. Monastyrskyi, M.P. Semtsiv, and W.T. Masselink. Scaling the output power of quantum-cascade lasers with a number of cascades. *Journal of Crystal Growth*, 323(1):484 – 487, 2011. Proceedings of the 16th International Conference on Molecular Beam Epitaxy (ICMBE).

[137] Matthais Zigler. *Calculating band paramteres and band diagrams with QW*. Humboldt-Unviersität zu Berlin, 2005.

[138] Yohei Matsuoka, Sven Peters, Mykhaylo P. Semtsiv, and W. Ted Masselink. External-cavity quantum cascade laser using intra-cavity outcoupling. *Opt. Lett.*, 43(15):3726–3729, Aug 2018.

[139] Tatsuo Dougakiuchi, Kazuue Fujita, Atsushi Sugiyama, Akio Ito, Naota Akikusa, and Tadataka Edamura. Broadband tuning of continuous wave quantum cascade lasers in long wavelength (¿ 10μm) range. *Opt. Express*, 22(17):19930–19935, Aug 2014.

[140] Richard Maulini, Arkadiy Lyakh, Alexei Tsekoun, Rowel Go, Christian Pflügl, Laurent Diehl, Federico Capasso, and C. Kumar N. Patel. High power thermoelectrically cooled and uncooled quantum cascade lasers with optimized reflectivity facet coatings. *Applied Physics Letters*, 95(15):151112, 2009.

[141] Bujin Guo, Y. Wang, C. Peng, H. L. Zhang, G. P. Luo, H. Q. Le, C. Gmachl, D. L. Sivco, M. L. Peabody, and A.Y. Cho. Laser-based mid-infrared reflectance imaging of biological tissues. *Opt. Express*, 12(1):208–219, Jan 2004.

[142] Pietro Malara, Romain Blanchard, Tobias S. Mansuripur, Aleksander K. Wojcik, Alexey Belyanin, Kazuue Fujita, Tadataka Edamura, Shinichi Furuta, Masamichi Yamanishi, Paolo de Natale, and Federico Capasso. External ring-cavity quantum cascade lasers. *Applied Physics Letters*, 102(14):141105, 2013.

[143] Wenjia Zhou, Donghai Wu, Ryan McClintock, Steven Slivken, and Manijeh Razeghi. High performance monolithic, broadly tunable mid-infrared quantum cascade lasers. *Optica*, 4(10):1228–1231, Oct 2017.

[144] Quanyong Lu, Donghai Wu, Steven Slivken, and Manijeh Razeghi. High efficiency quantum cascade laser frequency comb. *Scientific Reports*, 7(43806), 2017.

[145] Hyungtak Seo, Sung Bae Kim, Jongkook Song, Yangdo Kim, Hyun Soh, Young Chai Kim, and Hyeongtag Jeon. Low temperature remote plasma cleaning of the fluorocarbon and polymerized residues formed during contact hole dry etching. *Journal of Vacuum Science & Technology B: Microelectronics and Nanometer Structures Processing, Measurement, and Phenomena*, 20(4):1548–1555, 2002.

Acknowledgements

First of all, I deeply thank to my supervisor, Prof. Dr. W. Ted Masselink, for giving this PhD opportunity and supporting my research for this three year. He always encouraged my work and helped me for moving forward.

I would also give a special appreciation to Dr. M. P. Semtsiv, for helping experiment procedures, especially the QCL growth part. Thanks to his contribution, we could achieve great results. I also express great appreciation to Dr. J. Kischkat and Ms. E. Ränger for the instruction of e-beam system as well as its know-how. I thank my special colleagues, Mr. S. Mathoniere, and Mr. J. Tomko for good discussions.

I give great appreciation to Ms. K. Braune for supporting my experiments and for maintaining good working environment, and to Ms. I. Newton for managing every administrative work and smoothing our daily work. Overall, I thank all the colleagues in our group for their supports and also sharing wonderful time during this PhD work,

I have also very special thanks for Mr. E. Travkin, Ms. H. Memmi, and Dr. S. Kalusniak at Photonics group, for FTIR measurement and also for giving me constructive advice for better measurements.

I appreciate the staffs of workshop at the institute for manufacturing tailor-made experimental setup. I was always impressed their high quality works, which finally gives a good number of papers.

I appreciate for funding of our project (MidTECH), Horizon 2020 Framework Programme (H2020) under the Marie Skłodowska-Curie grant agreement.

Finally, I thank to my mother, father, sisters, and my friend, Yuri.

Publications

Journal papers

- **Y. Matsuoka**, S. Mathonnèire, S. Peters and W. T. Masselink; *Appl. Opt.*, 7, 57(2018), 1645–1649
"Broadband multilayer anti-reflection coating for mid-infrared range from 7 μm to 12 μm"

- **Y. Matsuoka**, S. Mathonnèire, M. P. Semtsiv and W. T. Masselink; *Proc. SPIE*, 10553(2018), 10553–10553–6
"Angled facet waveguide quantum cascade laser for external cavity system"

- S. Mathonnière, J. Tomko, **Y. Matsuoka**, S. Peters, J. Kischkat, M. Semtsiv and W. Ted Masselink; *Applied Physics B*, 124(7), 149, 2018
"External cavity quantum cascade laser emitting from 12.3 to 13.2 μm"

- **Y. Matsuoka**, S. Peters, M. P. Semtsiv and W. T. Masselink; *Opt. Lett.*, 43, 3726-3729 (2018)
"External cavity quantum cascade laser using intra-cavity out-coupling"

- M. P. Semtsiv, S. S. Kurlov, D. Alcer, **Y. Matsuoka**, J.-F. Kischkat, O. Bierwagen and W. T. Masselink; *Appl. Phys. Lett.*, 113(12), 121110, 2018
"Reduced interface roughness scattering in InGaAs/InAlAs quantum cascade lasers grown on (411)A InP substrates"

- **Y. Matsuoka**, M. P. Semtsiv, S. Peters, and W. T. Masselink; *Opt. Lett.*, 43, 4723-4726 (2018)
"Broadband multilayer antireflection coating on quantum cascade laser facets"

- **Y. Matsuoka**, S. Mathonnèire, S. Peters, M. P. Semtsiv and W. T. Masselink; (*in submission*)
  "External cavity quantum cascade laser using angled facet optical amplifier tunable from 8.5 to 10.5 μm"

Conference

- **Y. Matsuoka**, JF. Kischkat, MP. Semtsiv, and WT. Masselink
  "Broadly Tunable External Cavity Quantum Cascade Laser for Medical Hyperspectral Imaging at 11 μm Wavelength Region"
  Poster in CLEO Europe 2017 JSIII-P.1, June 27, 2017 @Munich, Germany

- **Y. Matsuoka**, S. Mathonnèire, M. P. Semtsiv and W. T. Masselink
  "Angled facet waveguide quantum cascade laser for external cavity system"
  Poster in SPIE Photonic West 2018, 10553, Novel In-Plane Semiconductor Lasers XVII, @San Francisco

- **Y. Matsuoka**, S. Peters, M. P. Semtsiv and W. T. Masselink
  "Demonstration of broadband multilayer anti-reflection coating on quantum cascade laser facet from 8.0 to 12.0 μm range"
  Oral presentation in the 65$^{\text{th}}$ Japan Society of Applied Physics, Spring meeting 2018: 17p-B403-4, March 17, 2018 @Waseda University

- **Y. Matsuoka**, S. Peters, M. P. Semtsiv and W. T. Masselink
  "Tunable external cavity quantum cascade laser using intra-cavity outcoupling"
  e-Poster in CLEO 2018, 2929654, May 15th @San José

Selbständigkeitserklärung

Ich erkläre, dass ich die vorliegende Arbeit selbständig und nur unter Verwendung der angegebenen Literatur und Hilfsmittel angefertigt habe.

Berlin, den 07.03.2019 Yohei MATSUOKA